REPORT DOCUMENTATION PAGE

AFRL-SR-AR-TR-05-0205

Public reporting burden for this collection of information is estimated to average 1 hour per response, including the time for re maintaining the data needed, and completing and reviewing this collection of information. Send comments regarding this bur suggestions for reducing this burden to Washington Headquarters Services, Directorate for Information Operations and Repc to the Office of Management and Budget, Paperwork Reduction Project (0704-0188), Washington, DC 20503

1. AGENCY USE ONLY (Leave blank)	2. REPORT DATE	3. REPORT TYPE AND DATES COVERED
	April 22, 2005	Final Report 03/01/2002 - 12/31/2004

4. TITLE AND SUBTITLE
Effects of Stress on Localized Corrosion in Al and Al Alloys

5. FUNDING NUMBERS
AFOSR Grant No. F49620-02-1-0148

6. AUTHOR(S)
Gerald S. Frankel and Stanislav I. Rokhlin

7. PERFORMING ORGANIZATION NAME(S) AND ADDRESS(ES)
The Ohio State University Research Foundation
1960 Kenny Rd.
Columbus, OH 43210

8. PERFORMING ORGANIZATION REPORT NUMBER
GRT869577 / 742142

9. SPONSORING / MONITORING AGENCY NAME(S) AND ADDRESS(ES)
Maj. Jennifer Gresham, PhD
AFOSR Program Manager
Surface & Interfacial Science
875 North Randolph St.
Suite 325, Room 3112
Arlington, VA 22203

NL

303 10. SPONSORING / MONITORING AGENCY REPORT NUMBER
Air Force Office of Scientific Res
(50010105)

11. SUPPLEMENTARY NOTES
N/A

12a. DISTRIBUTION / AVAILABILITY STATEMENT
Unclassified and Unlimited

DISTRIBUTION STATEMENT A
Approved for Public Release
Distribution Unlimited

12b. DISTRIBUTION CODE
N/A

13. ABSTRACT *(Maximum 200 Words)*

In order to predict the development of corrosion, a fundamental understanding of the corrosion processes is required. In particular, the effects of mechanical stress on corrosion and their synergistic interactions must be understood. In this project, certain effects of stress on localized corrosion in AA2024-T3 were studied by a variety of techniques, including in situ microfocal x-ray radiography. Specifically oriented slices of material were taken from a wrought plate, stressed in tension either to a fixed displacement or a fixed load, exposed to special electrochemical cells, and imaged by radiography. These experiments image the full distribution of corrosion sites and allow for competition between multiple sites. For instance, the longest crack, at which the stress intensity is the highest, has been seen to stop growing and be overtaken by another crack that had been shorter. Quantitative aspects of phase-contrast microfocus X-ray imaging of Al alloys have been developed. Phase-contrast X-ray imaging provides enhanced image contrast and improved edge definition and is important for further development toward NDE of structural materials. The effects of compressive stress and prior deformation on localized corrosion have also been studied. The first breakdown in AA7075-T6 has been shown to be caused by transient dissolution of a surface active layer created by deformation during sample preparation.

14. SUBJECT TERMS Stress corrosion cracking, Intergranular corrosion, Foil penetration, Aluminum alloys, Extended brick wall model, Grain size distribution, Localized corrosion kinetics, Random number generation, Intermetallic particles, X-ray radiography, Compressive stress, Low plastic burnishing

15. NUMBER OF PAGES
172

16. PRICE CODE N/A

17. SECURITY CLASSIFICATION OF REPORT	18. SECURITY CLASSIFICATION OF THIS PAGE	19. SECURITY CLASSIFICATION OF ABSTRACT	20. LIMITATION OF ABSTRACT
Unclassified	Unclassified	Unclassified	Unclassified and Unlimited

Final Report

AFOSR Grant No. F49620-02-1-0148

Effects of Stress on Localized Corrosion in Al and Al Alloys

Principal Investigators:

Gerald S. Frankel
Fontana Corrosion Center
Department of Materials Science and Engineering

Stanislav I. Rokhlin
Dept. of Industrial, Welding and Systems Engineering

The Ohio State University
477 Watts Hall, 2041 College Rd.
Columbus, OH 43210

April 14, 2005

DISTRIBUTION STATEMENT A
Approved for Public Release
Distribution Unlimited

20050608 049

Table of Contents

1. **FOREWORD** 3

2. **OBJECTIVES AND STATUS OF EFFORT** 3

3. **ACCOMPLISHMENTS** 4

3.1 EFFECT OF APPLIED TENSILE STRESS ON INTERGRANULAR CORROSION OF AA2024 4
3.2 STATISTICAL MODELING AND COMPUTER SIMULATION OF INTERGRANULAR CORROSION GROWTH IN AA2024-T3 ALUMINUM ALLOY 4
3.3 STATISTICAL MODELING OF MINIMUM INTERGRANULAR CORROSION PATH LENGTH IN HIGH STRENGTH ALUMINUM ALLOY 5
3.4 PHASE-CONTRAST X-RAY IMAGING FOR NONDESTRUCTIVE EVALUATION OF MATERIALS 5
3.5 IN SITU X- RAY RADIOGRAPHIC STUDY OF STRESS CORROSION CRACKING IN AA2024-T3 5
3.6 APPLICATION OF PHASE-CONTRAST MICRORADIOGRAPHY IN NDE 6
3.7 EFFECTS OF COMPRESSIVE STRESS ON LOCALIZED CORROSION IN AA2024-T3 ALLOY 6
3.8 THE EFFECTS OF PRIOR DEFORMATION ON LOCALIZED CORROSION OF AL ALLOYS 7
3.9 IN SITU STUDY OF INTERGRANULAR CORROSION AND INTERGRANULAR STRESS CORROSION CRACKING IN AA2024-T3 7

4. **PERSONNEL** 8

5. **PUBLICATIONS** 8

5.1 PEER REVIEWED PUBLICATIONS - FULL MANUSCRIPTS IN APPENDIX 8
5.2 BOOK CHAPTERS AND PUBLICATIONS IN CONFERENCE PROCEEDINGS 8
5.3 THESES 9

6. **INTERACTIONS/TRANSITIONS** 9

6.1 PARTICIPATION/PRESENTATION AT MEETINGS, CONFERENCES, SEMINARS 9
6.2 CONSULTATIVE AND ADVISORY FUNCTIONS 10
6.3 TRANSITIONS 10

7. **NEW DISCOVERIES, INVENTIONS, AND PATENT DISCLOSURES** 10

8. **HONORS/AWARDS** 10

9. **APPENDICES** 10

1. Foreword

This report summarizes research performed for the Air Force Office of Scientific Research under Contract No. F49620-02-1-0148, "Effects of Stress on Localized Corrosion in Al and Al Alloys." The contract began on March 1, 2002, and is scheduled to run for a total of 36 months. The Principal Investigators are Prof. G. S. Frankel, Department of Materials Science and Engineering, The Ohio State University, and Prof. Stanislav I. Rokhlin, Dept. of Industrial, Welding and Systems Eng. The AFOSR program manager has been Lt. Col. Paul Trulove, Ph.D., and is now Major Jennifer Gresham, Ph.D. This is a final report covering the accomplishments during the full term of the contract.

2. Objectives and Status of Effort

In order to predict the development of corrosion, a fundamental understanding of the corrosion processes is required. In particular, the effects of mechanical stress on corrosion and their synergistic interactions must be understood. This project addresses certain effects of stress on localized corrosion in AA2024-T3.

The effects of an applied tensile stress on the kinetics of both intergranular and pitting corrosion are studied using the foil penetration technique. The technique employs a jig that applies a constant tensile displacement onto the foil sample. Penetration times through the foil provide a quantitative measurement of the growth kinetics. The work focuses on alloy AA2024-T3. The effect of a number of parameters are studied, including applied stress level, applied potential, orientation relative to the rolling direction, microstructure, temper, and environment. The type of corrosion can be controlled by means of the applied potential. The effects of applied compressive stress have also been studied.

X-ray radiography is required to assess the extent of corrosion for certain approaches, and this technique has the further advantage of providing information on the full distribution of corrosion sites, not just the fastest-growing site as in the case of the foil penetration technique.

The effect of prior applied stress on the corrosion susceptibility of AA2024-T3 is also being determined. This work is complementary to several programs that have been studying the converse, i.e. the effects of prior corrosion on mechanical properties. The prior applied stress is in the form of fatigue or tensile stress into the elastic or plastic region (in inert environment). The samples are not stressed to failure. The effects of this pretreatment on the sample surface are documented and the samples are exposed to corrosive environments in the unloaded condition to determine the effects of the stress on the susceptibility to localized corrosion initiation.

The results of the proposed program will provide a fuller understanding of the synergistic interactions of stress and environment on the localized corrosion of Al alloys, which will in turn facilitate the development of predictive models for damage development.

3. Accomplishments

Most of the accomplishments of this program already have been or soon will be submitted for publication. The full publications are given in appendices, and the work is summarized in this section.

3.1 Effect of Applied Tensile Stress on Intergranular Corrosion of AA2024

Xiaodong Liu, G. S. Frankel, B. Zoofan and S. I. Rokhlin, *Corr. Sci.*, **46**, 405-425 (2004).

The effect of uniaxial tensile stress on intergranular corrosion (IGC) of AA2024-T3 was studied using the foil penetration technique. Standard ASTM G49 fixed-displacement jigs were modified to allow the use of sheet samples, which were then attached to an electrochemical cell as in the foil penetration setup. The time for IGC to penetrate samples of varying thickness was monitored. This method provides a new approach to bridge the gap between GC and intergranular stress corrosion cracking (IGSCC). Samples with various orientations elative to the rolling direction were studied in 1.0 M NaCl at controlled anodic potentials. Potentiodynamic polarization measurements indicated that the two breakdown potentials typically observed for AA2024-T3 were lower for stressed samples than for unstressed samples, and the current at a given potential was higher. The penetration rate depended on potential and was higher for stressed samples than for unstressed samples. The primary form of attack above the higher breakdown potential was IGSCC, whereas pitting dominated between the two breakdown potentials. Stress had a larger effect on penetration rate at higher applied potentials, indicating that pitting is less susceptible to the effects of stress than a properly oriented IGC crevice. The effects of stress on the penetration rates in various orientations were strongly linked to the anisotropic microstructure. X-ray microfocal radiography and optical microscopy of cross-sections were used to characterize IGSCC defects in thin penetrated foils. In certain orientations, crack faces were parallel rather than perpendicular to the stress direction as a result of the constraints of the microstructure on the orientation of the IGC. Implications for the mechanisms of IGC and IGSCC are discussed.

3.2 Statistical Modeling and Computer Simulation of Intergranular Corrosion Growth in AA2024-T3 Aluminum Alloy

Shiling Ruan, D. A. Wolfe, and G. S. Frankel, *J. Stat. Plan. Inference*, **126,** 553-568 (2004). (work funded by previous funding cycle of this grant)

An extension of a brick wall model developed in a previous paper (Technometrics, to appear) was used to describe intergranular corrosion in AA2024-T3 aluminum alloys. The extended model simulates the behavior of corrosion paths at intersections of grain

boundaries within the metal sample. Situations considered include the cases where a corrosion path might assume an upward turn, skip an intersection (not turn) or split into branches. The splitting of a corrosion path results in a smaller median of the minimum order statistic while the other factors increase the median of the minimum order statistic. Moreover, a larger number of grain layers increases the minimum path length for a sample with given thickness. With a proper combination of these factors, the extended model is able to provide a good 5t to the experimental data developed by the foil penetration technique.

3.3 Statistical Modeling of Minimum Intergranular Corrosion Path Length in High Strength Aluminum Alloy

S. Ruan, D. Wolfe, Weilong Zhang, and G. S. Frankel, *Technometrics*, **46**, 69-75 (2004). (work funded by previous funding cycle of this grant)

In this article a brick wall model is developed to describe the relationship between the minimum intergranular corrosion (IGC) path length and the aspect ratio of grains of high strength wrought aluminum alloy AA 2024-T3. We study the distribution of the horizontal distance that a corrosion path will travel in the metal and fit the model to an actual corrosion data set using the method of moments. The distribution of the horizontal distance of a corrosion path along a given grain is assumed to be uniformly distributed given the length of the grain, which is itself modeled by a gamma distribution. A modified brick wall model is proposed that imposes a distribution on the vertical distance traveled by the corrosion path as well. We use computer simulation to evaluate the fit of these models.

3.4 Phase-contrast X-ray imaging for nondestructive evaluation of materials

B. Zoofan, J.-Y. Kim, S. I. Rokhlin, and G. S. Frankel, submitted to *J. Appl. Phys.,* 1/04.

Quantitative aspects of phase-contrast microfocus X-ray imaging of structural materials (Al alloys and polymers) are considered. The effect of the experimental parameters on the phase contrast in the hard X-ray regime is investigated for application to nondestructive evaluation (NDE) of materials. For this the diffraction field in an object from a small finite X-ray source is simulated and the effects of geometrical and material parameters on the X-ray phase-contrast image are obtained. Experimental phase-contrast images of small defects are obtained with a 5 micron microfocal X-ray source and compared with those from computer simulation as a function of geometrical magnification and photon energy. The phase-contrast X-ray imaging provides enhanced image contrast and improved edge definition and is important for further development toward NDE of structural materials.

3.5 In Situ X- ray Radiographic Study of Stress Corrosion Cracking in AA2024-T3

Xiaodong Liu, G. S. Frankel, B. Zoofan and S. I. Rokhlin, submitted to *Corrosion*, 2/05.

Despite the many studies that have addressed stress corrosion cracking (SCC) in high strength aluminum alloys, the separate contributions of stress and electrochemistry to the SCC process is still a matter of dispute. Moreover, the conventional fracture mechanics approaches constrain SCC to a single crack per specimen, which eliminates interaction between nearby cracks. In this study, a new non-destructive evaluation approach was developed to investigate stress corrosion cracking in AA2024-T3 (UNS A92024). A microfocal x-ray radiography technique was employed to image multiple intergranular SCC cracks in situ. A modified ASTM G49 stressing jig was used to apply a fixed tensile displacement to a thin sheet sample, and a novel electrochemical cell containing flowing 1 M NaCl was attached to the edge of the sample. Potentiostatic polarization was applied at a potential that promoted intergranular corrosion. The initiation and growth of multiple intergranular stress corrosion cracks were characterized using transmission microfocal x-ray radiography. The kinetics of intergranular stress corrosion cracking growth was found to be in good agreement with the results of a completely different technique, the foil penetration method, which reflects the validity of the new approach. Interestingly, in many experiments the deepest crack at the beginning of the experiment was found to slow and stop growing, and was then surpassed by another crack that eventually penetrated through the sample. The competition between multiple intergranular stress corrosion cracks is not explained by the theory of mechanical fracture in inert environments. The possible mechanisms underlying this competition between cracks are discussed.

3.6 Application of Phase-Contrast Microradiography in NDE

B. Zoofan, S. I. Rokhlin and G. S. Frankel, submitted to *Mat. Eval.*, 3/05.

Practical aspects of microfocal X-ray image enhancement utilizing phase-contrast effects are considered. Optimization of the experimental method to achieve phase contrast is described for application to nondestructive evaluation of materials. Experimental phase-contrast images of porosity and corrosion pits obtained with a 5-micron microfocal X-ray source are compared with absorption-contrast images demonstrating significant enhancement of image quality. The phase-contrast X-ray imaging provides enhanced image contrast, improved edge definition and X-ray phase information on the material.

3.7 Effects of Compressive Stress on Localized Corrosion in AA2024-T3 Alloy

Xiaodong Liu and G. S. Frankel, submitted to *Corrosion*, 4/05.

The effect of compressive stress on intergranular corrosion (IGC) of AA2024-T3 was studied under a constant load with simultaneous electrochemical measurement. A specially designed electrochemical cell was used to compress a pillar-shaped sample and control the potential at a value that promoted IGC. The extent of IGC was assessed by metallurgical cross sectional images. The effect of the compressive stress depended on the orientation of the stress relative to the elongated microstructure. Application of a compressive stress halfway to yield in the S or through-thickness direction significantly reduced the growth kinetics of IGC in the longitudinal direction, but did not eliminate it

totally. The strain change during exposure was used to quantify the change in radius of the cylindrical sample as a function of time during IGC growth. The effect of compression on reducing IGC was also assessed by the current density measured during potentiodynamic and potentiostatic polarization. The effects of residual compressive stress on IGC were studied using samples treated by low plastic burnishing (LPB), which produces a surface layer with high residual compressive stress. The results depended on the plane of the treatment.

3.8 The Effects of Prior Deformation on Localized Corrosion of Al Alloys

Zhijun Zhao and G. S. Frankel, in preparation.

In this study, the effects of prior deformation on the localized corrosion of high strength Al alloys is studied. Samples were deformed in tension to various extents and examined using electrochemical techniques and by simple immersion and observation. In AA2024-T3, prior deformation resulted in an increase in the passive current density and elimination of the peak associated with the first breakdown. In AA7075-T6, both the first and second breakdown potentials decreased with increasing amounts of prior deformation. The amount of attack on the surface of AA2024-T6 during open circuit exposure to chloride solutions increased with increasing amount of prior deformation. An in situ observation technique was developed to investigate the cause of the first breakdown in AA7075-T6. Compelling evidence was generated to support the notion that the first breakdown is caused by transient dissolution of a surface active layer created by deformation during sample preparation.

3.9 In Situ Study of Intergranular Corrosion and Intergranular Stress Corrosion Cracking in AA2024-T3

Xiaodong Liu, G. S. Frankel, B. Zoofan and S. I. Rokhlin, in preparation.

Microfocal x-ray radiography was used as an in situ non-destructive evaluation method to study intergranular corrosion (IGC) and intergranular stress corrosion cracking (IGSCC) in AA2024-T3. This method provides information on the morphology and growth kinetics of multiple IGC and IGSCC sites, as well as the transition between IGC and IGSCC. An elastic strain was applied using a modified ASTM G49 fixed displacement jig. Application of tensile stress in the transverse direction, parallel to the IGC faces growing in the L direction, led to coalescence of the IGC sites and transition into IGSCC that was nominally normal to the applied stress. Fractography and micrography of penetrated foils presented ex situ visions of the coalesced IGCs. Potentiodynamic polarization revealed that the small elastic strain decreased the breakdown potential. Current transient measured during potentiostatic polarization showed the effects of stress on IGC growth.

4. Personnel

1. Gerald S. Frankel, Professor
2. Stanislav I. Rohklin, Professor
3. Xiaodong Liu, Graduate Student, 100%
4. Zhijun Zhao, Graduate Student, 100%
5. Bahman Zoofan, Graduate Student , 50%
6. J.-Y. Kim, Post Doc, 50%

5. Publications

5.1 Peer reviewed publications - full manuscripts in Appendix

Xiaodong Liu, G. S. Frankel, B. Zoofan and S. I. Rokhlin, "Effect of Applied Tensile Stress on Intergranular Corrosion of AA2024-T3," *Corr. Sci.*, **46**, 405-425 (2004).

Shiling Ruan, D. A. Wolfe, and G. S. Frankel, "Statistical Modeling and Computer Simulation of Intergranular Corrosion Growth in AA2024-T3 Aluminum Alloy," *J. Stat. Plan. Inference*, **126,** 553-568 (2004). (work funded by previous funding cycle of this grant)

S. Ruan, D. Wolfe, Weilong Zhang, and G. S. Frankel, "Statistical Modeling of Minimum Intergranular Corrosion Path Length in High Strength Aluminum Alloy," *Technometrics*, **46**, 69-75 (2004). (work funded by previous funding cycle of this grant)

B. Zoofan, J.-Y. Kim, S. I. Rokhlin, and G. S. Frankel, "Phase-contrast X-ray imaging for nondestructive evaluation of materials," submitted to *J. Appl. Phys.*, 1/04.

Xiaodong Liu, G. S. Frankel, B. Zoofan and S. I. Rokhlin, "In Situ X- ray Radiographic Study of Stress Corrosion Cracking in AA2024-T3," submitted to *Corrosion*, 2/05.

B. Zoofan, S. I. Rokhlin and G. S. Frankel, "Application of Phase-Contrast Microradiography in NDE," submitted to *Mat. Eval.*, 3/05.

Xiaodong Liu and G. S. Frankel, "Effects of Compressive Stress on Localized Corrosion in AA2024-T3 Alloy," submitted to *Corrosion*, 4/05.

Zhijun Zhao and G. S. Frankel, "The Effects of Prestress on Localized Corrosion of Al Alloys," in preparation.

Xiaodong Liu, G. S. Frankel, B. Zoofan and S. I. Rokhlin, In Situ Study of Intergranular Corrosion and Intergranular Stress Corrosion Cracking in AA2024-T3, in preparation.

5.2 Book chapters and publications in conference proceedings

S. I. Rokhlin, B. Zoofan, G. S. Frankel, "Microradiographic and Foil Penetration Methods for Quantification of Localized Corrosion," in *Nondestructive Materials*

Characterization with Application to Aerospace Materials, N. Meyendorf, P. Nagy, S. Rokhlin, editors, Springer-Verlag GmbH & Co. 2003.

G. S. Frankel, "Pitting Corrosion," in *Metals Handbook*, Vol 13A, S. D. Cramer and B. S. Covino, Jr., eds, ASM International, 2003.

Xiaodong Liu, G. S. Frankel, B. Zoofan and S. I. Rokhlin, "Imaging and Characterization of Multiple Stress Corrosion Cracks in AA2024-T3 by X-ray Radiography," The Electrochemical Society, PV 2004-14, 2004.

B. Zoofan, J.-Y. Kim, S. I. Rokhlin and G. S. Frankel "Phase contrast X-ray imaging for nondestructive evaluation of materials" in *Review of Progress in Quantitative NDE*, D. O. Thompson and D. E. Chimenti, eds., American Institute of Physics, New York, Vol. 23, 546 - 553 (2004).

X. Liu, Z. Zhao, G. Frankel, B. Zoofan, S. Rokhlin, "Effects of Stress on Localized Corrosion in Al and Al Alloys," proceedings of Triservice Corrosion Conference, Las Vegas, 2003.

B. Zoofan, J.-Y. Kim, S. I. Rokhlin and G.S. Frankel, "Phase-contrast X-ray image enhancement of corrosion damage," proceedings of Triservice Corrosion Conference, Las Vegas, 2003.

5.3 Theses

Bahman Zoofan "Quantitative microradiography and its applications to microdamage assessment", Ph.D.,Dissertation, OSU, 2004.

Xiaodong Liu, "Effects of Stress on Intergranular Corrosion in AA2024-T3," Ph.D. Thesis, OSU, expected June, 2005.

Zhijun Zhao, "Effects of Prior Deformation on Localized Corrosion of Al Alloys," Ph.D. Thesis, OSU, expected June 2006.

6. Interactions/Transitions

6.1 Participation/Presentation at Meetings, Conferences, Seminars

"Characterization of Stress Corrosion Cracking In AA2024-T3 by X-ray Radiography," Xiaodong Liu, G.S. Frankel, B. Zoofan, S.I. Rokhlin (presented by R.G. Buchheit), International Conf. on Fracture, Turin, Italy, 3/22/05.

"Imaging and Characterization of Multiple Stress Corrosion Cracks in AA2024-T3 by X-ray Radiography," Xiaodong Liu, G. S. Frankel, B. Zoofan and S. I. Rokhlin, ECS Meeting, Honolulu, HI, 10/4/04.

"Effect of Stress on Localized Corrosion in Al Alloys," Xiaodong Liu, Zhijun Zhao, G. S. Frankel, B. Zoofan and S. I. Rokhlin, Triservice Corrosion Conference, Las Vegas, 11/18/03.

B. Zoofan, J.-Y. Kim, S. I. Rokhlin and G. Frankel, "Phase-contrast X-ray image enhancement of corrosion damage" Triservice Corrosion Conference, Las Vegas, November, 2003.

6.2 Consultative and Advisory Functions

none

6.3 Transitions

none

7. New discoveries, inventions, and patent disclosures

none

8. Honors/Awards

G. S. Frankel was awarded the Alexander von Humboldt Foundation Research Award for Senior US Scientists, 2003.

G. S. Frankel was named a fellow of NACE International, 2004.

S.I. Rokhlin received two research awards form the Ohio State University: the 2004 Lumley Research Award from the College of Engineering and the 2004 Lumley Interdisciplinary Research Award.

G.S. Frankel received the OSU College of Engineering Awards Lumley Research Award, 2003.

9. Appendices

List of papers in Appendix:

Xiaodong Liu, G. S. Frankel, B. Zoofan and S. I. Rokhlin, "Effect of Applied Tensile Stress on Intergranular Corrosion of AA2024-T3," *Corr. Sci.*, **46**, 405-425 (2004).

Shiling Ruan, D. A. Wolfe, and G. S. Frankel, "Statistical Modeling and Computer Simulation of Intergranular Corrosion Growth in AA2024-T3 Aluminum Alloy," *J. Stat. Plan. Inference*, **126**, 553-568 (2004). (work funded by previous funding cycle of this grant)

S. Ruan, D. Wolfe, Weilong Zhang, and G. S. Frankel, "Statistical Modeling of Minimum Intergranular Corrosion Path Length in High Strength Aluminum Alloy," *Technometrics*, **46**, 69-75 (2004). (work funded by previous funding cycle of this grant)

B. Zoofan, J.-Y. Kim, S. I. Rokhlin, and G. S. Frankel, "Phase-contrast X-ray imaging for nondestructive evaluation of materials," submitted to *J. Appl. Phys.,* 1/04.

Xiaodong Liu, G. S. Frankel, B. Zoofan and S. I. Rokhlin, "In Situ X- ray Radiographic Study of Stress Corrosion Cracking in AA2024-T3," submitted to *Corrosion*, 2/05.

B. Zoofan, S. I. Rokhlin and G. S. Frankel, "Application of Phase-Contrast Microradiography in NDE," submitted to *Mat. Eval.*, 3/05.

Xiaodong Liu and G. S. Frankel, "Effects of Compressive Stress on Localized Corrosion in AA2024-T3 Alloy," submitted to *Corrosion*, 4/05.

Zhijun Zhao and G. S. Frankel, "Effects of Prior Deformation on Localized Corrosion of Al Alloys," in preparation.

Xiaodong Liu, G. S. Frankel, B. Zoofan and S. I. Rokhlin, In Situ Study of Intergranular Corrosion and Intergranular Stress Corrosion Cracking in AA2024-T3, in preparation.

Available online at www.sciencedirect.com
SCIENCE DIRECT®
ELSEVIER
Corrosion Science 46 (2004) 405–425
CORROSION SCIENCE
www.elsevier.com/locate/corsci

Effect of applied tensile stress on intergranular corrosion of AA2024-T3

Xiaodong Liu [a], G.S. Frankel [a,*], B. Zoofan [b], S.I. Rokhlin [b]

[a] *Fontana Corrosion Center, Department of Materials Science and Engineering, The Ohio State University, 477 Watts Hall, 2041 College Road, Columbus, OH 43210, USA*
[b] *Department of Industrial, Welding and Systems Engineering, The Ohio State University, Columbus, OH 43210, USA*

Received 5 January 2003; accepted 15 May 2003

Abstract

The effect of uniaxial tensile stress on intergranular corrosion (IGC) of AA2024-T3 was studied using the foil penetration technique. Standard ASTM G49 fixed-displacement jigs were modified to allow the use of sheet samples, which were then attached to an electrochemical cell as in the foil penetration setup. The time for IGC to penetrate samples of varying thickness was monitored. This method provides a new approach to bridge the gap between IGC and intergranular stress corrosion cracking (IGSCC). Samples with various orientations relative to the rolling direction were studied in 1.0 M NaCl at controlled anodic potentials. Potentiodynamic polarization measurements indicated that the two breakdown potentials typically observed for AA2024-T3 were lower for stressed samples than for unstressed samples, and the current at a given potential was higher. The penetration rate depended on potential and was higher for stressed samples than for unstressed samples. The primary form of attack above the higher breakdown potential was IGSCC, whereas pitting dominated between the two breakdown potentials. Stress had a larger effect on penetration rate at higher applied potentials, indicating that pitting is less susceptible to the effects of stress than a properly oriented IGC crevice. The effects of stress on the penetration rates in various orientations were strongly linked to the anisotropic microstructure. X-ray microfocal radiography and optical microscopy of cross-sections were used to characterize IGSCC defects in thin penetrated foils. In certain orientations, crack faces were parallel rather than perpendicular to the stress direction as a result of the constraints of the microstructure on the orientation of the IGC. Implications for the mechanisms of IGC and IGSCC are discussed.
© 2003 Published by Elsevier Ltd.

* Corresponding author. Tel.: +1-644-688-4128; fax: +1-614-292-9857.
E-mail address: frankel.10@osu.edu (G.S. Frankel).

0010-938X/$ - see front matter © 2003 Published by Elsevier Ltd.
doi:10.1016/S0010-938X(03)00149-5

Keywords: Stress corrosion cracking; Intergranular corrosion; Foil penetration; Aluminum alloy

1. Introduction

Localized corrosion of Al alloys in aqueous chloride solutions has been investigated using different techniques [1–5]. However, few techniques exist to study the kinetics of localized corrosion growth [6,7]. Electrochemical methods typically measure current for a given potential. In order to convert current to rate, the active area needs to be known. It is often assumed that the current flows from hemispherical pits, but this is a poor assumption for localized corrosion in Al alloys.

The foil penetration technique, which was developed by Hunkeler and Bohni [8,9], is an ideal approach to determine localized corrosion growth kinetics. It is a non-electrochemical technique in which the time to penetrate a thin foil is determined by sensing the emergence of electrolyte on the backside of the foil sample. By measuring the penetration time for foils of different thickness, the depth of the fastest growing localized corrosion site as a function of time is determined. This powerful technique has been utilized by only a few investigators [10–15]. A recent study used the foil penetration technique to show that the pit growth rate in AA2024-T3 at open circuit was strongly reduced by the presence of a small amount of dichromate in solution, whereas the growth rate at a slightly elevated applied potential was practically unchanged, even in the presence of high dichromate concentrations [11]. In another recent study, the foil penetration technique was used to show that the rate of localized corrosion growth in AA2024-T3 plate was anisotropic [12,13]. The rate of growth in the through-thickness or short transverse direction was much slower than in the longitudinal or long transverse directions. Cross-sectioning of samples proved that the growth rate was anisotropic because the attack was intergranular corrosion (IGC) and the grains were elongated in the rolling direction. The nominal growth rate in the short transverse direction was slower because of the longer path length around grains in that direction. The intergranular nature of the attack was supported by X-ray microfocal radiography analysis of penetrated foils [11].

Rota and Bohni studied IGC of an Al–4Cu-alloy aged to maximum IGC susceptibility using the foil penetration technique [14]. They then took the further step of investigating the influence of an applied tensile stress on growth kinetics of IGC [15]. Interestingly, they found the application of 80% of the proof stress had very little influence on the penetration kinetics of IGC in this alloy. The enhancement of IGC by an applied tensile stress is actually a form of stress corrosion cracking (SCC). The SCC process includes crack initiation and growth. The mechanism of crack growth involves either anodic dissolution or hydrogen embrittlement [15–19]. The grain boundary region is often the site of SCC because it can be preferentially susceptible to dissolution and is an easy ingress path for atomic hydrogen. SCC growth kinetics are usually studied with compact tension fracture mechanics specimens. The foil penetration approach can be used either with or without an applied stress, so it can be used to address the transition from IGC to IGSCC.

Rota and Bohni were not aware of the anisotropy of IGC kinetics without applied stress as was demonstrated in the recent studies, and their experiments were performed on rolled sheet with nominal growth in the through-thickness direction. The current study was undertaken to investigate the effects of stress and orientation on stress-assisted IGC growth using the foil penetration technique. X-ray microfocal radiography was also used to examine the morphology of the corrosion features.

2. Experimental

A plate of AA2024-T3 plate (Cu 4.5%, Mg 1.45%, Mn 0.57%, Si 0.11%, Fe 0.25%, Zn 0.09%, Ti 0.02%, Cr 0.01%, and other elements total 0.05% max) of thickness 1.9 cm was purchased from Metalmen Sales, Inc. Dog-bone shaped samples were machined from the plate in different orientations relative to the rolling direction. Slices of thickness 0.1–0.9 mm were then fabricated using electrical discharge machining (EDM). Details of the specimen shape are given in Fig. 1. The orientations of tested samples and the AA2024-T3 microstructure are given in Fig. 2. It should be noted

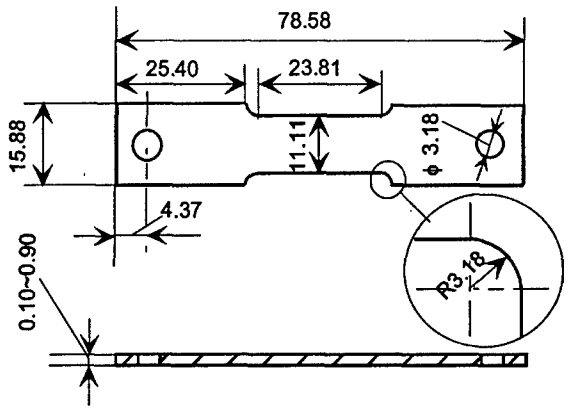

Fig. 1. Sheet sample used for stressed foil penetration experiments, all dimensions in mm.

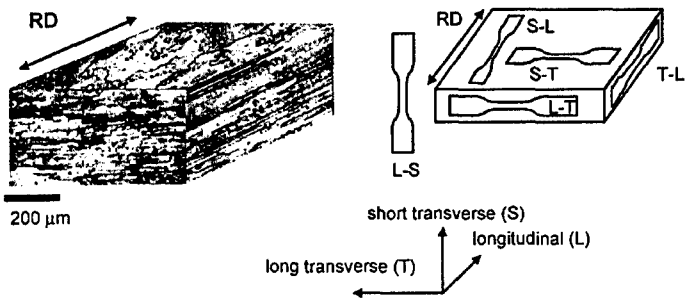

Fig. 2. Microstructure of AA2024-T3 plate and notation used for orientation of stressed sheet samples.

that the notation of orientation shown in Fig. 2 is slightly different than the notation used in previous papers from this laboratory [12,13]. The three perpendicular directions are considered to be longitudinal (L, along the rolling direction), short transverse (S, through-thickness), and transverse (T). The orientation of a stressed sheet sample is noted by first indicating the sheet perpendicular (direction of nominal penetration) and then the stressing direction. For example, an S–L sample is stressed in the L or rolling direction, with penetration in the S or through-thickness direction. Prior to testing, the samples were polished to 1200 grit in methanol or ethanol to minimize corrosion.

Rota and Bohni used a large tensile frame and ganged samples to apply a constant uniaxial load simultaneously to six samples [15]. In the current study, uniaxial stress was applied using modified ASTM G49 constant-displacement jigs (Fig. 3). Gripping plates were designed into the end pieces of the ASTM G49 test frame to handle sheet samples rather than the standard round tensile bars. A fixture is used to squeeze together the sides of the frame, which then push out the end pieces to apply a uniaxial tensile stress and a fixed displacement. A strain gauge extensometer (0.5 in. gage length, Model 3542-0100-050-ST, Interlaken Technology Corp.) was attached to the samples during the squeezing of the frame in order to sense and control the sample strain. Fig. 4 shows a stress–strain curve for an AA2024-T3 sheet in the S–T orientation measured in a standard tension testing machine. Using this stress–strain curve as a guide, strains in the elastic region were applied. Typically, a strain associated with about half of the yield stress was applied for the foil penetration testing.

The stressing jigs require the sheet samples to have a length of 79 mm, whereas the tested AA2024-T3 plate was only 19 mm in thickness. In order to study the effect of tensile stresses applied in through-thickness direction (S), extension tabs were welded to the ends of full thickness plate sections with thickness in either the L or T

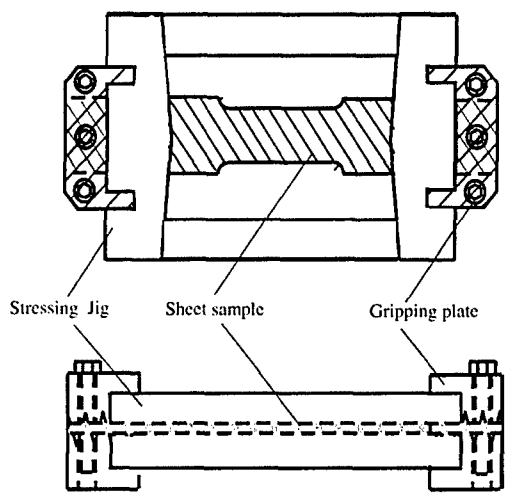

Fig. 3. Schematic of modified ASTM G49 jig used to apply constant displacement.

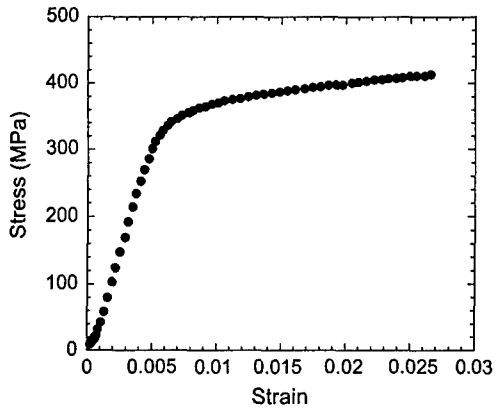

Fig. 4. Stress–strain curve for an AA2024-T3 sheet in the S–T orientation.

direction. The tabs were laser welded (at Edison Welding Institute) in an attempt to minimize the metallurgical changes associated with weld heat. Two 30 × 200 mm pieces were cut from a 2 mm thick sheet of AA2024-T3 and laser welded to either side of a 200 mm long, 2 mm thick section of the 19 mm plate that was oriented either in the L or T direction. This resulted in a 2 mm thick plate with dimensions about 79 × 200 mm containing two welds along the length. Dog-bone tensile samples were then cut from this plate, as shown schematically in Fig. 5. These samples were reduced in thickness for the penetration experiment by grinding and polishing.

The foil penetration cell used in earlier studies had to be modified to handle the sheet sample mounted in the stressing jig. The sample was pressed against a Teflon

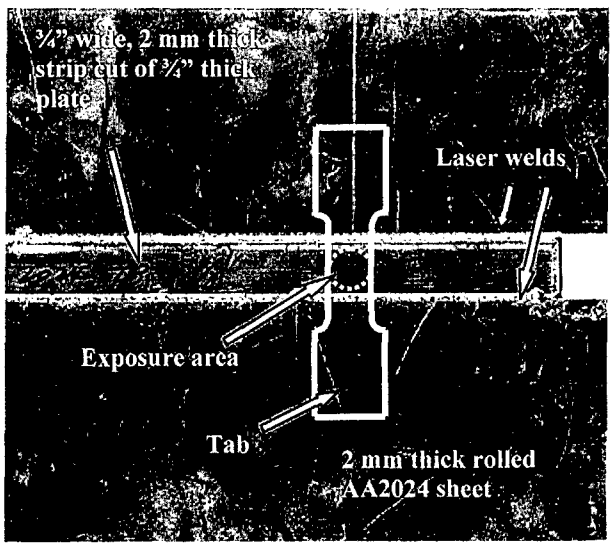

Fig. 5. Laser welded sheet sample for AA2024-T3 in the L–S orientation.

O-ring at the bottom of a Plexiglas cell to expose an area of 1 cm^2. The sample was backed with a piece of filter paper and a Cu foil. Penetration was sensed by monitoring the resistance between the sample and the Cu foil using a detection circuit described previously [11]. A Pt counter electrode and saturated calomel reference electrode (SCE) were used in the foil penetration cell. The solution was prepared in 1 M NaCl by mixing A.C.S. grade NaCl crystals with 18.2 MΩ cm Millipore deionized water.

Penetration experiments were performed under anodic potentiostatic polarization in 1.0 M NaCl solution. Oxygen was continuously bubbled into the solution during the test. Because the main goal of this study was to investigate the growth kinetics of IGC under the stress, samples were initially polarized at −0.29 V SCE for 1 s, which is similar to a traditional opening precrack in the study of SCC growth. Subsequently, the potential was stepped down to a given value and held there until the sample penetrated. The anodic current was recorded during the penetration time. Penetrated samples were cross-sectioned, polished, and examined by optical microscopy.

Anodic potentiodynamic polarization curves were measured on stressed samples in different orientations using the penetration cell and stressing jig in deaerated 1 M NaCl solution (pH = 6.1). A Gamry FAS potentiostat/galvanostat (Gamry Instruments, Inc.) system was used to control the potential. The solution was deaerated in a reservoir by Ar for 24 h before the polarization experiments. Ar gas deaerated the cell at least 15 min before filling in the solution and purged the solution continuously during the measurement. The potential was scanned at 0.1 mV/s from 30 mV below the open circuit potential (OCP) to a potential above the breakdown potentials.

Potentiostatic polarization experiments were carried out to understand the kinetics of localized corrosion at a specific potential. A sample was first potentiodynamically polarized as described above and then held at some potential for a certain time. Current was recorded during the holding time. The polarized surface was examined by optical microscopy, scanning electron microscopy (Philips XL30 FEG-SEM) and energy-dispersive X-ray spectroscopy (EDS). The potentiostatic polarization experiments were conducted between and above the two breakdown potentials.

X-ray microfocal radiography was used as a non-destructive evaluation (NDE) method to analyze samples generated by foil penetration experiments. Sheet samples removed from the cell immediately upon penetration provide ideal samples for radiography since they are just penetrated [11,20]. NDE morphology was combined with destructive cross-sectioning to develop a full description of the corrosion sites. The morphology of the corrosion defects was found to vary strongly depending on the orientation and the application of stress.

3. Results

3.1. Potentiodynamic polarization curves of foils under stress

Representative anodic polarization curves for S surfaces with and without tensile stress are given in Fig. 6. Three replicate measurements were made for each of the

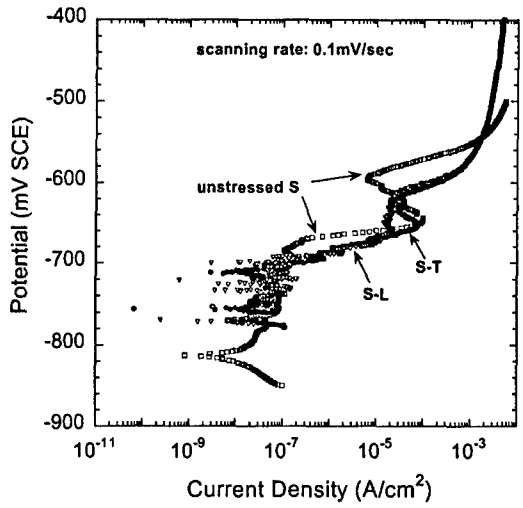

Fig. 6. Anodic polarization curves of S, S–L and S–T samples in deaerated 1 M NaCl solution.

conditions: unstressed S samples and stressed S–L and S–T samples. The S–L and S–T samples were loaded to an initial strain of 0.28%. The current increased quickly above the first lower breakdown potential and either reached a higher limiting value (S–L), or exhibited a peak and decreased (unstressed S and S–T). Above the second breakdown potential at higher potentials, the current increased again. The polarization curves in other orientations followed similar trends. The phenomenon of two breakdown potentials was studied in Al–4%Cu alloy in deaerated 1 M NaCl by Galvele and de Micheli [21]. They proposed that the lower breakdown potential corresponded to the dissolution of Cu-depleted zone along the grain boundary and the higher one corresponded to the dissolution of the grain bodies. Guillaumin and Mankowski gave a different explanation for the two breakdown potentials found for AA2024-T351 in aerated 1 M NaCl [22]. The lower breakdown potential was proposed to be associated with dissolution of S phase particles (Al_2CuMg) and the higher one with pits and IGC in the alloy matrix. Recently, Zhang and Frankel refined this view by describing that transient S phase attack triggers the first breakdown, and primarily IGC is responsible for the second breakdown [13].

In Fig. 6, the two breakdown potentials for stressed S–L and S–T are almost the same values, i.e. −715 to −695 and −625 to −610 mV SCE for the first and second breakdown potentials, respectively. These values are significantly lower than the counterparts for unstressed S samples: −675 to −665 and −590 to −595 mV SCE, respectively. This indicates that samples under tensile stress are more susceptible to localized corrosion in chloride solution. In the passive region, below the lower breakdown potential, the current density exhibited unstable oscillations for the stressed samples, whereas unstressed S sample maintained a steady current density. These oscillations might be associated with stress effects on induction of metastable pits, but this is still unclear. The 40 mV lower first breakdown potential for the

stressed samples indicates that transient attack of S phase particles is enhanced by tensile stress. This might be an influence of stress on the S phase surface oxide film or at the particle/matrix interface. The lower second breakdown potential indicates that stress enhances IGC-initiation. Above the second breakdown potential (e.g. −580 mV SCE), the current densities of stressed S–L and S–T samples were larger than that of unstressed S by as much as a factor of 100. These findings correspond with the foil penetration results, which are described below.

3.2. Potentiostatic polarization of foils under stress

In order to understand better the effect of stress on the forms of corrosion in AA2024-T3, potentiostatic polarization was performed at different potentials. S–L samples were potentiostatically polarized at −660 mV SCE, which is between the two breakdown potentials, in deaerated 1 M NaCl for 1 or 3 h and removed from solution immediately. The morphology of the exposed surface was recorded using optical microscopy and examined by SEM and EDS. The current density recorded during potentiostatic polarization increased initially to a sharp peak and then dropped down to a low level within about 10 min (Fig. 7). The initial peak of current density was associated with initiation of localized attack, but the subsequent decrease indicates that the attack did not propagate. Fig. 8(a) is an optical microscopy image of the exposed surface. The spherical black and irregular gray particles are partially dissolved, but no intergranular attack is evident. These particles were observed by SEM as shown in Fig. 8(b) and (c). EDS analysis indicates that the spherical small S phase particles in Fig. 8(b) were depleted of Mg, and trenching occurred around the particles. The large Al–Cu–Fe–Mg particles were etched and cracked (Fig. 8(c)). These observations show that IGC does not initiate below the second breakdown potential even with applied tensile stress.

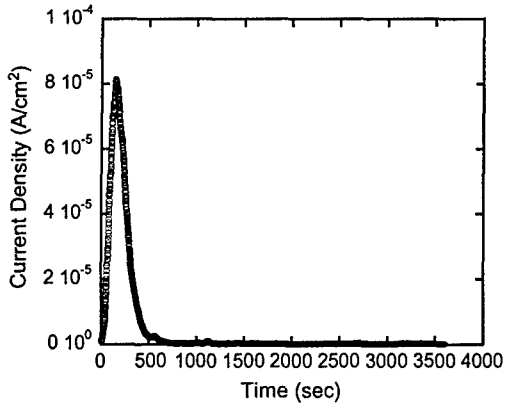

Fig. 7. Current density transient for S–L sample potentiostatically polarized at −660 mV SCE in deaerated 1 M NaCl for 1 h.

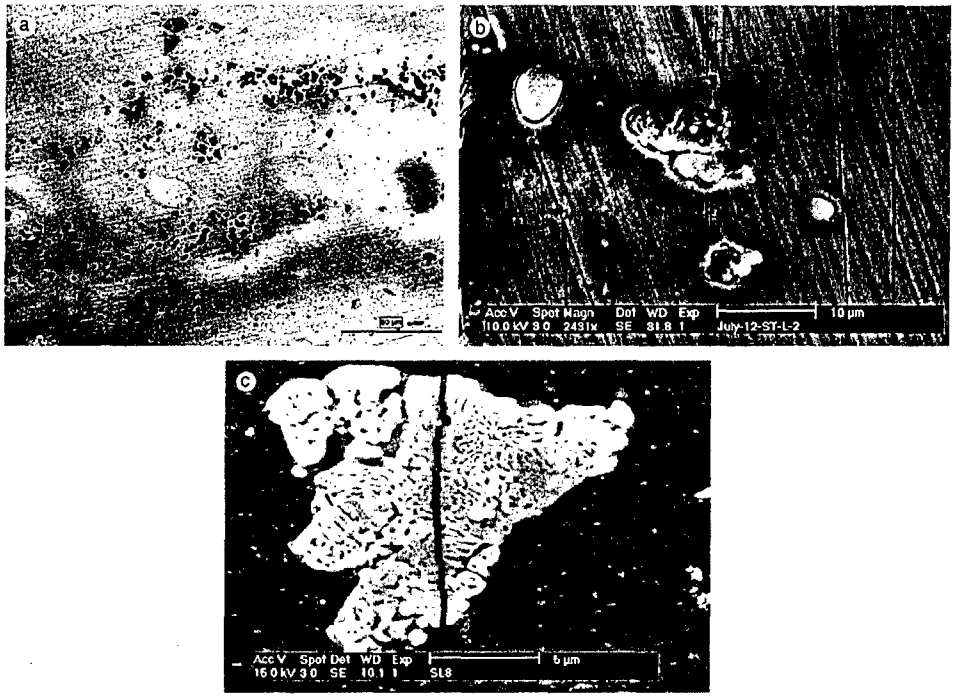

Fig. 8. Surface morphology of S–L sample exposed to deaerated 1 M NaCl at −660 mV SCE for 3 h. (a) Optical image; (b) secondary electron image of S phase particle; (c) secondary electron image of Al–Cu–Fe–Mn particle.

Potentiostatic polarization was performed above the second breakdown potential on an S–L sample in oxygenated 1 M NaCl. The sample was initially polarized at −290 mV SCE for 1 s and the potential was then stepped down to −580 mV SCE and held for 2 h. After an initial spike, the current density increased gradually (Fig. 9). Examination of the sample by optical microscopy after removal from solution indicated the presence of severe IGC dissolution and attack of some grain bodies (Fig. 10). The results are consistent with the behavior of unstressed samples [13,22], and indicate that stressed samples exhibit IGC at high potentials.

3.3. Foil penetration experiments

The foil penetration method was used to study the growth kinetics of IGC on stressed samples. Foil penetration experiments measure the penetration time for foils of varying thickness under a given condition. However, the results are typically plotted in the inverse fashion, to show depth of the fastest growing sites as a function of time. A comparison of penetration data for stressed S–T and unstressed S under applied potentials around the second breakdown potential is given in Fig. 11. At a potential above the second breakdown potential, −580 mV SCE, the growth rate of

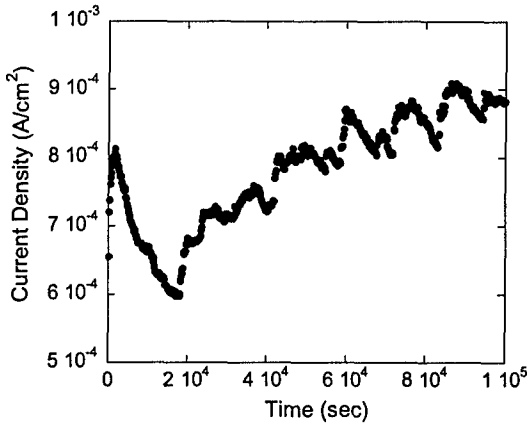

Fig. 9. Current density transient for S–L sample potentiostatically polarized at −580 mV SCE for 2 h.

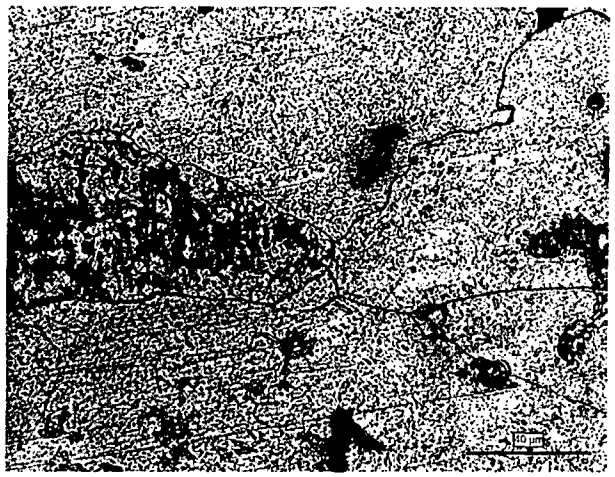

Fig. 10. Optical image of S–L sample exposed to oxygenated 1 M NaCl at −580 mV SCE for 2 h.

stressed S–T sample is faster than that of unstressed S. In Fig. 6, the current density of S–T during potentiodynamic polarization was shown to be much larger than that of unstressed S at −580 mV SCE. The penetration rate of S–T at −610 mV SCE is similar to that of S at −580 mV SCE. Interestingly, the current densities during potentiodynamic polarization are similar for the two conditions (Fig. 6). So despite the complications involved with determining growth kinetics directly from electrochemical measurements, the polarization curves correlate well with foil penetration data. A similar effect of potential on penetration rate has been found in L-oriented samples. Fig. 12 shows that IGC in L–T samples grows faster at −580 than at

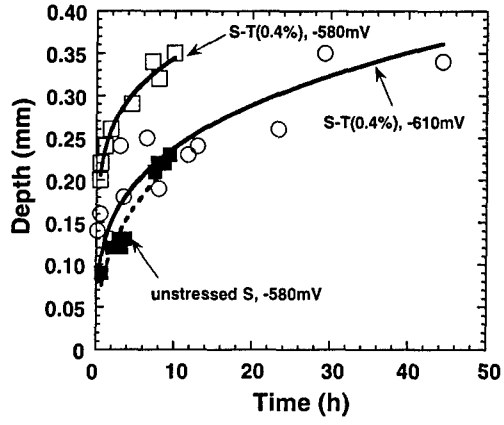

Fig. 11. Penetration data for S-oriented samples of AA2024-T3 without and with applied stress in oxygenated 1 M NaCl at −580 and −610 mV SCE. The values in parentheses are the initial strains.

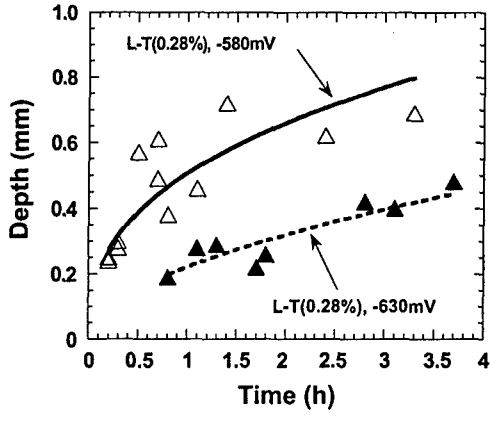

Fig. 12. Penetration data for L-oriented samples of AA2024-T3 without and with applied stress in oxygenated 1 M NaCl at −580 mV SCE and in Ar-bubbled 1 M NaCl at −630 mV SCE. The values in parentheses are the initial strains.

−630 mV SCE in oxygenated 1.0 M NaCl, which correlates with the higher current density at −580 than at −630 mV SCE.

Fig. 13 shows foil penetration data for stressed AA2024-T3 samples in three different orientations, S–T, T–L, and L–T, at −580 mV SCE in oxygen-bubbled 1.0 M NaCl. The growth rate of the stressed samples is seen to be anisotropic, with the rate of penetration for the S–T sample being much slower than the other orientations. IGC growth anisotropy, which was previously reported for unstressed samples [12], is therefore not changed by the application of a tensile stress. The penetration depth under an applied stress for the L–T and T–L orientations was found to vary

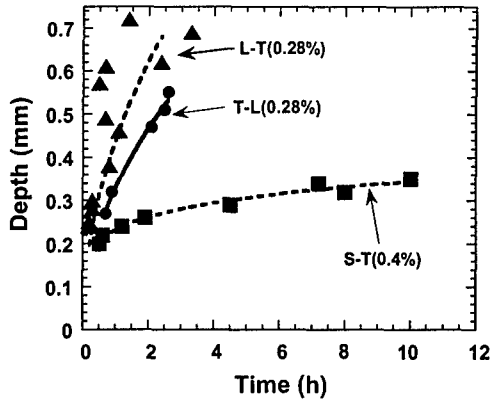

Fig. 13. Penetration data for AA2024-T3 with applied stress varying amount of fixed displacement in oxygen-bubbled 1 M NaCl at −580 mV SCE. The values in parentheses are the initial strains.

approximately with $t^{1/2}$, similar to what has been observed for pitting corrosion and IGC in unstressed samples [8,9,12].

Comparisons of the penetration data for stressed and unstressed samples are given in Figs. 14–16. Fig. 14 shows data for unstressed L samples, and stressed L–T and L–S samples, Fig. 15 shows data for unstressed T samples and stressed T–L samples, and Fig. 16 shows data for the unstressed S and stressed S–L and S–T samples. In any given orientation for the L and T stressing directions, the rate of growth was slightly enhanced by the application of stress. This marginal increase resulting from the application of stress is similar to that observed by Rota and Bohni for Al–4Cu, and can be understood by considering the relationship of the stress direction to the microstructural orientation, as shown in Fig. 2. Tensile stress applied in either the T or L direction is aligned with the elongated grain structure in the T and L sections.

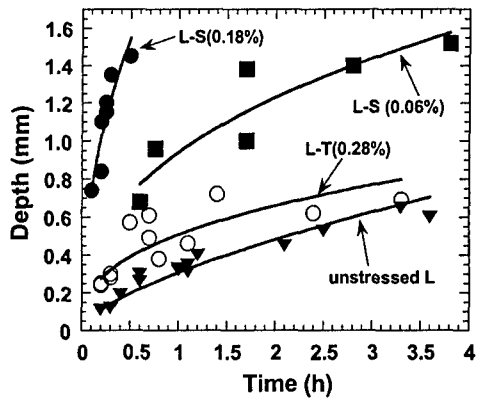

Fig. 14. Penetration data for L-oriented samples of AA2024-T3 without and with applied stress in oxygenated 1 M NaCl at −580 mV SCE. The values in parentheses are the initial strains.

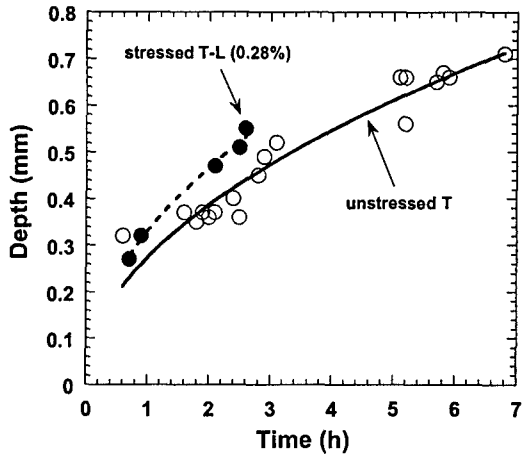

Fig. 15. Penetration data for T-oriented samples of AA2024-T3 without and with applied stress in oxygenated 1 M NaCl at −580 mV SCE. The values in parentheses are the initial strains.

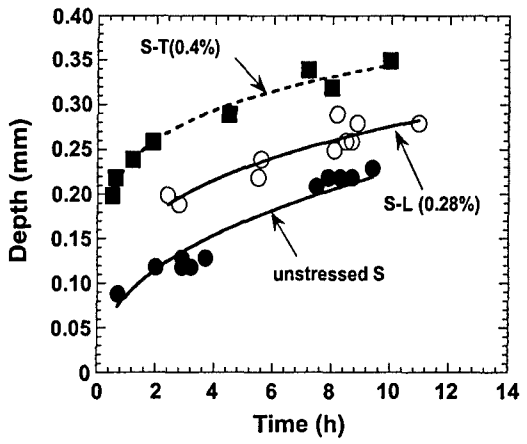

Fig. 16. Penetration data for S-oriented samples of AA2024-T3 without and with applied stress in oxygenated 1 M NaCl at −580 mV SCE. The values in parentheses are the initial strains.

On the other hand, tensile stress in the S direction is perpendicular to the elongated grain structure. Fig. 14 shows the effect of stress for penetration in the L direction (along the rolling direction). Application of a tensile strain about halfway to yield in the T direction increased the penetration rate by a small amount. In sharp contrast, application of stress in the S direction had a huge effect on the penetration rate. The application of 0.06% strain, which is barely measurable and equivalent to an applied stress of about 3 ksi, greatly increased the penetration rate. A higher strain of 0.18% increased the rate about 7× compared to the unstressed condition. This effect of

stress orientation on SCC resistance has been known for some time [1,5]. However, these data show the transition from IGC to IGSCC.

The enhancement in growth kinetics with stress was greater for penetration in the S direction (S–L and S–T samples) than for either L–T or T–L samples. This may be related to the lower anisotropy of the microstructure in the S plane. The higher rate for S–T samples compared to S–L is probably associated with the fact that the T direction is the short axis of the grain structure in that plane (Fig. 2). Interestingly, when fitting the S–T and S–L data to an equation of the form $d = At^n$, the fit is better when the time exponent n is in the range of 0.15–0.26 rather than 0.5. The L–S and L–T penetration data exhibit a time exponent in the range of 0.38–0.46, which is higher, but still less than 0.5. It is possible that the growing defects resulted in a stress relaxation with time and thus a decrease in the rate of penetration with time. As described presently, the difference in growth kinetics can be explained by characterization of the corrosion defects, which were found to be IG in nature.

3.4. Characterization of the corrosion defects

X-ray radiography along with cross-sectional optical microscopy provides a full description of the corrosion defects. X-ray microfocal radiography generates a gray-scale image in which the intensity depends on the integrated X-ray absorption through the sample thickness [20]. The absorption of X-rays in these samples varies with the amount of corroded material; the image on the X-ray film is a negative in that a dark region is associated with low attenuation of X-rays traveling through a region of lower density where metal was lost to corrosion. Magnification is achieved by simple optical projection from the X-ray source through the sample onto a distant film plate. The small focus spot of the electron beam that generates the X-rays results in enhanced lateral resolution in the microfocal radiography technique.

Fig. 17 shows the radiograph and optical cross-section of an unstressed S sample exposed to oxygen-bubbled 1 M NaCl at a potential of −580 mV SCE. The attack is IG in nature, as is clearly seen by the optical micrograph of the sample cross-section. The radiograph of this sample shows lots of broad and diffuse corrosion sites. The radiograph has this nature because it is a through-thickness integration of the IG attack, which spreads laterally in the foil in this orientation. The long path for IGC to propagate through S samples causes the slower penetration rate relative to the T and L orientations [12].

Fig. 18 shows an S–T sample that was penetrated at the same potential in the same solution. This image is different than that of the unstressed sample in several respects. There was much less attack in the stressed sample than in the unstressed sample. This is partly a result of the faster penetration time of the stressed sample. Furthermore, the stress concentrated the attack at cracks that were perpendicular to the applied stress direction. The higher magnification radiograph shows that the cracks were wavy and not perfectly perpendicular to the stress. As will be shown below, this is a result of the IG crack propagating around the pancake-shaped grains, but generally maintaining a direction perpendicular to the applied stress.

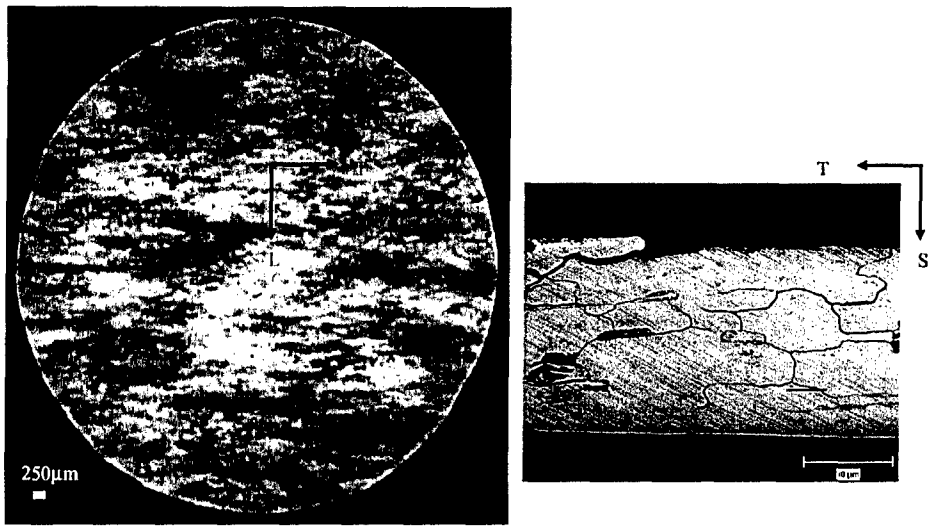

Fig. 17. AA2024-T3 S sample, 0.22 mm thick polarized at −580 mV SCE in 1 M NaCl, and penetrated in 8.2 h, unstressed. Left—radiograph, right—optical cross-section [12].

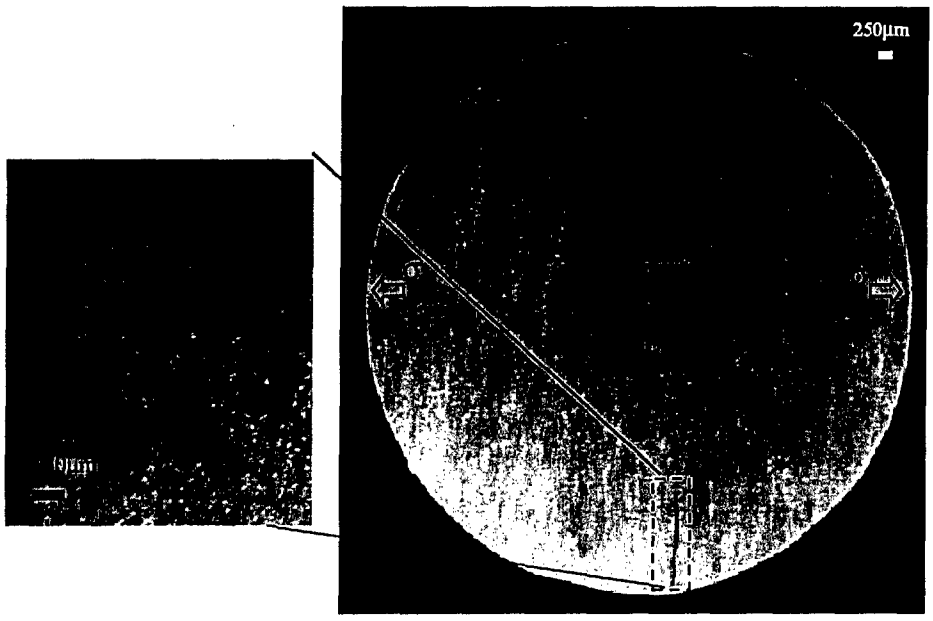

Fig. 18. AA2024-T3 S–T sample, 0.2 mm thick polarized at −580 mV SCE in 1 M NaCl, stressed. Right—radiograph, left—magnified view of crack.

An unstressed L sample exposed to the same 1 M NaCl solution at −580 mV SCE is shown in Fig. 19. The corrosion sites in the radiograph are much more focused

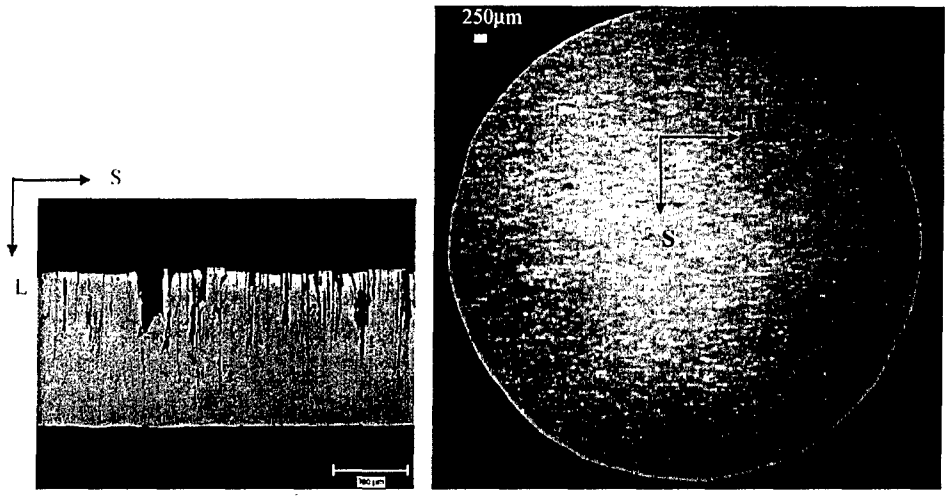

Fig. 19. AA2024-T3 L sample, polarized at −580 mV SCE in 1 M NaCl, unstressed. Left—radiograph [12], right—optical cross-section.

than in the S sample shown in Fig. 17. The optical image of the cross-section shows that the IG corrosion path is essentially straight through the foil. Because of the orientation of the elongated grains, the grain boundaries go almost straight through L-oriented foils. The white spots are higher density regions associated with intermetallic particles. The particle number density is very high because the radiograph senses all of the particles through the whole cross-section. These particles are not evident in Fig. 17 because of all of the corrosion damage spread through the cross-section of that sample.

Images of a penetrated L–S sample are shown in Fig. 20. As for the unstressed L sample, the optical cross-section shows that the attack is straight through along the L direction. In the X-ray radiography image of this sample, the defects are seen to be elongated in the T direction and somewhat opened up in the S direction, which is the stressing direction. The optical section indicates that these defects propagate through the foil. Thus the combination of the two images provides a 3-D morphology of the defects in the L–S samples.

Unstressed T samples exhibit corrosion morphologies very similar to those shown in Fig. 19 for an unstressed L sample. The optical cross-section and radiograph for a T–L sample exposed under the same conditions but under an applied stress are given in Fig. 21. Careful examination of the defects in the radiographs shows them to be short straight cracks oriented in the direction of stress. It is quite strange to have cracks oriented in the stressing direction rather than perpendicular to the stress. However, the optical micrograph of the cross-section shows that the cracks penetrated through the thickness in the T direction, which is perpendicular to the stressing direction. (Actually, only one of them penetrated completely through.) The crack dimensions were about 50–100 μm in the L direction, but they penetrated through the 550 μm thick sample in the T direction. They were limited to the L

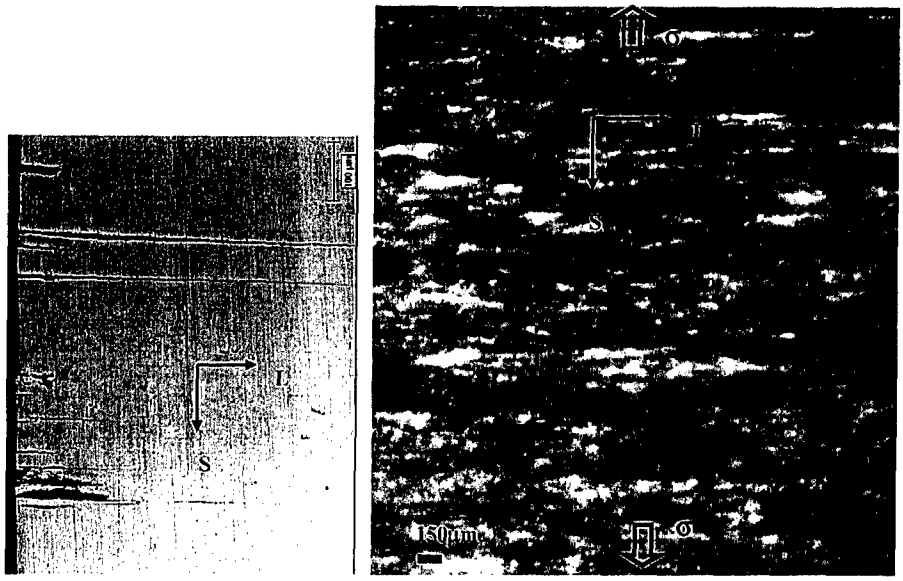

Fig. 20. Images of L–S penetrated sample at −580 mV SCE. Left—optical cross-section, right—micro-radiograph image.

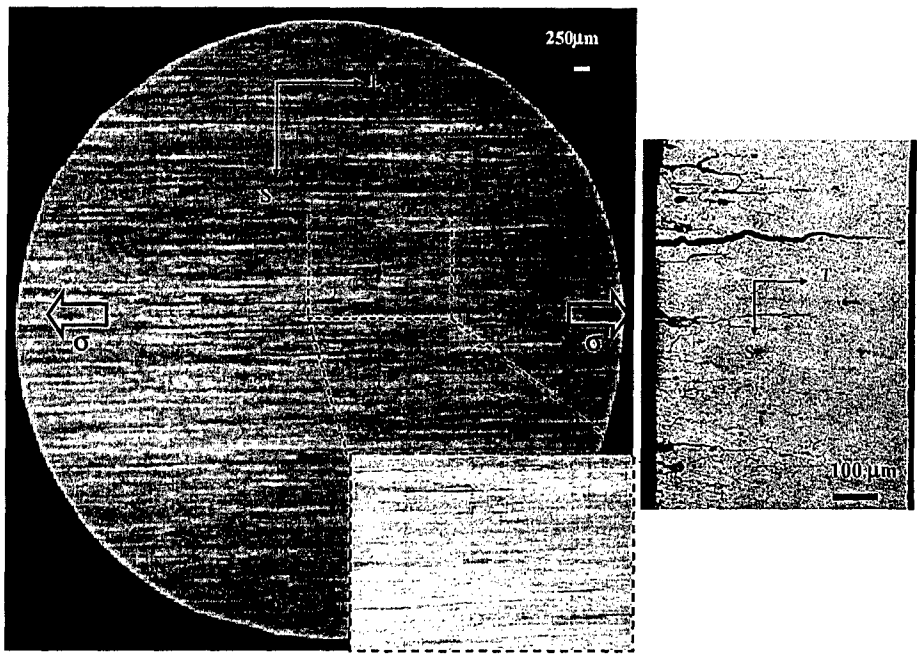

Fig. 21. AA2024-T3 T–L sample, 0.55 mm thick polarized at −580 mV SCE in 1 M NaCl, and penetrated in 2.6 h, stressed. Left—radiographs, right—optical cross-section.

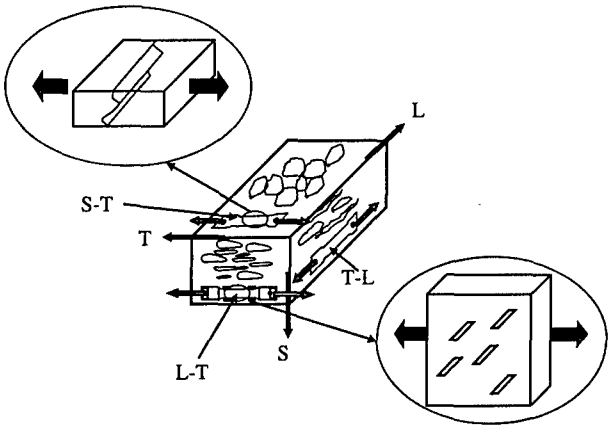

Fig. 22. Schematic representation of three-dimensional nature of the cracks in stressed foil penetration samples. Not drawn to scale.

direction in the L–S plane because of the orientation of the grains and the constraints imposed by the IGC nature of the attack.

The radiographic and optical microscopy results are combined in Fig. 22, which shows a schematic representation of the morphology of the cracks in the stressed samples. A schematic 3-D view of the elongated grain structure is also given. For the S–T sample, the cracks were perpendicular to the stress, but wavy and broad since they had to find their way between the elongated grains. The T–L sample exhibited straight cracks whose long axes were perpendicular to the stress. However, the radiography showed a projection of those cracks on the T plane. In that projection, they appeared to be parallel to the stress. The crack faces, which were S faces, were parallel to the applied stress even though the long axis was perpendicular to the stress. It is clear that the combination of radiography and cross-sectional microscopy gives a complete picture of the cracks.

4. Discussion

In this work, AA2024-T3 samples stressed in tension about halfway to yield exhibited a lower breakdown potential than unstressed samples. The higher current at a given potential above the breakdown potential was associated with IGC and selected grain attack. The penetration data showed that at higher potential the localized corrosion growth rate was faster for stressed samples than for unstressed samples. In particular, the growth rate of L–S samples was considerably faster than both L–T and unstressed L samples. Furthermore, the penetration rate increased with initial strain. X-ray radiography images showed that there was much less attack in S–T samples than in unstressed S samples, and that the attack was wavy and elongated rather than broad and diffuse. Because of constraints imposed by the microstructure, the cracks in the L–S samples were normal to applied stress, while those in the T–L samples were parallel to the stress direction.

Intergranular corrosion is accelerated attack at or near grain boundaries resulting from an enhanced susceptibility of the grain boundary or neighboring region. Stress corrosion cracking is driven by the synergistic actions of mechanical and electrochemical factors occurring at a crack tip. IGC and IGSCC are closely linked and even overlap in exfoliation corrosion, a form of IGC in which the stress generated by the intergranular corrosion product effectively wedges apart the elongated grain structure near the surface of wrought high strength Al alloys. One view of IGSCC is that it is simply stress-assisted IGC, though the role of hydrogen in the SCC of Al alloys has been debated. Owing to its low breakdown potential and the reactivity of freshly exposed Al surfaces (high exchange current density for hydrogen evolution), hydrogen gas is always evolved within localized corrosion sites in Al and Al alloys. Burleigh reviewed a number of studies on SCC of Al alloys and concluded that an anodic dissolution mechanism is generally favored for the 2xxx series alloys, whereas hydrogen-induced cracking is favored for 7xxx series alloys [1].

The foil penetration data shown in Fig. 14 suggest that, as stress is applied, there is a smooth transition from unstressed IGC to IGSCC, which indicates that the mechanisms for the two phenomena are similar. There can be different influences of stress on the cracking process. Stress applied in the S direction is perpendicular to the elongated grain structure and therefore perpendicular to the IGC fissures. In this work, stress applied in the S (through-thickness) direction was extremely effective at increasing penetration rates, which is a well-known effect in SCC of Al alloys. Such stress would tend to both rupture any film that might form at the crack tip and also effectively open the crack, thereby increasing mass transport and decreasing the ohmic potential drop down the crack. Stress applied in either the L or T direction would have similar though less effective influences on intergranular fissures penetrating in the S direction. The smaller effect of stress on penetration for S–T and S–L samples relative to L–S samples is borne out by the data presented in Figs. 11 and 14.

Interestingly, the penetration rates for L–T and T–L samples are slightly larger than for the unstressed L and T samples, respectively. The microstructure constrains the IG crack faces in L–T and T–L samples to be parallel to the direction of the applied stress, and Poisson effects should generate a compressive stress in the S direction, which is perpendicular to the grain faces. Because of this, the applied stress acts to close rather than open cracks, and the accelerating effect of stress for the L–T and T–L samples is difficult to explain.

If the mechanism for IGC is the same as that for IGSCC, as indicated by the smooth transition between the two, it is possible that IGC involves a stress component even in the absence of an applied stress, like exfoliation corrosion. AA2024-T3 is susceptible to exfoliation corrosion, and it is likely that the IGC observed in the foil penetration samples would have turned into exfoliation corrosion if it were at an unconstrained surface. There is no reason to expect that the corrosion product formed during IGC would be any less voluminous than that formed during exfoliation near the surface. The constraints of the surrounding material in the foil penetration experiment prevent exfoliation for the L- and T-oriented samples. However, the voluminous corrosion still forms. It is possible that the IGC is assisted by wedging stresses generated by the corrosion product. The sample does not exfoliate

because of the constraints of the sample, but the local wedging stress from the corrosion product could be significant enough to prevent repassivation in the localized corrosion environment. Nominal elastic stress on the order of half of the yield stress was shown in this work to decrease the breakdown potential in a neutral chloride environment, so it is reasonable that wedging stress in the crack environment would destabilize passivity. Once initiated, the IG cracking continues along the solute depleted zone along a grain boundary because this region is the least likely to repassivate in the localized corrosion environment. An applied stress in the S direction would clearly enhance this process. For stress applied in the L or T directions, it is likely that the compressive stress from the Poisson effect would be small compared to the wedging stress from the corrosion product. Therefore, the net effect of an applied stress in the L or T direction would be to create a biaxial stress state at the crack tip: a wedging stress from the corrosion product and a perpendicular stress along the crack width. This biaxial stress state at the crack tip would further destabilize the passive film.

Another factor that could also play a role is the fact that not all of the grain boundaries are perfectly aligned with stress applied in the L or T direction. The grains in the tested plate are certainly elongated as shown in Fig. 2. However, portions of the boundary region around most of the grains are angled away from the rolling direction to a certain extent. Any misalignment during machining of the samples would also create a situation where part of the applied stress could be resolved into a stress acting perpendicular to the boundary. As shown above, a small stress normal to the grain boundary is sufficient to accelerate growth.

5. Conclusions

The effect of uniaxial tensile stress on intergranular corrosion of AA2024-T3 was studied using the foil penetration technique in an attempt to bridge the gap between IGC and intergranular stress corrosion cracking. The following observations were made:

1. Potentiodynamic polarization measurements in 1 M NaCl indicated that the two breakdown potentials typically observed for AA2024-T3 were lower on stressed samples, and the current at a given potential was higher.
2. The penetration rate depended on potential and was higher for samples with an applied stress than for unstressed samples. Stress applied in the S direction was particularly effective at increasing penetration rates, although stress in the L and T direction also accelerated attack. The primary form of attack above the higher breakdown potential was IGSCC, whereas pitting dominated above the lower breakdown potential.
3. Stress had a larger effect on penetration rate at higher applied potentials, indicating that pitting is less susceptible to the effects of stress than a properly oriented IGC crevice.

4. The effects of stress on the penetration rates in various orientations were strongly linked to the anisotropic microstructure. X-ray microfocal radiography and optical microscopy of cross-sections were used to characterize IGSCC defects in thin penetrated foils. In certain orientations, crack faces were parallel rather than perpendicular to the stress orientation as a result of the constraints of the microstructure on the orientation of the IGC.
5. A smooth transition in penetration response with applied stress suggests that the mechanisms of IGC and IGSCC are similar. It is suggested that the stress imparted at the crack tip by the formation of a voluminous corrosion product plays an important role in IGC propagation even in the absence of an applied stress.

Acknowledgements

The authors thank Jian Xie at Edison Welding Institute for performing the laser welding. This work was supported by the United States Air Force Office of Scientific Research through Grant No. F49620-02-1-0148. The contract monitor is Lt. Col. Paul Trulove.

References

[1] T.D. Burleigh, Corrosion 47 (1991) 89.
[2] F.D. Wall, G.E. Stoner, Corros. Sci. 39 (1997) 835.
[3] A. Conde, B.J. Fernandez, J.J. De Damborenea, Corros. Sci. 40 (1998) 91.
[4] M.R. Bayoumi, Eng. Fract. Mech. 54 (1996) 879.
[5] D. Najjar, T. Magnin, T.J. Warner, Mater. Sci. Eng. A 238 (1997) 293.
[6] G.S. Frankel, J. Electrochem. Soc. 145 (1998) 2186.
[7] A. Sehgal, D. Lu, G.S. Frankel, J. Electrochem. Soc. 145 (1998) 2834.
[8] F. Hunkeler, H. Bohni, Corrosion 37 (1981) 645.
[9] F. Hunkeler, H. Bohni, Corrosion 40 (1984) 534.
[10] W.K. Cheung, P.E. Francis, A. Turnbull, Mater. Sci. Forum 192–194 (1995) 185.
[11] A. Sehgal, G.S. Frankel, B. Zoofan, S. Rokhlin, J. Electrochem. Soc. 147 (2000) 140.
[12] W. Zhang, G.S. Frankel, Electrochem. Solid-State Lett. 3 (2000) 268.
[13] W. Zhang, G.S. Frankel, J. Electrochem. Soc. 149 (2002) B510.
[14] A. Rota, H. Bohni, Werkst. Korros. 40 (1989) 219.
[15] A. Rota, H. Bohni, Werkst. Korros. 40 (1989) 295.
[16] R.H. Jones, R.E. Ricker, Mechanisms of stress-corrosion cracking, in: R.H. Jones (Ed.), Stress-Corrosion Cracking, Material Performance and Evaluation, ASM International, 1992, p. 1.
[17] H. Vogt, M.O. Speidel, Corros. Sci. 40 (1998) 251.
[18] V.S. Sinyavskii, Prot. Metals 37 (2001) 521.
[19] V.S. Sinyavskii, A.M. Semenov, Prot. Metals 38 (2002) 155.
[20] B. Zoofan, S.I. Rokhlin, Mater. Eval. 52 (1998) 191.
[21] J.R. Galvele, S.M. de Micheli, Corros. Sci. 10 (1970) 795.
[22] V. Guillaumin, G. Mankowski, Corros. Sci. 41 (1999) 421.

Available at
www.ElsevierMathematics.com
POWERED BY SCIENCE DIRECT
Journal of Statistical Planning and Inference 126 (2004) 553–568

journal of statistical planning and inference

www.elsevier.com/locate/jspi

Statistical modeling and computer simulation of intergranular corrosion growth in AA2024-T3 aluminum alloy

Shiling Ruan[a], Douglas A. Wolfe[a,*], Gerald S. Frankel[b]

[a] *Department of Statistics, Ohio State University, Columbus, OH 43210, USA*
[b] *Department of Materials Science and Engineering, Ohio State University, Columbus, OH 43210, USA*

Received 23 December 2002; accepted 10 August 2003

Abstract

An extension of a brick wall model developed in a previous paper (Technometrics, to appear) was used to describe intergranular corrosion in AA2024-T3 aluminum alloys. The extended model simulates the behavior of corrosion paths at intersections of grain boundaries within the metal sample. Situations considered include the cases where a corrosion path might assume an upward turn, skip an intersection (not turn) or split into branches. The splitting of a corrosion path results in a smaller median of the minimum order statistic while the other factors increase the median of the minimum order statistic. Moreover, a larger number of grain layers increases the minimum path length for a sample with given thickness. With a proper combination of these factors, the extended model is able to provide a good fit to the experimental data developed by the foil penetration technique.
© 2003 Elsevier B.V. All rights reserved.

Keywords: Intergranular corrosion (IGC); Extended brick wall model

1. Introduction

High strength aluminum alloys such as AA2024-T3 are widely used in aerospace applications. They are resistant to uniform corrosion but highly susceptible to localized corrosion. Localized corrosion, usually in the forms of intergranular corrosion (IGC), pitting corrosion, crevice corrosion, exfoliation and stress corrosion cracking

* Corresponding author. Tel.: +1-614-2922866; fax: +1-614-2922096.
E-mail addresses: ruan.8@osu.edu (S. Ruan), daw@stat.ohio-state.edu (D.A. Wolfe), frankel.10@osu.edu (G.S. Frankel).

0378-3758/$ - see front matter © 2003 Elsevier B.V. All rights reserved.
doi:10.1016/j.jspi.2003.08.008

(Davis, 1999), is unpredictable in terms of the exact places of initiation and initiation time. With traditional deterministic approaches, such as the electrochemical theory of corrosion, localized corrosion cannot be well explained due to the scattering of the corrosion data. On the other hand, considering localized corrosion as rare events, statistical approaches could provide an appropriate way to describe the mechanism of corrosion (Shibata, 1996), potentially to evaluate quantitatively localized corrosion behavior.

Among all the forms of localized corrosion in high strength aluminum alloys in aqueous environment, IGC and pitting attack are two common forms that have received a good deal of attention. IGC is a preferential attack of grain boundaries or nearby adjacent regions without appreciable attack of the grain matrix, while pitting corrosion occurs at the intermetallic particles or in the grain matrix. Both forms of attack are similar from an electrochemical point of view (Galvele and De Micheli, 1970; Muller and Galvele, 1977). However, IGC might have very different growth kinetics from pitting. For predictive modeling of corrosion propagation, it is important to understand these growth kinetics independently. In this paper, we describe a model predicting the growth kinetics of IGC in aluminum alloy.

There are many factors that determine the resistance and susceptibility of an alloy to IGC, such as alloy composition, microstructure, and the environment (Davis, 1999; Scully et al., 1992; Scully, 1999). The exact role of each of these factors is still unclear. For example, even though there are a few reports on quantitative measurements of IGC in aluminum alloys, little is known about the relationship between alloy microstructure and IGC growth kinetics. Zhang and Frankel (2000) made quantitative measurements of localized corrosion kinetics in AA2024-T3 using the foil penetration technique. They reported that the growth kinetics of localized corrosion in this type of alloy exhibit a strong anisotropy as a result of anisotropy in the microstructure of the wrought aluminum alloy. AA2024-T3 has a typical laminated structure with grains elongated in the longitudinal (rolling) and long transverse directions relative to their dimension in the short transverse (through-thickness) direction. The time for intergranular corrosion to penetrate a given distance along the longitudinal or long transverse direction is much less than the time to penetrate the same nominal distance in the short transverse direction (Zhang and Frankel, 2000). The ratio of nominal penetration rates for the longitudinal direction to that for the short transverse direction was found by Zhang to be 4.29. The local intergranular growth rate should not depend on the direction of growth, though it is likely a function of total path length from the surface exposed to the bulk solution. The difference in nominal growth rate with through-thickness direction relative to the rolling direction is a result of the anisotropic grain dimensions and the resulting difference in path length. Any intergranular path in the through thickness direction of a plate with an elongated microstructure will be very convoluted, resulting in nominal rate of penetration that is much less than the local rate of intergranular growth. It is of interest to be able to determine the influence of a grain structure with a particular size and shape anisotropy on the kinetics of intergranular growth in the through thickness direction.

Ruan et al. (2004) proposed a statistical model to describe the relationship between the microstructure and the IGC growth rate based on foil penetration data and

quantification of the microstructure of AA2024-T3. In the model, a brick wall represents the laminated microstructure of AA2024-T3. The distributions of the grain size (both width and length) are approximated by gamma distributions. Since the grain size in the longitudinal or rolling direction is much larger than that in the long transverse direction, the problem can be simplified into two dimensions, the short and long transverse dimensions. IGC in the longitudinal direction is assumed not to contribute to penetration in the short transverse direction. Given the length and the width of the grain, the distance that a corrosion path travels along a given grain is assumed to be uniformly distributed. Then, a Matlab program was used to simulate the distribution of the minimum order statistic of the corrosion path length. The simulation gives estimates with a small amount of underestimation compared to the actual result from Zhang's (2001) experiments.

The brick wall model relates the growth kinetics of AA2024-T3 aluminum alloy to the microstructure of the alloy. It provides a simple way to quantitatively evaluate the growth kinetics of IGC for a given microstructure in AA2024-T3. However, the brick wall model was based on a series of simplified assumptions, which do not provide a totally accurate description of the corrosion propagation process. In particular, there are two cases that were not accounted for in the model. First, corrosion was assumed to turn toward the bottom surface (away from the environment) at every intersection with a vertical grain boundary. However, a corrosion path might actually skip an intersection and not turn. Moreover, when a corrosion path does make a turn, it might turn up toward the top surface (toward the environment) or down toward the bottom surface of the metal strip depending on the nature of the three-way intersection. When a corrosion path turns upward and reaches the top surface, the propagation can be assumed to terminate. Second, a corrosion path was assumed not to split at any intersection while it might actually split into two corrosion paths at an intersection. Each of these two corrosion paths might propagate independently in the metal. Accordingly, the number of corrosion paths increases. Based on the above considerations of corrosion behavior, a more realistic brick wall model is discussed in this paper.

2. Modeling corrosion growth at an intersection

2.1. Basic assumptions

Consider a strip of metal with thickness T and a total of k grain layers across the thickness. The widths b_j of the grains are taken to be common within a given layer but they are permitted to vary across different layers. That is,

$$T = \sum_{j=1}^{k} b_j. \tag{2.1}$$

Let a denote grain length and assume that it has a distribution with pdf $f(a)$. As stated in the previous paper (Ruan et al., 2004), both the grain length and width are reasonably modeled by gamma distributions with appropriate parameter values α and β. Suppose there are m corrosion initialization points on the surface of the metal. For

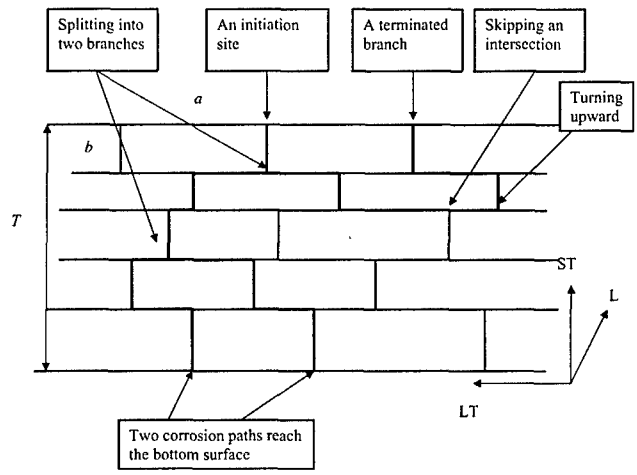

Fig. 1. A graphical representation of the growth behavior of a corrosion path at a three-way intersection in a strip of metal with $k = 5$ grain layers. The bold line represents $W_{i,D}$ and a and b are random variables representing the length and width, respectively, of a grain model. (Note: ST—short-transverse direction; LT—long-transverse direction; L-longitudinal direction.)

$i = 1, \ldots, m$, let $W_{i,D}$ denote the distance that the ith initial corrosion path travels to reach a fixed depth, say D, of the metal. If the corrosion path reaches the bottom surface, $W_{i,D}$ corresponds to $W_{i,T}$. Assume these m corrosion paths are independent. Fig. 1 is a graphical representation of a brick wall model that represents an aluminum sample with a simplified layered microstructure. The corrosion path initiated from the top surface travels along a grain boundary that is perpendicular to the surface. It propagates along the grain boundary until it meets an intersection. Then, it might turn to a horizontal direction (either left or right on the figure), or it might split into two horizontal corrosion paths. In the former case, it propagates along the length direction of the grains until it meets another intersection. Depending on the nature of this new three-way intersection, it might turn upward, or downward, or might skip the intersection and continue propagation along the horizontal direction. Since the widths of the grains are small compared to the lengths of the grains, it is reasonable to assume that a corrosion path will always make a turn toward a horizontal direction at the end of a vertical step. If a corrosion path turns upward and reaches the top surface again, it is considered to be a terminated path since IGC corrosion does not propagate on the surface of the alloy. Additionally, it is assumed that a corrosion path cannot terminate anywhere except the top or bottom surface of the metal strip. In the case where a corrosion path splits into two horizontal pieces at an intersection, these pieces are viewed as two corrosion paths having initiated from the same place on the top surface with a common previous path length. These paths are then assumed to propagate independently in the remainder of the metal sample under the previously described assumptions. However, in the case of such a split, the total number of corrosion paths increases.

The foil penetration technique measures the time taken by the fastest corrosion growth path to reach the bottom surface. With the vital assumption that the local corrosion growth rate is identical in all directions, the fastest corrosion growth corresponds to the shortest corrosion path length (Zhang, 2001; Zhang et al., 2003). Correspondingly, any path that terminates before reaching the bottom surface should not be considered the shortest corrosion growth path (minimum order statistic) for our purposes.

When a horizontal corrosion path meets an intersection, it can either continue to propagate in the horizontal direction or turn toward a vertical direction that is perpendicular to the surface. There are two types of intersections, represented by "⊤" and "⊥". For the "⊤" type intersection, the horizontal corrosion path can turn downward toward the bottom surface. For the "⊥" type intersection, the horizontal corrosion path can turn upward toward the top surface. Therefore, the probability that a horizontal corrosion path turns upward depends on the proportion of the "⊥" type intersections among all the intersections it meets. Similarly, the probability that a corrosion path turns downward depends on the proportion of "⊤" type intersections among all the intersections it meets. Let $p_{\perp}$ and $p_{\top}$ denote these two proportions, respectively. Then,

$$p_{\perp} + p_{\top} = 1. \tag{2.2}$$

Let p_{skip} represent the probability that a horizontal corrosion path skips an intersection and let p_{up} and p_{down} be the probabilities that it turns upward and downward, respectively. Then, according to our previous assumptions, we have

$$p_{\text{up}} + p_{\text{down}} + p_{\text{skip}} = 1. \tag{2.3}$$

If a horizontal corrosion path is known to make a turn at an intersection, the two conditional probabilities $p_{\text{up}}/(1 - p_{\text{skip}})$ and $p_{\text{down}}/(1 - p_{\text{skip}})$ describe the likelihood that a corrosion path would turn upward and downward, respectively, corresponding to the proportions of the "⊥" and "⊤" types of intersections, respectively. That is,

$$\begin{aligned} p_{\perp}(1 - p_{\text{skip}}) &= p_{\text{up}}, \\ p_{\top}(1 - p_{\text{skip}}) &= p_{\text{down}}. \end{aligned} \tag{2.4}$$

Next, let p_{split} denote the probability that a corrosion path splits into two branches at an intersection at the end of a vertical step. We assume all of these probabilities are identical for every intersection.

We consider a total of m initial corrosion sites on the top surface of a metal strip. Propagation with possible splitting results in $(m + u)$ path lengths, where $u \geqslant 0$ is the total number of branches resulting from splitting of corrosion paths. Among these lengths, we let $v \geqslant 0$ be the number of paths terminated on the top surface instead of the bottom surface. Therefore, the $(m + u - v)$ paths lead to a random number of corrosion path lengths and the minimum of these lengths is recorded as a random observation $W_{\min,T}$ from the distribution of the minimum path length for a metal strip of thickness T. The minimum order statistic for the corrosion path lengths is thus

given by

$$W_{\min,T} = \min_{i=1,\ldots,m+u-v} W_{i,T}, \quad i = 1,\ldots,m+u-v, \tag{2.5}$$

where $W_{i,T}$ is the length of the ith corrosion path.

Let $W_{i,D,\text{horizontal}}$ and $W_{i,D,\text{vertical}}$ represent the total horizontal distance and the total vertical distance, respectively, traveled by the ith corrosion path, so that

$$W_{i,D} = W_{i,D,\text{vertical}} + W_{i,D,\text{horizontal}}, \quad i = 1,\ldots,m+u. \tag{2.6}$$

Let $T_i(j)$ be the vertical distance that the ith corrosion path travels along the width of the jth grain before it turns toward a horizontal direction. That is,

$$W_{i,D,\text{vertical}} = \sum_j T_i(j), \quad i = 1,\ldots,m+u, \tag{2.7}$$

where $j \in \{1,2,\ldots,k\}$, and k is the total number of grain layers across the thickness. Since corrosion paths might turn upward and travel on previous layers again, the total vertical distance for a given corrosion path might not exactly equal the thickness T. Each $T_i(j)$ is, however, equal to the width of the jth layer. Since the width of the grain in each layer is modeled by a gamma distribution, all the $T_i(j)s$ have a common gamma distribution. Let $D_i(j)$ represent the horizontal distance that the ith corrosion path travels on the bottom surface of the jth layer of the metal, for $j \in \{1,\ldots,k-1\}$, where k is the total number of grain layers across the thickness. Note that no corrosion paths propagate on either the top surface of the first layer or on the bottom surface of the kth layer. Then,

$$W_{i,D,\text{horizontal}} = \sum_j D_i(j), \quad i = 1,\ldots,m+u. \tag{2.8}$$

When a corrosion path skips an intersection and keeps propagating in the horizontal direction, the associated $D_i(j)$ would include at least two horizontal pieces. In Fig. 2, we show such a situation where a corrosion path skips three successive intersections on the bottom surface of the first layer leading to four horizontal pieces that add up to $D_i(1)$. The corrosion path turns downward at the fourth intersection. (Note that a grain might be intercepted by other grains randomly on either the top or bottom surface.) Given the length of the grain, the first piece of $D_i(1)$ is modeled by a uniform distribution and is denoted by $H_i(1)$. The unconditional distribution of this random variable was discussed in detail in Ruan et al. (2004). Briefly, the pdf, $h(d)$, of $H_i(1)$ is given by the following:

$$\begin{aligned} h(d) &= \int_d^\infty \frac{1}{a} \frac{1}{\Gamma(\alpha)\beta^\alpha} a^{\alpha-1} \mathrm{e}^{-a/\beta}\, \mathrm{d}a \\ &= \frac{1}{(\alpha-1)\beta} \int_d^\infty \frac{1}{\Gamma(\alpha-1)\beta^{\alpha-1}} a^{\alpha-2} \mathrm{e}^{-a/\beta}\, \mathrm{d}a, \quad 0 < d < \infty, \end{aligned} \tag{2.9}$$

where $\alpha > 0$ and $\beta > 0$ are the parameters of the gamma distribution used to model the distribution of grain lengths in the metal.

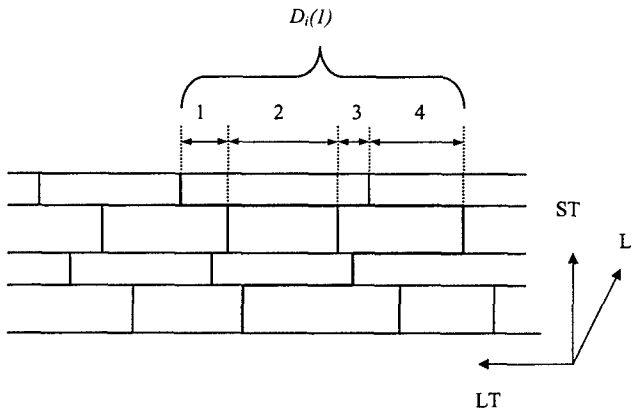

Fig. 2. The bold line represents a corrosion path $W_{i,D}$. $D_i(1)$ is the horizontal distance that the ith corrosion path travels in the second grain layer.

Once a corrosion path skips an intersection, however, the remaining horizontal pieces on the grain layer are modeled solely by the gamma distribution without use of a conditional uniform distribution. We denote these pieces by $[G_i(1)]_s$, $s = 1,\ldots,n$, where n is the total number of such complete horizontal pieces. We note that this is actually an upper bound approximation since the last piece of the horizontal distance might not cover an entire grain length before the path turns again. However, during propagation, we believe that a horizontal corrosion path is likely to meet many more "⊤" type intersections than "⊥" type intersections. Therefore, the probability that a corrosion path turns downward is likely to be greater than the probability that it turns upward. As a result, the upper bound approximation from using these complete horizontal gamma distances when a corrosion path skips an intersection should not result in serious overestimation. With this notation, we have

$$D_i(1) = H_i(1) + \sum_{s=l}^{n} [G_i(1)]_s. \tag{2.10}$$

2.2. Computer simulation

Under the discussed assumptions, we used a Matlab algorithm to simulate the distribution of the minimum path length. First, the thickness of each layer, b_j, $j = 1,\ldots,k$, is generated from a gamma distribution. The parameters of the gamma distribution are estimated via the method of moments (Ruan et al., 2004). The sum of this set of random numbers is subject to the constraint $T = \sum_{j=1}^{k} b_j$. We must adjust the width of the last grain layer to accommodate.

For a corrosion path, the first step is always taken to be a vertical step $T_i(1)$, which is equal to b_1. Next, the first $H_i(1)$ from the distribution with pdf (2.9) is generated. Then, probabilities p_{up}, p_{down}, p_{skip} and p_{split} are assigned. As an example, consider $p_{\text{down}} = 0.8$ and $p_{\text{skip}} = 0.1$ so that $p_{\text{up}} = 1 - p_{\text{down}} - p_{\text{skip}} = 0.1$ by (2.3). A random

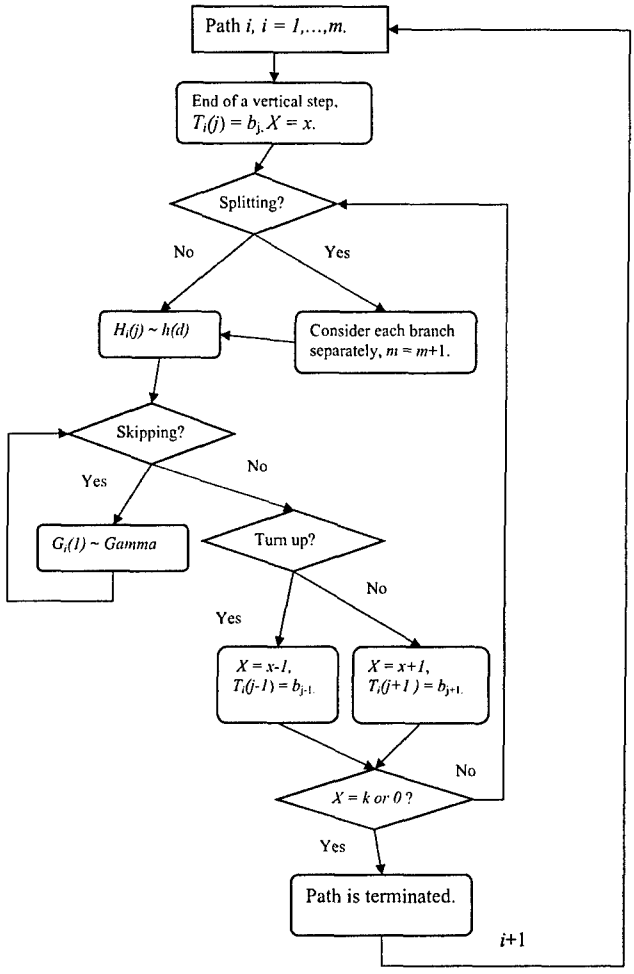

Fig. 3. A flow chart representing the computer simulation algorithm.

number w is generated from the uniform $(0,1)$ distribution. If $w < 0.1$, the corrosion assumes an upward turn. Accordingly, a vertical step is generated with the distance b_1, the thickness of the first grain layer. If $w > 0.9$, the corrosion skips the intersection and a random number $G_i(1)$ is generated. If w falls between 0.1 and 0.9, the corrosion path assumes a downward turn and the vertical step takes the value of b_2, the thickness of the second grain layer. An indicator variable, X, is used to record the layer number that the corrosion path is currently on. The initial value of X is zero. When the corrosion path makes a downward turn, X is increased by 1. When the corrosion path makes an upward turn, X is reduced by 1. Otherwise, X retains its current value. $X = 0$ (except initially) corresponds to a corrosion path that is terminated at the top surface. Similarly, $X = k$ if a corrosion path reaches the bottom surface. The minimum path length is obtained from those corrosion paths that reach the bottom surface.

Starting from the first vertical step, it is necessary to consider whether a corrosion path might split into two branches. For example, assume $p_{\text{split}} = 0.2$. A random number r is generated from the uniform $(0,1)$ distribution. If $r < 0.2$, the corrosion path is split into two horizontal pieces. Each of the branches is then simulated separately from this point on. The total number of branches and the number of the current layer where the splitting occurs are recorded. For branch 1, the horizontal and vertical distances it travels are simulated accordingly given the known probabilities p_{up}, p_{down}, p_{skip} and p_{split}. If there is another split somewhere along the path, the layer number and the number of total splits are again recorded. After branch 1 reaches the bottom surface or terminates at the top surface, the program starts to simulate branch 2. This branch has a portion overlapping with the first one, so the new simulation starts from the layer where the split occurs until the second branch is also terminated. This entire procedure is repeated until all of the branches have been simulated.

The entire set of corrosion paths constitutes a random sample from the distribution of $W_{i,D}$, $i = 1,\ldots,m+u$. Using the indicator variable X which records the current layer of the corrosion path, a random sample is generated from the distribution of $W_{i,T}$, $i = 1,\ldots,m+u-v$; that is, from the distribution of corrosion path lengths that reach the bottom surface. The number of corrosion initialization sites, m, is estimated to be in the order of 10^3 for this type of aluminum foil penetration samples (Ruan et al., 2004; Zhang et al., 2003). However, m is assumed to be 100 in this paper in order to reduce the amount of computation and still illustrate the application of the simulation procedure. The minimum of these lengths is recorded as a random observation $W_{\min,T}$ from the distribution of the minimum path length. A sufficient number (e.g., sample size = 100) of minimum path length values are generated by repeating the above procedure. The algorithm of the computer program is summarized in Fig. 3.

3. Simulation results and discussion

We use the method of moments to estimate the parameters of the gamma distributions in order to simulate the grain sizes. From previous work (Ruan et al., 2004), the method of moments estimators for the parameters a and β for grain length of the AA2024-T3 sample tested by Zhang (2001) are 4 and 0.075, respectively. In addition, from Zhang (2003), the sample mean and standard deviation of the grain thickness measurements are 0.05 and 0.032 mm, respectively. Assuming that the thickness of the grains is distributed as a gamma (a', β') distribution, it follows from the method of moments that solving

$$a'\beta' = 0.05$$

and

$$a'\beta'^2 = 0.032^2 \tag{3.1}$$

simultaneously yields $\hat{\alpha}' = 2.44$ and $\hat{\beta}' = 0.02$. However, since a' must be an integer for the gamma distribution in our model, we could use either gamma $(2, 0.0255)$ or gamma

Table 1
Comparison of the results for gamma (2, 0.0255) and gamma (3, 0.017)

	Median of minimum path length ($p_{down} = 1$, $p_{up} = 0$, $p_{skip} = 0$, $p_{split} = 0$) (mm)	Median of minimum path length ($p_{down} = 0.94$, $p_{up} = 0.05$, $p_{skip} = 0.01$, $p_{split} = 0.03$) (mm)
Gamma (2, 0.0255)	1.296	1.325
Gamma (3, 0.017)	1.294	1.385

The number of sums is $m = 100$ and the number of layers is $k = 12$. A random sample of size 100 was taken from the distribution of the minimum path length for each model.

Table 2
Simulation results for minimum corrosion path length when a corrosion path can turn upward or downward but not skip an intersection or split into branches ($p_{skip} = 0$, $p_{split} = 0$)

Sample	p_{down}	p_{up}	Median of minimum path length (M) (mm)	Normalized ratio
1	1.00	0.00	1.296	3.24
2	0.95	0.05	1.358	3.39
3	0.90	0.10	1.438	3.59
4	0.85	0.15	1.485	3.71
5	0.80	0.20	1.580	3.95
6	0.75	0.25	1.701	4.25
7	0.70	0.30	1.828	4.57
8	0.65	0.35	2.123	5.31
9	0.60	0.40	2.275	5.69
10	0.55	0.45	2.787	6.97
11	0.50	0.50	3.686	9.22

(3, 0.017) to simulate the distribution of grain thickness. In the case that a corrosion path can only assume a downward turn, these two sets of parameters give close results in terms of the median from the distribution of the minimum path length, as shown in Table 1. In the case when $p_{up} = 0.05$, $p_{skip} = 0.01$ and $p_{split} = 0.03$, however, the agreement between these two sets of parameters is not as good as the previous case, since the median for gamma (2, 0.0255) is 1.325 while the median for gamma (3, 0.017) is 1.385. This small difference is most likely due to the randomness of the simulation rather than the difference in the parameters, i.e., the number of times that a corrosion path skips an intersection or splits into two pieces is different from path to path. Hence, either gamma (2, 0.0255) or gamma (3, 0.017) can be used to model the distribution of the grain width. For the rest of our study, we use only gamma (2, 0.0255) to simulate the distribution of the grain thickness.

Using the algorithm described in Section 2.2, the influences of turning upward, skipping an intersection and splitting into two branches on the minimum corrosion path lengths are investigated separately and the results are summarized in Tables 2–4, respectively. The thickness of the grain is simulated by a gamma (2, 0.0255) distribution. The number of corrosion initialization sites is $m = 100$, the number of

Table 3
Simulation results for minimum corrosion path length when a corrosion path can turn downward or skip an intersection but not turn upward or split into branches ($p_{up} = 0$, $p_{split} = 0$)

Sample	p_{down}	p_{skip}	Median of minimum path length (M) (mm)	Normalized ratio
12	0.95	0.05	1.362	3.40
13	0.90	0.10	1.435	3.59
14	0.85	0.15	1.486	3.72
15	0.80	0.20	1.586	3.96
16	0.75	0.25	1.701	4.25
17	0.70	0.30	1.812	4.53
18	0.65	0.35	1.955	4.89
19	0.60	0.40	2.124	5.31
20	0.55	0.45	2.246	5.61
21	0.50	0.50	2.488	6.22

Table 4
Simulation results for minimum corrosion path length when a corrosion path can split into two branches at the end of a vertical step, but not turn upward or skip an intersection ($p_{up} = 0$, $p_{skip} = 0$)

Sample	p_{down}	p_{split}	Median of minimum path length (M) (mm)	Normalized ratio
22	0.95	0.05	1.232	3.08
23	0.90	0.10	1.196	2.99
24	0.85	0.15	1.154	2.89
25	0.80	0.20	1.142	2.86
26	0.75	0.25	1.092	2.73
27	0.70	0.30	1.054	2.63
28	0.65	0.35	1.042	2.60
29	0.60	0.40	1.016	2.54
30	0.55	0.45	0.991	2.48
31	0.50	0.50	0.960	2.40

layers is $k = 12$, and the sample thickness T is assumed to be 0.4 mm. A random sample of size 100 is taken from the distribution of the minimum path length and the median of these observations M is computed, along with the normalized ratio, given by the expression

$$\text{Normalized ratio} = \frac{M}{T}. \tag{3.2}$$

This ratio is expected to be close to 4.29 for the sample of AA2024-T3 tested by Zhang (2001).

Table 2 summarizes the simulation results for the setting where a corrosion path can turn up or down but not skip or split at an intersection ($p_{skip} = 0$, $p_{split} = 0$). The probability of turning upward, p_{up}, varies from 0 to 0.5 in steps of 0.05. As p_{up} increases, the median of the minimum path length tends to increase. For p_{up} between 0 and 0.5,

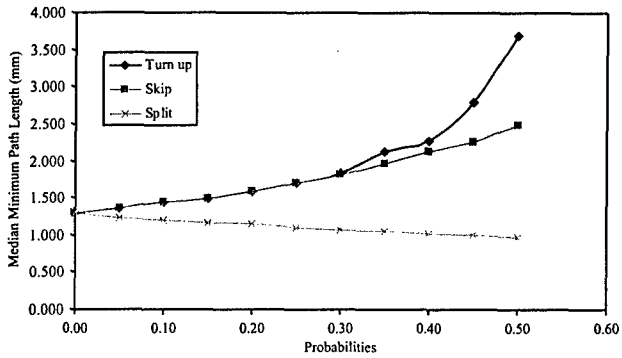

Fig. 4. Effect of probabilities (p_{up}, p_{skip}, p_{split}) on the median of the minimum path length.

the median M increase is roughly linear in the range of 0.1–0.3 but the increase is more dramatic for $p_{up} > 0.3$ (Fig. 4). When $p_{up} = 0$, some underestimation exists in the estimated median minimum path length because the normalized ratio is smaller than the target 4.29. When p_{up} is large, the model overestimates this nominal median minimum path length as the normalized ratio increases dramatically. The increase in simulated median minimum path length can be attributed to two factors. When a corrosion path assumes an upward turn, it propagates along a more tortuous route than those paths that do not turn upward. On the other hand, some corrosion paths that turn upward might terminate at the top surface of the metal strip, thus decreasing the total number of paths reaching the bottom surface. In this case, the minimum order statistic is likely increased. However, the influence of m on minimum order statistic is small (Zhang et al., 2003).

Table 3 summarizes the simulation results for the setting where a corrosion path can assume a downward turn at an intersection or skip the intersection but it cannot turn upward or split ($p_{up} = 0$, $p_{split} = 0$). The probability of skipping an intersection, p_{skip}, varies from 0.05 to 0.5 in steps of 0.05. As p_{skip} increases, the median of the minimum path length tends to increase. We note that when the two probabilities p_{up} and p_{skip} are small, they have similar influence on both the median of the minimum path length and the normalized ratio. They demonstrate similar amounts of random variation with slightly increasing trends. When both probabilities are large, p_{up} is more influential than p_{skip}, as clearly shown in Fig. 4. When a corrosion path skips an intersection and continues to propagate in the horizontal direction, the total horizontal distance it travels will increase. However, when a corrosion path assumes an upward turn, both its horizontal distance and vertical distance traveled will increase. Additionally, p_{skip} does not have the potential to decrease the number of corrosion paths that reach the bottom surface as does p_{up}.

Table 4 summarizes the simulation results for the setting where a corrosion path can split into two branches at an intersection at the end of any vertical step but it cannot turn upward or skip an intersection ($p_{up} = 0$, $p_{skip} = 0$). As with other settings, the probability of splitting at an intersection, p_{split}, varies from 0.05 to 0.5 in steps of 0.05.

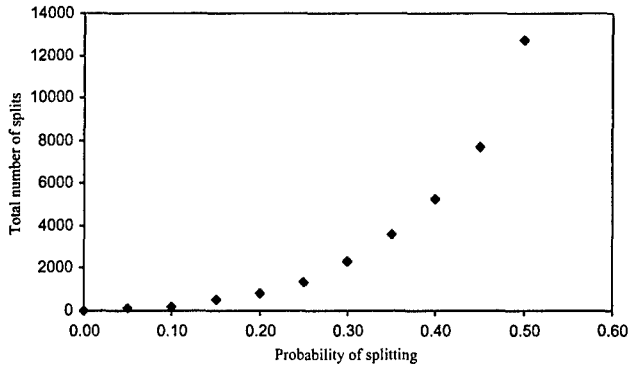

Fig. 5. Effect of the total number of splits on the median minimum path length.

As p_{split} increases, the median of the minimum path length tends to gradually decrease linearly (Fig. 4). The influence of p_{split} is relatively small compared to the influences of p_{up} and p_{skip}. The decrease in the median of the minimum path length is due to the fact that the minimum order statistic is likely to decrease as the number of paths reaching the bottom surface increases. In the case that p_{up} and p_{skip} are both equal to zero, the total number of paths that reach the bottom surface is the sum of the number of initial corrosion sites m and the number of splits that occurred during corrosion propagation. However, the effect of the total number of paths on the minimum order statistic is relatively small compared to the effects of p_{up} and p_{skip}. Fig. 5 shows a representative sample of the number of splits that occurred for each p_{split}. As p_{split} increases from 0.05 to 0.5, the observed number of splits changes from a magnitude of 10^2 to 10^4, but the variation in the median of the minimum path length is less than 0.3 mm, as shown in Table 4.

When the horizontal step is allowed to split into two pieces, one that keeps propagating horizontally and the other that turns to a vertical direction, the total number of paths increases. However, compared to the case where only vertical steps are allowed to split, the effect of the added number of splits by the splitting of the horizontal direction on the minimum order statistic does not provide additional interesting information. There are two explanations. First, when p_{split} is small, the total number of splits is small and the number of splits added by the splitting of horizontal pieces is also very small. Therefore, the decrease in the minimum order statistic due to a slightly larger number of paths is small. When p_{split} is larger, the number of splits increases substantially for both vertical steps and horizontal steps, from the magnitude of 10^2 to the order of 10^4–10^5. With such larger number of paths, the decrease in the minimum order statistic levels off. Therefore, the number of splits by adding the splitting of the horizontal paths also does not significantly affect the minimum order statistic. These simulation results agree with previous comments by Zhang (2001). In conclusion, our previous assumption that a horizontal step is not allowed to split does provide sufficient information about the influence of the splitting of corrosion paths on the minimum order statistic.

Table 5
Effect of increases in the number of layers on the median of the minimum order statistic ($p_{down} = 0.94$, $p_{up} = 0.05$, $p_{skip} = 0.01$, $p_{split} = 0.05$). Sample thickness $T = 0.4$ mm

Number of layers	Median of minimum path length, M	Normalized ratio
8	0.932	2.33
9	1.004	2.51
10	1.130	2.83
11	1.251	3.13
12	1.325	3.31

Table 6
Simulation results for combinations of probabilities (p_{up}, p_{skip}, p_{split}). Sample thickness $T = 0.4$ mm

Sample	p_{down}	p_{up}	p_{skip}	p_{split}	Median of minimum path length (M) (mm)	Normalized ratio
32	0.85	0.05	0.1	0.1	1.348	3.37
33	0.8	0.1	0.1	0.1	1.395	3.49
34	0.75	0.15	0.1	0.1	1.531	3.83
35	0.7	0.2	0.1	0.05	1.799	4.50
36	0.7	0.2	0.1	0.1	1.703	4.26
37	0.7	0.2	0.1	0.15	1.728	4.32

In addition to the behavior of a corrosion path at intersections, the number of layers in a metal strip is another influential factor that affects the minimum path length. The more layers there are in a metal strip, the smaller will be the thickness of the grains. Clearly, the minimum path length is an increasing function of the number of grain layers since that means more intersections within the metal strips. Thus, there are more opportunities for corrosion paths to turn up or skip an intersection. Of course, this also provides more opportunities to split into two branches, but, as noted, the effect of splitting is much less than the effect of either turning up or skipping. For example, suppose metal strips of the same thickness (e.g., $T = 0.4$ mm) are used for the simulated experiment. All other parameters are the same as described previously except the strips have different numbers of grain layers. The simulation results are summarized in Table 5. It is interesting to note that the median M is increased by approximately 0.1 when the number of layers increases by 1. In this model, the number of layers is variable because the grain thickness exhibits a distribution. In reality, the variability in the number of layers for a sample of a give thickness is small.

For a given metal strip, the number of layers is fixed. Therefore, we can adjust the probabilities (p_{up}, p_{skip}, p_{split}) to provide combinations that yield good fits to the data. This can be useful in providing information about the possible corrosion behaviors in the metal. The following are simulation results for several combinations of probabilities. Comparing the normalized ratio to 4.29, it seems that the samples 36 and 37 in Table 6 provide a good fit to the data. Such a combination is not unique. As

mentioned, the p_{up} and p_{down} are related to the chances that a corrosion path meets "$\perp$" and "$\top$" types of intersections and p_{up} is much smaller than p_{down}. It seems that for given p_{up} and p_{down}, p_{skip} and p_{split} can be adjusted to get different normalized ratios. However, estimation of these probabilities is not yet available from experiments.

4. Conclusions

In this paper, we discuss an extension of the brick wall model proposed by Ruan et al. (2004). The basic brick wall model underestimates the minimum path length that a corrosion path travels along grain boundaries in an aluminum alloy sample. This problem is addressed by modeling the behavior of corrosion paths at intersections of grain boundaries. Situations considered include the cases where a corrosion path might assume an upward turn, skip an intersection or split into branches. We found that small percentage changes in the probabilities of any of these options can result in significant changes in the median of the minimum order statistic and the normalized ratio. However, with a proper combination of these probabilities, the extended model is able to obtain a good fit to the experimental data. This extension of the brick wall model represents a more precise description of the growth kinetics for AA2024-T3.

Even though it is still unknown in practice what values are reasonable to assign to these probabilities for this type of alloy, the simulation of such phenomena can provide useful quantitative insights into the understanding of the corrosion kinetics in AA2024-T3. If deemed necessary for a given metal alloy, further refinement of this model is also possible. For example, a corrosion path might have positive probabilities to turn to one direction or split into two branches no matter whether it is at a horizontal or vertical step. That is, even at the end of a horizontal step the corrosion path might split into two branches, where one branch skips the intersection and the other turns to a vertical direction. Also, it is reasonable to allow a corrosion path to terminate within the metal when it meets another corrosion path from an opposite direction.

Acknowledgements

S. Ruan and D.A. Wolfe were supported by the National Science Foundation under Award Number DMS-9802358. G.S. Frankel was supported by the United States Air Force through a grant from S& K Technologies. We thank the referees and the associate editor for their comments, which led to an improved presentation of our results.

References

Davis, J.R. (Ed.), 1999. Corrosion of Aluminum and Aluminum Alloys. ASM International, Materials Park, OH.

Galvele, J.R., De Micheli, S.M., 1970. Mechanism of intergranular corrosion of Al–Cu alloys. Corrosion Science 10, 795–807.

Muller, I.L., Galvele, J.R., 1977. Pitting potential of high purity binary aluminum alloys—I, Al–Cu alloys. Pitting and intergranular corrosion. Corrosion Science 17, 179–193.

Ruan, S., Wolfe, D.A., Zhang, W., Frankel, G.S., 2004. Statistical modeling of minimum intergranular corrosion path length in high strength aluminum alloy. Technometrics, to appear.

Scully, J.R., Peebles, D.E., Romig, A.D., Frear, D.R., Hills, C.R., 1992. Metallurgical factors influencing the corrosion of aluminum, Al–Cu, and Al–Si alloy thin-films in dilute hydrofluoric solution. Metallurgical Transactions A – Physical Metallurgy and Material Science 23, 2641–2655.

Scully, J.R., 1999. Environment-assisted intergranular cracking. Materials Research Society Bulletin 24, 36–42.

Shibata, T., 1996. Statistical and stochastic approaches to localized corrosion. Corrosion 52 (11), 813–830.

Zhang, W., 2001. Localized corrosion and its kinetics in high strength Al alloy. Ph.D. Dissertation, Ohio State University, Department of Materials Science and Engineering.

Zhang, W., Frankel, G.S., 2000. Anisotropy of localized corrosion in AA2024-T3. Electrochemical and Solid State Letters 3, 268–270.

Zhang, W., Ruan, S., Wolfe, D.A., Frankel, G.S., 2003. Statistical model for intergranular corrosion growth kinetics. Corrosion Science 45, 353–370.

Statistical Modeling of Minimum Intergranular Corrosion Path Length in High-Strength Aluminum Alloy

Shiling Ruan
Department of Statistics
Ohio State University
Columbus, OH 43210
(*ruan.8@osu.edu*)

Douglas A. Wolfe
Department of Statistics
Ohio State University
Columbus, OH 43210
(*daw@stat.ohio-state.edu*)

Weilong Zhang
Department of Materials Science and Engineering
Ohio State University
Columbus, OH 43210
(*zhangw@utrc.utc.com*)

Gerald S. Frankel
Department of Materials Science and Engineering
Ohio State University
Columbus, OH 43210
(*Frankel.10@osu.edu*)

In this article a brick wall model is developed to describe the relationship between the minimum intergranular corrosion path length and the aspect ratio of grains of high-strength wrought aluminum alloy AA2024-T3. We study the distribution of the horizontal distance that a corrosion path will travel in the metal and fit the model to an actual corrosion dataset using the method of moments. The distribution of the horizontal distance of a corrosion path along a given grain is assumed to be uniformly distributed given the length of the grain, which is itself modeled by a gamma distribution. A modified brick wall model is proposed that also imposes a distribution on the vertical distance traveled by the corrosion path. Computer simulation is used to evaluate the fit of these models.

KEY WORDS: Brick wall model; Grain size distribution; Localized corrosion kinetics; Random number generation

1. INTRODUCTION

High-strength aluminum alloys are widely used in the aerospace and defense industries. However, it is well known that localized corrosion can be a major cause of aluminum alloy failures in practice. Aluminum alloys are highly resistant to uniform corrosion but extremely susceptible to localized corrosion. Davis (1999) discussed various forms of localized corrosion in aluminum alloys, including intergranular corrosion (IGC), pitting corrosion, crevice corrosion, exfoliation, and stress corrosion cracking. Of these types of localized corrosion, IGC is of special interest. Recent research suggests that pits could develop into intergranular attacks and penetrate deeply into the microstructure of the alloys (Guillaumin and Mankowski 2000; Zhang and Frankel 2000). Stress corrosion cracking can also result from intergranular attacks (e.g., in the presence of tensile stress), and this can lead to substantial loss of mechanical properties and eventually to failure of the aluminum alloys (Wenzel, Knornschild, and Kaesche 1991; Chung, Stran, and Shack 2001). Therefore, understanding the mechanisms and growth kinetics of IGC is critical. Although the susceptibility of aluminum alloys to IGC has been studied extensively, little in-depth work has been done in quantitatively predicting the susceptibility and resistance of IGC corrosion growth in aluminum alloys. Furthermore, as a special case of localized corrosion, IGC can be properly considered rare events that are unpredictable in terms of both initialization and places of attack. Therefore, a statistical treatment is appropriate (Evans 1960). However, very little previous work has addressed the issue of applying statistical models to IGC growth kinetics.

Metal samples are typically composed of numerous grains, regions where the metallic atoms are aligned in particular arrangement. Grain boundaries, the interfaces between grains, are two-dimensional surfaces that represent discontinuities in the atomic arrangements. Grain sizes can vary from nanometers (nm) to millimeters (mm), but the grain size distribution in a piece of metal is typically limited to a smaller range. IGC is a preferential attack of grain boundaries or nearby adjacent regions without appreciable attack of the grain bodies themselves. Three factors determine the resistance and susceptibility of an alloy to IGC: alloy microstructure, metallurgical factors, and environment (Davis 1999; Scully, Peebles, Romig, Frear, and Hills 1992; Scully 1999). An alloy's microstructure includes grain size and shape, solute precipitate-free zones, and structure of its grain boundaries. All of these factors play important roles in localized corrosion growth. Unfortunately, the exact role of each of these influential factors is not yet fully understood. Zhang (2001) observed that the growth kinetics of localized corrosion in wrought AA2024-T3 exhibited a strong anisotropy, and indicated that IGC might be heavily dependent on the aspect ratio (ratio of grain length to width) of the grains. In this article we develop statistical models to describe the relationship between grain sizes and the nominal IGC rate for wrought AA2024-T3, under certain simplified assumptions about corrosion growth in such an alloy.

© 2004 American Statistical Association and
the American Society for Quality
TECHNOMETRICS, FEBRUARY 2004, VOL. 46, NO. 1
DOI 10.1198/004017004000000121

2. BRICK WALL MODEL

Modeling the relationship between grain size and the minimum IGC path length for AA2024-T3 must take into account two considerations. First, wrought AA2024-T3 has a layered structure with grains flattened in the thickness direction and elongated in the rolling direction, as shown in Figure 1, which is an optical micrograph for the long-transverse section of the AA2024-T3 sample. The size of three-dimensional grains is measured on a two-dimensional cross-section that is polished and etched. Zhang, Ruan, Wolfe, and Frankel (2003) provided more details about the method used to measure the grain dimensions. Second, it is reasonable to consider the local intergranular growth rate to be the same for different orientations (Zhang 2001; Zhang et al. 2003). Therefore, the nominal growth rate is a function only of the anisotropic microstructure, because the various sizes and aspect ratios of grains result in different intergranular path lengths. We model the numerous intergranular paths initiated on the surface of the metal as a series of randomly distributed events. The shortest corrosion path, which would usually result in failure of the material, then corresponds to the minimum order statistic for these intergranular paths.

Based on these considerations, we use a brick wall model to describe the influence of the aspect ratio of the grains on minimum IGC path length. Consider a strip of metal composed of k layers, each with a constant thickness b. The thickness of the strip is thus $T = kb$. Suppose that there are a fixed number of m corrosion initialization points on the surface of the metal. For $i = 1, \ldots, m$, let $W_{i,D}$ denote the distance that the ith initial corrosion path travels to reach a fixed depth, say D, of the metal. Then $D = jb$ for some $j \in \{1, \ldots, k\}$. Let a denote grain length and assume that it has a distribution with pdf $f(a)$. Let $D_i(j)$ represent the horizontal distance that the ith corrosion travels on the surface of the jth layer of the metal, for $j = 1, 2, \ldots, k$. We assume that the collection of mk variables $D_i(j)$, $i = 1, \ldots, m$ and $j = 1, \ldots, k$, are mutually independent. Then the sum of the k random variables $D_i(j)$, $j = 1, \ldots, k$, is the total horizontal distance that the ith corrosion path travels in the metal.

In Figure 2, a sketch of the brick wall model, the first horizontal leg at the top of the brick wall is a representation of the initiation stage of the intergranular attack. Obviously, the random variable W_i can be represented as the sum of the horizontal and vertical distances that the ith corrosion path travels in the metal to reach a depth D. Symbolically, this is expressed by

$$W_i = kb + \sum_{j=1}^{k} D_i(j) \qquad \text{for } i = 1, \ldots, m. \tag{1}$$

When a corrosion path penetrates the entire metal strip, it will have traveled a total vertical distance of $T = kb$. In such a case, $W_i = T + \sum_{j=1}^{k} D_i(j)$. Equivalently, $\sum_{j=1}^{k} D_i(j) = W_i - T$, denoted by $W_{i,D,\text{horiz}}$, is the total horizontal distance that the corrosion path travels. Therefore, studying the minimum order statistic for the W_i is equivalent to studying the minimum order statistic for the horizontal distances $W_{i,D,\text{horiz}}$ that the corrosion paths travel.

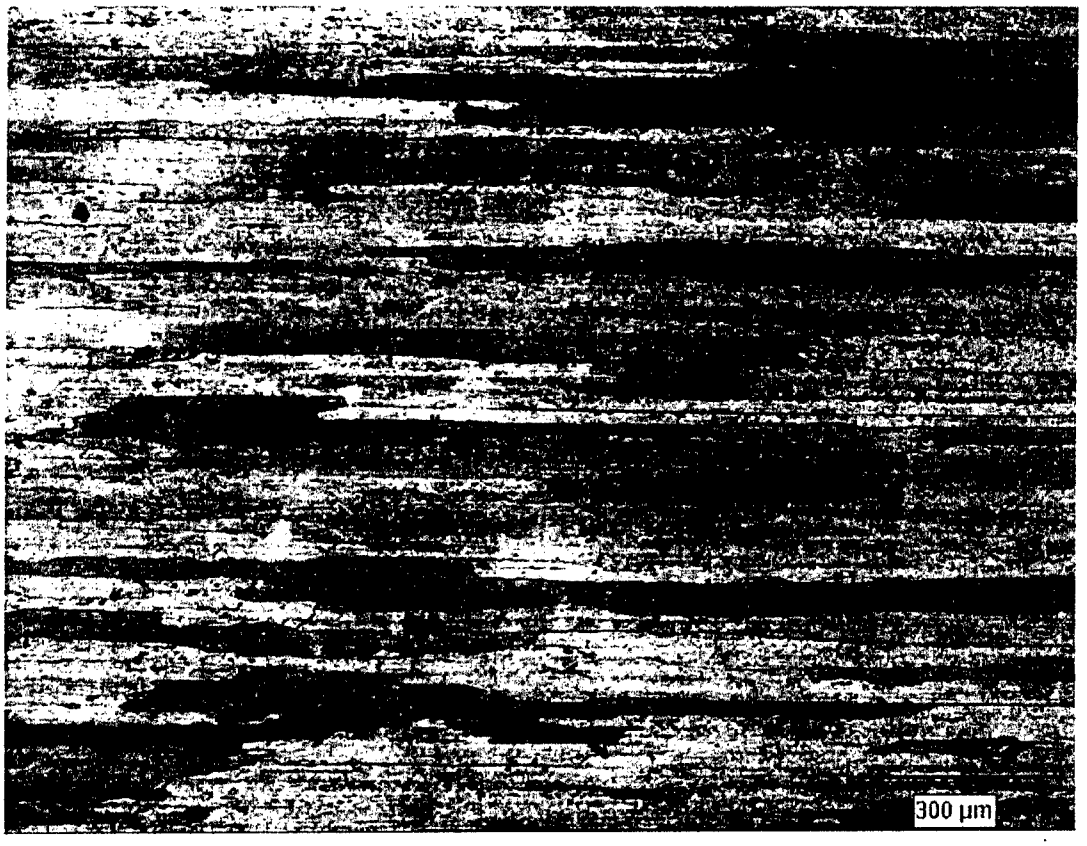

Figure 1. An Optical Micrograph of the Long-Transverse Section of the AA2024-T3 Sample.

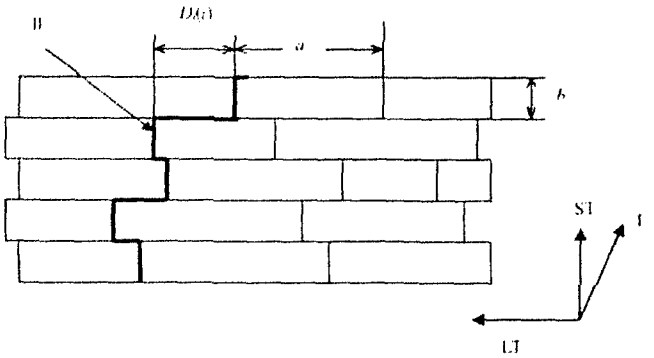

Figure 2. Brick Wall Model. The bold line represents W_i. $D_i(j)$ is the horizontal distance that the ith corrosion travels in the jth grain, a is a random variable representing the length of a grain, and b is the width of a grain and is assumed to be fixed in this model. (ST, short-transverse direction; LT, long-transverse direction; L, longitude direction.)

3. STATISTICAL FORMULATION

The grain aspect ratio is determined by the grain length, a, and width, b. Because the grains in any sample can have a range of sizes, a and b can be viewed as random variables with certain distributions. In the brick wall model described previously, b is assumed to be fixed. From the study by Zhang (2001), grain size a has a distribution skewed slightly to the right. We choose to model this behavior by a gamma distribution with parameters α and β, denoted by gamma(α, β). When the mean, $\bar{L}$, and standard deviation, S_L, of the observed grain lengths are known, the parameters α and β can be estimated by the method of moments through the following two equations:

$$\hat{\alpha}\hat{\beta} = \bar{L}, \qquad \hat{\alpha}\hat{\beta}^2 = S_L^2. \tag{2}$$

For intergranular corrosion, the corrosion path is always supposed to follow the grain boundaries. However, the path might or might not assume a turn at an intersection of several grains, and a grain can intersect with other grains above or below it randomly along its length. Therefore, for a given grain of length a, the horizontal distance that a corrosion travels on the surface of the grain can be modeled as a random variable uniformly distributed on the interval $[0, a]$. Thus for given grain length a, $D_i(j)$ is uniformly distributed on $[0, a]$. Combining the marginal gamma pdf for a with the conditional uniform pdf of $D_i(j)$ given a, the unconditional marginal pdf of $D_i(j)$ is given by

$$\begin{aligned} h(d) &= \int_d^\infty f(a) f(d|a)\, da \\ &= \frac{1}{(\alpha-1)\beta} \int_d^\infty \frac{1}{\Gamma(\alpha-1)\beta^{\alpha-1}} a^{\alpha-2} e^{-a/\beta}\, da. \end{aligned}$$

$$0 < d < \infty,\ \alpha > 0,\ \beta > 0. \tag{3}$$

Using iterated expectation and moments of the gamma and uniform distributions, it follows that $E[D_i(j)] = \alpha\beta/2$ and $\mathrm{var}[D_i(j)] = \alpha\beta^2(4+\alpha)/12$, for $i = 1, \ldots, m$ and $j = 1, \ldots, k$.

A closed-form expression for $h(d)$ is not always attainable. However, such an expression can be obtained in two special cases.

Special Case 1. When $\alpha = 2$ and β is arbitrary, $D_i(j)$ has a gamma$(1, \beta)$ distribution. Because $W_{i,D,\text{hordis}}$ is the sum of k iid gamma$(1, \beta)$ random variables, it will be distributed as gamma(k, β). Using the well-known relationship between incomplete gamma integrals and sums of Poisson probabilities, its cdf can be expressed as

$$\begin{aligned} F_{D,\text{hordis}}(w) &= \int_0^w \frac{1}{\beta^k \Gamma(k)} t^{k-1} e^{-t/\beta}\, dt \\ &= 1 - \int_{w/\beta}^\infty \frac{1}{\Gamma(k)} v^{k-1} e^{-v}\, dv \\ &= 1 - \sum_{i=0}^{k-1} \frac{w^i e^{-w/\beta}}{\beta^i i!}, \qquad w > 0,\ \beta > 0. \end{aligned} \tag{4}$$

Letting $W_{(1),D,\text{hordis}}$ denote the minimum horizontal distance traveled by the m corrosion growth paths, the cdf for $W_{(1),D,\text{hordis}}$ is given by

$$\begin{aligned} P(W_{(1),D,\text{hordis}} \le w) &= 1 - [1 - F_{D,\text{hordis}}(w)]^m \\ &= 1 - \left[\sum_{i=0}^{k-1} \frac{w^i e^{-w/\beta}}{\beta^i i!}\right]^m. \end{aligned} \tag{5}$$

For given k, m, and β, we can easily simulate observations from this distribution of the minimum corrosion path length in the special case of $\alpha = 2$.

Special Case 2. When α is an integer ≥ 2 and β is arbitrary, proceeding as we did for Special Case 1, we find the cdf for $D_i(j)$ to be:

$$\begin{aligned} F(d) &= \int_0^d h(u)\, du = \frac{1}{(\alpha-1)\beta} \int_0^d \sum_{t=0}^{\alpha-2} \frac{(u/\beta)^t e^{-u/\beta}}{t!}\, du \\ &= \frac{1}{\alpha-1} \sum_{t=0}^{\alpha-2} \left[\int_0^d \frac{u^t e^{-u/\beta}}{\beta^{t+1}\Gamma(t+1)}\, du\right] \\ &= 1 - \frac{e^{-d/\beta}}{\alpha-1}\left[\left(\alpha - 1 - \frac{d}{\beta}\right)\sum_{t=0}^{\alpha-2} \frac{(d/\beta)^t}{t!} + \frac{(d/\beta)^{\alpha-1}}{(\alpha-2)!}\right], \end{aligned}$$

$$0 < d < \infty. \tag{6}$$

Closed-form expressions for the distributions of $W_{i,D,\text{hordis}}$ and $W_{(1),D,\text{hordis}}$ are not as tractable in this more general setting. However, numerical methods can still be used to simulate the distributions of $W_{i,D,\text{hordis}}$ and $W_{(1),D,\text{hordis}}$. We carried out such a simulation by first generating a random sample of $D_i(j)$ values with $j = 1, \ldots, k$ from the distribution of $D_i(j)$. We then computed the sum of these k random numbers, yielding a random observation from the common distribution of $W_{i,D,\text{hordis}}$, $i = 1, \ldots, m$, where m is the number of corrosion initiation sites. We repeated this process until m such observations were generated as a random sample from the distribution of $W_{i,D,\text{hordis}}$. Because $W_{(1),D,\text{hordis}}$ is the minimum horizontal distance among the m corrosion paths, the minimum of these m simulated values from the distribution of $W_{i,D,\text{hordis}}$ represents a single random observation from the distribution of $W_{(1),D,\text{hordis}}$. Thus the distribution of $W_{(1),D,\text{hordis}}$ can be simulated by repeating this entire process a sufficient number of times.

4. APPLICATION OF THE BRICK WALL MODEL TO CORROSION DATA

Zhang (2001) collected data on grain lengths for samples of aluminum alloy AA20024-T3. For a sample of size 120, he found the average grain length to be .3 mm and the sample standard deviation for these lengths to be .15 mm. We use these data to illustrate the application of our brick wall model to corrosion data for this alloy. First, according to the method-of-moments expression (2), we solve the two equations

$$\hat{\alpha}\hat{\beta} = .3 \qquad \text{and} \qquad \hat{\alpha}\hat{\beta}^2 = (.15)^2$$

to obtain the estimated parameters $\hat{\alpha} = 4$ and $\hat{\beta} = .075$. This leads to the use of a gamma(4, .075) distribution to model the population of grain lengths. (Note: We require that $\hat{\alpha}$ be an integer.) Figure 3(a) gives the histogram of the grain lengths, and Figure 3(b) gives the plot of quantiles for the data versus quantiles of the gamma(4, .075) distribution. The Kolmogorov–Smirnov goodness-of-fit test to a gamma distribution yields a p value $> .25$. Thus the gamma(4, .075) distribution provides a reasonable fit for the grain length data, although the agreement is not as good at the extreme quantiles.

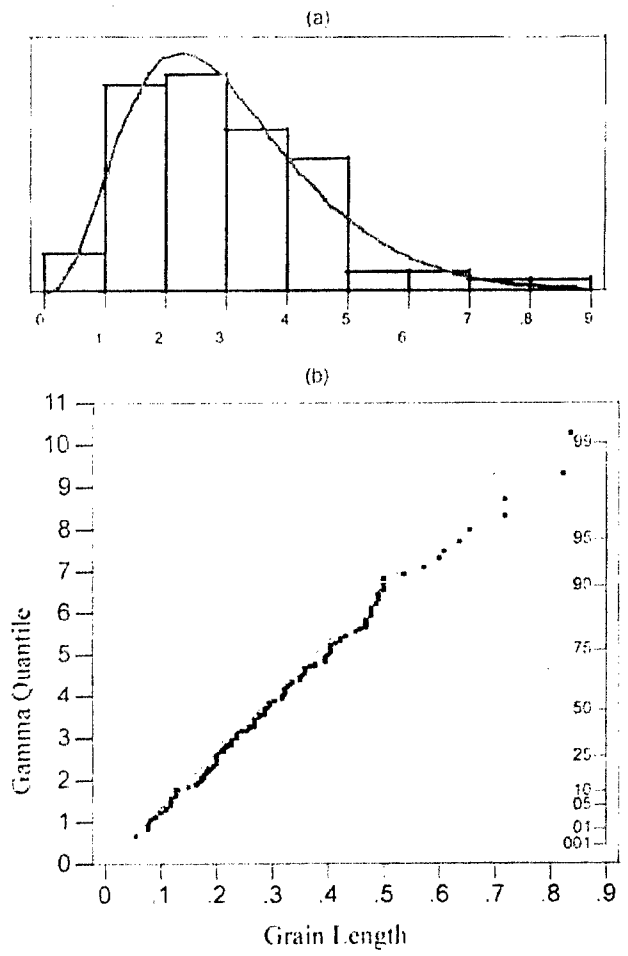

Figure 3. (a) Histogram of Grain Length, a, Measured From a Short-Transverse Section of an Aluminum Plate. Along With the Density Curve of Gamma(4, .075), and (b) Plot of Quantiles of the Data Versus Quantiles of the Gamma(4, .075) Distribution. In (b), the dotted lines provide a 95% confidence interval, and the probability label is given in the right side of the plot.

Zhang (2001) also collected a sample of 120 grain widths for which the average width was $\bar{b} = .05$ mm. Viewing this as a fixed constant width (as assumed for the brick wall model) for our alloy strip of total thickness $T = .4$ mm, the number of grains traversed by each corrosion path was taken to be

$$k = \frac{T}{\bar{b}} = \frac{.4}{.05} = 8, \tag{7}$$

which corresponds to representing the metal strip as comprising eight grain layers, each such grain of average width $\bar{b} = .05$ mm. Thus for our brick wall model, each horizontal corrosion path can be represented as a sum of $k = 8$ iid random variables $D_i(j)$, $j = 1, \ldots, 8$.

The number of corrosion initialization sites, m, is estimated from the grain dimensions and the possible number of corrosion initialization sites associated with each grain. Zhang et al. (2003) estimated the number of initial corrosion sites, m, to be 1,000 for the following conditions: grain size given by the microstructure of short-transverse samples of the alloy used in the experiments, exposed area equal to that used in the foil penetration experiment (1 cm^2), and each grain producing about four initial corrosion sites for IGC growth along the longitude direction. Therefore, in this simulation study, m is fixed at 1,000. To simulate the length of a given, say the ith, corrosion path under this brick wall model, we generated eight independent random variables $D_i(1), \ldots, D_i(8)$ and added them to obtain the total random horizontal length $W_{i,D,\text{hordis}} = \sum_{j=1}^{8} D_i(j)$ for the ith corrosion path. We repeated this process 1,000 times to obtain a random sample of 1,000 independent corrosion horizontal path lengths $W_{1,D,\text{hordis}}, \ldots, W_{1000,D,\text{hordis}}$ simulated from our brick wall model for this alloy. The smallest sum among these 1,000 horizontal path lengths then represents a single random observation from the distribution of the minimum order statistic $W_{(1),D,\text{hordis}} = \min\{W_{1,D,\text{hordis}}, \ldots, W_{1000,D,\text{hordis}}\}$. We repeated this complete process 5,000 times to provide a random sample of size 5,000 from the distribution of $W_{(1),D,\text{hordis}}$.

We performed these simulations using the Broyden method in MatLab (Broyden 1970) to invert the cdf $F(d)$ in (6) with precision 1.4×10^{-8}. To illustrate the application of this computer program, Figure 4 presents an example of the histogram

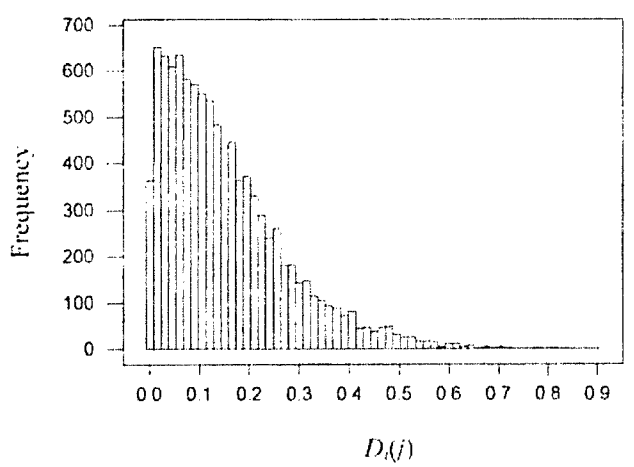

Figure 4. Histogram of a Random Sample of Size 10,000 Generated From the Distribution of $D_i(j)$.

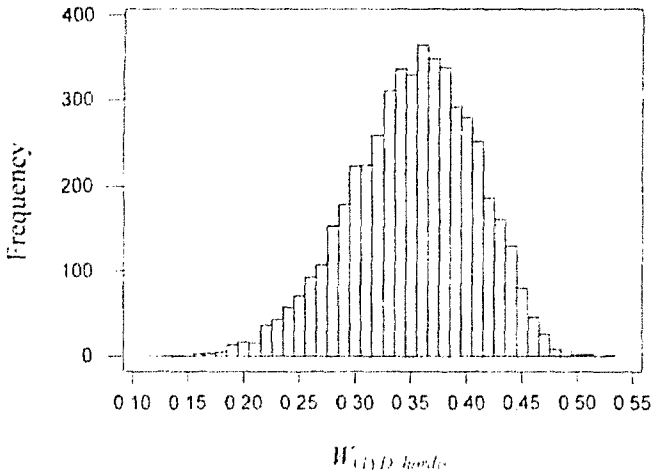

Figure 5. Histogram of a Random Sample of Size 5,000 From the Distribution of $W_{(1),D,\text{hordis}}$ With Fixed $k = 8$.

for 10,000 random observations from the common $D_i(j)$ distribution, and Figure 5 presents the histogram for the random sample of 5,000 observations from the distribution of $W_{(1),D,\text{hordis}}$. The median for these 5,000 minimum observations was then calculated to be $\tilde{W}_{(1),D,\text{hordis}} = .36$ mm.

On the basis of foil penetration experiments for AA20024-T3, Zhang (2001) found that the ratio of the median of the minimum total (horizontal and vertical) corrosion path length normalized by the sample thickness is approximately 4.29; that is, he found that

$$\frac{\text{median horizontal path length} + T}{T} = 4.29. \qquad (8)$$

However, our simulation results yielded a simulated value of

$$\frac{\tilde{W}_{(1),D,\text{hordis}} + T}{T} = \frac{.36 + .4}{.4} = 1.9$$

for this normalized ratio, which substantially underestimates Zhang's experimental results.

One possible reason for this low normalized ratio obtained from our simulated brick wall model is the potential inaccuracy of the simplified assumption that the grain width is the same ($\tilde{b}$) for every grain. According to Zhang (2001), grains vary in both width and length. Therefore, we need to modify our brick wall model to account for the randomness of the grain width (vertical path distances) as well as that of the grain length (horizontal path distances).

5. MODIFIED BRICK WALL MODEL

To modify the brick wall model, we assume that the grains are rectangular in shape and that adjoining grains can intercept with each other randomly along either the length or the width of other grains. Under these conditions, we drop the assumption that b is fixed and instead model it as a random variable with pdf $f(b)$. The other assumptions in the previous brick wall model remain applicable here. For example, we continue to assume that the corrosion paths start from one side of the strip and travel through the metal to the other side, propagating only along the grain boundaries. The thickness of the metal strip is still fixed to be T; $D_i(j)$ represents the horizontal distance that the ith corrosion travels in the jth grain, and $W_{i,D,\text{hordis}}$ is the total horizontal distance that the ith corrosion path travels in the metal, with $j = 1, \ldots, k$ and $i = 1, \ldots, m$. Let $H_i(j)$ be the vertical distance that the ith corrosion travels along the width of the jth grain before it turns onto the $(j+1)$st horizontal layer. Finally, let $W_{i,H,\text{vertical}}$ be the total vertical distance traveled by the ith corrosion; that is,

$$W_{i,H,\text{vertical}} = \sum_{j=1}^{k} H_i(j), \qquad i = 1, \ldots, m.$$

Of course, a corrosion path must travel through the same number of steps in the vertical direction as it does in the horizontal direction, and we let k be the number of turns. It is important to note that $W_{i,H,\text{vertical}}$ is not random, because it must equal the thickness of the metal strip T; that is,

$$W_{i,H,\text{vertical}} = T, \qquad i = 1, \ldots, m.$$

However, the number of turns, k, for a corrosion path in this modified brick wall model is now a random quantity that depends on the distribution of the width variable b. That is, the number of terms, k, in the sum for $W_{i,H,\text{vertical}}$ is now random. To indicate this randomness, we use the notation K rather than k throughout the rest of our discussion about the modified brick wall model. Suppose that the pdf of b is $f(b)$. Given b, $H_i(j)$ will have a distribution with conditional pdf $f(h|b)$. Therefore, the total distance traveled by the ith corrosion through the metal is

$$\begin{aligned} W_i &= W_{i,H,\text{vertical}} + W_{i,D,\text{hordis}} \\ &= \sum_{j=1}^{K} H_i(j) + \sum_{j=1}^{K} D_i(j) \\ &= T + \sum_{j=1}^{K} D_i(j), \qquad i = 1, \ldots, m. \end{aligned} \qquad (9)$$

Now we can use our experimental data to estimate K, the number of turns that a typical corrosion path will make during its propagation through the metal. Assume that K is independent of $H_i(j)$, $j = 1, \ldots, K$. Because the metal strip thickness is $T = \sum_{j=1}^{K} H_i(j)$ and the $H_i(j)$, $j = 1, \ldots, K$, are identically distributed, we have

$$E[K] = \frac{T}{E[H_1(1)]}. \qquad (10)$$

Taking the same approach that we used with the horizontal grain lengths, we assume that the vertical grain width b also has a gamma distribution but with different parameters α' and β'. Given b, we assume that $H_i(j)$ has a uniform $[0, b]$ distribution. Again using iterated expectations, it follows that

$$E[H_1(1)] = \alpha'\beta'/2 = E[b]/2. \qquad (11)$$

Combining (10) and (11) leads to

$$E[K] = \frac{2T}{E[b]}. \qquad (12)$$

We can then use the observed data on grain widths to estimate $E[b]$ and, subsequently, the number of turns K.

6. APPLICATION OF THE MODIFIED BRICK WALL MODEL TO CORROSION DATA

Note that for fixed T and $\bar{b} = \hat{E}[b]$, the estimated value for the average number of grains, $\hat{E}[K]$, traversed by a typical corrosion path obtained from (12) is twice as large as the value suggested by (7) when the randomness of the grain width was not taken into account. The fact that the value of $\hat{E}[K]$ from (12) is larger than that obtained from (7) is not surprising, because taking into account additional randomness is bound to lead to an increase in this figure. However, we were a bit surprised that the estimate of the average number of turns taken by a corrosion path actually doubled when the randomness of the grain width was taken into account.

Once again we used simulation and the experimental findings of Zhang (2001) to evaluate the modified brick wall model. The estimates $\hat{\alpha} = 4$ and $\hat{\beta} = .075$ in the gamma model for the horizontal distances remain the same for the modified model. The only change in the simulation process is that the total horizontal distance traveled by a corrosion path is now modeled to be a sum of $\hat{E}[K] = 16$ (the estimated average number of turns) independent horizontal distances, rather than 8 as used in the original brick wall model.

To simulate the horizontal length of a given corrosion path under this modified brick wall model, we generated 16 independent random variables $D_i(1), \ldots, D_i(16)$ and added them to obtain the total random horizontal length for the path. We once again repeated this process 1,000 times to obtain a random sample of 1,000 simulated independent corrosion horizontal path lengths for the modified brick wall model. As before, the smallest sum from these 1,000 simulated horizontal path lengths represents a single observation from the distribution of the minimum order statistic $W_{(1),D,\text{hordis}}$. We repeated this complete process 5,000 times to provide a random sample of size 5,000 from the distribution of $W_{(1),D,\text{hordis}}$. The histogram for these 5,000 values of $W_{(1),D,\text{hordis}}$ is presented in Figure 6. The sample median for these 5,000 minimum observations for the modified brick wall model was calculated to be $\tilde{W}_{(1),D,\text{hordis}} = 1.10$ mm.

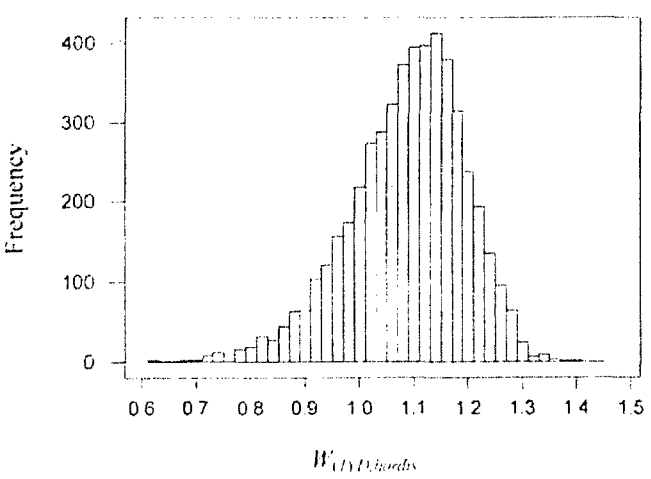

Figure 6 Histogram of a Random Sample of Size 5,000 From the Distribution of $W_{(1),D,\text{hordis}}$ With $\hat{E}[K] = 16$.

With the doubled value for $\hat{E}[K]$ and a fixed metal thickness, the median of the minimum order statistics will certainly be larger under this modified brick wall model. This will lead to an improved normalized ratio and a better fit of the model to Zhang's experimental findings (Zhang 2001; Zhang et al. 2003). Specifically, the modified brick wall model yielded a simulated normalized ratio value of

$$\frac{\tilde{W}_{(1),d,\text{hordis}} + T}{T} = \frac{1.10 + .4}{.4} = 3.75. \tag{13}$$

Clearly, this provides a much closer match with the experimental value (8) of 4.29 observed by Zhang (2001). However, a small amount of underestimation remains. One possible reason for this is that the actual corrosion likely propagates in three dimensions rather than the simplified two-dimension model that we have assumed. It has been noted that the typical grain size in that third dimension is considerably larger than that in either of the other two directions (Zhang 2001; Zhang et al. 2003). Allowing for more complicated three-dimensional travel could lead to an even larger estimate for the average number of steps, $\hat{E}[K]$, and, subsequently, to a larger simulated value of the minimum corrosion path length. Another possible cause of underestimation is that a corrosion path might not turn at every intersection. This could lead to a considerable increase in path length. Still another possibility is that a corrosion path could turn in both directions at an intersection. This would lead to an increase in the number of corrosion sites and a decrease in the minimum path length. Dealing with all of the aforementioned possibilities requires more complicated models; however, the experimental data needed to evaluate these more complicated models are not available at present.

7. CONCLUSION

In this article we report a brick wall model to describe the IGC growth kinetics. The model considers the influence of the size and aspect ratio of grains on continued propagation of a corrosion path along the grain boundaries in an aluminum alloy. Based on this model, we derived the distribution of the minimum order statistic corresponding to the shortest path length from the distribution of the distance that corrosion travels along one grain. We discussed the appropriateness of the model and modified the model to take into account varying grain widths. The modified brick wall model provides a good fit to the actual experimental result and can also be used to describe the corrosion kinetics of other alloys with layered structures. Future study will include various modifications of the models to make them less restrictive. Nevertheless, modeling of corrosion growth kinetics is a complicated task that merits further effort in light of the various features of corrosion theories for different alloys.

[Received February 2002. Revised December 2002.]

REFERENCES

Broyden, C. G. (1970), "The Convergence of a Class of Double-Rank Minimization Algorithms," *Journal of the Institute of Mathematics and Its Applications*, 6, 76–90.

Chung, H. M., Stran, R. V., and Shack, W. J. (2001), "Tensile and Stress Corrosion Cracking Properties of Type 304 Stainless Steel Irradiated to a Very High Dose," *Nuclear Engineering and Design*, 208, 221–234.

Davis, J. R. (ed.) (1999), *Corrosion of Aluminum and Aluminum Alloys*. Materials Park, OH: ASM International.

Evans, U. R. (1960), *Corrosion and Oxidation of Metals*. London: Edward Arnold, Chap. 22.

Guillaumin, V., and Mankowski, G. (2000), "Localized Corrosion of 6056-T6 Aluminum Alloy in Chloride Media," *Corrosion Science*, 42, 105–125.

Scully, J. R. (1999), "Environment-Assisted Intergranular Cracking," *Materials Research Society Bulletin*, 24, 36–42.

Scully, J. R., Peebles, D. E., Romig, A. D., Frear, D. R., and Hills, C. R. (1992), "Metallurgical Factors Influencing the Corrosion of Aluminum, Al–Cu, and Al–Si Alloy Thin-Films in Dilute Hydrofluoric Solution," *Metallurgical Transactions A—Physical Metallurgy and Materials Science*, 23, 2641–2655.

Wenzel, G., Knornschild, G., and Kaesche, H. (1991), "Intergranular Corrosion and Stress Corrosion Attacking of an Aged AlCu Alloy in 1-N NaCl Solution," *Materials and Corrosion*, 42, 449–454 (in German).

Zhang, W. (2001), "Localized Corrosion and Its Kinetics in High-Strength Al Alloy," unpublished doctoral dissertation, Ohio State University, Dept. of Materials Science and Engineering.

Zhang, W., and Frankel, G. S. (2000), "Anisotropy of Localized Corrosion in AA2024-T3," *Electrochemical and Solid-State Letters*, 3, 268–270.

Zhang, W., Ruan, S., Wolfe, D. A., and Frankel, G. S. (2003), "Statistical Model for Intergranular Corrosion Growth Kinetics," *Corrosion Science*, 45, 353–370.

Phase-contrast X-ray imaging for nondestructive evaluation of materials

B. Zoofan [1], J.-Y. Kim [1], S. I. Rokhlin [1,*] and G. S. Frankel [2]

1) The Ohio State University, Nondestructive Evaluation Program
Edison Joining Technology Center, Columbus, OH 43221

2) The Ohio State University, Fontana Corrosion Center
Department of Materials Science and Engineering, Columbus, OH 43210

Abstract

Quantitative aspects of phase-contrast microfocus X-ray imaging of structural materials (Al alloys and polymers) are considered. The effect of the experimental parameters on the phase contrast in the hard X-ray regime is investigated for application to nondestructive evaluation (NDE) of materials. For this the diffraction field in an object from a small finite X-ray source is simulated and the effects of geometrical and material parameters on the X-ray phase-contrast image are obtained. Experimental phase-contrast images of small defects are obtained with a 5 micron microfocal X-ray source and compared with those from computer simulation as a function of geometrical magnification and photon energy. The phase-contrast X-ray imaging provides enhanced image contrast and improved edge definition and is important for further development toward NDE of structural materials.

---

* Corresponding author *rokhlin.2@osu.edu*

1. INTRODUCTION

Due to their high penetration depth in materials, hard X-rays are widely used to study the internal structure of objects. With increasing photon energy, the ratio between refraction and absorption coefficients of X-rays increases, indicating a substantial phase modulation effect by the object of the X-ray beam transmitted through a material. This phase modulation may significantly enhance X-ray images when properly used. A noninterferometric phase-contrast X-ray imaging technique was explored by Davis et al. 1995[1, 2]. They first introduced a phase-contrast technique using highly coherent monochromatic parallel X-ray beams produced by a synchrotron source equipped with a monochromator, a reflector and a crystal analyzer. The technique was realized in an in-line projection setup. The advantages of the phase-contrast technique over conventional radiographic imaging for low-absorbing objects such as biological tissues were demonstrated. In the same year, Ingal and Beliaevskaya[3] reported a similar phase-contrast technique using a slightly more complicated X-ray optical apparatus. Snigirev et al [4] showed the possibilities of the X-ray phase-contrast imaging technique using radiation from a third-generation synchrotron source. They also demonstrated the technique for simple objects and later applied it to microtomography of thin fibers[5]. The same synchrotron X-ray source was used by Cloetens et al [6].

The phase-contrast technique based on highly coherent parallel X-ray beams is costly and is restricted by the need of access to a high-energy synchrotron source[4-7] and sophisticated X-ray optics [1-3]. A significant advance in the field was made by Wilkins et al[8] who found that a source with high spatial coherence such as an ideal point source can be used instead of monochromatic radiation with high lateral coherence. Moreover, the possibility of using a polychromatic X-ray source was suggested. These significantly simplified the instrumentation method indicating that the conventional fine-focus polychromatic X-ray source is suitable for phase-contrast X-ray imaging. A theoretical formulation of X-ray phase imaging with a monochromatic point source and a phase retrieval method were presented by Gureyev and Wilkins[9]. More recently the phase-

contrast technique has been applied to phase retrieval from X-ray images [9, 10] and for X-ray tomographic phase object reconstruction. An introductory review has been given in Ref [11].

The main objective of this paper is to demonstrate the applicability of the phase contrast method to nondestructive evaluation (NDE) and to optimize the method for imaging of structural materials, such as aluminum alloys. We first describe a model for phase-contrast X-ray imaging using a polychromatic, finite size X-ray source and how we apply it to experimental parameter optimization. Next we discuss phase-contrast microradiographic experiments performed using a polychromatic micro-focal X-ray source on epoxy and aluminum samples with defects and compare experimental and simulated results. The effect of parameters that determine the structure of phase contrast images is examined with relation to the technique is applicability for NDE of materials.

2. THEORY

2.1 X-ray transmission through material

The physical principle of image formation in conventional industrial or medical radiography is based on X-ray absorption in an object. However the thickness or density variation of the object leads not only to X-ray intensity change, but also to change of phase of X-rays passing through the object. The change of phase, in turn, leads to change of direction of the X-ray propagation (refraction).

Let us consider X-rays propagating through an inhomogeneous body D(x,y,z) in the z direction. The absorption and the phase induced modulation of the X-rays transmitted through the body along path L described by the complex transmission function $F(x,y)$ of the wave u

$$u = F(x,y)\exp(ikz); \quad F(x,y) = e^{-k\mu(x,y)+ik\psi(x,y)} \tag{1}$$

where $k = 2\pi/\lambda$ is the wavenumber of the X-ray in vacuum and λ is the wavelength. The phase change of the X-ray passing through the object is expressed as a line integral of the decrement of the X-ray refractive index δ along the X-ray path L

$$\psi(x,y) = -\int_L \delta(x,y,z';k)dz', \tag{2}$$

and the X-ray amplitude as a line integral of the absorption index β

$$\mu(x,y) = \int_L \beta(x,y,z';k)dz' \ . \tag{3}$$

where the complex X-ray refractive index of the object is defined as $n = (1-\delta) + i\beta$ .One should notice that the real part of the refraction index has the opposite sign to that for light. Both the refractive index and the absorption index depend on frequency or photon energy. As an example, Figure 1 shows the complex X-ray refractive index of polystyrene and aluminum, which were calculated based on the available data[12]. Since the decrement of the refractive index δ is extremely small, for example of order 10^{-5} at 10 keV, the refraction angle, that is, the shift of the X-ray beam is also very small, i.e., a few arc seconds in a distance of several meters. As shown in Figure 1, δ and β are of the same order for very low X-ray energies while with the increase of energy the absorption index drops sharply so that the absorption imaging loses contrast. In the higher energy region the refraction index δ is everal orders of magnitudes higher than the absorption coefficient (in most materials $\delta \approx (10^3 \sim 10^5) \times \beta$) and phase contrast imaging may be possible even when the absorption contrast is too small. In medical X-ray imaging, this allows minimizing radiation dose during radiological examination. As shown in Fig. 1, the δ / β ratio for epoxy is higher than that for aluminum; this indicates that for low density materials the phase contrast advantage is even more significant.

2.2 X-ray Fresnel diffraction for a monochromatic point source

In this paper, we consider the diffraction of polychromatic X-rays from a finite focal size source accounting for the X-ray absorption in materials. We start with the theoretical framework of Gureyev and Wilkins[9] by analyzing the diffraction field of a monochromatic point X-ray source as a spatial Green function in the frequency domain;

however we retain higher-order terms in the asymptotic evaluation of the Green function in the image plane. Then, we obtain the diffraction field of polychromatic X-rays radiated from a finite aperture by integrating the Green function in a frequency band and over the source area.

Let us consider an aligned X-ray setup with the coordinate origin at the object center. The X-ray point source is located at $(x_o, y_o, -R_1)$ and the image plane is at $z = R_2$ in which the refracted X-rays form an image of the object as shown in Figure 2 (to allow further integration over the finite size of the source we shift the point source from the axis z). The X-ray field from the point radiation source at a point (x, y) in the plane immediately behind the object can be expressed as a product of the point source radiation field in the absence of the object with the complex transmission function $F(x, y)$ defined in Section 2.1,

$$\bar{u}(x, y; x_o, y_o, -R_1) = \frac{e^{ik\sqrt{R_1^2+(x-x_o)^2+(y-y_o)^2}}}{\sqrt{R_1^2 + (x-x_o)^2 + (y-y_o)^2}} F(x, y). \tag{4}$$

For large source-to-object distance $R_1 >> \lambda$ and $R_1 >> D$ (D is the size of the object field of view), the transmitted X-ray field can be approximated as

$$\bar{u}(x, y; x_o, y_o, -R_1) \approx \frac{e^{ik\left[R_1 + \frac{(x-x_o)^2+(y-y_o)^2}{2R_1}\right]}}{R_1} F(x, y). \tag{5}$$

During the transmission of the X-rays through the object, the X-ray wavefront is disturbed by the object and its direction of propagation is modified. Appling the paraxial (small angle) approximation[13,9], one obtains the standard Fresnel diffraction integral for the

diffraction field of the transmitted X-rays in the point (x', y', R_2) of the image plane as shown in Fig.2

$$u(x', y', R_2; x_o, y_o, -R_1) = -\frac{ik}{2\pi}\frac{e^{ikR}}{R_1 R_2}\iint e^{ik\left[\frac{(x-x_o)^2+(y-y_o)^2}{2R_1}+\frac{(x-x')^2+(y-y')^2}{2R_2}\right]}F(x,y)dxdy, \tag{6}$$

where $R = R_1 + R_2$ and $R_2 \geq D, \lambda$. The asymptotic values of this integral (Eq. (6)) for $R_2 \geq D, \lambda$ are evaluated approximately using the method of stationary phase[13,9]. The stationary points (x_s, y_s) are obtained by solving the following two algebraic equations

$$x_s - \frac{x_o}{N} - \frac{x'}{M} + \frac{R_2}{M}\frac{\partial\psi}{\partial x}(x_s, y_s) = 0, \tag{7}$$

$$y_s - \frac{y_o}{N} - \frac{y'}{M} + \frac{R_2}{M}\frac{\partial\psi}{\partial y}(x_s, y_s) = 0, \tag{8}$$

where $M = R/R_1$, and $N = R/R_2$. Note that M is the projection magnification factor of the object in the image plane. The stationary points are physically those points in the object through which the refracted rays path and produce the most wave contribution in the given point of the image plane (x', y', z'). Only one stationary point exist in this approximation[9] indicating that for a given point in the image there is a single ray path connecting it with the object. The diffraction field is now obtained as

$$u(x', y', R_2; x_o, y_o, -R_1) \approx \frac{1}{R_1}\frac{e^{ik\left[R+\frac{(x_s-x_o)^2+(y_s-y_o)^2}{2R_1}+\frac{(x_s-x')^2+(y_s-y')^2}{2R_2}+\psi(x_s,y_s)\right]-k\mu(x_s,y_s)}}{M\sqrt{\left|1+\frac{R_2}{M}\nabla^2\psi_s+\frac{R_2^2}{M^2}\left(\frac{\partial^2\psi_s}{\partial x^2}\frac{\partial^2\psi_s}{\partial y^2}-\left(\frac{\partial^2\psi_s}{\partial x\partial y}\right)^2\right)\right|}}. \tag{9}$$

The subscript s in Eq. (10) denotes the function at stationary point (x_s, y_s). The reference X-ray field in the absence of the object can be expressed as

$$u_o(x', y', R_2; x_o, y_o, -R_1) = \frac{1}{R} e^{ik\left[R + \frac{(x'-x_o)^2 + (y'-y_o)^2}{2R} + \psi_o\right] - k\mu_o}, \tag{10}$$

where ψ_o and μ_o are the phase shift and the attenuation in the medium containing the object. If the medium is air, the phase shift and attenuation can be neglected. After a tedious algebraic manipulation for the phase factor in Eq. (9), the following relation is obtained

$$\begin{aligned} &\frac{(x_s - x_o)^2 + (y_s - y_o)^2}{2R_1} + \frac{(x_s - x')^2 + (y_s - y')^2}{2R_2} \\ &= \frac{(x' - x_o)^2 + (y' - y_o)^2}{2R} + \frac{R_2}{2M}\left[\left(\frac{\partial \psi_s}{\partial x}\right)^2 + \left(\frac{\partial \psi_s}{\partial y}\right)^2\right]. \end{aligned} \tag{11}$$

Using Eq. (11) and the reference X-ray radiation field Eq. (10), the normalized diffraction field of the transmitted X-rays is finally obtained as

$$\frac{u(x', y', R_2; x_o, y_o, -R_1)}{u_o(x', y', R_2; x_o, y_o, -R_1)} = \frac{e^{ik\left\{\frac{R_2}{2M}\left[\left(\frac{\partial \psi_s}{\partial x}\right)^2 + \left(\frac{\partial \psi_s}{\partial y}\right)^2\right] + \psi(x_s, y_s) - \psi_o\right\} - k[\mu(x_s, y_s) - \mu_o]}}{\sqrt{\left|1 + \frac{R_2}{M}\nabla^2 \psi_s + \frac{R_2^2}{M^2}\left(\frac{\partial^2 \psi_s}{\partial x^2}\frac{\partial^2 \psi_s}{\partial y^2} - \left(\frac{\partial^2 \psi_s}{\partial x \partial y}\right)^2\right)\right|}}. \tag{12}$$

The normalized intensity is thus

$$\frac{I(x', y', R_2; x_o, y_o, -R_1)}{I_o(x', y', R_2; x_o, y_o, -R_1)} = \frac{e^{-2k[\mu(x_s, y_s) - \mu_o]}}{1 + \frac{R_2}{M}\nabla^2 \psi_s + \frac{R_2^2}{M^2}\left(\frac{\partial^2 \psi_s}{\partial x^2}\frac{\partial^2 \psi_s}{\partial y^2} - \left(\frac{\partial^2 \psi_s}{\partial x \partial y}\right)^2\right)}. \tag{13}$$

The obtained diffraction field Eq. (13) and Eq. (14) accounts for effects of both refraction and absorption in the object. In the denominator the multiplications of derivatives are retained in the equations since these are not ignorable when density changes abruptly in the object, as for example when a discontinuity exists. When the absorption in the object can be neglected (a pure phase object) and the density changes gradually in the object (thus, the diffraction angle is small and there is no focusing between the object and the imaging planes;[9] $\nabla^2\psi << 1, \partial^2\psi / \partial x^2 << 1, \partial^2\psi / \partial y^2 << 1, \partial^2\psi / \partial x \partial y << 1$), the above equation simplifies to

$$\frac{I(x', y', R_2; x_o, y_o, -R_1)}{I_o(x', y', R_2; x_o, y_o, -R_1)} = 1 - \frac{R_2}{M}\nabla^2\psi_s, \tag{14}$$

which has been derived by Wilkins et al.[8] and Gureyev and Wilkins.[9] Eq. (14) shows that the phase contrast image of a phase object is essentially a map of the Laplacian of the phase distribution in the object plane. When the refraction in the object can be ignored (an absorption object or by locating the image plane immediately after the object plane), the intensity is

$$\frac{I(x', y', R_2; x_o, y_o, -R_1)}{I_o(x', y', R_2; x_o, y_o, -R_1)} = e^{-2k[\mu(x_s, y_s) - \mu_o]} \tag{15}$$

resulting in the conventional absorption mechanism of radiographic image formation.

As an example of numerical simulation let us consider the X-ray phase contrast imaging of a spherical void (pore) in an epoxy layer. In the following section, we will describe an experiment for the same object. Calculations using the two approximate formulas Eq. (13) and Eq. (14) shown that the difference occurs inside the Fresnel

diffraction fringe. Since the second order derivatives of the phase are not small near the edges of the object, the deviation occurs in the edge region.

2.3 Model for finite focal size and polychromatic energy band

To optimize experimental conditions and to compare quantitatively the modeling results with the experiment one need to account in the model for the finite source size and the source polychromaticity. We also apply the phase-contrast imaging technique to materials with relatively high density and thus both the effect of absorption as well as the effect of refraction is considered. When the X-ray source has a finite size, the diffraction field is obtained as an integral of the point source field over the source region S,

$$u = \frac{1}{R_1 M} \iint_S \frac{e^{ik\left\{R + \frac{(x'-x_o)^2+(y'-y_o)^2}{2R} + \frac{R_2}{2M}\left[\left(\frac{\partial \psi_s}{\partial x}\right)^2 + \left(\frac{\partial \psi_s}{\partial y}\right)^2\right] + \psi(x_s, y_s)\right\} - k\mu(x_s, y_s)}}{\sqrt{\left|1 + \frac{R_2}{M}\nabla^2\psi_s + \frac{R_2^2}{M^2}\left(\frac{\partial^2\psi_s}{\partial x^2}\frac{\partial^2\psi_s}{\partial y^2} - \left(\frac{\partial^2\psi_s}{\partial x \partial y}\right)^2\right)\right|}} ds(x_o, y_o). \quad (16)$$

A frequency dependent function $H(f)$ that relates the diffraction X-ray field $U(f)$ to a monochromatic incident field $U_o(f)$ in the frequency domain is introduced through

$$U(f) = H(f)U_o(f). \quad (17)$$

where $U_o(f)$ contains the information on the X-ray source frequency spectrum. Next, the intensity of a diffracted X-ray normalized by the reference X-ray intensity is

$$\frac{I}{I_o} = \frac{\int_{f_1}^{f_2} |H(f)|^2 G_{u_o u_o}(f) df}{\int_{f_1}^{f_2} G_{u_o u_o}(f) df}. \tag{18}$$

where $G_{uu}(f)$ is the power spectral density. The X-ray image is calculated using Eqs. (16) and (18) for a known frequency spectrum and size of the X-ray source.

Figure 3 compares the intensity profiles for a spherical pore in epoxy resine across the Fresnel diffraction fringe for different sources: monochromatic point, monochromatic finite, polychromatic point and polychromatic finite sources. The focal spot size of the finite source is 5 μm. In the simulations shown in Figure 3, the photon energy for a monochromatic source is 20 keV and the applied tube voltage is 30 kV. The polychromatic X-ray source spectra at different applied tube voltages were selected based on the approximation of the experimental spectra[14]. The photon energy (in keV) for a polychromatic source at the peak of its intensity was determined as 2/3 of the applied value in kV. Both the Fresnel diffraction fringe width and intensity variation across it, change with the frequency of the incident X-ray. While both the polychromaticity and the finite size of the X-ray source affect the fringe width and contrast, the effect of the polychromaticity is much stronger than that of the finite source size.

3. EXPERIMENT

The schematic of the microfocal experimental system for the in-line projection phase-contrast X-ray imaging is shown in Figure 4. The X-ray source, an object and the X-

ray detector (film or image intensifier) were aligned linearly along the optical axis. A Feinfocus® 225 kV X-ray unit with 5 μm focal size was the X-ray source. A precise positioning system with three linear (with 2 μm resolution) and one rotating (with 0.01° resolution) computer controlled axis is used to control the position of the sample. One high-resolution linear axis is used for translating the position of the image plane (receiver). An additional X-Y manipulator is used for positioning of the X-ray source. The micron resolution movement of the sample provides accurate projection magnification of the image. High resolution film or image intensifier integrated with a CCD camera is used for real-time microradiography and also for alignment of the sample prior to film microradiography. The exposure parameters are carefully selected such that during exposure the focal spot size remains in the micro-focus region of the tube to get the optimum resolution. For film microradiography the film is placed in the front face of the image intensifier, which in this case serves as a mechanical support. Exposed and processed films are digitized by illuminating them in front of a TV camera. A PCVision® Frame Grabber (from Imaging Technology) was used for digitization of the films and transferring the image to a PC. The digital profiles of the images were saved in the computer and further processed to obtain the X-ray intensities. Two different types of high resolution films were used; Agfa Structurix D7 films as a high-speed film and D2 film with fine grains and very high contrast.

The samples used in the experiment were a 1.5 mm thick transparent epoxy layer on a thin Plexiglas plate and a 1 mm thick Al 2024-T3 sample. The epoxy layer on the Plexiglas plate contains spherical voids with diameters up to 1.2 mm. The Al 2024 sample

contains an artificial pit. The diameter of the pit was 340 μm and the depth 770 μm. Microradiography was performed to obtain images in absorption-contrast and phase-contrast modes by changing the distance between the object and the film. Also, the effects of the X-ray energy and the object to detector distance were examined.

4. RESULTS AND DISCUSSION

X-ray images of the voids in epoxy and pit in the Al 2024 samples obtained in absorption-contrast and phase-contrast modes are compared in Figure 5. The absorption-contrast image was taken with a very short object-to-film distance (OFD) 182 mm for epoxy and 290 mm for Al-2024 while the phase-contrast image was taken for a larger OFD 1000 mm for epoxy and 1430 mm for Al-2024 (Figure 5). The projection magnification ($M= (R_1+R_2)/R_1$) is the same 2.5X for epoxy and 10X for Al-2024. The X-ray exposure was selected such that both images on the film have the same optical density; a longer (11 min. for epoxy and 9 min. for Al-2024) exposure of film was required for the phase-contrast image due to the large distance.

Remarkable enhancement of the contrast in the phase-contrast image (Figs. 5(b) and 5(d)) should be noted, especially as the boundaries of the spherical voids and a pit are clearly defined. The existence of a bright ring around the cavity (white ring around dark area in the image) indicates that X-rays refract from the material surrounding the cavity toward the cavity center which is accompanied by bright fringe formation and the image darkness increases in the object region. (Note that a lens shape which diverges visible light

converges X-rays.) The width of the bright fringe on the film at geometrical X-ray magnification M=2.5 is ~10 μm.

The common feature (the bright fringe) in the structure of the phase contrast images can be interpreted more quantitatively on the basis of the theory discussed. When there is density variation in the material, X-rays refract from the higher density side to the lower density region. Consequently, the X-ray beam shifts toward the low density region and only a small amount of X-rays arrives in the fringe region, which makes the film underexposed with the formation of bright fringes. In the area surrounded by the fringe, the intensity distribution depends on the Laplacian of the phase ($\nabla^2\psi$ in Eq. (15)) and the spatial absorption variation.

Figure 6 shows normalized intensity profiles across the diffraction fringes in the phase-contrast image of a void in epoxy, obtained by the experiments and simulations. The profile lengths are shown in the image by a horizontal line. The intensity in the area outside the void is taken as the reference. For this particular image the tube voltage was 60 kV and magnification was 2.5X. The simulated and experimental profiles are in good agreement.

To investigate the effect of photon energy (tube voltage) on the phase-contrast image we performed the experiment at tube voltages ranging from 20 to 180 kV. In this series of measurements, two different projection magnifications of 2.5x and 20x for epoxy and a single magnification of 20x for Al-2024 were used. Two types of film were used in the experiment. The widths of the main diffraction fringe around the objects were measured directly on film under an optical microscope in order to avoid any quantization

error during digitization. The measured widths are normalized by the applied X-ray projection magnification M. The results are compared with the simulations in Figure 7 for both epoxy and Al-2024 samples. The width of the main fringe decreases with energy increase. To determine the dependence of image contrast on applied tube voltage, the films were digitized with large optical magnification. The variation of gray level across the main fringe in the image, which is produced by the phase contrast was measured and converted to variation of the normalized X-ray intensity. For this the brightness of the film illuminator was calibrated and the relation between the brightness of the digitized images and the X-ray intensity has been established based on the film exposure characteristic curves. It was found that the normalized fringe intensity also drops gradually with tube voltage.

The effect of the OFD on the image contrast is investigated. According to Fresnel diffraction theory, the image contrast should be better with the distance to detector in the Fresnel zone. In order to see this OFD effect on the phase-contrast images, the object-to-film distance is changed while the projection magnification is kept constant at M=2.5X at all times. Figure 8 shows the simulated and experimental normalized intensities in the fringe for different object-to-film distances (tube voltage is 32 kV). Improvement in the image contrast is observed with increase of OFD. In each case the exposure is corrected such that the same optical density is achieved for each radiograph. Although larger OFD seems to improve the phase contrast significantly, very large OFD is not practical due to the necessity to increase the exposure by the inverse-square law. Due to the low current in the micro-focus tubes this leads to a very long exposure time.

Figure 9 shows the effect of projection magnification on the phase contrast in term of the normalized X-ray intensity variation ($\Delta I/I_o$) across the fringe for the pit in the Al-2024 sample. For this case, the kV was 180 kV and the source to film distance was 1630 mm. Due to the increasing effect of geometric unsharpness with magnification the intensity variation decreases. Very good agreement between experiment and theory is obtained.

4. SUMMARY

The paper presents theoretical and experimental aspects of phase-contrast X-ray imaging using a micro-focus X-ray source. Polychromatic finite source radiation is simulated to select experimental conditions used in microfocal X-ray imaging. Simulations and experiments are illustrated by examples of a corrosion pit in an Al-2024 sample and voids in an epoxy resin. Good agreement is found between the experimental and modeling results. In most prior work, the technique has been used to image light materials such as biological tissue. In this work, the phase-contrast technique is demonstrated for aluminum samples showing significant contrast improvement and image edge enhancement for both materials. The results show promise in application of the phase contrast method to nondestructive evaluation of materials.

ACKONWLEDGEMENT

The work was supported by the United States Air Force Office of Scientific Research through Grant No. F49620-02-1-0148. The contract monitor is Lt. Col. Paul Trulove.

REFERENCES

1. T. J. Davis, D. Gao, T. E. Gureyev, A. W. Stevenson and S. W. Wilkins, "Phase-contrast imaging of weakly absorbing materials using hard X-rays," Nature, **373**, 595-598,1995.
2. T. J. Davis, T. E. Gureyev, D. Gao, A. W. Stevenson and S. W. Wilkins, "X-ray image contrast from a simple phase object," Phys. Rev. Lett, **74**, 3173-3176,1995.
3. V. N. Ingal and E. A. Beliaevskaya, "X-ray plane-wave tomography observation of the phase contrast from a noncrystalline object," J. Phys. D: Appl. Phys., **28**, 2314-2317, 1995.
4. A. Snigirev, I. Snigireva, V. Kohn, S. Kuznetsov and I. Schelokov, "On the possibilities of X-ray phase contrast microimaging by coherent high-energy synchrotron radiation," Rev. Sci. Instrum., **66**, 5486-5492, 1995.
5. C. Raven, A. Snigirev, I. Snigireva, P. Spanne, A. Souvorov and V. Kohn, "Phase-contrast microtomography with coherent hi-energy snychrotron x rays," Appl. Phys. Lett., **69**, 1826-1828, 1996.
6. P. Cloetens, R. Barrett, J. Baruchel, J.-P. Guigay and M. Schlenker, "Phase-objects in synchrotron radiation hard x-ray imaging," J. Phys. D: Appl. Phys., **29**, 133-146, 1996.

7. K. A. Nugent, T. E. Gureyev, D. F. Cookson, D. Paganin and Z. Barnea, "Quantitative phase imaging using hard X rays," Phys. Rev. Lett., **77**, 2961-2964, 1996.

8. S. W. Wilkins, T. E. Gureyev, D. Gao, A. Pogany and A. W. Stevenson, "Phase-contrast imaging using polychromatic hard X-rays," Nature, **384**, 335-338, 1996.

9. T. E. Gureyev and S. W. Wilkins, "On x-ray phase imaging with a point source," J. Opt. Soc. Am. A., **15**, 579-585, 1998.

10. T. E. Gureyev and S. W. Wilkins, "On x-ray phase retrieval from polychromatic images," Opt. Comm. **147**, 229-232, 1998.

11. R. Fitzgerald, "Phase-sensitive X-ray imaging," Phys. Today, 53, 2000.

12. http://www-cxro.lbl.gov/optical_constants/

13. M. Born and E. Wolf, *Principles of optics*, pp.883-892, Cambridge University Press, New York, 1999.

14. B.E. Stern and D. Lewis X-ray, Pitman Publ. New York, N.Y. 1970.

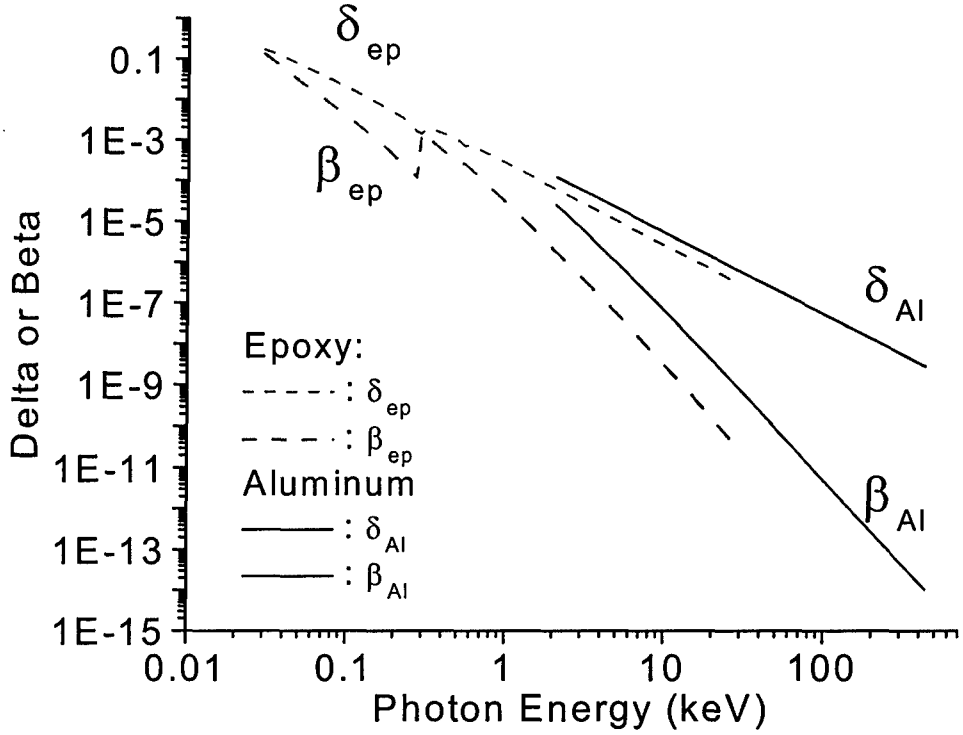

Figure 1 X-ray refractive indices of epoxy and aluminum.

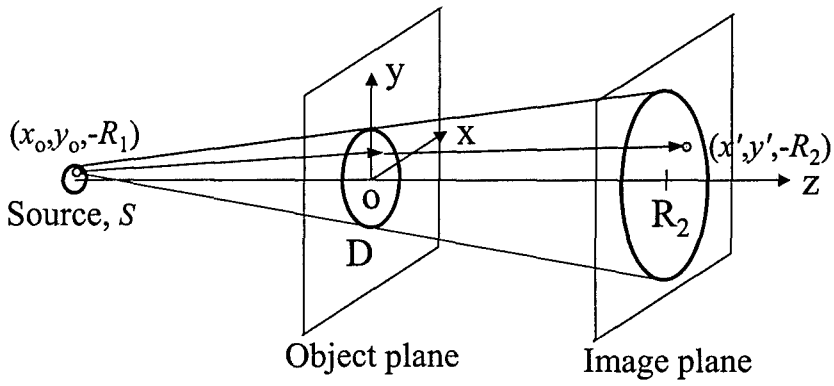

Figure 2 Schematic of in-line phase-contrast imaging

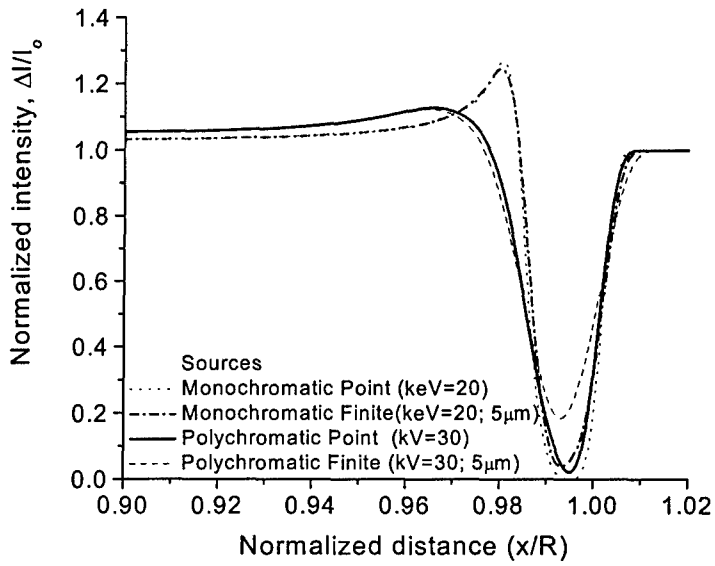

Figure 3 X-ray intensity of the spherical void in an epoxy layer for different types of X-ray source.

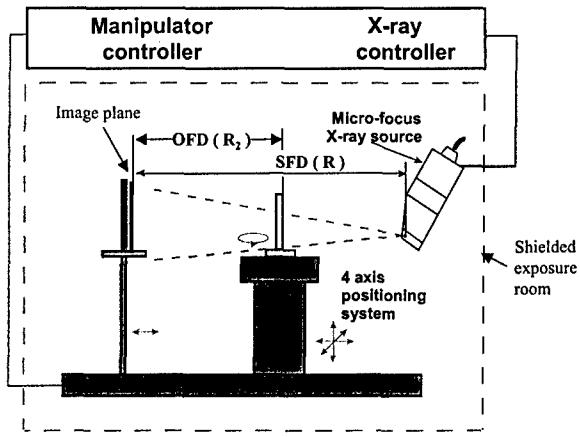

Figure 4 Schematic of the experimental setup for in-line phase-contrast X-ray imaging

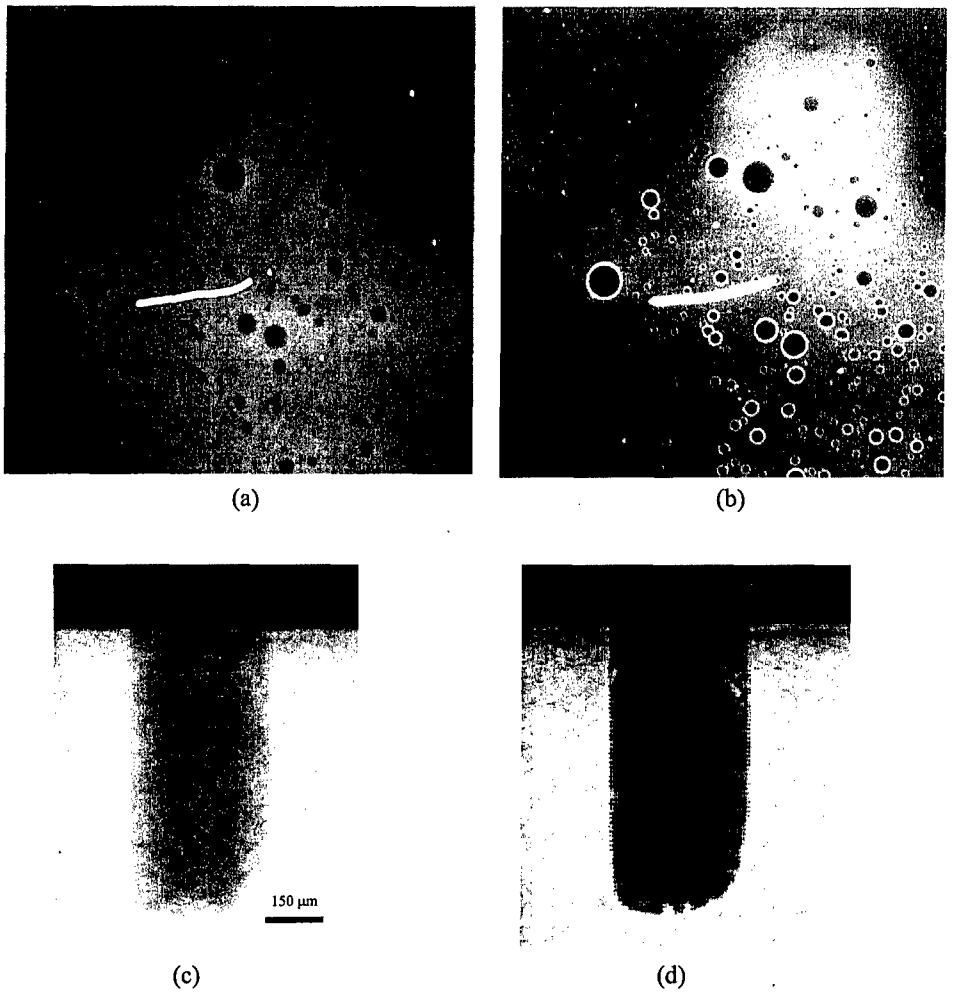

Figure 5. Comparisons of absorption-contrast and phase-contrast images on same type of radiographic film: (a) Absorption -contrast image produced with a short OFD (190 mm) for epoxy; (b) Phase-contrast image with long OFD (500 mm)for epoxy; tube voltage=32 kV, and X-ray projection magnification=2.5 X, (c) Absorption -contrast image of a pit in Al-2024 alloy produced with a short OFD (190 mm); (b) Phase-contrast image with long OFD (500 mm) for Al2024; tube voltage=90 kV, X-ray projection magnification=10X.

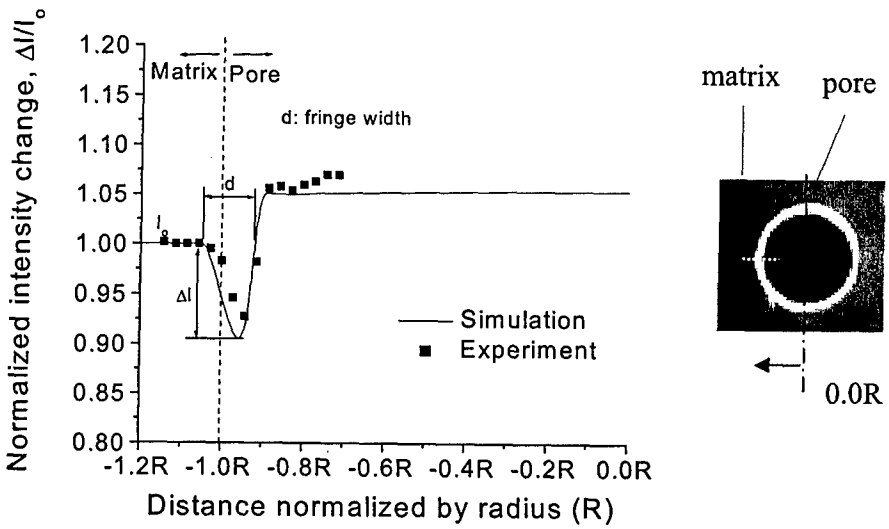

Figure 6. Normalized X-ray intensity profile across the refraction fringe of a void in epoxy

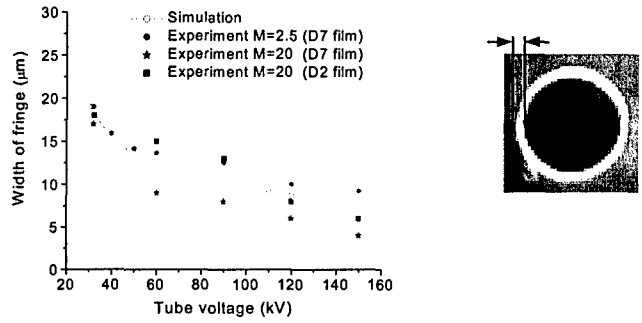

(a)

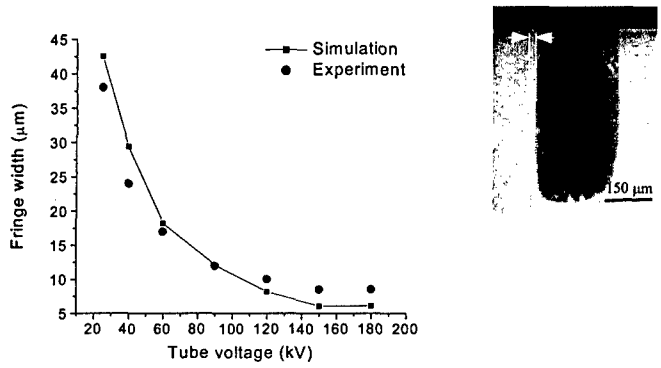

(b)

Figure 7. Dependence of the fringe width on the tube voltage. The fringe width is measured on the phase contrast images. (a) Void in epoxy; for projection magnification 20X, SFD=760 mm, OFD=720 mm and for projection magnification 2.5X, SFD=1630 mm, OFD=980 mm. (b) Pit in Al-2024; projection magnification is 20X; SFD=1630 mm, and OFD=980 mm.

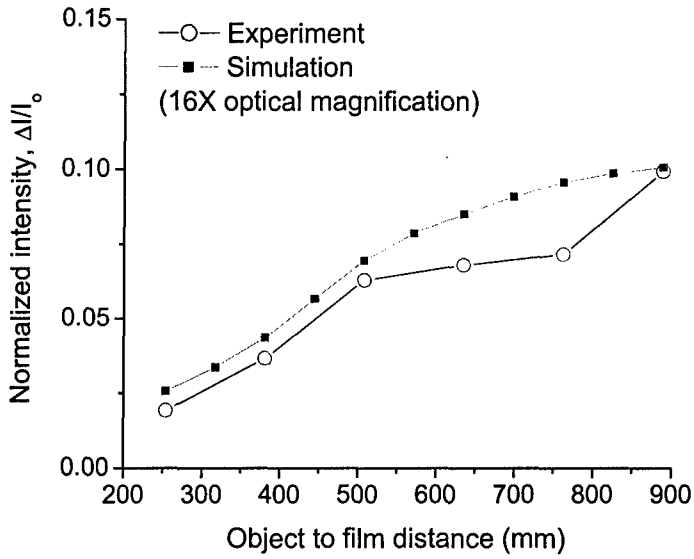

Figure 8. Effect of object- to- film distance on the normalized intensity ($\Delta I/I_o$) of phase contrast images. Tube voltage is 32 kV and projection magnification is kept constant at M=2.5X.

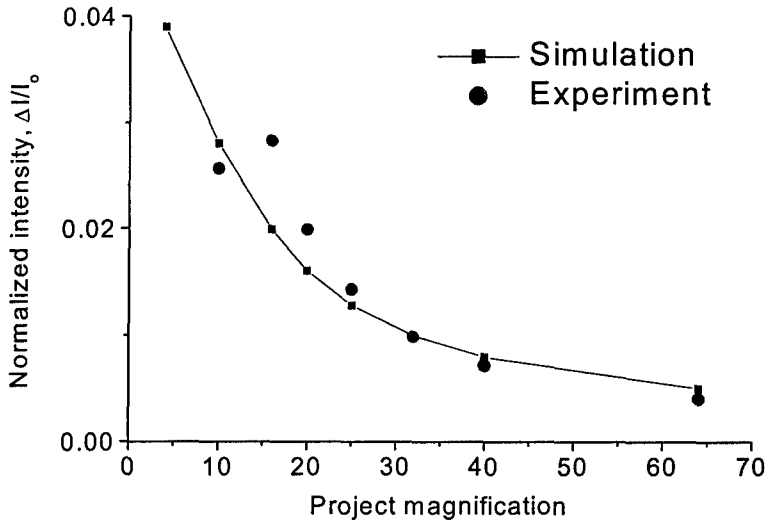

Figure 9. Effect of projection magnification on the phase contrast ($\Delta I/I_o$) of the image. Tube voltage is 180 kV and SFD is kept constant to be 1.63 m.

In Situ X- ray Radiographic Study of Stress Corrosion Cracking in AA2024-T3

Xiaodong Liu*, G. S. Frankel*, B. Zoofan** and S. I. Rokhlin**
*Fontana Corrosion Center, Department of Materials Science and Engineering
**Department of Industrial, Welding and Systems Engineering
The Ohio State University, Columbus, OH 43210, USA

ABSTRACT

Despite the many studies that have addressed stress corrosion cracking (SCC) in high strength aluminum alloys, the separate contributions of stress and electrochemistry to the SCC process is still a matter of dispute. Moreover, the conventional fracture mechanics approaches constrain SCC to a single crack per specimen, which eliminates interaction between nearby cracks. In this study, a new non-destructive evaluation approach was developed to investigate stress corrosion cracking in AA2024-T3 (UNS A92024). A microfocal x-ray radiography technique was employed to image multiple intergranular SCC cracks in situ. A modified ASTM G49 stressing jig was used to apply a fixed tensile displacement to a thin sheet sample, and a novel electrochemical cell containing flowing 1 M NaCl was attached to the edge of the sample. Potentiostatic polarization was applied at a potential that promoted intergranular corrosion. The initiation and growth of multiple intergranular stress corrosion cracks were characterized using transmission microfocal x-ray radiography. The kinetics of intergranular stress corrosion cracking growth was found to be in good agreement with the results of a completely different technique, the foil penetration method, which reflects the validity of the new approach. Interestingly, in many experiments the deepest crack at the beginning of the experiment was found to slow and stop growing, and was then surpassed by another crack that eventually penetrated through the sample. The competition between multiple intergranular stress corrosion cracks is not explained by the theory of mechanical fracture in inert environments. The possible mechanisms underlying this competition between cracks are discussed.

Keywords: Al alloys, intergranular corrosion, stress corrosion cracking, intermetallic particles, x-ray radiography.

Corresponding author: G.S. Frankel, frankel.10@osu.edu

INTRODUCTION

Stress corrosion cracking (SCC), which involves the combined effects of stress and an aggressive environment on a susceptible microstructure, has been investigated extensively for decades. SCC of high strength Al alloys is almost always intergranular in nature, resulting in intergranular stress corrosion cracking (IGSCC).[1-3] In contrast, intergranular corrosion (IGC) is attack at grain boundaries that takes place in the absence of applied stress as a result of a variation in the microstructure at or near grain boundaries. In contrast to SCC, stress is not typically considered to be an important factor in the IGC process. One goal of this work is to understand the effect of stress on IGC and the relationship between IGC and IGSCC. In trying to clarify the dominant effects of electrochemistry and stress on IGC and SCC, it would be useful to

be able to image the various forms of corrosion in situ. However, few in situ non-destructive evaluation (NDE) approaches exist to study IGC and SCC.

Recently, Zhao et al. described the use of in situ x-ray radiography to study IGC and exfoliation corrosion in AA2024 and AA7178.[4] Exfoliation corrosion is a form of IGC that occurs on surface of wrought Al alloys.[5, 6] The radiographic images presented by Zhao et al. provided information on the initiation and growth kinetics of a full population of IGC sites. Standard fracture mechanics approaches for the study of SCC kinetics, such as the double cantilever beam (DCB) specimen, are constrained to have only a single crack. This technique simplifies the study of SCC, but real structures can have multiple cracks so the ability to image and study samples containing multiple cracks is of great interest. The interaction of stress and electrochemical reactions can alter the local environment at an IGC tip, which might assist or slow down growth rate, or favor the SCC initiation at other sites. There is a close connection between IGC and IGSCC; IGSCC can be considered to be stress-assisted IGC, particularly if the mechanism of IGSCC is anodic dissolution rather than hydrogen embrittlement.

We have recently reported the use of X-ray radiography to characterize the IGC and IGSCC in AA2024-T3 foil samples stressed to a constant displacement in tension using a modified ASTM G49 jig and exposed on one side to a corrosive environment.[7, 8] The nature of the intergranular cracks depended on the orientation of the sample as a result of the constraints imposed by the microstructure. This work was performed on samples after exposure; it was not done in situ.

While much is known about SCC of Al alloys, there are still unresolved issues regarding the connection between IGC and IGSCC that are not fully understood. For instance, if the microstructure is elongated in a direction that is not perpendicular to the applied stress, how does IGC turn into a crack? It is generally assumed that a resolved tensile stress normal to a crack tip is required for SCC propagation. How does tensile stress parallel to the crack tip or compressive stress normal to the crack affect IGC advance? The primary mechanism for SCC in 2xxx series Al alloys is commonly regarded to be anodic dissolution,[9] but this is disputed[10-12] because the local hydrogen evolution always accompanies the anodic dissolution in Al cracks, so effects of hydrogen embrittlement cannot be easily ruled out.

In the current study, a novel electrochemical cell associated with a modified ASTM G49 stressing jig was used along with x-ray microfocal radiography to study SCC in situ. The approach was compared to the foil penetration technique, which determines the kinetics of localized corrosion growth by measuring the penetration time at the fastest growing site.[7, 13, 14]

EXPERIMENTAL

Specimens were machined from a 19 mm thick wrought AA2024-T3 plate (nominal composition Cu 4.5%, Mg 1.45%, Mn 0.57%, Si 0.11%, Fe 0.25%, Zn 0.09%, Ti 0.02%, Cr 0.01%, and other elements totaling 0.05% max). Thin sheet samples were cut in specific orientations relative to the rolling direction. The nomenclature used to describe the different orientations is shown in Figure 1a. The three perpendicular directions are considered to be longitudinal (L, along the rolling direction), short-transverse (S, through-thickness), and transverse (T). The orientation of a stressed sample is noted by two perpendicular orientations, the first indicating the nominal direction of corrosion propagation and the second indicating the direction of applied stress. For instance, thin slices removed from the plate along the T or L direction were rotated and used as the T-S or L-S samples (Figure 1b), which were stressed in the

S direction and corrosion proceeded in the T (transverse direction) or L (longitudinal direction), respectively. Stress was applied using a modified ASTM G49 fixed-displacement jig described previously.[7] The notation is the same as used previously, but the exposed face in the current experiments was the thin edge of the sliced samples rather than the broad face. To stress in the S or through-thickness direction given the limited plate thickness, laser-welded tabs were used to allow gripping by the stressing jig, which is the same approach that was used in the stressed foil penetration experiments.[7] Figure 1c shows the configuration of the welded T-S and L-S samples. The samples were typically stressed at an initial strain of 0.18%, which is in the elastic region, less than halfway to yield according to the stress strain curve measured in a standard tension testing machine on an AA2024-T3 blank.

Pieces 80 mm long and 5 mm wide were cut from the plate using electrical discharge machining (EDM), and reduced to a thickness of 1.05 mm by grinding. The surfaces were polished to 1200 grit in methanol or ethanol to minimize corrosion. The stress was applied along the sample length direction, and a specially-designed electrochemical cell was positioned on the thin edge of the sample exposing only that edge to solution, Figure 1d. The nominal direction of corrosion was perpendicular to that edge, through the width of the sample. Microradiography was used to image the corrosion cracks as a function of time. The images were recorded on the x-ray negative films.

The electrochemical cell used to expose the thin edge of the sample to solution and control the potential is shown in Figure 2. The cell was machined from a rectangular piece of Teflon with nominal dimensions of 15 x 15 x 23 mm. A 9.5 mm diameter hole was drilled through the body and then capped to create the inner cell cavity. A 1.05 x 18.5 mm slot was machined in one side of the cell. Two lips that were 0.5 x 1.5 x 23 mm in dimension extended from the edges of the slot as guides for the sample. The thin edge of the sample was slipped between the lips and exposed to the inside of the cell through the slot. Four holes were drilled and threaded into the side walls of the cell to allow connection of 1/8" I.D. nylon nozzles for attachment of tubing. The tubing was used to accommodate pumping of electrolyte and to provide access for a saturated calomel reference electrode (SCE) and a counter electrode. A strip sample was inserted in the stressing jig cell, the desired displacement was applied, and then the cell was mounted on the edge of the sample. Finally, the cell was sealed along the lips with Miccrostop© lacquer. The exposed area was about 0.2 cm^2 (1.05 x 18.5 mm). The length of the slot allowed for testing of the sample section far from the weld and heat affected zone for samples with welded tabs. Because of the small volume of the cell chamber, the 1.0 M NaCl solution was circulated continuously by a mini pump from a reservoir through the cell and past the sample. The solution in the reservoir was refreshed every 24 h. The sample was potentiostatically polarized at –580 mV SCE to promote IGC of the AA2024-T3 and the current was recorded during the experiment.

Microfocal radiographic imaging was performed using a 225-kV, 3-mA x-ray source with 3-5 μm focal size and a positioning system with 2 μm linear resolution and 0.01° rotational resolution.[15, 16] The projection magnification was obtained by the ratio of the distance between the x-ray source and the film (d_i) to the distance between the source and the sample (d_0), i.e. d_i/d_0. X-ray images were recorded periodically during the experiment. To obtain optimum resolution for a 1 mm thick Al alloy sample at 10x magnification (d_i/d_0 = 76.2cm/7.62cm), the source voltage and current were 40 kV and 200 μA, respectively, and the exposure time was 275 s. The processed films were digitized using a charge-coupled device (CCD) camera. X-ray microfocal radiography generates a gray-scale image in which the intensity depends on the integrated X-ray

absorption through the sample thickness.[15] The absorption of X-rays varies as a result of density variations in the material. A higher density region, such as an intermetallic particle, generates a white spot on the negative X-ray film, whereas the lower density region associated with corrosion generates a dark region.

RESULTS

Figure 3 shows radiographic images of an L-S sample, i.e. it was stressed in the S direction and cracks grew in the L direction. The top edge of each image was the exposed L surface of the sample. Figure 3a is an image of the sample prior to testing. The vertical white streaks are associated with intermetallic particles aligned in the L direction in the wrought microstructure. Figures 3b-3i are images of the sample during exposure to 1.0 M NaCl at -580 mV SCE with 0.18% strain applied in the S or horizontal direction. The cracked grain boundaries (GBs) can easily be distinguished in these images. Two horizontal white lines are also visible. The line at the exposed face is associated with a thick part of the Teflon cell and the line 1.5 mm below the surface is from the lacquer used to seal the end of the cell lips. The white irregular patterns between the two white lines result from an excess of red lacquer along the sealing area. These patterns were used as references to identify the location of specific IGC sites. The intergranular cracks show up as thick, dark vertical lines. Figures 3b-3i show that the cracks were straight and sharp and propagated along the L direction for this sample. The radiographic images are an integration of the microstructure in the direction of x-ray propagation, the T direction, including the matrix, intermetallic particles and IGC, through the sample, rather than a reflection of continuous microstructural components in the sample. The average grain size of this particular AA2024-T3 plate at the ¼ T section was reported previously as approximately 50 μm in the S direction, 300 μm in the T direction and 2000 μm in the L direction.[17] The thickness of the sample used in this study is 1.05 mm along the T direction, which indicates that the sample had 3-4 grains through the thickness.

The feature labeled site 1 in Figure 3b formed first, and the crack at site 2 was found later. During the first hour of the experiment, the crack at site 1 was the longest and the fastest growing crack. However, this initial crack stopped growing, while IGC at site 2 initiated, grew faster, and ultimately overtook the first crack to become the deepest crack in the sample, as is evident in the series of images in Figure 3c-e. Figure 3d shows the crack at site 2 had a similar depth as that at site 1 after 60 min. Comparison with Figure 3c shows the crack at site 2 actively progressed, whereas the IGC at site 1 was stagnant. Figure 3e shows the longer crack length at site 2 after 90 min. This phenomenon was not an exception; almost every sample studied, in a variety of propagation and stressing orientations, exhibited a deceleration in growth of the initial crack and ultimate failure at another site. This observation is counter to the expectations of mechanical fracture in inert environments, in which the driving force of crack growth is stress intensity. Figure 3f shows that IGSCC at site 2 penetrated through the 5 mm sample in only 2 hours. Figure 3g and 3h show the magnified images of the two major IG cracks after 2.5 hours. Some short cracks are visible between the two major IGSCCs. IGC is seen to have spread to grains neighboring the main crack at site 2, in a fashion that seems to blunt the crack. Figure 3i shows a low magnification image after 3 h. The crack at site 1 closed slightly as a result of stress relief within the fixed displacement jig.

Experiments were also performed on T-S samples, which were oriented such that they were stressed in the S direction but with the IG cracks propagating in the T direction. Figure 4

shows a series of radiographic images for a T-S sample. These images exhibit different morphologies than those from the L-S sample in Figures 3. The white regions associated with intermetallic particles are seen clearly, Figure 4a. The thickness of the T-S sample in the L direction was about 1.05 mm, which is less than one grain dimension in that direction. However, the sample size in the T direction, the nominal growth direction, was larger than 10 grain dimensions. Figure 4b shows that a crack initiated at site 1 during the first 15 minutes and became the fastest growing crack. The crack passed about 3 grains and then stopped growing at a length of about 1 mm. The crack at site 1 is not as sharp as the IG cracks in the L-S sample shown in Figure 3. It shows that the IGCs branch to several neighboring grains in the S direction.

The first crack to form at site 1 stopped propagating like the initial cracks in the L-S sample. As shown in Figure 4b, cracks initiated at sites 2 and 3 after the crack at site 1 was well developed. After about 6 h, Figure 4c, the crack at site 3 was about as long as the crack at site 1 and the crack at site 2 had surpassed both of them to become the deepest crack. This crack at site 2 grew rapidly, but then also slowed. As shown in Figure 4c-e, it did not grow much during the 24 h period between the 6 and 30 h images. On the other hand, many short IGC cracks at other sites initiated and grew during this time. Two regions of severe attack occurred on the sample in the S direction at the ends of the exposed area in the cell, one of which was at site 2, where the failure crack was growing. This attack at the ends of the exposed area might have resulted from poor mass transport at stagnant regions in the flow cell or as a result of a stress concentration in this region. The anodic dissolution resulted in connection of the grain boundaries, grain fall out and a large area of mass loss, as shown at the right end of the T-S sample in Figure 4e. Careful examination of Figure 4e shows that at crack bottom at site 2, the sample was slightly bent perhaps as a result of this loss and wedging stresses created by corrosion products.

Figure 5 shows optical photographs of the T-S sample after the experiment with the electrochemical cell removed, but with the sample still held within the stressing jig. The lacquer sealed the cell lips and sample, and separation of the cell from the sample caused the corroded grains to be removed. The sample wastage is likely a result of non-Faradaic grain removal, and Figure 5 shows the remaining grains. Figure 5b is a magnified view of the region near site 2, the failure crack. As mentioned previously, although the sample was constrained in the stressing jig, the sample was bent beneath the crack as a result of the wedging by the IG corrosion product, indicating that the significant wedging stress overwhelmed the uniaxial stress.

To analyze the fracture morphology, the sample was overloaded in the stressing frame. The deepest crack, shown in Figure 5b, propagated to the other side, breaking the sample into two pieces. Figure 6 is an SEM image of the fractured T-S sample. The IG crack face shown is an S-oriented plane, and the crack propagated in the T direction from right to left. Regions with different surface morphology are evident. Figure 7 shows magnified secondary electron images taken at the regions indicated with arrows and the letters *a-d* in Figure 6. Figure 7a shows a region with extensive roughening by corrosion that occurred because this region was exposed to the environment through much of the test period. Figure 7b shows second region of intergranular cracking facture with clear grains facets and grain boundaries. The shorted exposure time for the region of the crack surface resulted in cleaner grain boundary faces. The fracture surface exhibited a large number of rod-shaped particles, which are analyzed below. Figure 7d shows the morphology of the region exhibiting mechanical fracture by overload as evidenced by dimples and ductile rupture. Figure 9c shows the morphology at the very end of the IGSCC region. It is a combination of the morphologies shown in Figure 7b and 7d; there is evidence of both ductile rupture and IG faces containing rod shaped particles. The surface exhibits relatively little

evidence of corrosion as a result of the relatively short time of exposure to the corrosive environment. So it appears that the IGSCC did not propagate with a clean front between cracked and uncracked regions. The IGC propagated in the T direction, but left some connections that fractured upon mechanical overload.

A higher magnification secondary electron image of the second fracture region is shown in Figure 8. The rods on the fracture face are about 1 μm in length and 0.15 μm in diameter. Some striations with separation of about 100 nm are pointed out by arrows, suggesting that the crack propagation was intermittent. EDS analysis performed at spots directly on the rod shaped particles found Al with a small amount of Cu and trace amounts of Mn and O. However, quantitative analysis could not be performed because the excited volume was larger than the rod size. A previous investigation using analytical TEM on the same AA2024-T3 plate found a large number of rod-like particles along grain boundaries, and identified their composition to be Al_2Cu (very little Mg), Al_2CuMg or $Al_{20}Mn_3Cu_2$ with no Mg,[18] but with smaller dimensions than those found in the current study.

An optical micrograph of an unetched cross section of the T-S sample is given in Figure 9. This sample in this micrograph has the same orientation as the sample in Figure 5. IGC is clearly seen propagating downward in the T direction, and distributed across many grains in the S direction. The slope along the top of the sample is the wide trench above the failure crack shown in Figure 5b. Figure 9b shows the shallow IGCs existing between the two major cracks. Some dark spots are found along the IGC path. These spots are regions attacked during the cross-sectional polishing by corrosive corrosion product that oozed out of the grain boundary crevices. The cross-sectional images of the unetched sections exhibit extensive intergranular attack and, other than the spots, represent the microstructure equivalent to an etched section.

DISCUSSION

In this work, x-ray micro-radiography was used to provide a new approach to in situ study IGSCC of AA2024-T3. In some ways, the IGC morphology found in this in situ study was different than that reported previously for ex-situ images taken of penetrated L-S stressed foil penetration samples.[7] The foil penetration method assesses IGC or SCC crack kinetics in a very different fashion: one side of a foil sample is exposed to solution and the shortest time for penetration of the foil by localized corrosion is detected.[19, 20] Therefore, the foil penetration method only provides information on the fastest growing site, whereas the radiographic approach provides information on all of the sites individually. For example, the ex situ x-ray image of an L-S foil penetration sample taken after the IGC had penetrated the sample showed IG cracks with similar gray scale sparsely distributed across the L face.[7] The similar gray scale value of the various cracks suggested that they had similar length. However, the in situ radiography could track every IGC site and it is clear from the current study that certain sites were longer than others.

On the other hand, there are similarities between the previous ex-situ images and in situ images. In the previous work an initial strain of 0.06% was applied to an L-S sample in the S direction. IGC penetrated the 1.38 mm thick foil in the L direction after 1.7 h.[7] The x-ray images were taken with x-rays transmitted along the L direction, which was the penetration direction. The width of IG cracks in the S direction was similar to that in the in situ L-S sample, and length of IG cracks in the T direction was about 1 mm, which was the dimension of the in situ L-S sample. So the results of the previous foil penetration experiments already suggested that the

cracks should penetrate the 1 mm thickness of the in situ L-S samples. In some ways these two different approaches reveal similar phenomena.

The lengths of individual cracks were measured using the x-ray images and are presented in Figure 10a for the L-S sample shown in Figure 3. This plot shows that the crack at site 1 initiated earlier than the one at site 2 and grew to a longer length over the first hour of the experiment. However, for some reason that site stopped growing. This stifling of SCC growth is quite interesting and unexpected because of the higher stress concentration at the end of the longest site at any given time. The mechanism behind this crack stifling is not understood. However, the length of the initial crack is approximately equal to the average grain dimension in the longitudinal direction, so crack stifling might be associated with grain triple points. Figure 10b compares the radiographic data to results from foil penetration experiments.[7, 8] Recall that the foil penetration experiment measures only the time for the first site to penetrate the foil, or the fastest growing site. The open diamonds in Figure 10b represent the depth of the deepest site at any given time in the in situ radiographic experiment, which is a combination of the data from sites 1 and 2. These data almost overlie the data from the foil penetration experiments under the same condition[7], which are indicated as filled circles in the plot. The similarity in the data from two vastly different techniques suggests that both approaches provide accurate assessments of crack growth rates. However, the foil penetration technique does not provide information on the propagation rates of individual sites, only the nominal fastest rate for an ensemble of sites. Also shown in Figure 10b are foil penetration data from an L-S sample with very low applied strain, an L-T sample, and an unstressed L sample.[7] From this comparison, it is clear that IGSCC growth in the L direction is greatly accelerated relative to IGC when small stresses are applied in the S direction. In comparison, stressing in the T direction has a smaller influence.

The depths of the large cracks in the T-S sample are plotted as a function of time in Figure 11a. As was shown in Figure 10a for the L-S sample, the crack that grew fastest at the beginning was surpassed by another crack. Figure 11b shows the depth of the deepest site at any given time in the radiographic experiment, which is a combination of the data from sites 1, 2 and 3. T-S samples were not studied by foil penetration. However, the rate of IGC crack growth is seen to be much faster than the penetration rate found in foil penetration experiments for unstressed T samples and for T-L samples stressed to a higher initial strain. Similar to what was found for penetration in the L direction, [7] an applied stress in the S direction is much more effective at enhancing growth kinetics in the T direction than an applied stress in the L direction.

Every experiment exhibited a failure crack that was not the fastest growing crack at the early stages of the experiment. For the sample configuration with dimensions of 1.05 mm thickness and 4-5 mm width, the plane strain criterion was not satisfied, i.e. the plate thickness was less than 15x the plastic zone radius[21], so the sample was in the condition of plane stress. Stress intensity at the crack tip is the dominant driving force in mechanical fracture. Under constant-displacement testing conditions, stress intensity decreases progressively as the crack propagates. However, the stress intensity is always higher at the longest flaw than at shorter cracks. Therefore, decay in stress intensity factor can not explain growth stifling of the leading crack in the multiple cracks. However, in a corrosive aqueous environment, several factors can complicate the situation. Corrosion can result in crack widening and blunting and in the formation of voluminous corrosion product. Figure 4 shows that branching of the crack occurred as it intersected various grain boundaries. Such branching will decrease the local stress intensity, possibly to a value lower than that at a shorter, sharper crack, which would then grow faster. So the local synergistic effects of stress and electrochemistry simultaneously drive the IGSCC

growth. Sprowl and Brown found that if a large number of nearly equal fissures are developed in close proximity, there will be no effective concentration of stress in any fissure, and cracking of the stressed member may not occur even if the metallurgical state of the metal permits stress corrosion.[22]

Stress corrosion cracking has been attributed to the solute-depleted zone (SDZ) along the grain boundaries.[23-25] These zones have quite different chemical composition and microstructure than the grain matrix.[26] AA2024-T3 is heat-treated by solution annealing followed by artificial aging at room temperature (RT). Although the precipitation process is sluggish at RT, extended artificial aging may affect the precipitate microstructure. The large number of rod particles with rather large dimensions at the fracture surface might have been the result of extended artificial RT aging. EDS analysis identified the rods as being an Al-Cu compound, but this analysis was complicated by the small size of the particles and possible changes in composition by corrosion during exposure to the local environment. It is possible that a galvanic interaction between these grain boundary particles and the solute depleted zone on either side of the grain boundaries played an important role in the crack development even though the potential was controlled using a potentiostat.

As with all stress corrosion cracking, the local interaction between stress, metallurgy and electrochemistry plays a significant role in the competition between multiple cracks. This competition cannot be addressed using traditional fracture mechanics approaches, but understanding how multiple cracks interact and how the synergistic actions of tensile stress and anodic dissolution control propagation is critical to the understanding of IGSCC in real structures.

CONCLUSIONS

1. X-ray micro-radiography technique is a non-destructive method that can be used to study stress corrosion cracking in situ using the proper orientation of samples and special cells. The technique can characterize the morphology of individual cracks and generates the kinetics of localized IGC growth.
2. The results of the radiographic analysis resulted in IGSCC kinetics that were similar to those generated by the foil penetration method.
3. In this approach the sample is not limited to the formation of a single crack and the competition between SCC cracks can be studied. The crack that led to the final failure was not the fastest growing crack at the early stages of the experiment.
4. The IGSCC fracture surface exhibited a large number of rod-shaped particles, which might play an important role in the propagation process.

ACKNOWLEDGEMENTS

This work was funded by the United States Air Force Office of Scientific Research through Grant No. F49620-02-1-0148. The authors are grateful for the support of the contract monitors Lt. Col. Paul Trulove and Maj. Jennifer Gresham.

REFERENCES

1 M.O. Speidel, Metallurgical and Materials Transactions A, 6A (1975): p. 631.
2 H. Vogt and M.O. Speidel, Corrosion Science, 40 (1998): p. 251.

3 R.C. Newman and R.P. M. Procter, Br. Corros. J., 25 (1990): p. 259.
4 X. Zhao, G.S. Frankel, B. Zoofan, and S.I. Rokhlin, Corrosion, 59 (2003): p.1012.
5 ASTMSTPG34, "Test for Exfoliation Corrosion Susceptibility in 7xxx Series Copper-Containing Aluminium Alloys, EXCO Test", (1979).
6 M.J. Robinson and N.C. Jackson, British Corrosion Journal, 34 (1999): p. 45.
7 X. Liu, G.S. Frankel, B. Zoofan, and S.I. Rokhlin, Corrosion Science, 46 (2004): p. 405.
8 X. Liu, Z. Zhao, G.S. Frankel, B. Zoofan, and S.I. Rokhlin. "Effects of Stress on Localized Corrosion in Al and Al Alloys," Proceedings of Triservice Corrosion Conference, Las Vegas, 2003.
9 T.D. Burleigh, Corrosion, 47 (1991): p. 89.
10 F. Zeides and I. Roman, Materials Science and Engineering, A125 (1990): p. 21.
11 G.H. Haidemenopoulos, N. Hassiotis, G. Papapolymerou, and V. Bontozoglou, Corrosion, 54 (1998): p. 73.
12 P.V. Petroyiannis, A.T. Kermanidis, P. Papanikos, and S.G. Pantelakis, Theoretical and Applied Fracture Mechanics, 41 (2004): p. 173.
13 F. Hunkeler and H. Bohni, Corrosion, 40 (1984): p. 534.
14 W. Zhang and G.S. Frankel, Electrochemical and Solid-State Letters, 3 (2000): p. 268.
15 B. Zoofan and S.I. Rokhlin, Materials Evaluation, 52 (1998): p. 191.
16 X. Liu, G.S. Frankel, B. Zoofan, and S.I. Rokhlin. "Imaging and Characterization of Multiple Stress Corrosion Cracks in AA2024-3 by X-ray Radiography", in Proc. of 206 Electrochemistry Society, 2004, eds.D. Shifler and T. Tsuru eds. p. 726.
17 W. Zhang, S. Ruan, D.A. Wolfe, and G.S. Frankel, Corrosion Science, 45 (2003): p. 353.
18 W. Zhang and G.S. Frankel, Electrochimica Acta, 48 (2003): p. 1193.
19 A. Rota and H. Bohni, Werkstoffe und Korrosion, 40 (1989): p. 219.
20 A. Rota and H. Bohni, Werkstoffe und Korrosion, 40 (1989): p. 295.
21 T.L. Anderson, ed., "Fracture Mechanics: Fundamentals and Applications", 2nd edn. (CRC press, 1995).
22 D.O. Sprowls and R.H. Brown. "Stress Corrosion Mechanisms for Aluminum Alloys", in Proc. of Conf. Fundamental Aspects of Stress Corrosion Cracking, OSU Columbus OH, 1967, eds. R.W. Staehle p.466-512 .
23 D.O. Sprowls, "Evaluation of Stress-Corrosion Cracking", Corrosion, Metals Handbook, Vol. 13, 9th ed., (ASM International, materials Park, OH 1986) p. 245-609.
24 M. Baumgartner and H. Kaesche, Corrosion, 44 (1988): p. 231.
25 F.D. Wall and G.E. Stoner, Corrosion Science, 39 (1997): p. 835.
26 T. Ramgopal, P.I. Gouma, and G.S. Frankel, Corrosion, 58 (2002): p. 687.

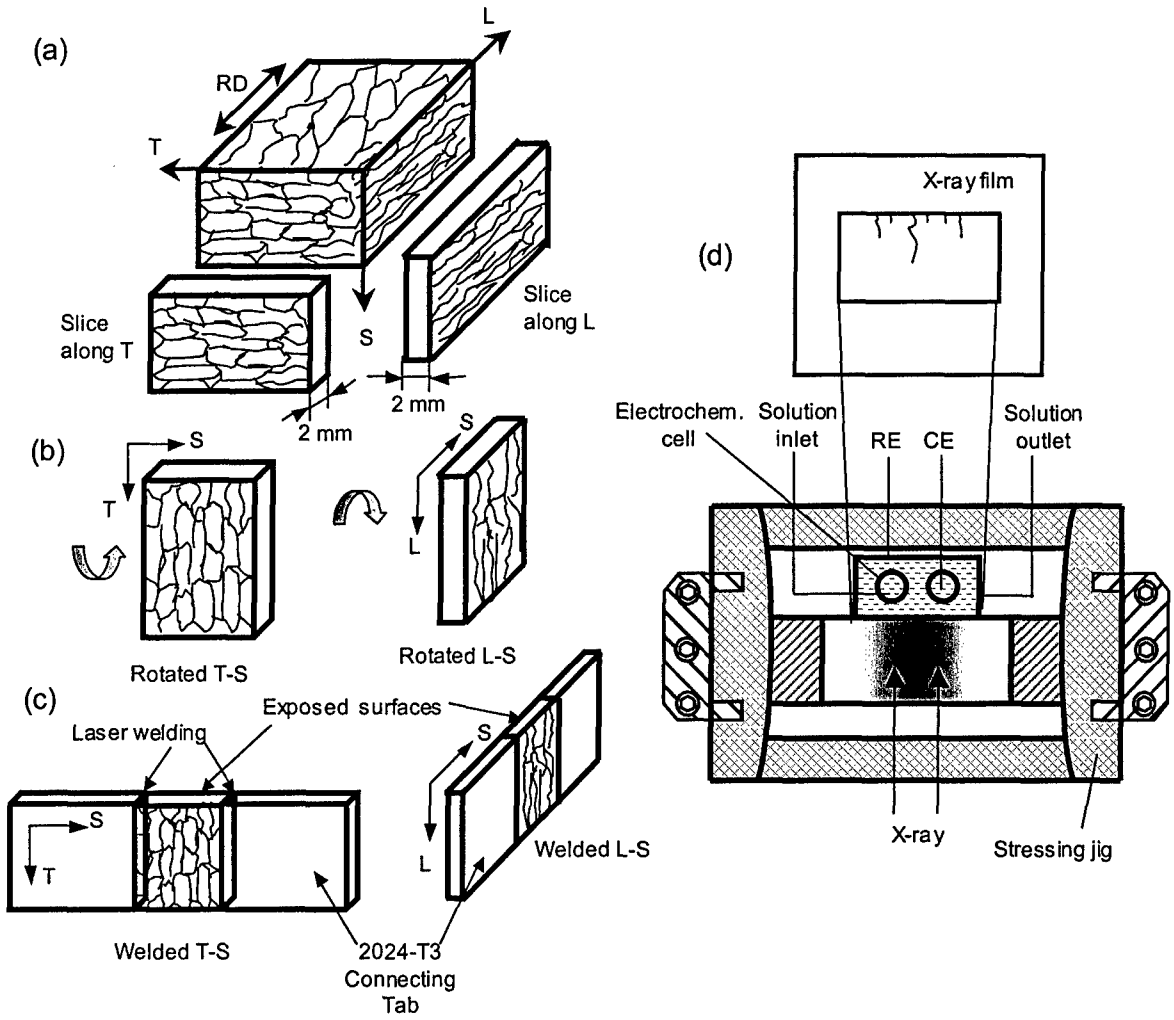

Figure 1. Schematic of procedure to make T-S and L-S sheet sample for in situ radiographic measurement. (a) Cut sheet sample from plate; (b) rotate sample; (c) laser weld sample with connecting tabs to fit for the ASTM G49 stressing jig; (d) apply constant displacement with stressing jig, constrain sample in electrochemical cell, control potential, and irradiate with x-rays.

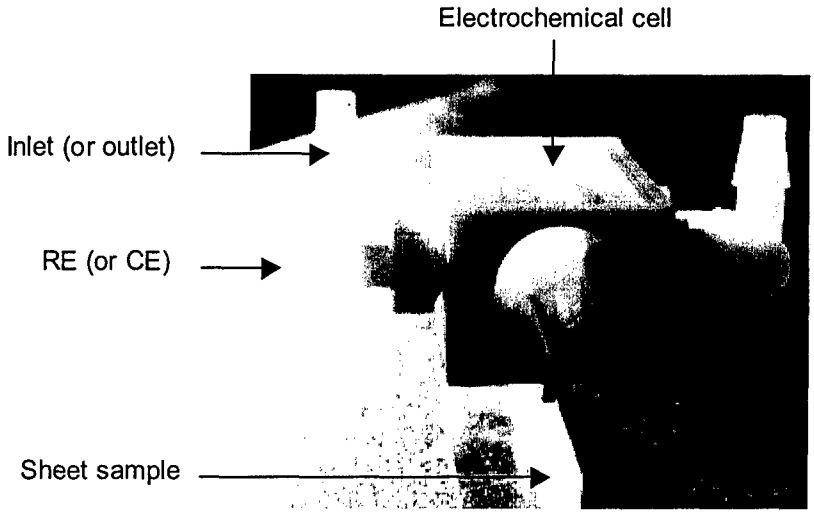

Figure 2. Electrochemical cell used in the in situ X-ray microfocal radiography experiment.

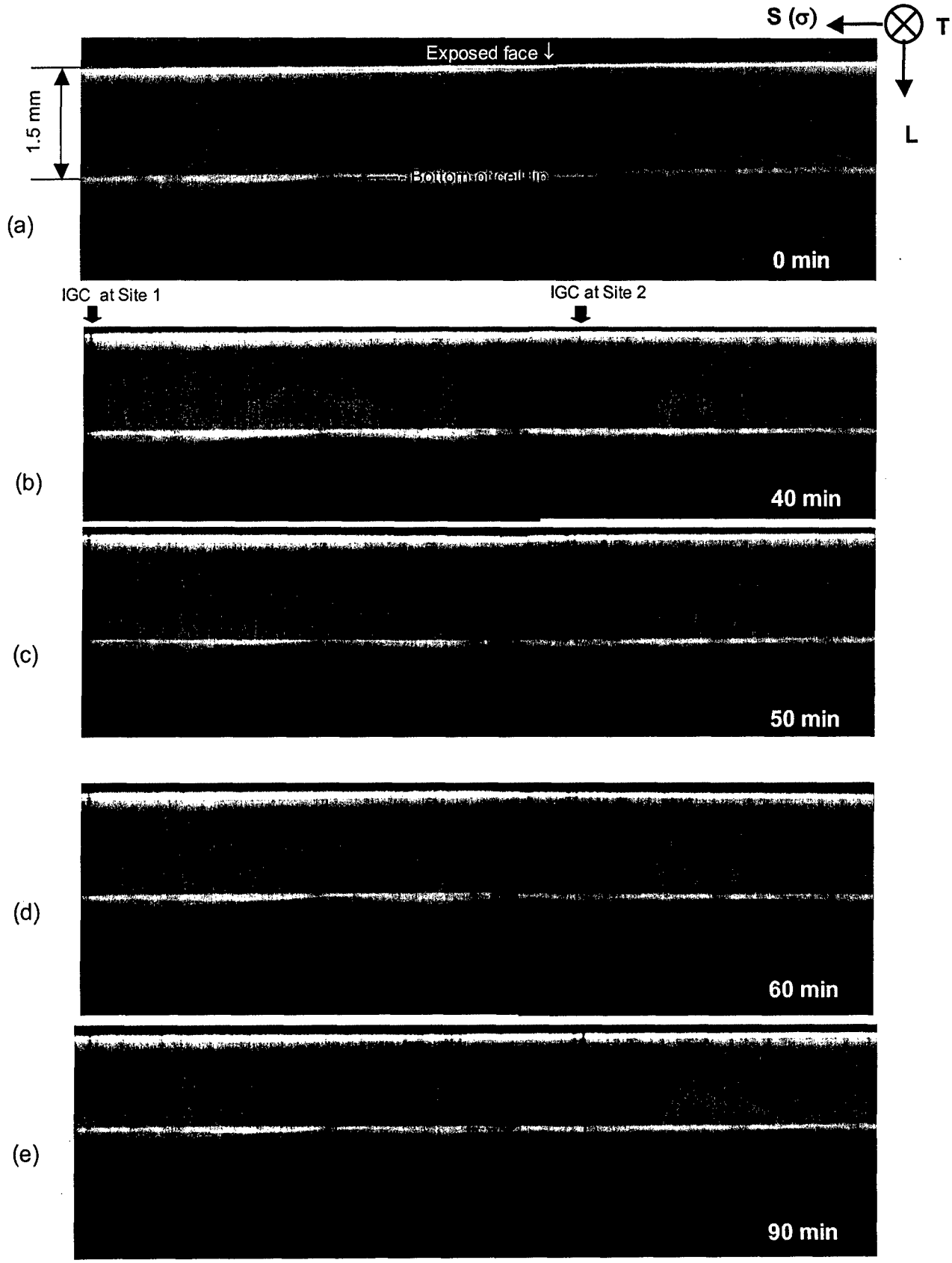
S (σ)
T
L
Exposed face ↓
1.5 mm
Bottom of crack tip
(a)
0 min
IGC at Site 1
IGC at Site 2
(b)
40 min
(c)
50 min
(d)
60 min
(e)
90 min

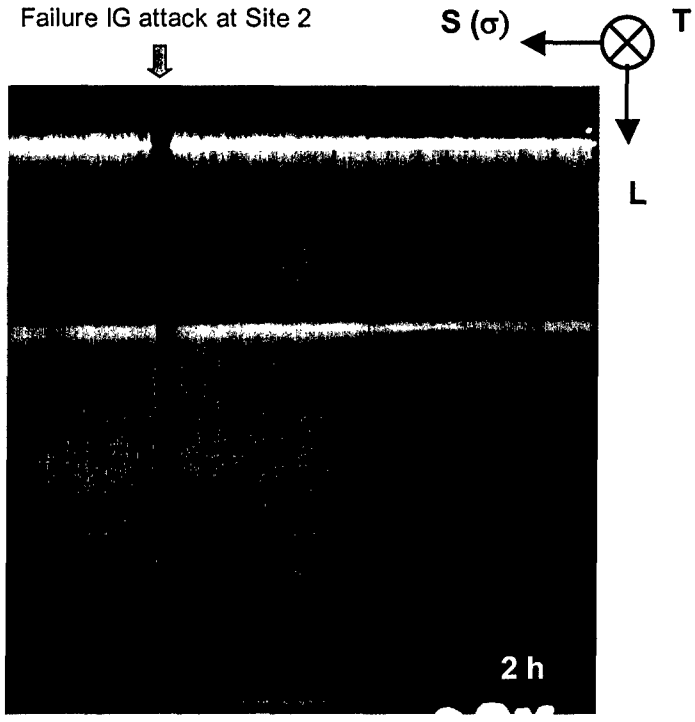
Failure IG attack at Site 2
S (σ)
T
L
2 h

(f)

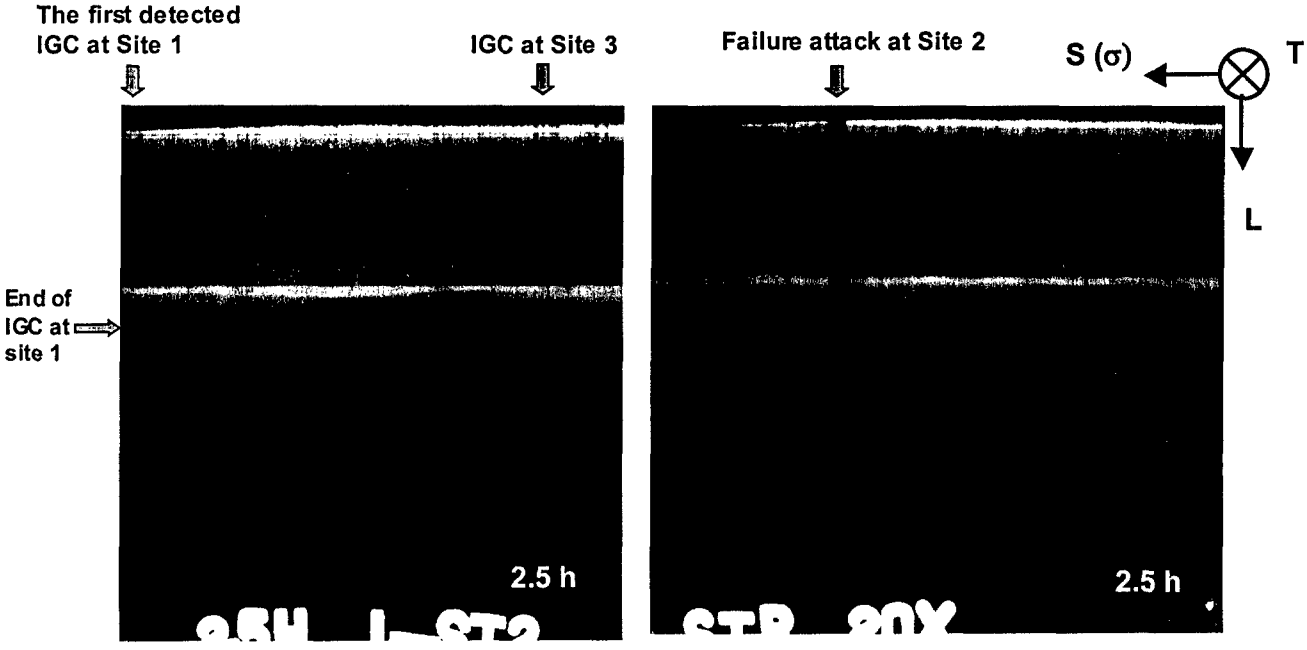
The first detected IGC at Site 1
IGC at Site 3
Failure attack at Site 2
S (σ)
T
L
End of IGC at site 1
2.5 h
2.5 h

(g) (h)

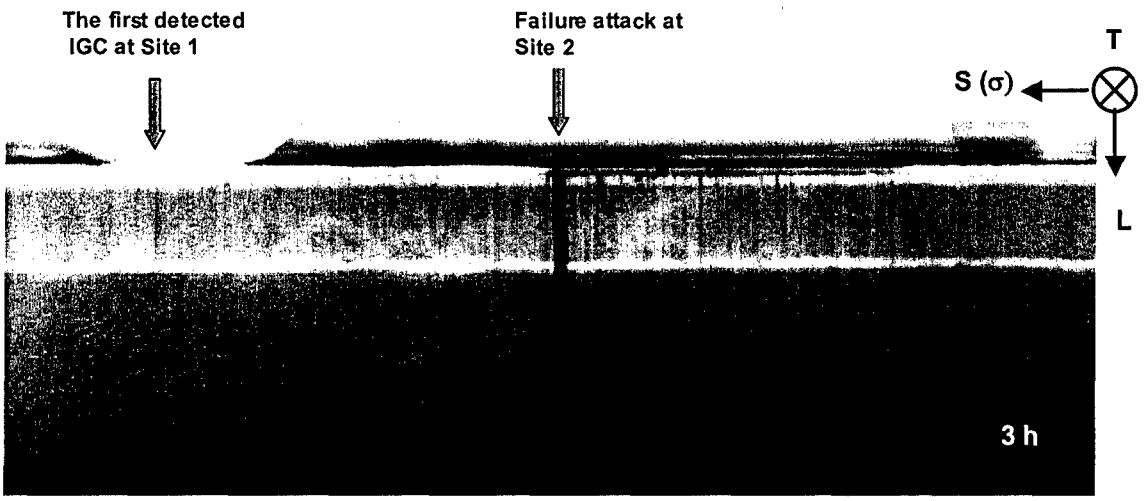

(i)

Figure 3. X-ray microfocal radiography images of IGSCC in L-S sample with initial strain of 0.18% at –580 mV SCE in 1.0 M NaCl. (a) prior to test, (b) after 40 min., (c) after 50 min., (d) after 60 min., (e) after 90 min (f) after 2h, site 2 (g) 2.5h, site 1 and (h) 2.5h, site 2 (i) after 3h.

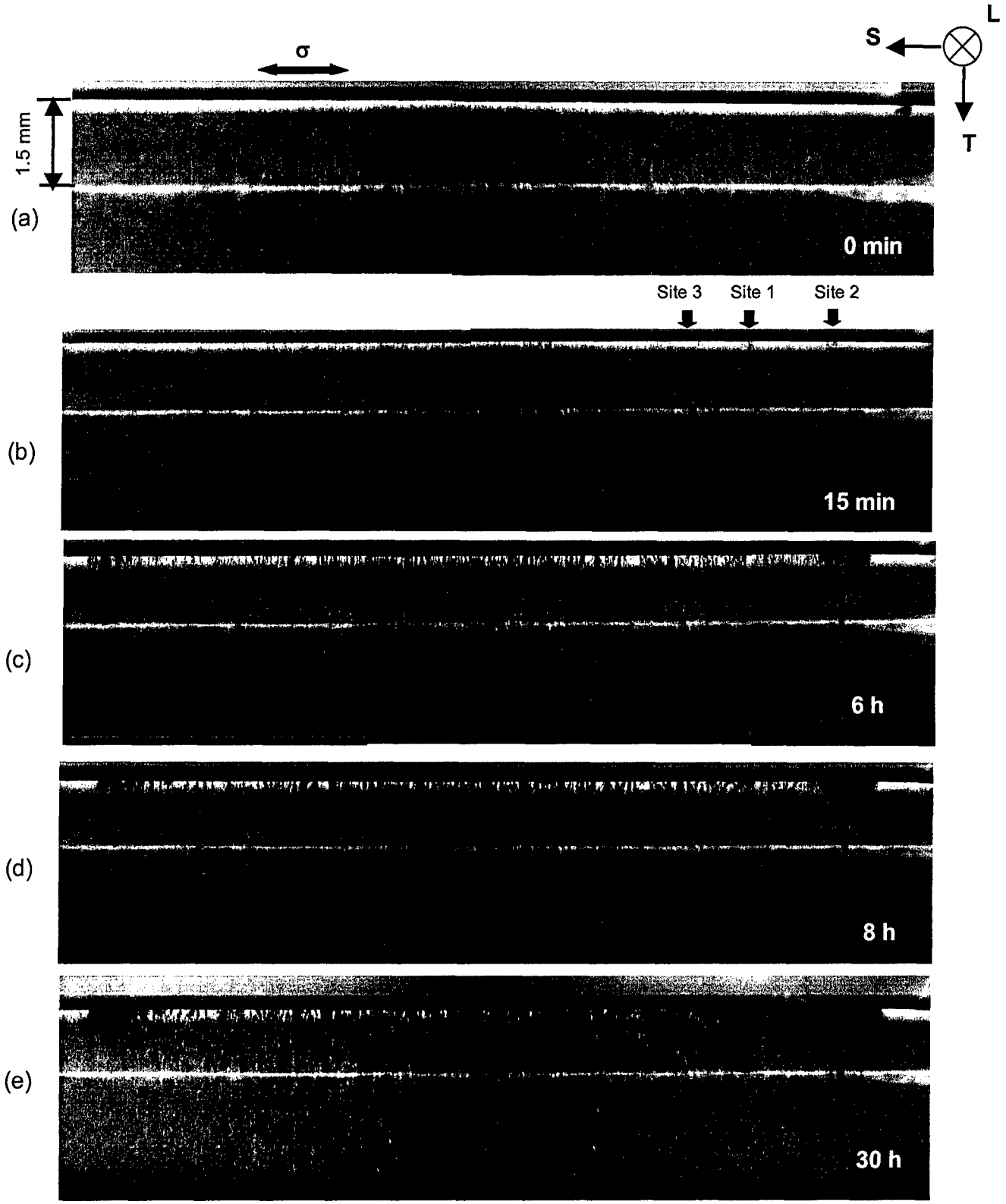

Figure 4. X-ray microfocal radiography images of IGSCC in T-S sample with initial strain of 0.18% at –580 mV SCE in 1.0 M NaCl. (a) prior to test, (b) after 15 min., (c) after 6 h., (d) after 8 h., (e) after 30 h.

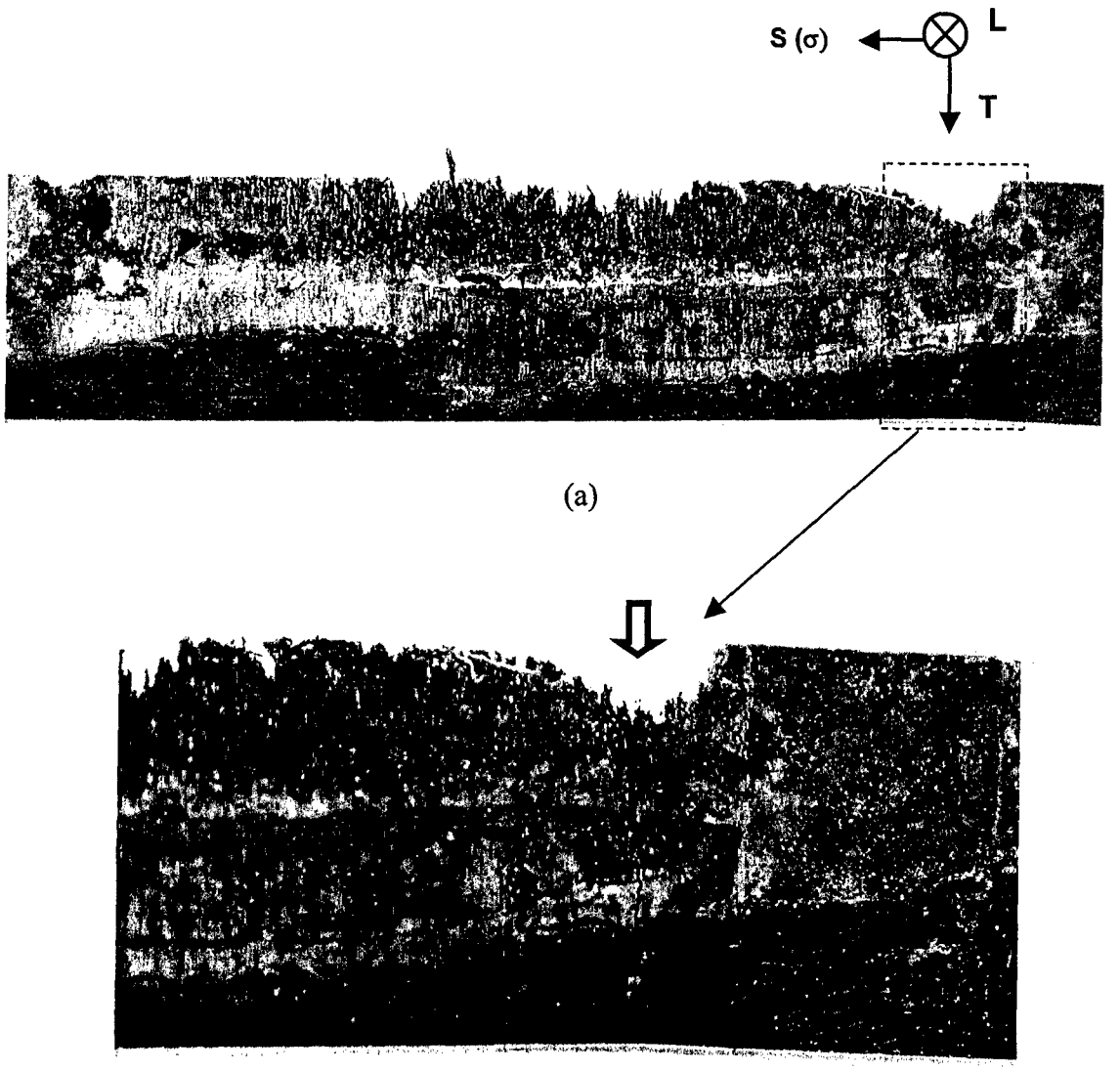

Figure 5. Optical images of T-S sample after experiment. (a) the entire exposed area (b) higher magnification at the site of the final crack.

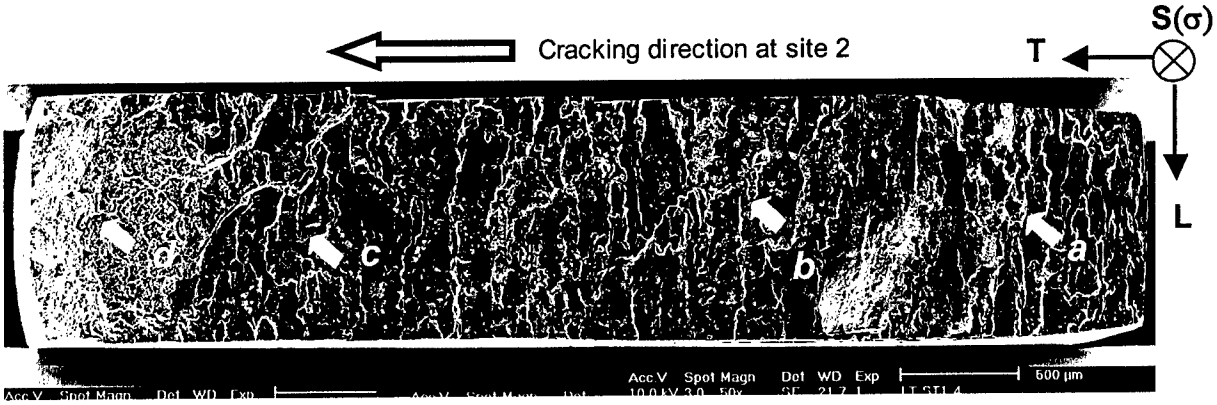

Figure 6. Secondary electron image of the T-S sample fractured at site 2 by overload after the experiment. The sample is 5 mm wide in T direction. Stress was applied in the S direction normal to paper. The arrows point to regions shown in detail in Figure 7.

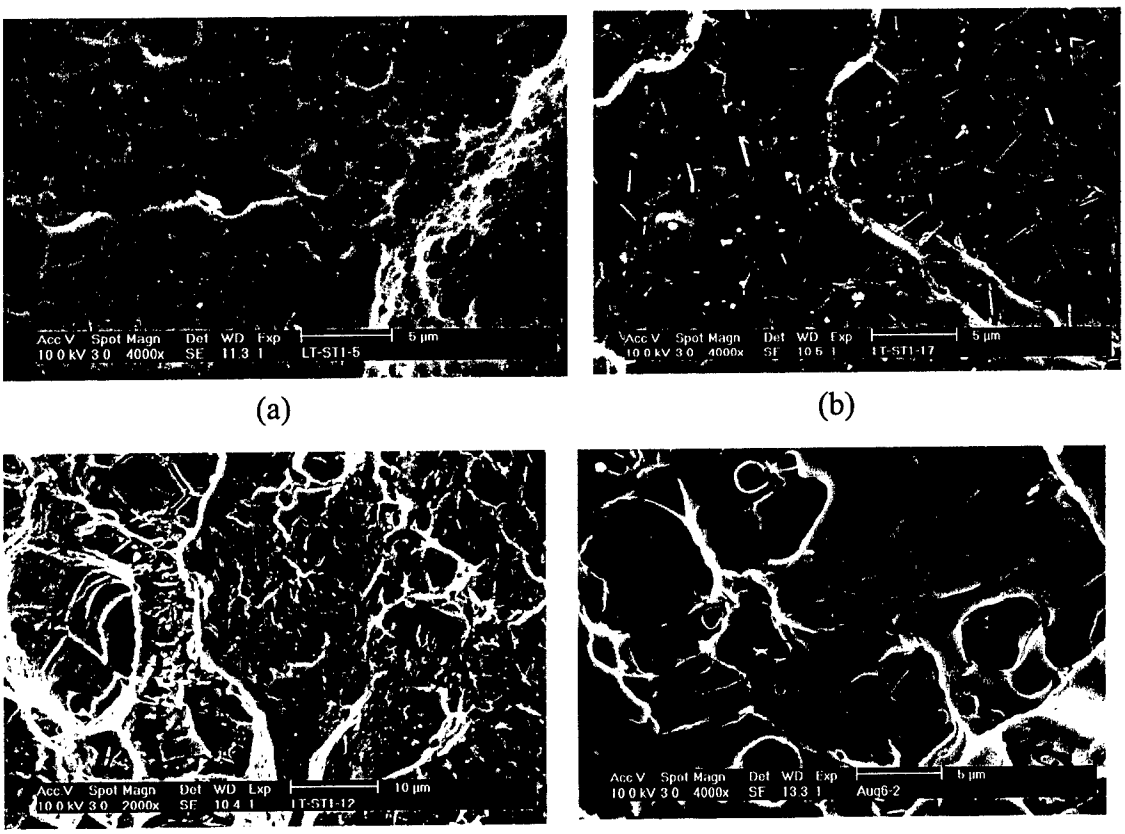

Figure 7. High magnification secondary electron images of the regions indicated by arrows in Figure 6.

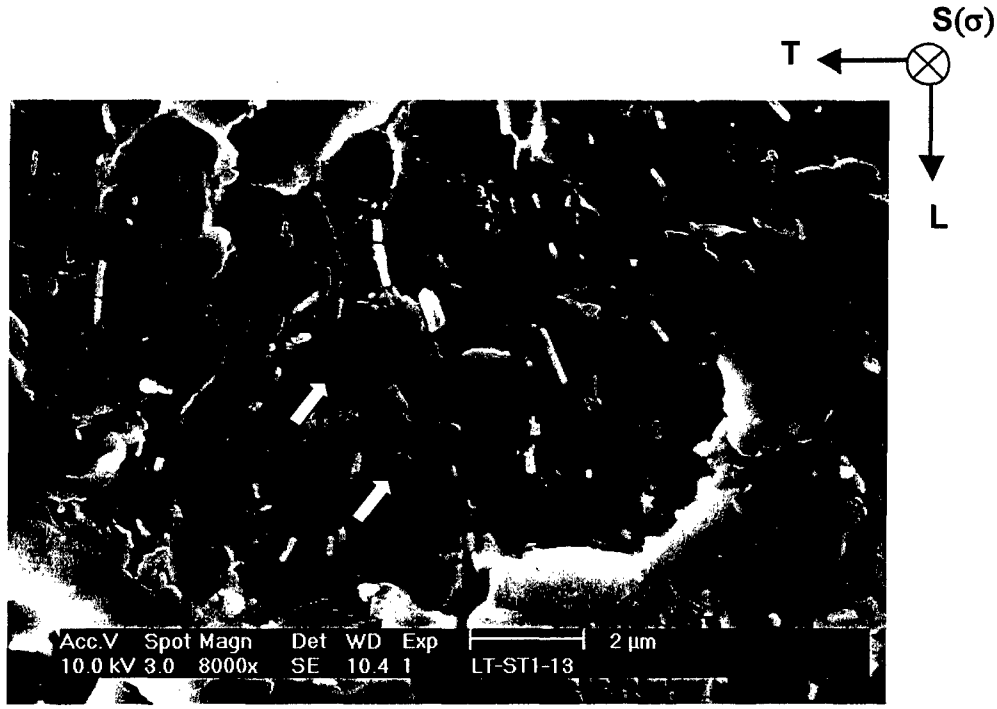

Figure 8. Higher magnification image of IGSCC region shown in Figure 7c. The arrows show the stress striations on the fracture facets.

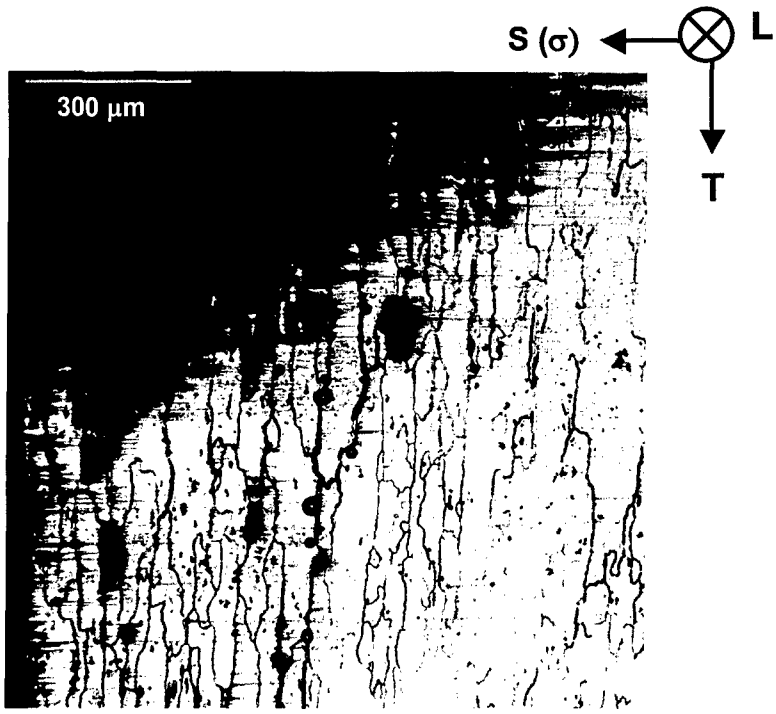

(a)

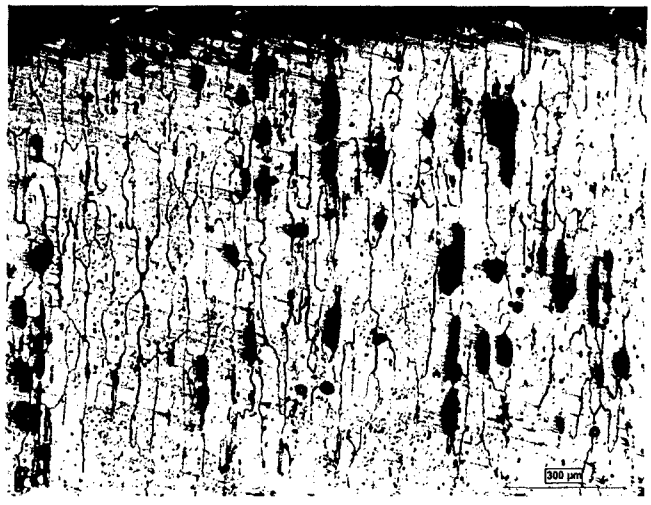

(b)

Figure 9. Unetched cross-sectional images of T-S AA 2024-T3 sample with 0.18% strain at –580 mV SCE in 1.0 M NaCl.

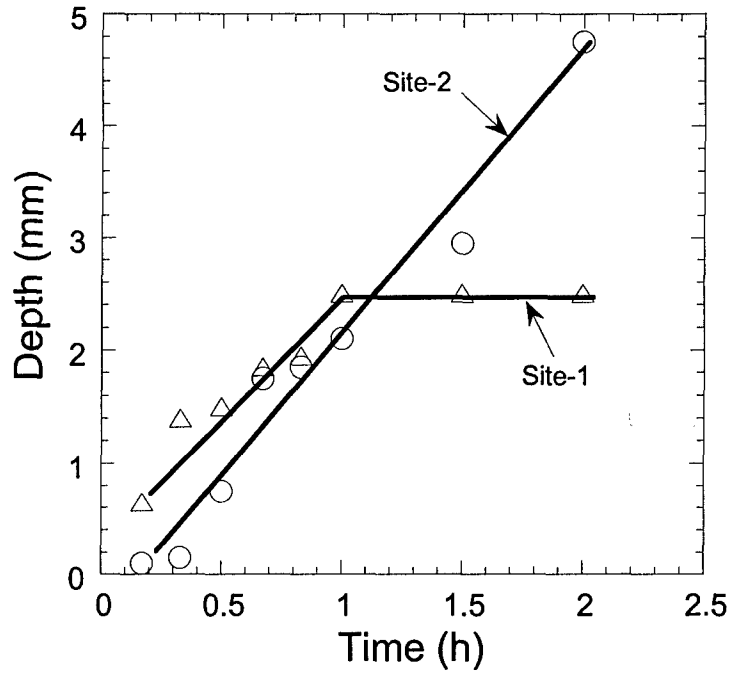

(a)

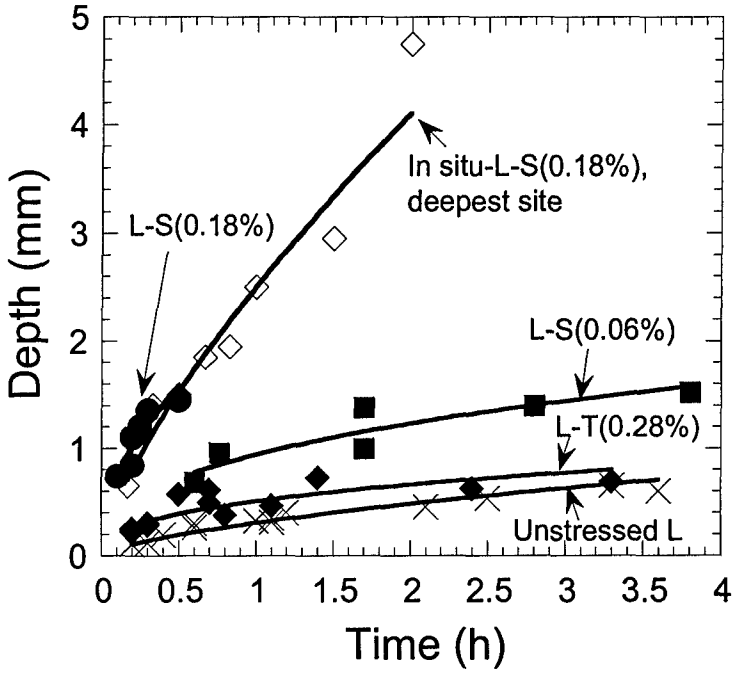

(b)

Figure 10. IGSCC kinetics from in situ radiographic experiments. AA2024-T3 at –580 mV SCE in 1.0 M NaCl. (a) depth of sites 1 and 2 from L-S in situ experiment (b) open diamonds - combined data from sites 1 and 2 to show the deepest site at a given time rate of IGSCC from in situ radiographic experiments, X – unstressed foil penetration data in the L direction, filled symbols – stressed foil penetration data in different orientations and stresses. The values in parentheses are the initial strains.

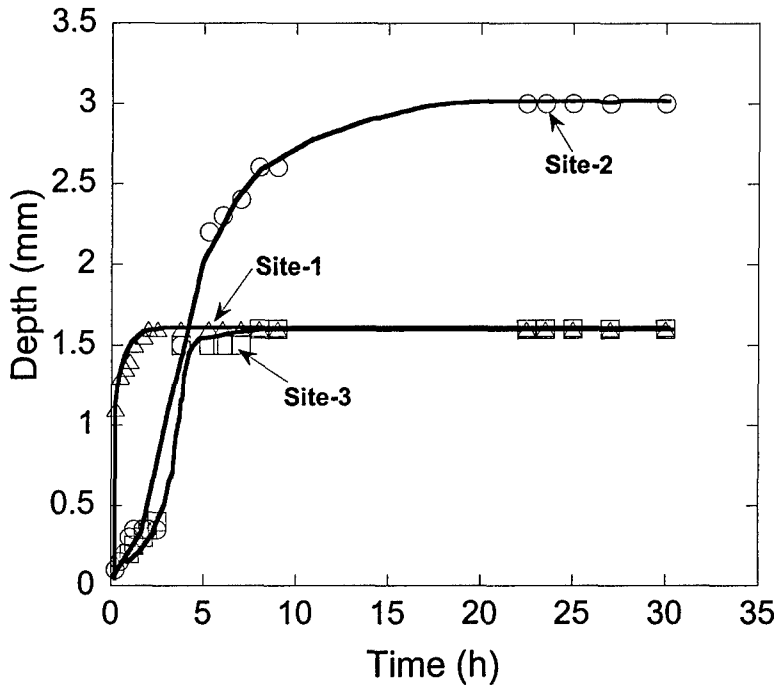

(a)

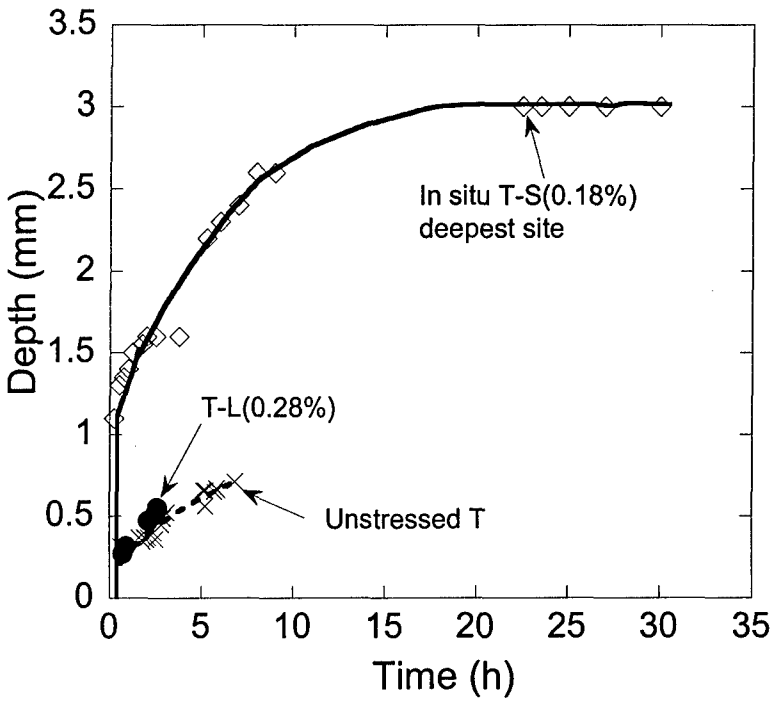

(b)

Figure 11. IGSCC kinetics from in situ radiographic experiments. AA2024-T3 at –580 mV SCE in 1.0 M NaCl. (a) depth of sites 1, 2 and 3 from T-S in situ experiment (b) open diamonds - combined data from sites 1 - 3 to show the deepest site at a given time rate of IGSCC from in situ radiographic experiments, X – unstressed foil penetration data in the T direction, filled circles – stressed T-L foil penetration data. The values in parentheses are the initial strains.

Application of Phase-Contrast Microradiography in NDE

B. Zoofan[1], S. I. Rokhlin[1]* and G. S. Frankel [2]
1) The Ohio State University, Nondestructive Evaluation Program
Edison Joining Technology Center, Columbus, OH 43221

2) The Ohio State University, Fontana Corrosion Center
Department of Materials Science and Engineering, Columbus, OH 43210

ABSTRACT

Practical aspects of microfocal X-ray image enhancement utilizing phase-contrast effects are considered. Optimization of the experimental method to achieve phase contrast is described for application to nondestructive evaluation of materials. Experimental phase-contrast images of porosity and corrosion pits obtained with a 5-micron microfocal X-ray source are compared with absorption-contrast images demonstrating significant enhancement of image quality. The phase-contrast X-ray imaging provides enhanced image contrast, improved edge definition and X-ray phase information on the material.

INTRODUCTION

Conventional radiographic imaging is based on X-ray beam intensity modulation by geometrical features of the object and by material defects. This modulation depends on X-ray absorption in the material and local changes of the object thickness. The modulated X-ray beam is recorded on film or any other recording medium to produce an object projection (2-D shadowgraph). This basic principle of X-ray image formation and its interpretation in radiography have remained basically unchanged since the discovery of X-rays.

The absorption control image contrast C depends on the thickness change Δh of the part and is defined as (Fig.1):

$$C = \frac{\Delta h}{h} \tag{1}$$

where h is the material thickness. It is difficult to achieve contrast sensitivity better than 1% and most codes usually require 2% contrast sensitivity. One should note that the contrast sensitivity defined by Eq. (1) is applicable only when the system unsharpness is much smaller than the defect size; when the defect diameter becomes smaller than the unsharpness the image contrast significantly decreases. Use of a microfocal X-ray source significantly reduces the system unsharpness and allows X-ray image magnification (Zoofan and Rokhlin, 1998 and Rokhlin et al., 2003). Radiographic imaging of dense structural materials requires increase of photon energy which leads to decrease of X-ray absorption and contrast sensitivity and thus contrast can be very poor for such materials with small defects.

However, during radiography, in addition to the object-induced X-ray intensity change, change of X-ray phase occurs. The change of phase by the object leads to change of direction of the X-ray propagation (refraction). The use of phase-contrast imaging may in some cases significantly improve image contrast achievable

by absorption radiography. In recent years significant effort has been put forward by different groups in developing this new imaging technique especially in low-attenuation materials like biological tissues for medical application. For the case with very low attenuation materials, this approach can significantly improve the contrast sensitivity of the image (Davis et al., 1995; Snigirev, et al., 1995; Cloetens, et al., 1996; Nugent, et al., 1996; Wilkins, et al., 1996). For historic background and introduction to phase contrast imaging readers are referr to Fitzgerald, 2000.

The main objective of this paper is to demonstrate the applicability of the phase contrast method to nondestructive evaluation (NDE) and to optimize the method for imaging of structural materials, such as aluminum alloys.

CONCEPT OF THE METHOD

Analogous to conventional optics, the behavior of X-rays passing through a sample can be described using a complex refractive index $n=1-\delta+i\beta$, where δ is the refractive decrement and β is related to the X-ray absorption; both these parameters depend on frequency or photon energy. One should note that the real part of the refractive index for X-rays has the opposite sign to that for light. For X-ray radiation the refractive index modulus deviates only slightly from unity.

As an example, δ and β are plotted in Figure 2 versus photon energy (Zoofan et al., 2003). As one can see δ and β are of the same order for very low X-ray energies while with increase of energy the absorption index β drops sharply so that absorption imaging loses contrast. The δ/β ratio for epoxy is higher than that for aluminum; this indicates that for low density materials the phase contrast advantage is even more significant. With increasing photon energy, the ratio between X-ray refraction and absorption coefficients increases, indicating a substantial effect of phase modulation by the object of the X-ray beam transmitted through the material. This phase modulation may significantly enhance X-ray images when properly used. In the higher-energy region the refractive decrement δ is several orders of magnitude higher than the absorption coefficient (in most materials $\delta \approx (10^3 \sim 10^5) \times \beta$) and phase contrast imaging may be possible even when the absorption contrast is too small.

The phase imaging method is based on the refraction of radiation at the boundaries separating different media in an object. The refraction angle depends on the difference $\Delta\delta$ of refractive decrements in these media. Since the refractive decrement δ is very small, the angle of refraction at the intermedia boundaries is about 10^{-5}-10^{-7} radians. Therefore, it is impossible to detect beams deviated at such small angles by conventional radiography. However with microfocal radiography using higher magnification it is possible to select geometric conditions so that phase-contrast imaging becomes possible.

The concept is illustrated in Figure 3 where X-rays are shown refracting on the boundary of a cavity in a material. When there is density variation in the material, X-rays refract from the higher density side to the lower density region. Consequently, the X-ray beam shifts toward the low density region and only a small amount of X-ray energy arrives in the fringe region, which makes the film underexposed with the formation of bright fringes. Due to X-ray refraction of the white ring is formed surrounding the dark circle corresponding to the absorption image of the object

(Figure 3(b)). Thus phase-contrast imaging produces analog edge enhancement of the image. This enhancement occurs even when absorption contrast disappears.

Wilkins et al., 1996 have demonstrated that in microfocal radiography, the high space coherence of phase-contrast imaging is achievable due to the X-ray source and that high spectral coherence in a frequency domain is not required and thus conventional polychromatic microfocal X-ray sources can be used for this purpose.

EXPERIMENTAL SYSTEM AND PROCEDURE

The schematic of our micro-focus experimental system for in-line projection phase-contrast X-ray imaging is shown in Figure 4 with a 5 μm focal size, 225 kV FeinFocus® X-ray unit used as an X-ray source. The X-ray source, an object and the X-ray detector (film or image intensifier) are aligned linearly along the optical axis. A precise positioning system with three linear (with 2 μm resolution) and one rotating (with 0.01 degree resolution) computer controlled axes is used to control the position of the sample. An additional high-resolution linear axis is used for translating the position of the image plane. A two-directional manipulator is used for positioning of the X-ray tube.

A micron resolution movement of the sample provides accurate projection magnification of the image. The X-ray exposure parameters have been carefully selected such that during exposure the focal spot size remains in the micro-focus region of the tube to get the optimum resolution. An image intensifier integrated with a CCD camera is used for real-time microradiography and also for alignment of the sample prior to film microradiography. After alignment of the sample and the image plane, the film is mounted on a 4 mm thick lead plate and placed in the front face of the image intensifier, which in this case serves as a mechanical support. Exposed and processed films are digitized by illuminating them in front of a TV camera. A PCVision® Frame Grabber (from Imaging Technology) is used for digitization of the films and transferring the image to a PC. The digital profiles of the images are saved in the computer and further processed to obtain the X-ray intensities. Two different types of films have been used; Agfa Structurix D7 films as a high-speed film and D2 film with fine grains and very high contrast.

Quantitative measurement were performed on a 1.5 mm thick epoxy layer cured on a 1.5 mm Plexiglas plate and on a 1 mm thick Al 2024-T3 sample. The epoxy layer contained spherical voids with diameters up to 1.2 mm. The Al 2024 sample contained a 340 μm diameter artificial pit of 770 μm depth. Microradiography was performed to obtain images in absorption-contrast and phase-contrast modes by changing the distance between the object and the film. Also multiple experiments have been performed on other types of objects to demonstrate the method applicability.

EXPERIMENTAL RESULTS AND DISCUSSION

Absorption and phase-contrast X-ray images are compared in Figure 5 for samples of epoxy with voids and an Al 2024 plate with cylindrical pit. The absorption-contrast image has been taken with a relatively short object-to-film distance (OFD) = 182 mm for epoxy and 290 mm for Al-2024 while the phase-contrast image was taken for a larger OFD =1 m for epoxy and 1.43 m for Al-2024. For both types of imaging the projection magnification was the same: 2.5X for epoxy and 10X for the Al-2024 sample. The X-ray exposure has been selected such that both

images on the film have the same optical density; a longer (11 min for epoxy and 9 min for Al-2024) exposure of film was required for the phase-contrast image due to larger source-to-film distance (SFD). Remarkable enhancement of the contrast in the phase-contrast image should be noted, especially as the boundaries of the spherical voids and a pit are clearly defined. Figure 6 illustrates this enhancement by sharp changes of the line profile across the fringes produced.

The existence of a bright ring around the objects (white ring around dark area in the image and picks in the line profiles) indicates that X-rays refract from the material surrounding the object toward the object center which is accompanied by bright fringe formation and increase of image darkness in the object region (dips in the line profile, which are especially clear for the Al sample, see Figure 6(b)). The width of the bright fringe on the film at geometrical X-ray magnification M=2.5 is about 10 μm.

The critical effect of the spatial coherence of the X-ray source on obtaining a phase-contrast image is demonstrated in Figure 3 (c) when the X-ray tube was not in micro-focus mode. It means the focal spot size was expanded to be much larger than 5 μm nominal focal spot size. For both cases the OFD was 1 m. The white fringe due to X-ray refraction disappeared and the image is similar to that with absorption contrast.

To investigate the effect of photon energy (tube voltage) on the phase-contrast image we have performed the experiment at tube voltages ranging from 20 to 180 kV. The width of the main diffraction fringe around the defect image was measured directly on film under an optical microscope in order to avoid any quantization error during digitization. The obtained width of the fringe allows us to determine the refracted angles of the X-ray. Figure 7 shows the variation of refracted angles (in μ radians) for different applied photon energies. The trend shows that for higher photon energy the diffracted angles become smaller which produces finer fringes around the object, which has different refractive index. Thus to observe the fringes at high photon energy (high X-ray source voltage) very high resolution of the image is required.

Although larger object-to-film distance seems to improve the phase-contrast significantly, very large object-to-film distance is not practical due to the necessity to increase the exposure time by the inverse-square law. These leads to very long exposure times since low level of tube current of the micro-focus tube is required to maintain microfocal conditions.

To illustrate the method we have performed the phase-contrast imaging on a variety of different samples and some of the examples are shown below. Figures 8 (a) and (b) show application of the technique to a 50 mm diameter 2.5 mm thick aluminum tube with weld. The projection magnification was 8X with a long SFD of 1.63 m; tube voltage was 50 kV. The image shows fine porosity in the weld with refraction induced white rings similar to those discussed above. Fig 8(c) shows phase contrast image of a hot-plate butt weld of the 4-mm thick polyethylene plates; lack of fusion is clearly observed. The white fringes in the phase-contrast image clearly define the non-fused area in the joint. A comparison of absorption (a) and phase (b) contrast images of the 1 mm aluminum sample with corrosion damage is shown in Figure 9. Significant improvement of the image is obtained in phase contrast mode showing the morphology of the tips of the crack and the details of the corrosion products on the sample. Figure 10 shows the phase-contrast images of (a) a spider and

(b) a bug with 3x projection magnification and OFD of 1 m on D7 films with 36 kV. The soft tissues and extremely fine details are clear on those images.

CONCLUSIONS

It is shown that microfocal X-ray phase-contrast imaging provides significant enhancement of image contrast. This is achieved by optimal selection of geometrical conditions such as object-to-film distance and projection magnification and of exposure parameters. Several examples of phase-contrast-enhanced images for metal and polymer samples with defects are shown. A remarkable feature of phase contrast imaging is analog edge enhancement which is manifested in the X-ray film images of material cavities as white contours on a boundary with the surrounding material and increased darkness of the cavities in the images.

ACKNOWLEDGMENT

The work was supported by the United States Air Force Office of Scientific Research through Grant No. F49620-02-1-0148.

REFERENCES

Cloetens, P., R. Barrett, J. Baruchel, J.-P. Guigay and M. Schlenker, "Phase-objects in synchrotron radiation hard x-ray imaging," *J. Phys. D: Appl. Phys.*, Vol. 29, 1996, pp.133-146.

Davis, T. J., D. Gao, T. E. Gureyev, A. W. Stevenson and S. W. Wilkins, "Phase-contrast imaging of weakly absorbing materials using hard X-rays," *Nature*, Vol. 373, 1995, pp. 595-598.

Davis, T. J., T. E. Gureyev, D. Gao, A. W. Stevenson and S. W. Wilkins, "X-ray image contrast from a simple phase object," *Phys. Rev. Lett*, Vol.74, 1995, 3173-3176.

Fitzgerald R, "Phase Sensitive X-ray imaging" Physics Today, 2000, 23-24.

Gureyev, T. E. and S. W. Wilkins, "On X-Ray Phase Imaging with a Point Source," *J. Opt. Soc. Am. A.*, Vol. 15, 1998, pp. 579-585.

Gureyev, T. E., C. Raven, A. Snigirev, I. Snigireva and S. W. Wilkins, "Hard X-Ray Quantitative Non-Interferometric Phase Contrast Microscopy," *J. Phys. D: Appl. Phys.*, Vol. 32, 1999, pp. 563-567.

Gureyev, T. E., S. Mayo, S. W. Wilkins, D. Paganin and A. W. Stevenson, "Quantitative in-Line Phase-Contrast Imaging with Multienergy X rays," *Phys. Rev. Lett.*, Vol. 86, 2001, pp. 5827-5830.

Ingal, V. N., and E. A. Beliaevskaya, "X-ray Plane-Wave Topography Observation of the Phase Contrast from a Noncrystalline Object," *J. Phys. D: Appl. Phys.*, Vol. 28, 1995, 2314-2317.

Kotre, C. J. and I. P. Birch, "Phase Contrast Enhancement of X-Ray Mammography: a Design Study," *Phys. Med. Biol.*, Vol. 44, 1999, pp. 2853-2866.

Nugent, K. A., T. E. Gureyev, D. F. Cookson, D. Paganin and Z. Barnea, "Quantitative Phase Imaging Using Hard X-Rays," *Phys. Rev. Lett.*, Vol. 77, 1996, 2961-2964.

Raven, C., A. Snigirev, I. Snigireva, P. Spanne, A. Souvorov and V. Kohn, "Phase-Contrast Microtomography with Coherent High-Energy Synchrotron X-Rays," *Appl. Phys. Lett.*, Vol. 69, 1996, 1826-1828.

Rokhlin, S. I., B. Zoofan, and G. S. Frankel, "Microradiographic and Foil Penetration Methods for Quantification of Localized Corrosion," in *Nondestructive Materials Characterization with Application to Aerospace Materials,* Chapter 3, Springer-Verlag, N. G. H. Meyendorf, P. B. Nagy and S. I. Rokhlin, eds., 2003, pp. 58-112.

Snigirev, A., I. Snigireva, V. Kohn, S. Kuznetsov and I. Schelokov, "On the Possibilities of X-Ray Phase Contrast Microimaging by Coherent High-Energy Synchrotron Radiation," *Rev. Sci. Instrum.*, Vol. 66, 1995, pp.5486-5492.

Wilkins, S. W., T. E. Gureyev, D. Gao, A. Pogany and A. W. Stevenson, "Phase-contrast imaging using polychromatic hard X-rays," *Nature*, Vol. 384, 1996, pp.335-338.

Zoofan, B. and S. I. Rokhlin, "Microradiographic Detection of Corrosion Pitting", *Material Evaluation*, Vol. 56, No.2, 1998, pp.191-194.

Zoofan, B., J.-Y. Kim, S. I. Rokhlin, and G. S. Frankel, "Phase-Contrast X-ray Imaging for Nondestructive Evaluation of Materials", *Review of Progress in Quantitative Nondestructive Evaluation,* Vol. 23A, D. O. Thompson and D.E. Chimenti, eds., New York, Plenum Press, 2003, pp. 546-553.

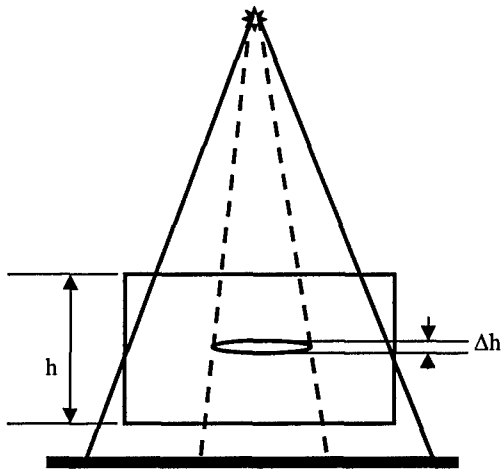

Figure 1- Formation of X-ray image based on X-ray absorption

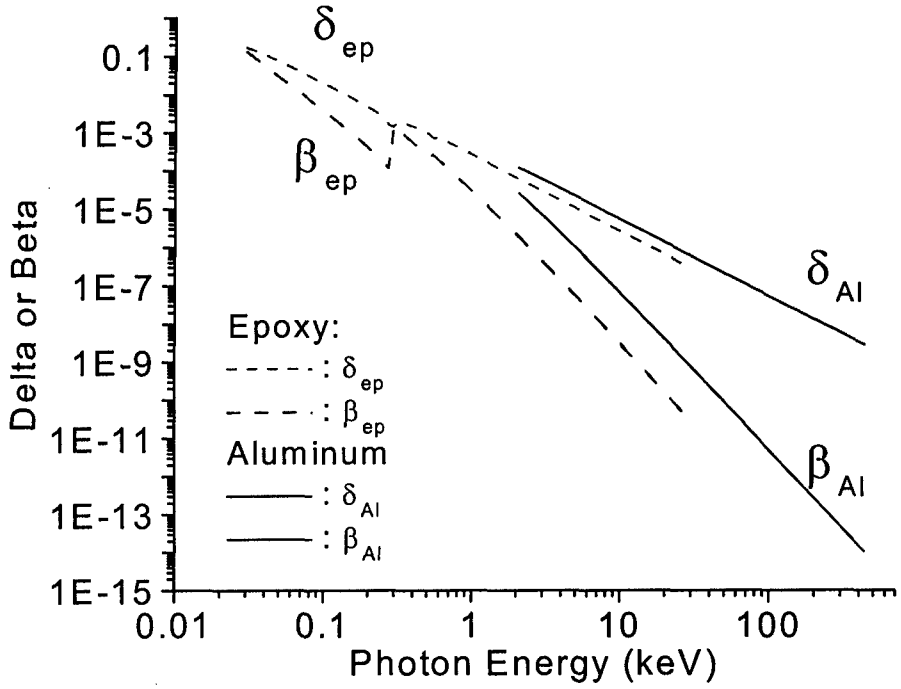

Figure 2- X-ray refractive indices for epoxyresin and aluminum

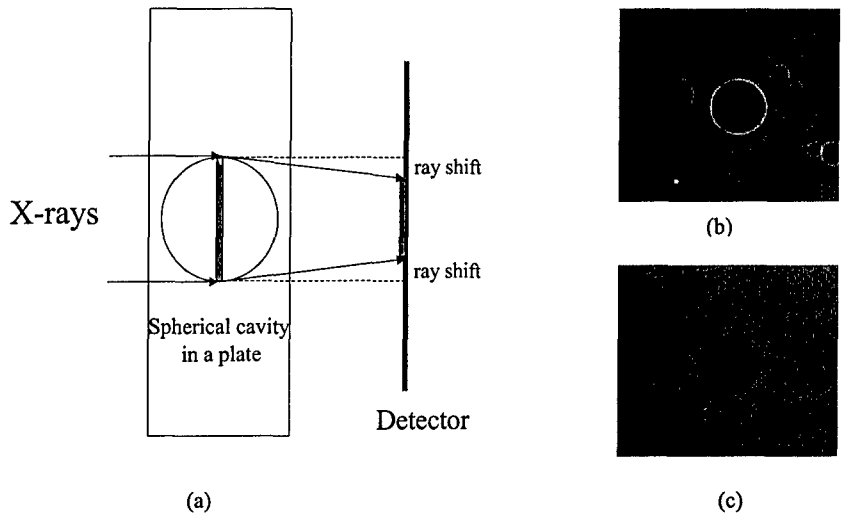

Figure 3- (a) Illustration of refraction ring formation for a spherical void (the void acts like an X-ray lens), (b) Experimental phase-contrast images of voids in epoxy resin with a micro-focus X-ray, (c) the image of the same sample and with the same exposure parameters while the X-ray tube was not in micro-focus mode

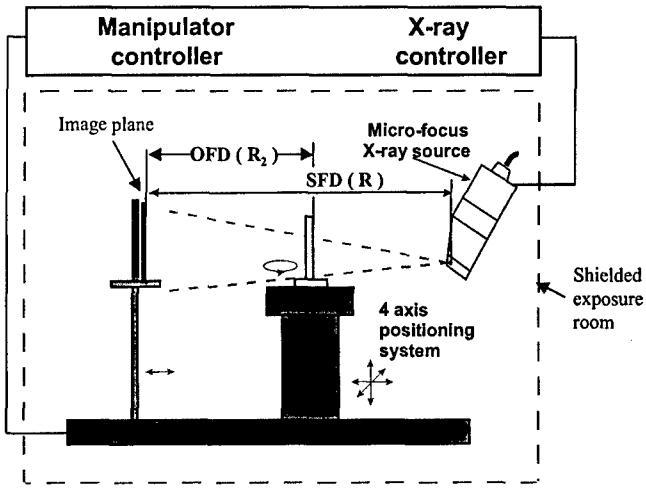

Figure 4- Schematic of the experimental microfocal system for in-line phase-contrast X-ray imaging

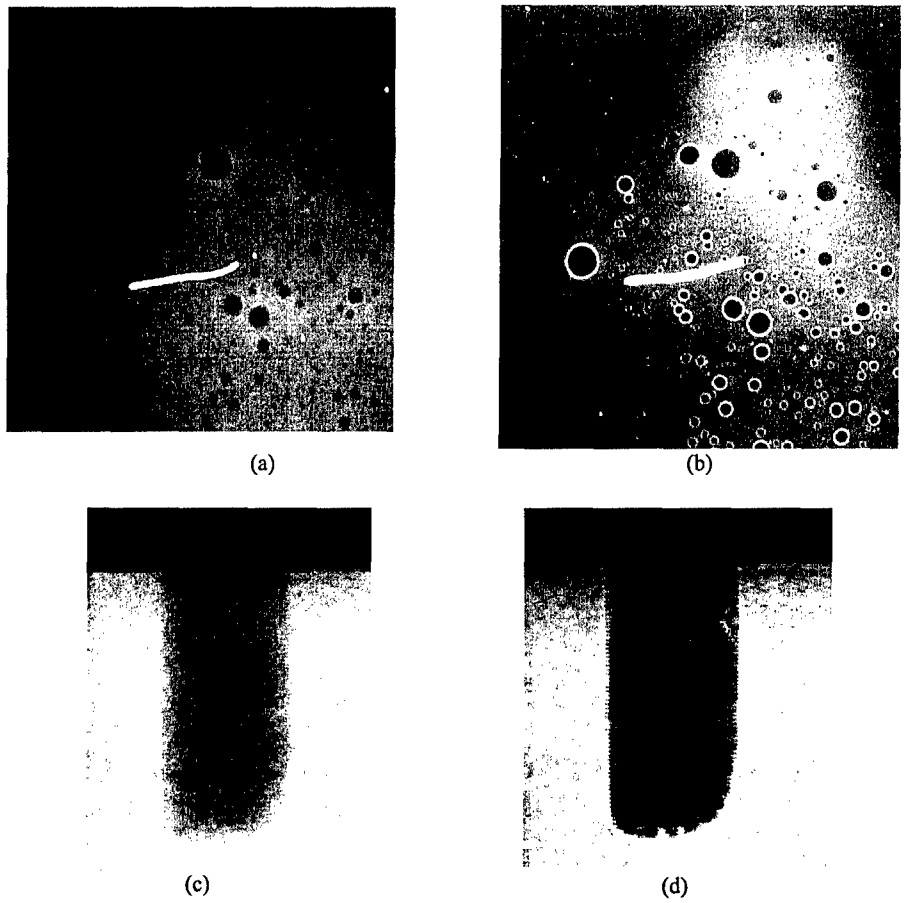

Figure 5 – Comparisons of absorption-contrast and phase-contrast images on the same type of radiographic film: (a) Absorption-contrast image produced with a short OFD (0.18 m) for epoxy resin; (b) phase-contrast image with long OFD (0.5 m) for epoxy resin; tube voltage=32 kV, and X-ray projection magnification=2.5X; (c) absorption-contrast image of a cylindrical pit in Al-2024 alloy produced with a short OFD (0.29 m); (d) phase-contrast image of the same sample with a long OFD (0.5 m); tube voltage=90 kV, projection magnification=10X

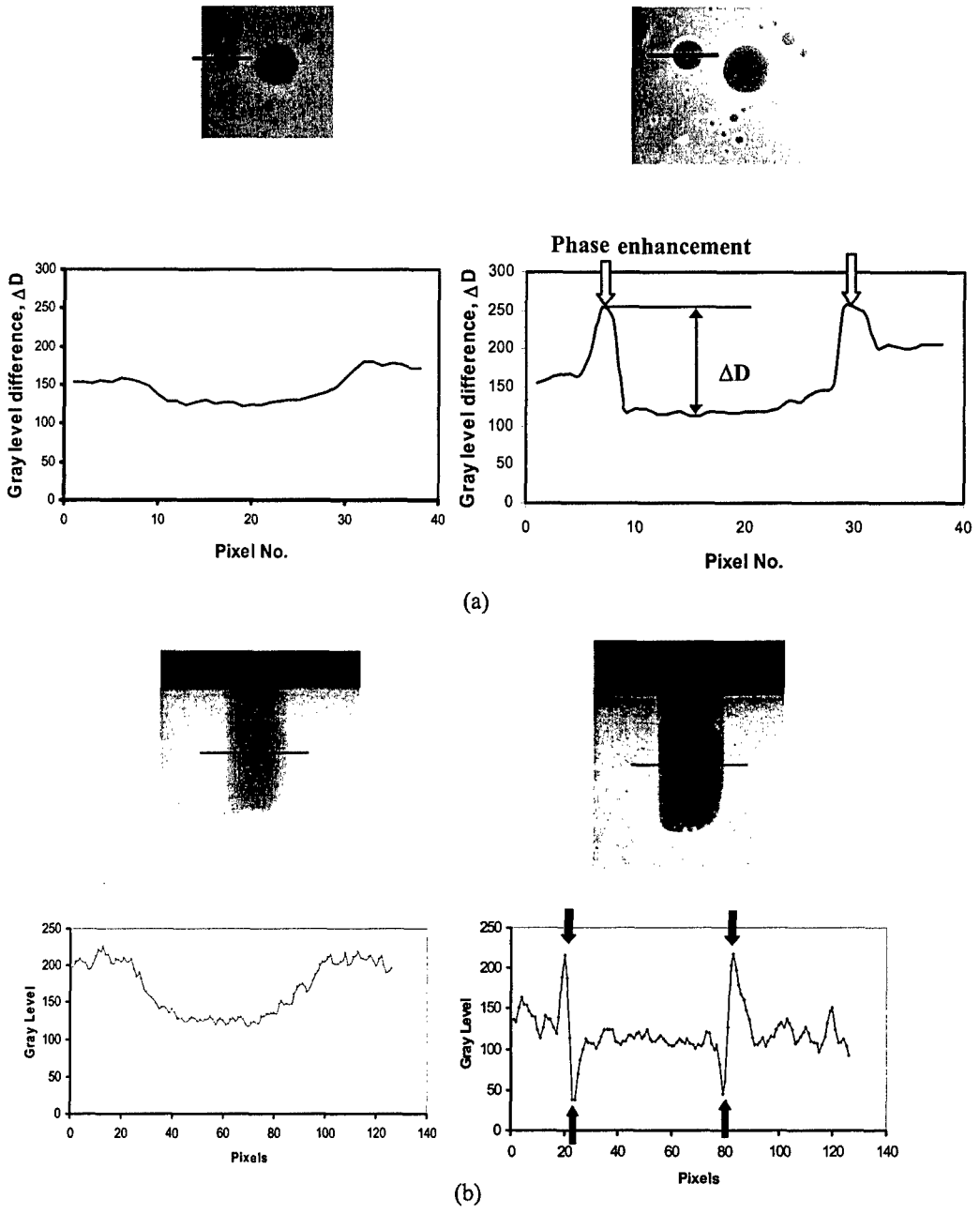

Figure 6- Comparison of absorption and phase-contrast images by line profiles across the digitized images (a) spherical pores in epoxy, (b) cylindrical pit in aluminum sample

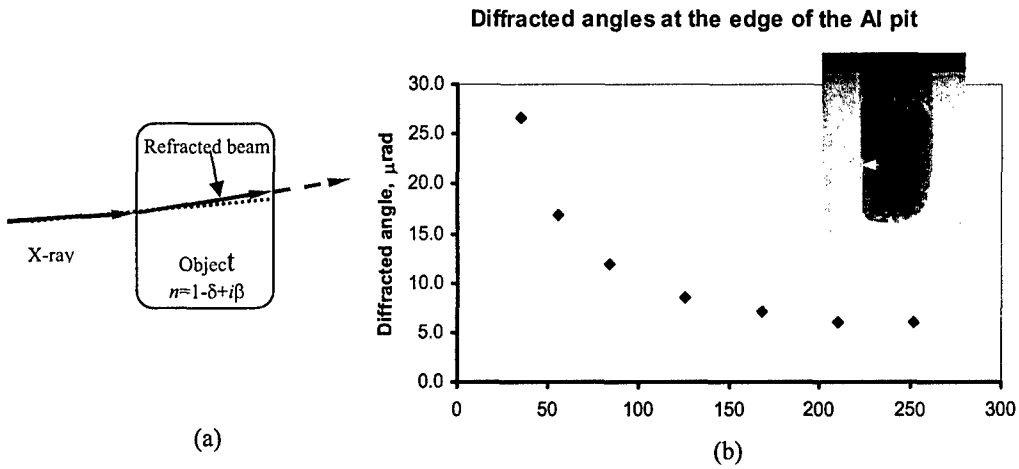

Figure 7- (a) Illustration of X-ray refraction effect (X-ray deviates in the sample from initial direction of propagation (dotted line)). (b) The refraction angle measured from fringe width versus X-ray energy. Data from the aluminum sample with an artificial pit.

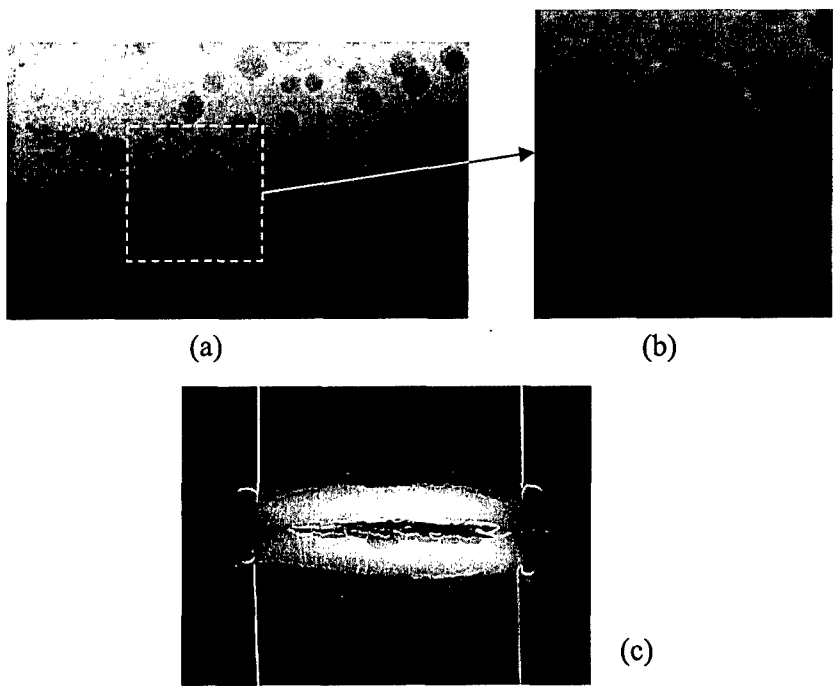

Figure 8- (a) Phase-contrast enhanced images of pores in the weld of an aluminum tube with 50 mm diameter and 2.5 mm thickness. (b) Magnified area indicated by dashed box in (a) obtained by optical magnification from the radiographic film. (c)Phase-contrast image of a hot-plate bonding of plastic, OFD: 1.5 m, exposure time: 21 minutes

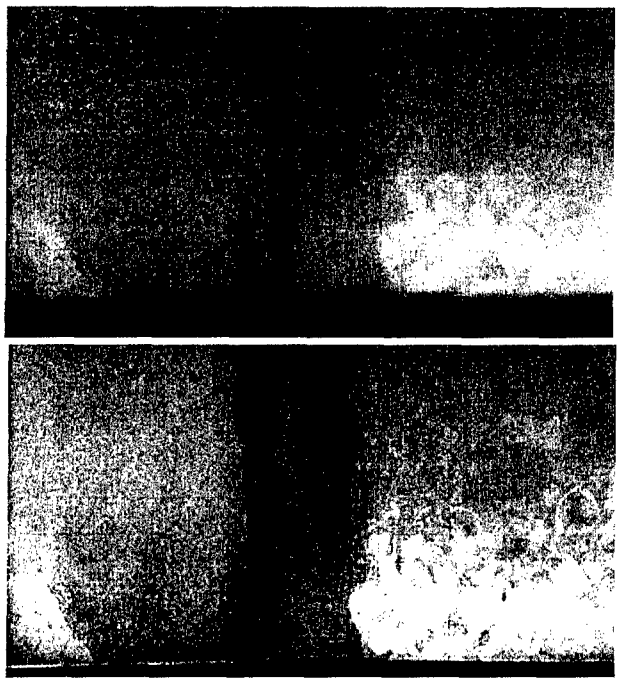

(a)

(b)

Figure 9- (a) Absorption-contrast image of a corroded 1mm thick aluminum sample, (b) phase-contrast image of the same sample

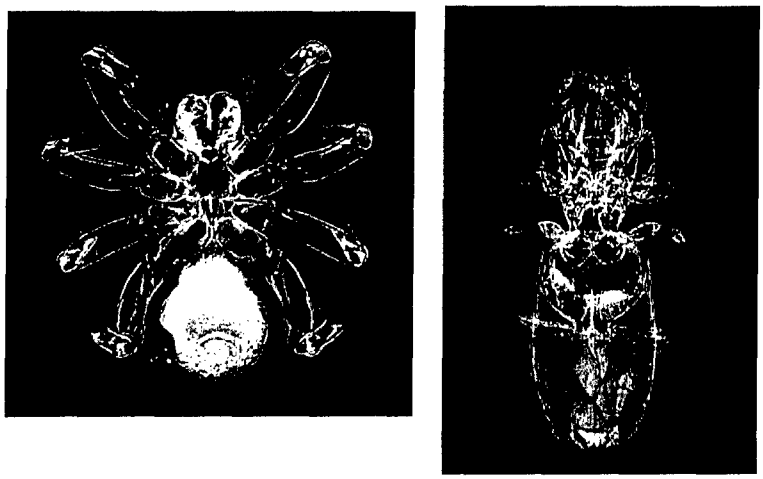

Figure 10- Phase-contrast images of insects (3X) showing soft tissues

Effects of Compressive Stress on Localized Corrosion in AA2024-T3 Alloy

Xiaodong Liu and G. S. Frankel
Fontana Corrosion Center, Department of Materials Science and Engineering
The Ohio State University, Columbus, OH 43210, USA

ABSTRACT

The effect of compressive stress on intergranular corrosion (IGC) of AA2024-T3 was studied under a constant load with simultaneous electrochemical measurement. A specially designed electrochemical cell was used to compress a pillar-shaped sample and control the potential at a value that promoted IGC. The extent of IGC was assessed by metallurgical cross sectional images. The effect of the compressive stress depended on the orientation of the stress relative to the elongated microstructure. Application of a compressive stress halfway to yield in the S or through-thickness direction significantly reduced the growth kinetics of IGC in the longitudinal direction, but did not eliminate it totally. The strain change during exposure was used to quantify the change in radius of the cylindrical sample as a function of time during IGC growth. The effect of compression on reducing IGC was also assessed by the current density measured during potentiodynamic and potentiostatic polarization. The effects of residual compressive stress on IGC were studied using samples treated by low plastic burnishing (LPB), which produces a surface layer with high residual compressive stress. The results depended on the plane of the treatment.

Keywords: Al alloys, intergranular corrosion, stress corrosion cracking, compressive stress, low plastic burnishing.

INTRODUCTION

Tensile stress has been conclusively recognized to be a necessary component for stress corrosion cracking (SCC) [1]. It is known that a crack tip under tensile stress is more active for SCC progression whereas in the compressive state the initiation and propagation of SCC can be mitigated and decelerated [2]. Compressive stress has been found to increase the incubation period for SCC of AA7075 ten times higher than under the tensile stress with the same K_I [3]. Application of a compressive stress modified electrochemical reactivity and inhibited pitting initiation [4]. More practically, the development of residual compressive stress at the surface of a part by shot peening is a standard preventive measure against SCC [5-8]. Recently, surface compressive residual stress layers have been found to retard pitting corrosion and corrosion fatigue in Al alloys[9, 10]. Low plasticity burnishing (LPB) is one new method that has been shown to reduce surface tensile stress and mitigate corrosion fatigue failure[11].

SCC of high strength Al alloys is almost always intergranular in nature. Intergranular corrosion (IGC) is a main form of localized corrosion in these alloys, and IGC can transition into intergranular SCC (IGSCC) under tensile stress[12, 13]. Tensile stress increases the penetration rate of IGC by an amount that depends on the orientation of the stress relative to the wrought microstructure[12, 13]. The effect of compressive stress on IGC growth has not been studied, but it is reasonable to expect that IGC would be stifled under compression. Compression is of interest because structures such as lower

airplane wings are under compression during on-field storage and are simultaneously exposed to atmospheric corrosion conditions.

The purpose of this paper is to investigate how compressive stress reduces IGC in AA2024-T3. The effect of the relationship between the direction of applied compressive stress and the microstructure orientation is studied. The effect of residual compressive stress is also investigated.

EXPERIMENTAL

Effects of applied elastic compressive stress on IGC

Cylindrical samples were machined from a 19 mm thick wrought AA2024-T3 plate (Cu 4.5%, Mg 1.45%, Mn 0.57%, Si 0.11%, Fe 0.25%, Zn 0.09%, Ti 0.02%, Cr 0.01%, and other elements total 0.05% max) purchased from Metalmen Sales, Inc. Figure 1a shows the microstructure of the wrought plate. The samples were 18 mm long and 8 mm in diameter to prevent buckling. A newly developed electrochemical cell was used to investigate the influence of compressive stress on IGC, figure 2. The cell was a piece of Teflon with through-holes drilled at right angles. The height of the cell was less than the length of the sample so that the ends of the sample protruded through the cell and physically contacted the mechanical frame fixture. The sample was sealed into the cell using Miccrostop lacquer and the exposed area was 3 cm^2. A constant load was applied either using weights hanging from a cantilevered arm in a creep rig or using a standard hydraulic Instron mechanical testing machine. The applied load was equivalent to half of the yield strength in compression. Cylindrical samples with different axial orientations relative to the rolling direction, and thus having different orientations of the compressive load, were tested: longitudinal (L or rolling direction), long transverse (T) and short transverse (S or plate through-thickness) directions, Figure 1b. The outer surface of the cylinder was exposed to the solution and developed IGC upon application of a constant potential of -580 mV SCE, which is in a range that will promote IGC. Because the samples were cylindrical, the exposed surface included every orientation perpendicular to the stress axis. For instance, IGC growth in the longitudinal (L or rolling direction) and long transverse (T) directions on S planes was possible for the S samples. Cross sectional optical microscopy was used to characterize the depth of IGC in the samples after the experiments.

Because of the small volume of the cell, the 1.0 M NaCl solution was circulated continuously from a reservoir through the cell past the sample. A Pt counter electrode and saturated calomel reference electrode (SCE) were located close to the sample. The circulation rate was about 55 ml/min. After applying the load and letting the system stabilize at a constant strain, the samples were potentiostatically polarized at –580 mV SCE, which is sufficient to initiate and grow IGC. The anodic current was recorded during the potentiostatic experiment.

The strain change during the experiment was measured by a 1 inch strain gauge extensometer or linear variable differential transformer (LVDT). Since the extensometer gauge length was greater than the sample length, SS416 stainless steel shims were used between the ends of the sample and the platens of the Instron testing machine. As IGC penetrated into the sample, the load bearing area decreased resulting in an increase in stress at constant load and thus an increase in strain. The IGC growth results in a change in effective radius as a function of time, $\Delta r_{(t)} = r_o - r(t)$, where r_o is the original radius of

the cylindrical sample, and r(t) is the effective radius as a function of time. As described below, $\Delta r(t)$ can be determined by the length change of the cylindrical sample, $\Delta l(t)$, which is the displacement measured by the extensometer or LVDT.

Effects of residual compressive stress on IGC

Residual compressive stress was developed by low plasticity burnishing (LPB), performed at LAMBDA Research Inc. LPB produces a layer of compressive residual stress of high magnitude and depth with minimal cold work by rolling a smooth ball across the surface under a normal force sufficient to plastically deform the surface of the material[10]. Hertzian loading creates a layer of compressive residual stress to a depth exceeding 1 mm[11].

Surfaces with two different orientations were treated by LPB. For S samples, the S or short transverse face was treated by LPB. To eliminate complications associated with microstructural differences near the surface of the as-received wrought plate, the S samples, with dimensions of 25.4 x 50.8 x 8.5 mm, were cut from the middle of the plate. The direction of the LPB treatment was either perpendicular to or along the rolling direction for the treatment of S surfaces. For L samples, the L or longitudinal face was rolled by LPB in the short transverse direction. Prior to applying LPB, all samples were polished to 6 μm SiC papers in ethanol. After LPB treatment, the residual stress and percent cold work profiles were determined using X-ray diffraction peak broadening [11]. Compressive residual stresses were found within a depth of 800 μm from the LPB-treated[14].

RESULTS AND DISCUSSION

Effects of applied compressive stress on corrosion

Figure 3 shows compressive stress-strain curves for AA2024-T3 cylindrical samples having axial orientations in the L, T and S directions. An average Young's modulus, *E,* of 72.4 GPa was exhibited. A load of 1020 kg was chosen to apply to the samples, as this represents a stress about halfway to the yield stress, which was found to be about 40 kg/mm^2.

Cylindrical samples subjected to a constant compressive load and exposed to 1 M NaCl at -580 mV SCE for different times were analyzed to study the growth kinetics of IGC under compression. Figure 4 shows optical microscopy images of axial sections of a compressed S sample after 10 h of polarization. The stress is applied vertically in these images and the perpendicular axial sections show IGC growth in the L and T directions. The primary form of corrosion is seen to be IGC. These images indicate that the depth of IGC attack is somewhat greater in the L direction compared to that in the T direction. The lengths of many individual IGC sites was measured and are shown in Figure 5 for the L and T direction, along with foil penetration data showing, for comparison, the rate of IGC growth in the L and T directions for unstressed samples[15]. The foil penetration experiment measures the time for the first site to penetrate the tested foil, so only the fastest growing site is sensed[16, 17 18]. In contrast, the sectioning method determines the depth of IGC on only the sectioned planes, so it is likely that the fastest growing site in the sample was not detected. Moreover, the measurements depend on the resolution of the cross-sectional images. Nonetheless, the data in figure 5 indicate that the IGC growth rates in the L and T directions measured using the compressed S sample are considerably

slower than IGC measured during foil penetration experiments on unstressed samples. Figure 6 shows sections of S samples after 20 or 23 h exposure in 1 M NaCl at -560 mV SCE with or without simultaneous application of compressive stress. The sections are oriented to show IGC growth in the L direction. Both the depth and density of IGC attack is seen to be less in the sample that was stressed in compression during exposure. So compression in the S or through thickness direction, which is across the principal plane of IGC attack, the L-T plane, significantly decreases the rate of IGC on that plane. This is expected as the stress should act to close up the IGC sites. Interestingly, the application of compressive stress half the magnitude of the yield stress does not completely eliminate IGC, which can continue under compressive stress at a reduced rate.

Figure 7 shows optical cross-sectional images for a compressed L sample after polarization for 10h. Longitudinal rather than axial cross sections are used for analysis of IGC in this orientation. Figure 7a is a macro section of the tested sample, which shows the material loss primarily aligning along the T or long transverse direction. Higher magnification cross sections for the L sample given in Figure 7b-c show that the primary form of corrosion is IGC along the T direction. The lengths of IGC sites growing in the T direction were measured from several cross sections. Figure 8 shows the data along with data generated from foil penetration experiments on unstressed samples for comparison[15]. Similar to samples with stress in the S direction, the growth of IGC in the T direction is lower in the presence of compressive stress in the L direction compared to unstressed samples. Compressive stress decreases the rate of IGC growth in the T direction by a factor of about 2.

Cross sections of a compressed T sample after 10 h of exposure in 1 M NaCl at -580 mV SEC are given in Figure 9. Longitudinal sections are also appropriate for viewing IGC in a sample of this orientation where it grows primarily in the L direction. Figure 10 shows the depth of IGC in the L direction along with the data from foil penetration experiments on unstressed L samples[15]. The decrease in IGC growth rate in the L direction for the compressed T sample relative to the stress-free sample is much less than the effect of compressive stress in the other orientations. For both this orientation and the compressed L sample, the stress direction is parallel rather than perpendicular to the primary grain boundary orientation along the elongated grains on the T-L plane. Therefore, the stress does not act to close down the IGC sites. In fact, the Poisson effect should create a tensile stress in the perpendicular S direction, and the application of very small tensile stresses in the S direction has been shown to greatly enhance the rate of IGC growth in the L direction[19]. So it is perhaps not surprising that the effect of compressive stress is smaller for the T sample compared to the S sample. However, a similar Poisson effect would be expected for the compressed L sample, which should also create a tensile stress in the S direction. As shown in figure 8, IGC growth in the T direction is significantly reduced by the application of compression in the L direction. The difference in behavior of these two cases is not understood, but might be related to the grain dimensions in the different directions; it has previously been reported that the average grain size in this plate is 50, 300 and 2000 μm in the S, T, and L directions, respectively[20].

Measurement of IGC growth kinetics using strain change:

During the constant load tests, the compressive strain was found to increase with time even though the applied stress was in the middle of the elastic range. From the basic principles of elasticity:

$$\varepsilon = \frac{\sigma}{E} = \frac{F}{EA} \qquad (1)$$

where F is the elastic load, σ is elastic stress, ε is elastic strain, E is the Young's modulus of the material, and A is the cross section of the cylindrical sample. Consider an S sample with IGC growing inward from the outer surface along the L and T directions. The effective radius of the round cross section of the cylindrical sample decreases as the corrosion process proceeds. Assuming that the IGC attack is uniform along the length of the exposed surface of the sample leaving an unattacked cylindrical core with effective radius $r(t)$:

$$\varepsilon = \frac{F}{E\pi r(t)^2} \qquad (2)$$

Engineering strain is defined as $\varepsilon = \Delta l/l_0$, where Δl is the change in length along the compressive stress direction and l_0 is the original length. Furthermore, the effective radius of the unattacked core region can be defined as $r(t) = r_0 - \Delta r(t)$, where r_0 is the original radius and $\Delta r(t)$ is the effective change in radius or depth of IGC attack. Substituting:

$$\frac{\Delta l}{l_0} = \frac{F}{E\pi(r_0 - \Delta r(t))^2} \qquad (3)$$

Solving for $\Delta r(t)$, the change in radius or depth of IGC can be determined from the strain or length change of the sample with time:

$$\Delta r(t) = r_0 - \sqrt{\frac{Fl_0}{E\pi\Delta l(t)}} \qquad (8)$$

In summary, as IGC proceeds inwards from the surface of an S sample along the L and T directions, the load-bearing cross section decreases, the stress increases in the elastic region, and the strain increases, which can be measured by a strain gauge. So the change in strain with time can be converted to a rate of IGC growth.

Figure 11 shows the measured strain and calculated radius change with time for a compressed S sample in 1 M NaCl at -580 mV SCE over 15 h. Clearly, the measured strain and thus $\Delta r(t)$ increased with time. Figure 12 compares the results of radius change with other measures of IGC growth. The filled diamonds are the same data shown in figure 11, but indicated here as IGC depth. Shown as filled circles are the radius changes. They line up with an extrapolation of the data from the first experiment. The depths of individual IGC sites measured from sections of different experiments are shown as open squares. The IGC depths determined by sectioning and by strain change, which were generated independently, correspond quite well and overlie each other, suggesting that both approaches provide accurate assessments of the same phenomenon. Figure 12 also contains the data from foil penetration experiments on unstressed L samples showing the large effect of compression in the S direction on IGC growth in the L direction.

Potentiodynamic and potentiostatic polarization under compressive stress

The anodic polarization curves for cylindrical S samples with and without compressive stress are shown in Figure 13. For these cylindrical S samples, the exposed sidewall area is a combination of L and T surfaces. The polarization curve for a flat, unstressed L sample is also shown in Figure 13 for comparison. The open circuit potential (OCP) measured for the unstressed flat L sample was lower than the others because that measurement was made in deaerated solution, whereas the measurements on the cylindrical samples were in aerated solution. The unstressed flat L sample exhibited two breakdown potentials. The lower breakdown potential in AA3034-T3 has been attributed to transient S phase attack and the higher breakdown potential to stable IGC and pitting[21]. Since the attack associated with the lower breakdown is transient in nature, it is not seen in aerated solutions. The current density of the unstressed S compression sample (which has L and S exposed sides) in aerated solution was in the same range as that of that for the unstressed flat L sample in deaerated solution near the second breakdown potential, which indicates that the dissolution rates were similar for unstressed samples in both aerated and deaerated solutions. Compared to the unstressed S compression sample, the OCP of the compressed sample was higher, and the anodic current density was lower by as much as a factor of 10.

In order to understand better the effects of compressive stress on IGC, AA2024-T3 S samples were potentiostatically polarized at –580 mV SCE, which is slightly above the second breakdown potential. For the stressed and unstressed samples, the current density increased and leveled off after a few hours near 15 and 90 $\mu A/cm^2$, respectively, Figure 14. These results are consistent with the cross-sections and provide further evidence for how applied compressive stress decreases the number of IGC initiation sites retards IGC propagation.

Others have shown that SCC can still occur in mild steel and stainless steel under compressive stress [22, 23]. It was suggested that microscopic tensile stress exists in front of the crack tip due to the inhomogeneity of the material. The AA2024-T3 studied in the present investigation is very susceptible to IGC under the test conditions. It is possible that corrosion products cause wedge-opening effects, which are reduced, but not eliminated, by the application of a compressive stress.

Effects of residual compressive stress on IGC

The effects of applied compressive stress on IGC are difficult to investigate in situ because of the physical constraints of applying a compressive load. The effects of compression can more-easily be studied by using residual stress. Residual compressive stress, such as developed by methods like shot peening, is commonly used on surfaces of engineering structures to prevent corrosion fatigue [8, 9]. Like shot peening, low plastic burnishing (LPB) imparts a high-magnitude residual compressive stress on the surface of a sample with minimal cold work [11]. In this study, LPB was performed on flat surfaces of AA2024-T3 with faces perpendicular to the S or L direction. As stated in the experimental section, x-ray diffraction analysis indicated that the samples had a compressive stress region extending 800 μm into the surface with maximum values of compressive stress and cold work of 50 ksi and 9%, respectively[14]. Figure 15 shows cross-sectional optical micrographs of the LPB treated samples. It is difficult to

distinguish changes in microstructure at the treated surfaces, which are the top edges of each image.

The LPB treated samples were potentiostatically polarized at –580mV SCE in 1 M NaCl for 12 h. Figure 16 show cross sectional micrographs of exposed S samples with and without prior LPB treatment. The cross-sectioning was performed to expose L sections. The untreated S sample in Figure 16a exhibited an interconnected network of IGC, with some grains lifting off, perhaps by exfoliation. The sample with prior LPB treatment, shown Figure 16b, did note exhibit the IGC network. It appears that the surface lost material almost to a uniform depth. The rate of exfoliation increases with applied compressive stress[24]. So it seems that the extent of IGC is less but exfoliation is greater. The depth of attack for both samples exhibited considerable variability, but the mean depth for 22 points along the LPB-treated sample, 193 ± 31 μm, was significantly less than that for the untreated sample, 141 ± 42 μm.

Figure 17 shows potentiodynamic polarization curves in deaerated 1 M NaCl for S surfaces with and without LPB treatment. The LPB treatment decreased the passive current density by a factor of about 3. Both curves exhibit passivation and breakdown potential in the polarization. Moreover, the treated sample exhibited only one breakdown potential; the current increased at a value between the breakdown potentials for the untreated sample, and the currents merged at potentials above the second breakdown. The phenomenon associated with the first breakdown in AA2024-T3, transient dissolution of S phase particles, apparently did not take place on the LPB treated sample.

Figure 18 shows cross-sectional micrographs of L surfaces following potentiostatic polarization at –580 mV SCE in 1 M NaCl for 12 h. The LPB treatment was applied by rolling in the S direction. The sample without LPB treatment exhibits IGC growing straight down the L direction, whereas the grains near surface of the LPB treated sample are bent in different directions. The depth of attack in the two samples was similar. The potentiodynamic polarization curves for the two L surfaces were also very similar, Figure 19. Both exhibit two breakdown potentials, but the second breakdown potential was lower for the LPB treated sample, and the current was higher just above the second breakdown. These results are in contrast to the strong benefits of applied compressive stress on L surfaces described above, and suggest that there can be a complex interaction between the stress direction and microstructure orientation.

The effects of compressive stress on intergranular corrosion in AA 2024-T3 are associated with the effect of compression on intergranular SCC. The initiation and propagation of IGC in Al alloys have been attributed to film rupture and anodic dissolution, or hydrogen embrittlement [25-27]. In the current study, the application of compressive stress normal to the orientated IGC significantly reduced the number of active sites and retarded the growth rate. Relative to applied tensile stress, compression makes film rupture more difficult. Moreover, the compressive vicinity at crack tip may delay the local hydrogen entry and mitigate the possible hydrogen embrittlement[28, 29]. However, the compressive stress did not eliminate IGC. The magnitude of compression studied was insufficient to fully close the intergranular sites. Dissolution could proceed under the influence of the local electrochemical conditions (grain boundary composition, potential, and electrolyte composition). The same was found with residual compressive stress. Furthermore, the orientation of the stress to the elongated microstructure is critical

CONCLUSIONS

1. The application of compressive stress at a level halfway to yield significantly reduced the growth kinetics of IGC in the perpendicular direction, but did not eliminate it totally.
2. The extent of the effect of applied compressive stress depended on the relationship between the direction of the applied stress and to microstructure orientation.
3. The change in strain was successfully used as a measure of IGC growth under applied compressive load.
4. Electrochemical measurements supported the findings of the beneficial effects of compression on localized corrosion.
5. Residual compressive stress imparted by the low plastic burnishing (LPB) technique improved the IGC resistance for certain conditions, but was not as effective as an applied compressive stress.

ACKNOWLEDGEMENTS

This work was supported by the United States Air Force Office of Scientific Research through Grant No. F49620-02-1-0148. The contract monitor has been Lt. Col. Paul Trulove and is now Major Jennifer Gresham.

REFERENCES

1 M.O. Speidel, *Metallurgical and Meterials Transactions A,* **6A,** 631 (1975).
2 R.H. Jones, *Stress Corrosion Cracking of Aluminum Alloys*, in Stress- Corrosion Cracking Materials Performance and Evaluation, R. H. Jones ed, (ASM International), (1992).
3 W.-Y. Chu, C.-M. Hsiao, and J.-W. Wang, *Metallurgical Transactions A,* **16A,** 1663 (1985).
4 J. Hahm and S.J. Sibener, *Applied Surface Science,* **161,** 375 (2000).
5 R.d. Los and R. Eduardo, *Proceedings of the International Conference on Shot Peening, 8th, Garmisch-Partenkirchen, Germany, Sept. 16-20, 2002 ,,* (2002).
6 G.A. Hawkes, *British Corrosion Journal,* **3,** 258 (1968).
7 T.Ford, *Aircraft Engineering and Aerospace Technology,* **71,** 249 (1999).
8 W.-T. Tsai, C.-S. Chang, and J.-T. Lee, *Corrosion,* **50,** 98 (1994).
9 C.P. Chan, T.M. Yue, and H.C. Man, *J. of Mat. Sci.,* **38,** 2689 (2003).
10 P.S. Prevey and J. Cammett, *Journal of Materials Engineering and Performance,* **10,** 548 (2001).
11 P.S. Prevey and J. T. Cammett, *Int. J Fatigure,* **26,** 975 (2004).
12 V.S. Sinyavskii and A.M. Semenov, *Protection of Metals,* **38,** 132 (2002).
13 X. Liu, G.S. Frankel, B. Zoofan, and S.I. Rokhlin, *Corrosion Science,* **46,** 405 (2004).
14 P. Prevey, Lambda Research, personal communication.
15 W. Zhang and G.S. Frankel, *Electrochemical and Solid-State Letters,* **3,** 268 (2000).
16 F. Hunkeler and H. Bohni, *Corrosion,* **37,** 645 (1981).
17 F. Hunkeler and H. Bohni, *Corrosion,* **40,** 534 (1984).
18 W. Zhang and G.S. Frankel, *Electrochimica Acta,* **48,** 1193 (2003).

19 X. Liu, G.S. Frankel, B. Zoofan, and S.I. Rokhlin, *Submitted to Corrosion,* (2005).
20 W. Zhang, S. Ruan, D.A. Wolfe, and G.S. Frankel, *Corrosion Science,* **45,** 353 (2003).
21 W. Zhang and G.S. Frankel, *J. Electrochem. Soc.,* **149,** B510 (2002).
22 W.-Y. Chu, J. Yao, and C.-M. Hsiao, *Corrosion,* **40,** 302 (1984).
23 W.-Y. Chu, R.-T. Ma, and C.-M. Hsiao, *Corrosion,* **43,** 251 (1987).
24 X. Zhao, G.S. Frankel, B. Zoofan, and S.I. Rokhlin, *Corrosion,* **59,** 1012 (2003).
25 T.D. Burleigh, *Corrosion,* **47,** 89 (1991).
26 D.A. Hardwick, M. Taheri, A.W. Thompson, and I.M. Bernstein, *Metallurgical and Meterials Transactions A,* **13A,** 235 (1982).
27 F. Zeides and I. Roman, *MATERIALS SCIENCE AND ENGINEERING,* **A125,** 21 (1990).
28 J. Toribio, *Construction and Building Materials,* **12,** 283 (1998).
29 J. Toribio and A.M. Lancha, *Construction and Building Materials,* **10,** 501 (1996).

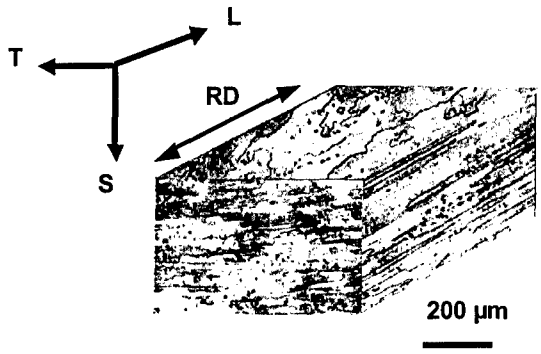

(a)

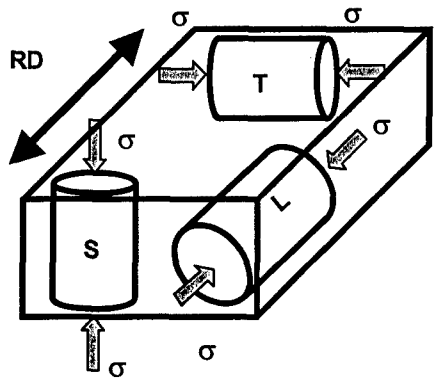

(b)

Figure 1. Microstructure and orienations of wrought plate AA2024-T3 (a) microstructure (b) notation and configuration of tested sheet sample.

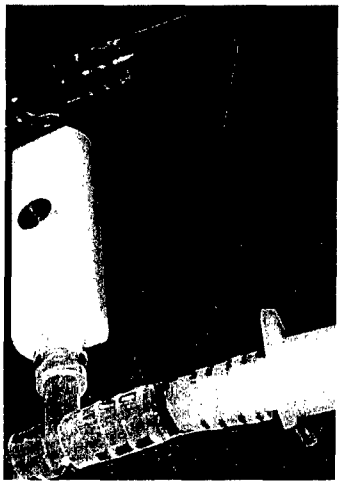

Figure 2. Specially designed cell for electrochemical control of compression sample, with sample inserted.

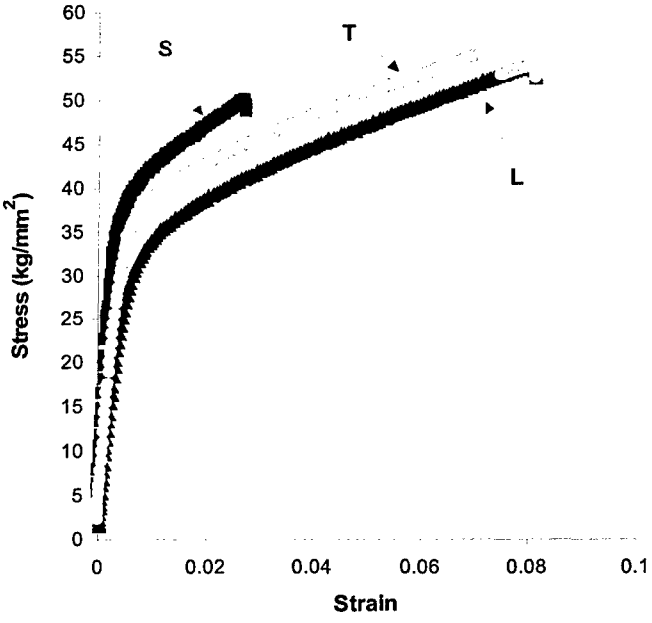

Figure 3. Stress-strain curve in compression for AA2024-T3 in three perpendicular directions.

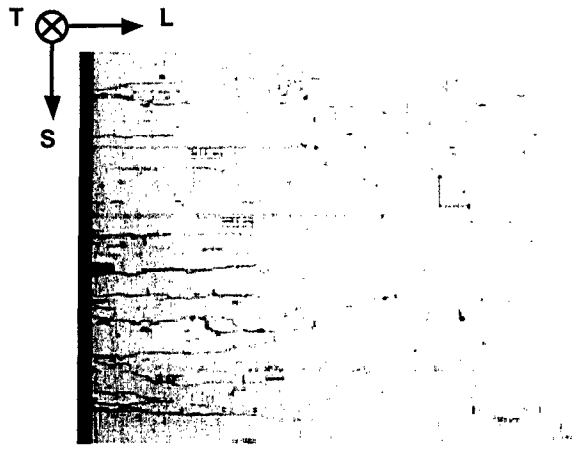

(a)

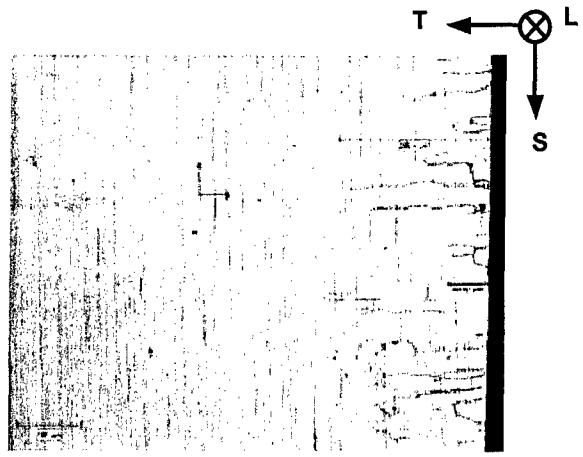

(b)

Figure 4. Optical microscopy images of axial sections of compressed S sample after 10 h in 1 M NaCl at –580 mV SCE . Compressive load was applied in S direction from top to bottom. (a) section showing IGC growth in the L direction (b) section showing IGC growth in T direction.

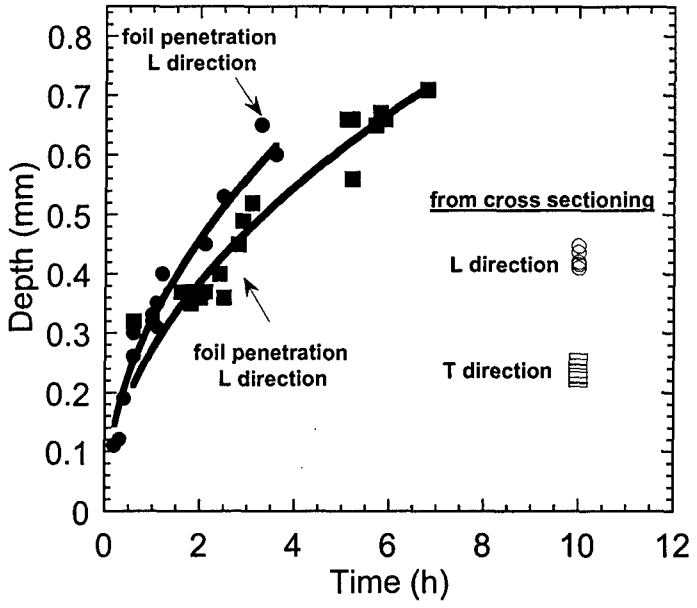

Figure 5. Length of IGC growth in L and T direction in compressed S sample after 10 h. Data from foil penetration experiments on unstressed L and T samples shown for comparison[15].

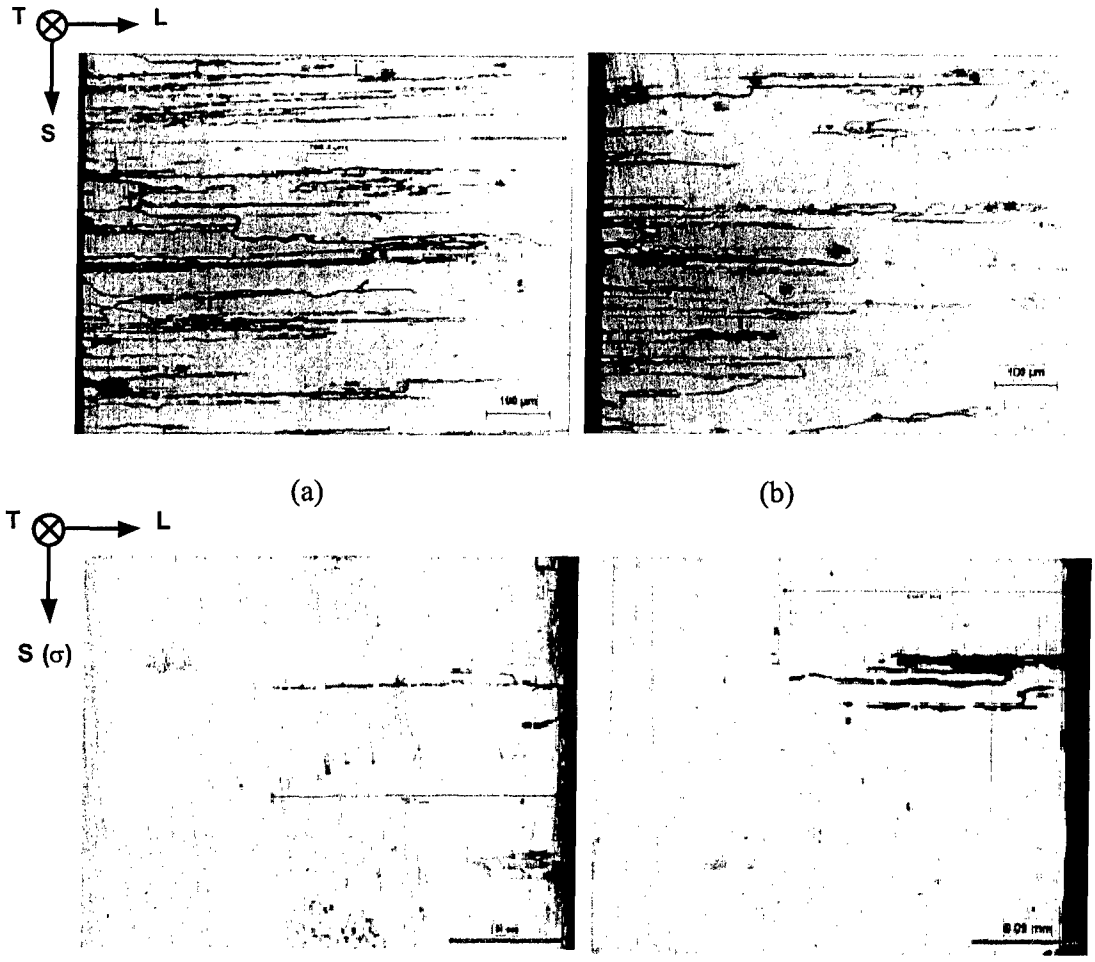

Figure 6. Comparison of cross sectional images S samples with and without S compressive load in 1 M NaCl at –580 mV SCE. Compressive load was applied in S direction from top to bottom. (a) and (b) unstressed S sample for 20 h; (c) and (d) S sample subjected to compressive load for 23h.

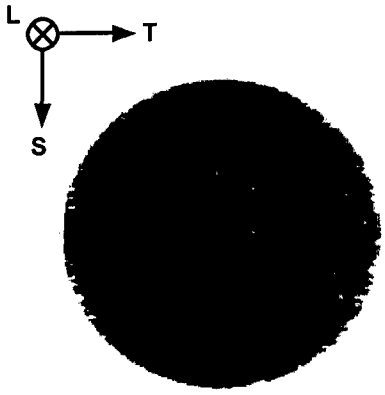

(a)

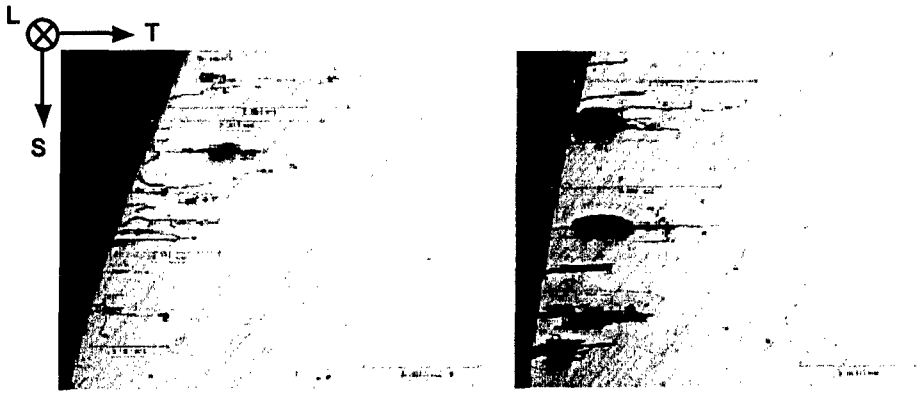

(b) (c)

Figure 7. Optical microscopy images of longitudinal sections of compressed L sample after 10 h in 1 M NaCl at –580 mV SCE . Compressive load was applied in L direction perpendicular to the page. (a) macro section showing orientation of IGC, (b and c) two higher magnification images showing IGC growth in the T direction.

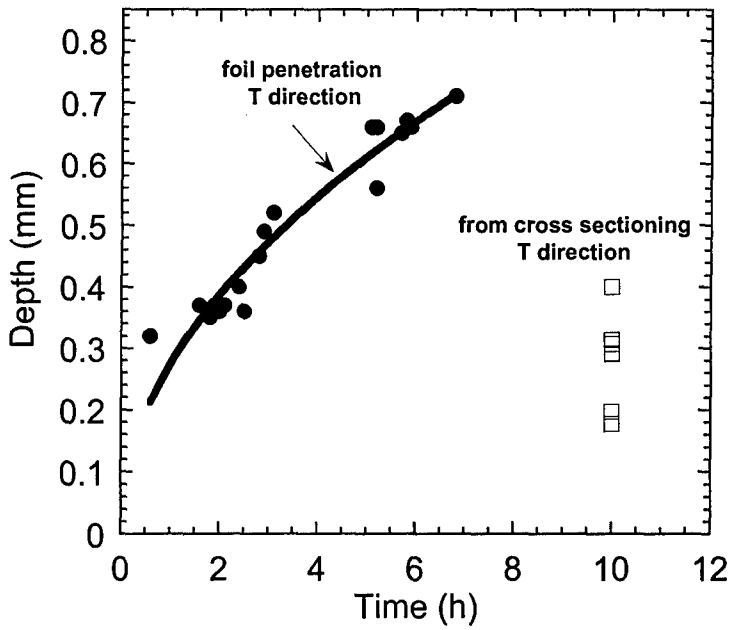

Figure 8. Length of IGC growth in T direction in compressed L sample after 10 h. Data from foil penetration experiments on unstressed T samples shown for comparison[15].

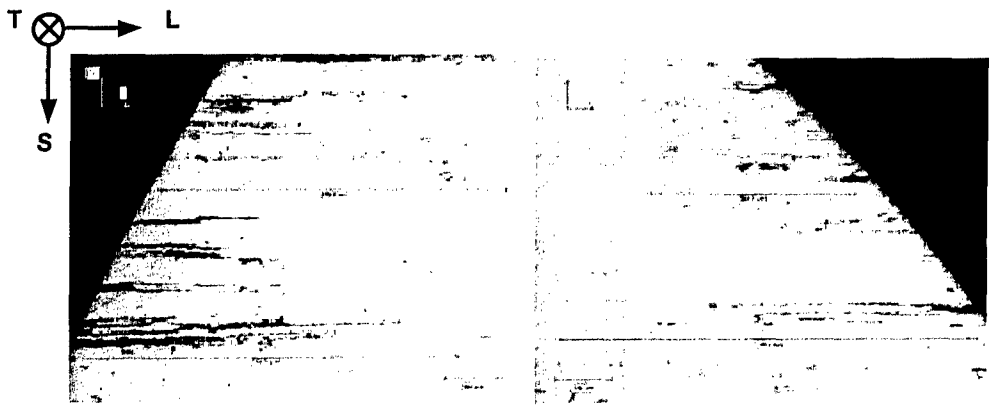

(a) (b)

Figure 9. Optical microscopy images of longitudinal sections of compressed T sample after 10 h in 1 M NaCl at –580 mV SCE . Compressive load was applied in T direction perpendicular to the page. (a and c) two images showing IGC growth in the L direction.

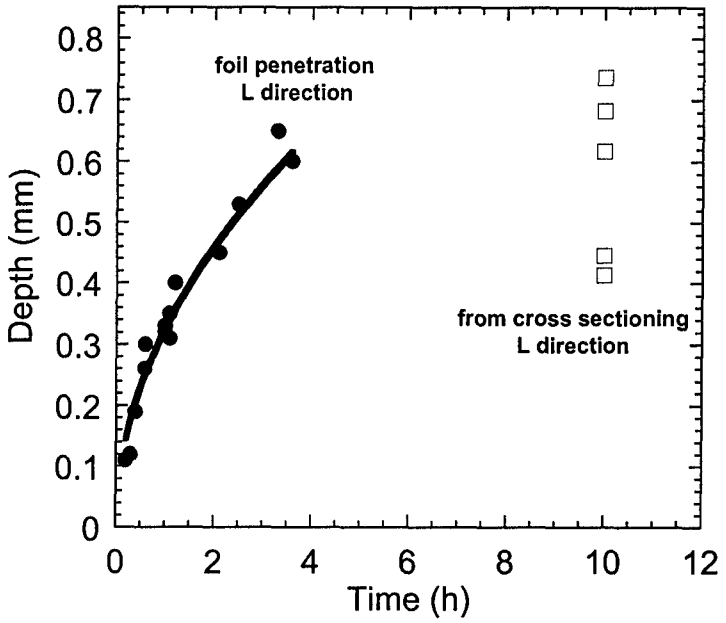

Figure 10. Length of IGC growth in L direction in compressed T sample after 10 h shown as open squares. Data from foil penetration experiments on unstressed L samples shown for comparison[15].

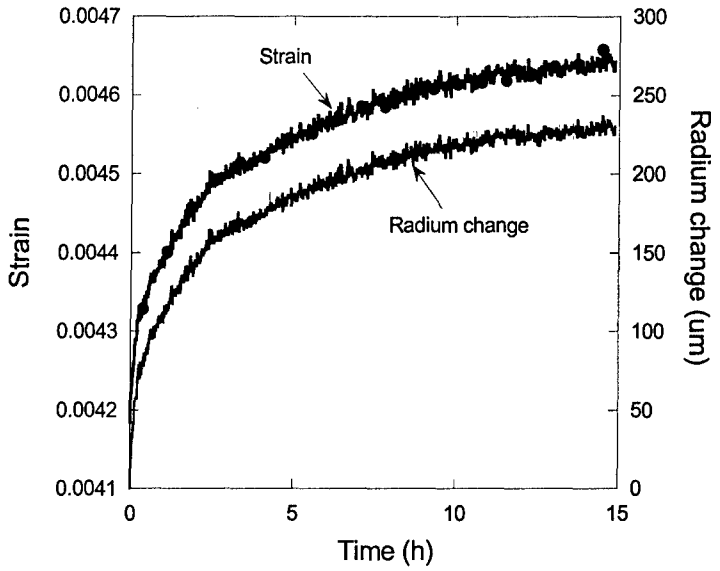

Figure 11. Strain transient and calculated radius change with time for compressed S sample in 1 M NaCl at –580 mV SCE.

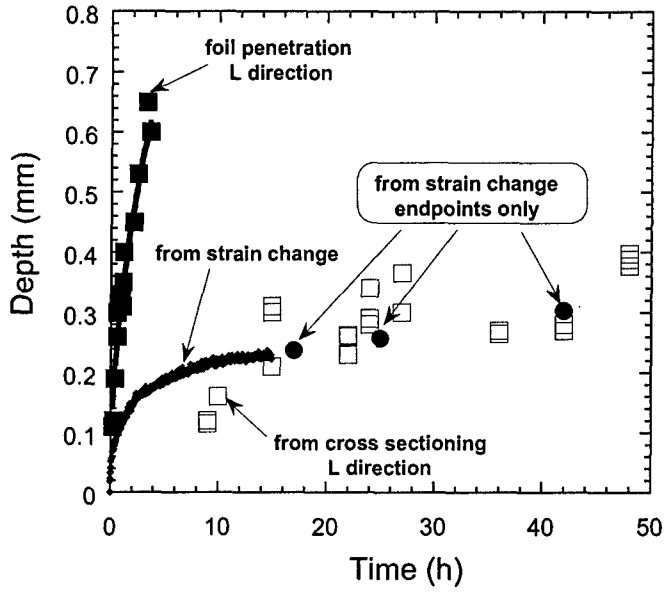

Figure 12. Depth of IGC in L direction for AA2024-T3 in 1 M NaCl at -580 mV SCE. Diamonds are calculated depth from strain change of S compression sample. Open circles are also from strain change, but are end points of separate experiments. Open squares are from cross sectioning S compression samples. Filled squares are unstressed foil penetration data for AA2024-T3 samples in L direction.

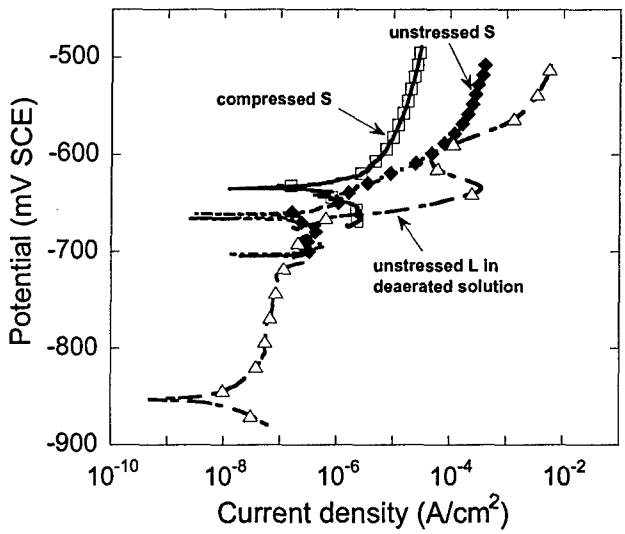

Figure 13. Anodic polarization curves of AA2024-T3 in 1 M NaCl at 0.1 mV/s. Squares are from S cylindrical sample under compression in aerated solution; diamonds are from S cylindrical sample in compression cell but with no applied stress, in aerated solution; triangles are from flat unstressed L sample in deaerated solution.

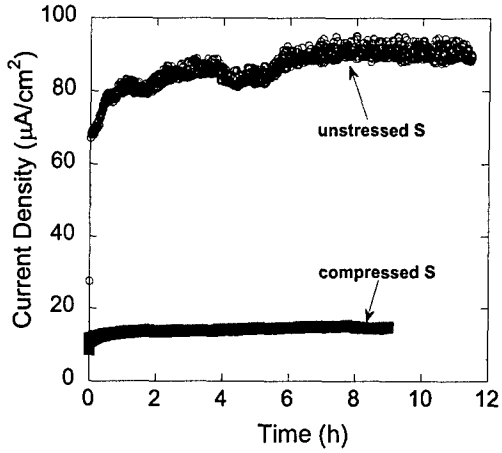

Figure 14. Current density for cylindrical S samples with and without compressive stress polarized at –580 mV SCE in 1.0 M NaCl.

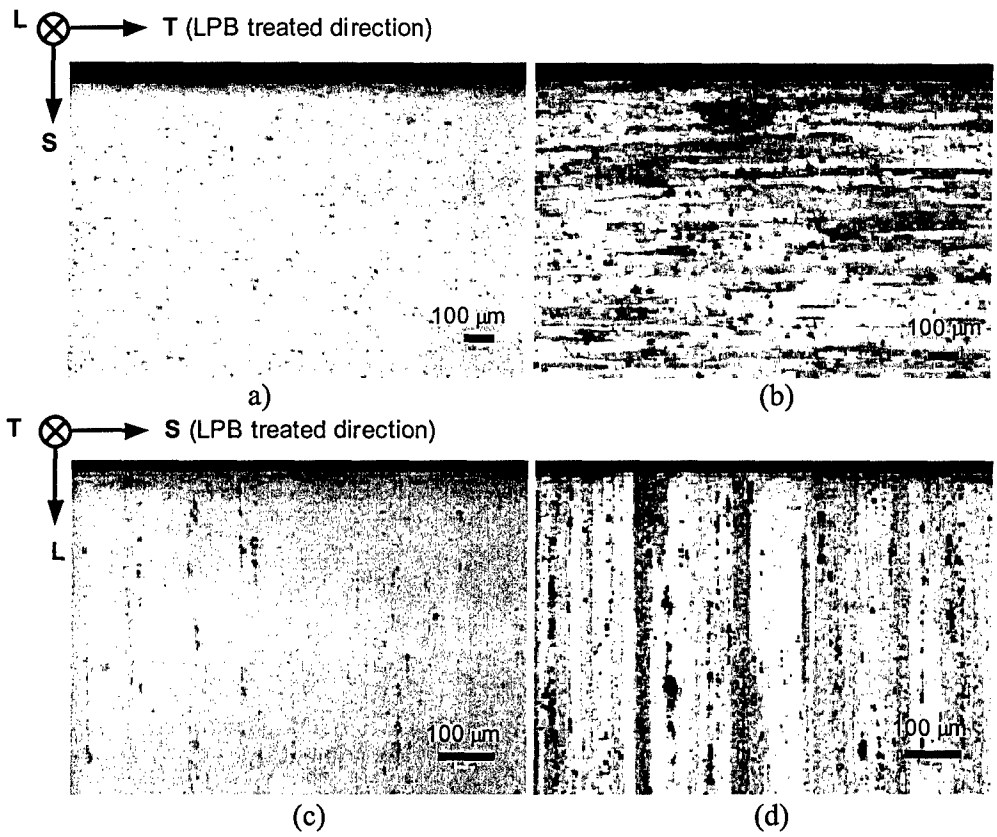

Figure 15. Cross-sectional optical micrographs of LPB treated samples. (a) unetched and (b) etched sections of sample treated on S surface in T direction; (c) unetched and (d) (d) etched sections of sample treated on L surface in S direction.

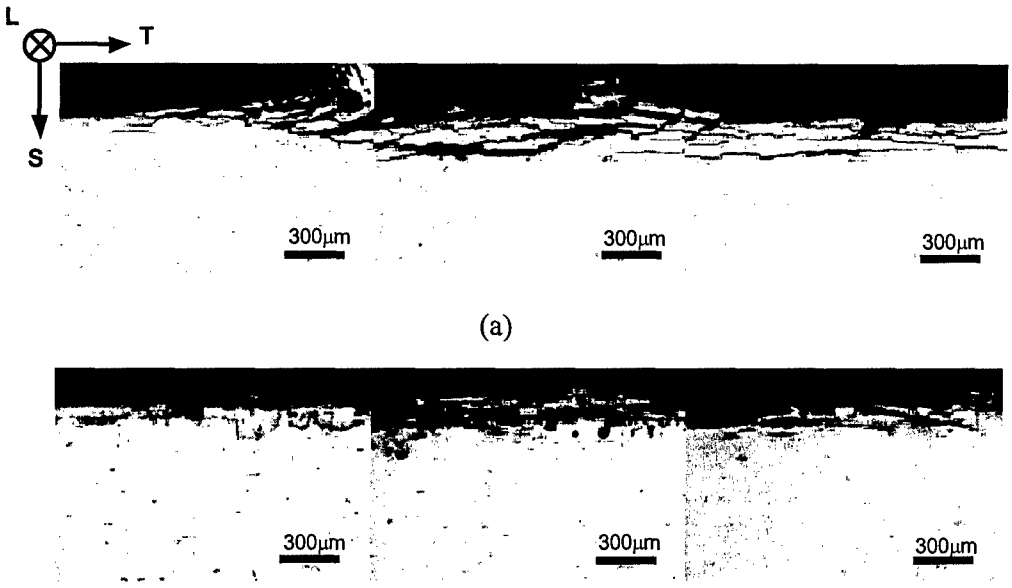

Figure 16. Cross sectional optical micrographs of AA2024-T3 S surfaces after potentiostatic polarization at –580 mV SCE in 1.0 M NaCl for 12h (a) no LPB treatment (b) LPB-treated S sample.

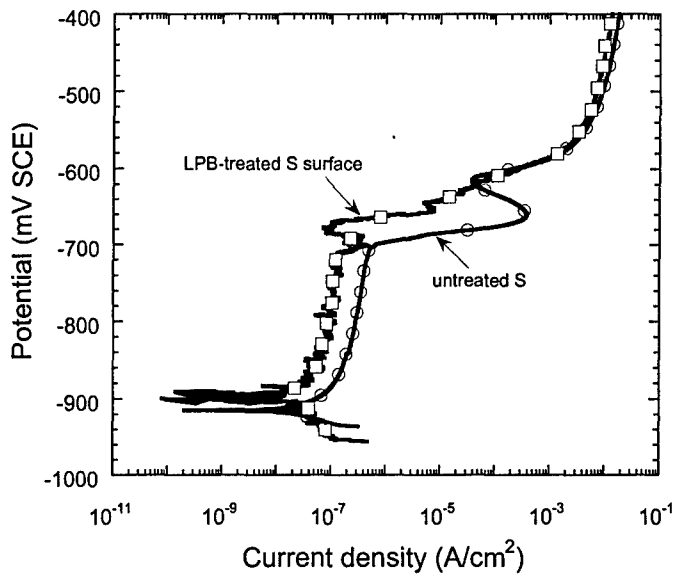

Figure 17. Anodic polarization curves of AA2024-T3 S surfaces with and without LPB treatment in deaerated 1.0 M NaCl at 0.1 mV/s.

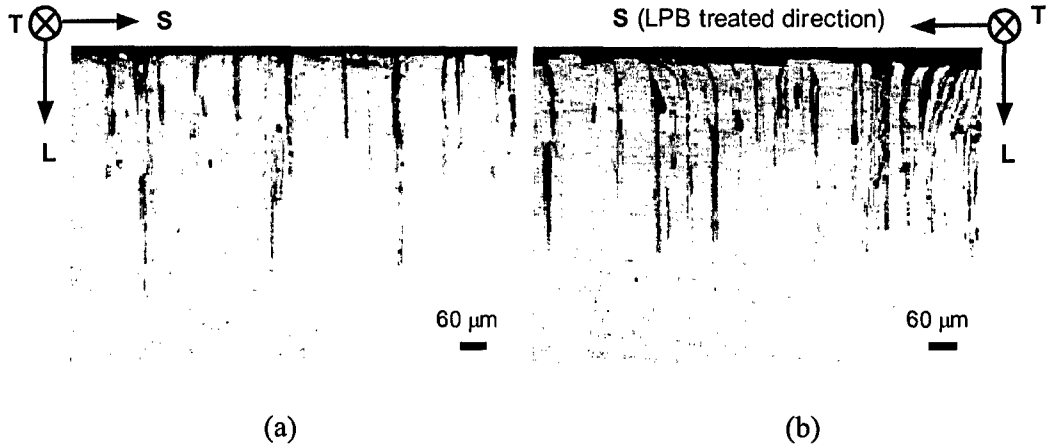

Figure 18. Cross sectional optical micrographs of AA2024-T3 L surfaces after potentiostatic polarization at –580 mV SCE in 1.0 M NaCl for 12h (a) no LPB treatment (b) LPB-treated S sample.

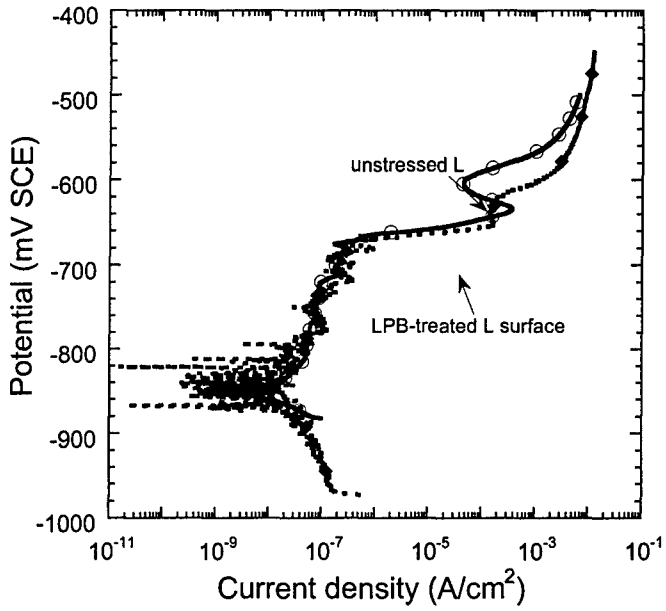

Figure 19. Anodic polarization curves of AA2024-T3 L surfaces with and without LPB treatment in deaerated 1.0 M NaCl at 0.1 mV/s

Not yet submitted for publication.

The Effects of Prior Deformation on Localized Corrosion of Al Alloys

Zhijun Zhao and G. S. Frankel
Fontana Corrosion Center, The Ohio State University
Columbus, OH 43210

Abstract

In this study, the effects of prior deformation on the localized corrosion of high strength Al alloys is studied. Samples were deformed in tension to various extents and examined using electrochemical techniques and by simple immersion and observation. In AA2024-T3, prior deformation resulted in an increase in the passive current density and elimination of the peak associated with the first breakdown. In AA7075-T6, both the first and second breakdown potentials decreased with increasing amounts of prior deformation. The amount of attack on the surface of AA2024-T6 during open circuit exposure to chloride solutions increased with increasing amount of prior deformation. An in situ observation technique was developed to investigate the cause of the first breakdown in AA7075-T6. Compelling evidence was generated to support the notion that the first breakdown is caused by transient dissolution of a surface active layer created by deformation during sample preparation.

Introduction

Aluminum alloy 2024-T3 is widely used in the aircraft industry because of its high mechanical strength and low density. During production, this wrought alloy is solution heat-treatmented, quenched, cold stretched to a certain amount and finally natural aged to a substantially stable condition[1]. The microstructure of AA2024-T3 has been shown to contain[2] (1) α Al matrix, (2) constituent particles from melt solidification and solid phase transformation products including S phase (Al_2CuMg) and AlCuFeMn phase, (3) fine precipitates of S phase both inside the grains and at the grain boundaries. The S and AlCuFeMn constituent particles not only survive (are not redissolved) but also grow in the T3 heat-treatment. The rolling operation results in a grain size between 50 μm and 700 μm. The constituent S and AlCuFeMn phase particles have a size as large as 30 μm. TEM has revealed smaller precipitates in the matrix as needle shaped hardening precipitates with a long length 200 nm. At the grain boundary, needle shaped precipitates (Al_2CuMg) with average length of 100 nm were found. Such heterogeneous microstructures primarily have been developed to optimize mechanical properties, but they also render the alloy more susceptible to different forms of corrosion like pitting corrosion, intergranular corrosion, stressing corrosion cracking and exfoliation corrosion[2].

High strength aluminum alloy 7075-T6 is another widely used alloy in the aircraft industry. SEM and TEM studies of AA7075-T6 revealed a heterogeneous microstructure[3]: Al matrix, large constituent second phase particles such as Al_2CuMg, Al_2Cu and Al_7Cu_2Fe, small strengthening precipitates (η' and η phases) and the grain boundary region which includes precipitate free zone and $Mg(ZnCuAl)_2$ precipitates.

Both of these alloys are susceptible to environmental cracking in aggressive environments. Most studies of the interaction of mechanical stress and corrosion deal with measurement of the mechanical properties either during or after exposure to a

corrosive environment. In most aerospace applications, corrosion occurs on the ground with minimal static loads and mechanical stressing occurs during flight when the temperatures are very cold and corrosion is not an issue. The effects of pre-corrosion on mechanical properties are certainly of interest, but the effects of pre-stress on corrosion should also be of interest and this has received little attention. Pre-stress is the focus of this project.

Microstructural changes due to deformation are of interest because the microstructure controls the electrochemical properties. The hypotheses of the ongoing work are: 1) Pre-stressing produces surface defects such as: slip lines, slip bands, micro-cracks, decohesion between phases, besides, the surface becomes rougher; 2) The surface defects make the passive film less stable than a flat surface; 3) Surface defects may serve as potential sites for pitting initiation; 4) Rougher surface may induce more meta-stable pitting and subsequent stable pitting; 5) Process-induced surface active layers can be very susceptible to attack; 6) All these changes will render the material less resistant to corrosion provided an aggressive environment is present.

Polarization curves for AA-2024-T3 and Cu-containing AA7xxx-T6 alloys exhibit two breakdown potentials, whereas the Cu-containing AA7xxx alloys in the T7 temper exhibit only one[4, 5]. It was shown that the first breakdown in AA7075-T6 was associated with transient dissolution of a surface layer and the second resulted from sustained localized corrosion[5]. Recently, Isaacs showed that this surface layer attack was associated with a susceptible region formed by abrasion during sample preparation[6]. He found a streak-like attack following polishing grooves on the surface. Surfaces treated electrochemically or by ion milling did not exhibit the same behavior. Afseth and coworkers had previously proven the existence of such an active surface layer on lower strength Al alloys[7], but Isaacs' work was the first to show the phenomenon in high strength materials. These active surface layers are another form of microstructural change caused by pre-deforming a sample.

Different tests were used to determine the difference in behavior of samples before and after deformation. Potentiodynamic polarization on macroscopic sample area was used to reveal the passive region and identify the values of the two breakdown potentials. Exposure to NaCl solutions at OCP condition has also been used to test the corrosion properties of samples. To study the corrosion behavior of individual second phase particle decohesion and micro-cracks, the microcell technique was used[8]. This technique allows the study of areas on the scale of microns. The background noise is greatly reduced and information of the studied object is obtained. Finally, the breakdown of surface active layers in AA7075-T6 and T7 were studied using in-situ observation of the surface during polarization.

Experimental

Dog-bone shape samples were cut from AA2024-T3 and AA7075-T6 sheets. The tested surface of all the samples was the ST or rolling surface and the tensile axis was the rolling direction. All the samples were ground in ethyl alcohol with SiC abrasive paper from 400 to 1200 grit, followed by final polishing in 1 μm diamond paste. The polished samples were then cleaned ultrasonically in ethyl alcohol. The ductilities in air of AA2024-T3 and AA7075-T6 are 12.5 and 16%, respectively and their 0.2% offset yield strains are 0.7% and 0.98%, respectively. The 810 MTS (Material Testing System)

tension testing machine was used to pull the samples to various strains along the rolling direction using an extensometer to measure the strain. The test machine automatically stopped as soon as the pre-set strain was reached. Scanning electron microscopy (SEM) and optical microscopy were performed to observe the sample surface microstructure. Surface features were documented on freshly polished, plastically deformed and corroded samples. Regions with big constituent particles, micro-cracks were given special attention. Solutions were prepared with reagent grade NaCl and deionized water. The solution was open to air when the tests were conducted at OCP condition in NaCl solution. Potentiodynamic polarization tests were performed in 1 M or 0.5 M NaCl solution deaerated with Ar.

Microcell tests were conducted using a microcell setup with 1 M NaCl solution, Figure 1. The microcell is basically a glass capillary with ground tip that is inserted into a microscope objective holder and is landed onto a specific location on the sample surface[9]. The tip size of 40 microns was used in this work, and the end of the tip was sealed with silicone rubber to prevent electrolyte leaking. A Pt wire is used as counter electrode, and an SCE reference electrode is connected to the cell with an electrolyte bridge.

The breakdown mechanisms of AA7075-T6 and -T7 were studied using a special cell placed in an optical microscope that allows in-situ observation of the surface during polarization, Figure 2. The image is captured by a VCR. The polarization curve from the potentiostat is recorded by the computer and subsequently animated using special software. Finally, a film of the sample surface and the changing polarization curve are combined in a single movie clip. The combination of the surface image and polarization curve on one screen allows for determination of the surface corrosion processes as a function of potential. The samples were made from AA7075-T6 and -T7 sheets polished to 1 micron with diamond paste. Samples were then potentiodynamically polarized at 0.2 mV/sec in 0.5 M NaCl solution in the special cell. Tests were stopped at different potentials and the samples were studied using optical microscope and SEM. The result was compared to the in-situ movie to determine the mechanism of the breakdown.

Results

Anodic polarization tests

Figure 3 shows typical potentiodynamic polarization curves for AA2024-T3 samples with 0, 1 or 2% tensile pre-strain. For the unstrained samples, two breakdown potentials were observed, as has been observed previously for this alloy. For samples tested after the application of a strain high enough to cause bulk plastic deformation, the first breakdown potential was not clearly exhibited. A slight change in slope was observed at a potential around –700 mV SCE. Plastic deformation increased the current density in the passive region up to the point just above the first breakdown. The second breakdown potential after plastic deformation was close to that for the unstressed samples but the current density was higher.

Potentiodynamic polarization curves for AA7075-T6 in deareated 0.5 M NaCl are shown in Figure 4. Both breakdown potentials decrease continuously with increasing amounts of prestressing. This is quite different behavior than AA2024-T3, which shows increased corrosion rate after pre-stressing, but little change in breakdown potentials. It is speculated that the transient dissolution associated with the first breakdown potential in

AA 2024 T3 is dominated by the active S (Al_2CuMg) particles, which are not changed much by deformation. However, in AA7075-T6 the transient dissolution is dominated by the surface active layer, details of which are discussed below.

Cathodic polarization tests

Cathodic polarization tests were also done to reveal the effect of pre-stressing on the cathodic reaction. Figure 5 shows typical cathodic curves for AA2024-T3 samples with 0%, 3% and 9% pre-strain. Measurements were made in deareated 1 M NaCl at a scan rate of 1 mV/s. In this deaerated electrolyte, the primary cathodic reaction is hydrogen evolution by the reduction of water. The cathodic reaction rate at a given potential increased slightly for increasing amounts of pre-strain. The increased cathodic reaction rate may have been due to the increased area of the roughened sample surface created by the plastic deformation. The same trend is seen in the tests on AA 7075 T6, Figure 6. Again there is a slight increase in the cathodic reaction rate at a given potential with increasing amount of pre-stress.

Observation at OCP

AA 2024 T3 samples with 0 or 9% pre-strain were exposed to aerated 0.0005 M NaCl solution at OCP condition for 20 h. Figures 7 and 8 are optical microscopic images of the surface of the sample with 0 and 9% prestrain, respectively, after OCP exposure. The 9% deformed samples showed more extensive corrosion with copper redistribution around the corroded sites. In addition, for the sample with 0% pre-strain, there were several clusters of constituent particles that appear to be untouched, neither being attacked nor inducing matrix dissolution around them. In contrast, deformed samples rarely exhibit such unaltered particles; in Figure 4 nearly every particle is altered.

Due to the focal depth limitation of optical microscopy, detailed information regarding corrosion of individual particle is not possible. So SEM was utilized to observe the feature on the corroded surface. Figure 9 and 10 are SEM images of samples with 0 and 9% prestrain, respectively, after exposure to 0.0005 M NaCl for 20 h. Small holes that might have resulted from dissolution of S phase particles are evident in both as is matrix dissolution around big constituent particles. However, similar to what was seen in the optical micrographs, the undeformed sample exhibits many AlCuFeMn particles with no corrosion around them, and the deformed sample exhibits extensive matrix dissolution even around small AlCuFeMn particles. This suggests that plastic deformation accelerates the matrix dissolution around noble AlCuFeMn particles.

Micro-cracks in the matrix were documented before and after the OCP corrosion tests. In general, these experiments revealed that the micro-cracks are not as active as S phase particles. The occlusions created by these microcracks can be sites where the environments supporting localized corrosion can be more-easily stabilized, so micro-cracks could act as preferential sites for stable pit formation. Figure 11a shows a microcrack formed on the surface of a sample deformed to 9% strain. After exposure in 0.001 M NaCl solution for 17 h, severe attack was found at this site, Figure 11b. However, other cracks remain totally inactive for long periods of OCP exposure. Reasons for such discrepancies might be the size of the cracks or how they are produced. Deep cracks might favor pit formation compared to shallow cracks. A crack associated

with an S phase particle just below the surface might also favor pit formation. More work is needed to understand these factors.

Microcell Tests

Figure 12 shows typical polarization curves from microcell tests on AA 2024 T3. in aerated 1 M NaCl at 1 mV per second. For each test, one big AlCuFeMn particle was included in the exposed area. For the pre-stressed samples a particle with an associated microcrack was chosen for testing. The deformed samples exhibit lower breakdown potentials and much higher current density above the breakdown potential, again supporting the enhanced reactivity of microcracks.

Mechanism for AA 7075 T6

Figure 13 shows a typical polarization curve for AA7075-T6 in aerated chloride with the different regions labeled. In an aerated solution, the corrosion potential is often pinned at the first breakdown potential, and polarization above the corrosion potential results in large currents, Stage I. This breakdown is not sustained, however, and as the potential is scanned further upward, the current reaches a maximum and then decreases, Stage II. At some higher potential the second breakdown potential is reached, and the current starts to increase once more, Stage III. As described in the experimental section, the image of the corroding surface was recorded during potentiodynamic polarization and subsequently combined with the animated polarization curve to facilitate determination of the potential range for each behavior. Figure 14 shows the result for AA7075-T6, with the image taken at the very beginning of the polarization experiment. The image of the surface is placed at the upper right corner while the animated polarization curve lies at the lower left corner. The complete polarization curve is shown above the animated one to allow recognition of the instantaneous potential. The movie is included in the attached file and the whole test can be reviewed by just clicking the movie twice.

As potential scans upward, the current increases in Stage I and the surface image shows gray areas initiating and spreading across the surface, Figure 15. These patches move in all directions; on a well polished sample there is no obvious preferential growth direction as Isaacs found on a ground surface. Very small hydrogen bubbles are left behind the moving dissolution front. Another test was stopped at a potential in the middle of Stage I as the current was increasing. The sample was dried and examined under an optical microscope. The images in Figure 16 were taken at the edge of one colony of dissolved surface thin layer at different magnifications. The thin layer was expanding from the top of these images downward. Most of the surface inside the colony is dissolved except for small unattacked areas in between the major patches of attack. At the periphery, the dissolution front looks discontinuous and separated. The current reaches a maximum and starts to decrease signifying the start of Stage II. However, the images of the surface indicate that the same phenomenon is occurring at the surface during Stage II as during Stage I – the patches continue to spread, Figure 17. It is likely that the current decreases because the total amount of patch perimeter decreases as the area is essentially consumed by the process. Figure 18 shows an optical microscope image of the surface of a sample from another test that was stopped at a potential in the stage II. Most of the exposed surface thin layer had dissolved at this potential, but small unattacked areas were still evident, indicating a very heterogeneous surface microstructure. All the big second

phase particles became darkened and discolored. However, no pitting or any localized corrosion were seen at this potential. Without sustainable forms of corrosion, the current in the polarization curve had to decrease even though the potential was stably stepping up.

As the potential was increased above the second breakdown, the current started to increase again. In this stage, the attack was dominated by stable localized corrosion, which is confirmed by the generation of hydrogen bubbles at a few fixed spots instead of uniform production across the whole surface, Figure 19. The forms of localized corrosion could be pitting, IGC or selective grain dissolution[5]. Examination by optical microscope found pits up to tens of microns. The whole surface appeared to be darker than just above first breakdown.

Only one breakdown was observed for AA7075-T7 polarized in 0.5 M NaCl solution at 0.1 mV/s. The single breakdown potential is similar in value to the first breakdown potential of the T6 temper, which suggests that the second breakdown potential simply decreased and current associated with this breakdown just dominated the lower current associated with the still present first breakdown. However, the surface image tells a different story, Figure 20. As the potential was increased above the OCP, the current increased, but there was no evidence of a layer spreading across the surface. Hydrogen bubbles started to form at fixed spots on the surface and the rest of the surface appeared bright. Optical microscopic observation after the experiment confirmed that the attack was localized corrosion; large pits with shiny bottoms were randomly distributed across the surface, Figure 21.

Discussion

Pre-mechanical stressing has different effects on the corrosion susceptibility of different high strength aluminum alloys. Both AA2024-T3 and AA7075-T6 exhibit two breakdown potentials, and the effect of prestrain on these potentials was studied using electrochemistry and video monitoring of the surface.

The first breakdown potential in AA2024-T6 is associated with transient dissolution of active S phase particles and the second with stable localized corrosion. Prior stressing has no effect on either of these processes, but the current density up to the first breakdown and at the onset of second breakdown is increased with increasing pre-strain, which is reasoned to be a result of defects due to deformation.

The first breakdown potential in AA7075-T6 is apparently associated with the attack of a surface active layer that is formed during sample preparation. It is speculated that the nm-size hardening $MgZn_2$ particles are destroyed during regular polishing, allowing Zn and Mg to redissolve into the matrix. The active elements redistribution in the matrix together with plastic flow makes the extreme surface layer significantly more susceptible to corrosion. Mechanical deformation makes the surface roughened and introduces defects into alloy surface. As a result, the first breakdown potential is decreased because the surface thin layer is easier to breakdown compared to as-polished sample that has a very flat surface. The second breakdown is decreased for the same reason.

For both alloys, mechanical deformation slightly increases their cathodic reaction rate and this might be attributed to the increased surface area of roughened surface.

References

1. Smith, W.F., *Structure and Properties of Engineering Alloys, McGraw Book Company.* 1981: p. 162-214.
2. Guillaumin, V. and G. Mankowski, Corrosion Science, 1999. **41**: p. 421-438.
3. Hatch, J.E., *Aluminum: Properties and Physical Metallurgy, Metals Park, OH.* 1983.
4. Zhang, W. and G.S. Frankel, J. Electrochem. Soc., 2002. **149(11)**: p. B510-B519.
5. Meng, Q. and G.S. Frankel, J. Electrochem. Soc., 2004. **151(5)**: p. B271-B283.
6. Huang, R.S., C.J. Lin, and H.S. Isaacs, *Localized Surface Attack of 7xxx Series Aluminum Alloys.* The Electrochemical Society Proceedings Series, 2004.
7. Afseth, A., et al., Corrosion Science, 2002. **44**: p. 2491.
8. Suter, T., et al., J. Electrochem. Soc., 2001. **148(5)**: p. B174-B185.
9. Suter, T. and H. Bohni, Electrochem. Soc. Proc., 1996. **127**: p. 95-105.

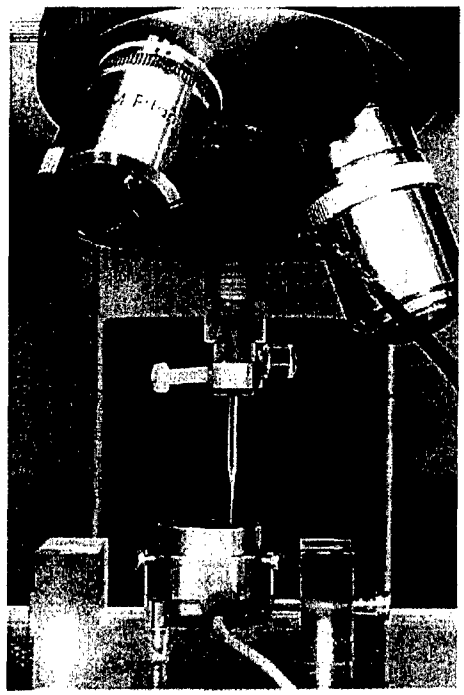

Figure 1. Configuration of microcell

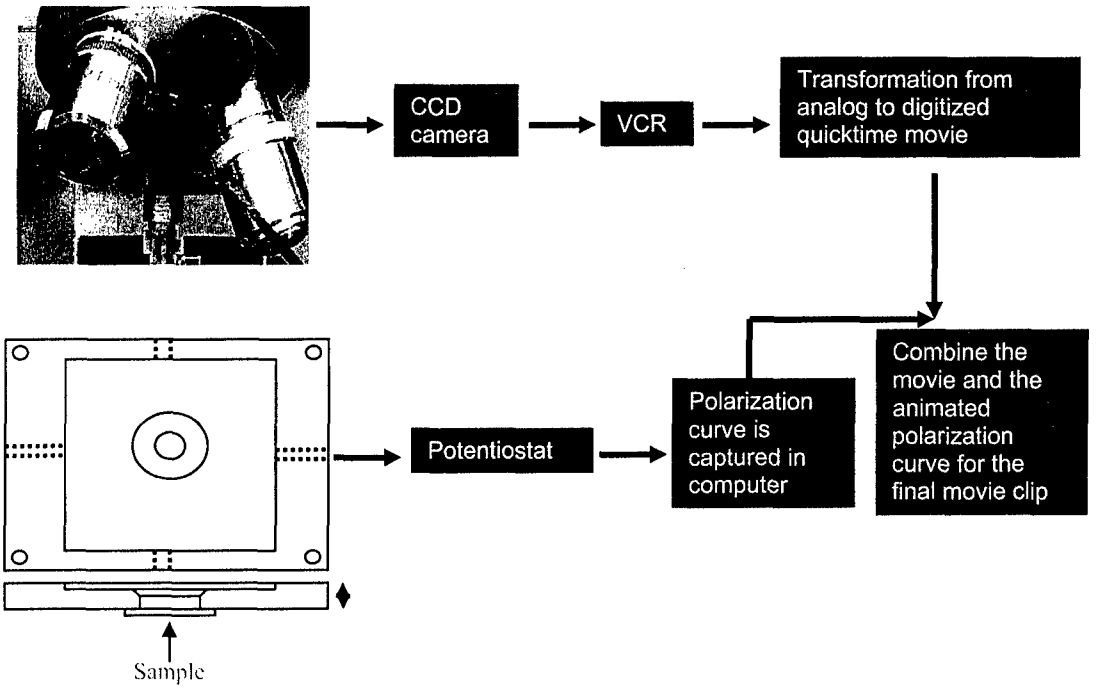

Figure 2. Flow chart of in-situ observation approach

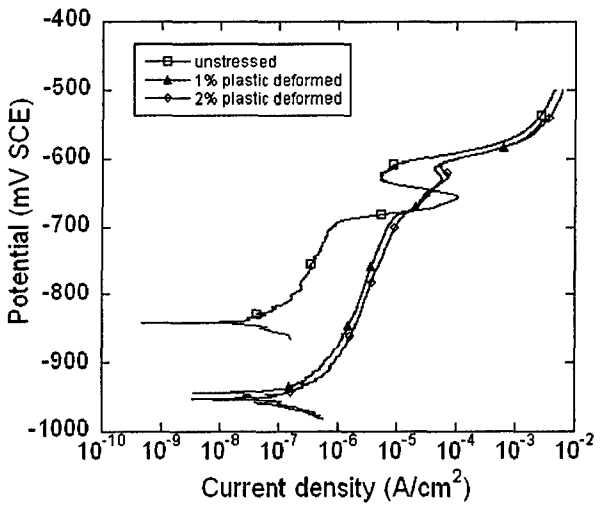

Figure 3. Potentiodynamic polarization test (in deareated 1M NaCl solution) of AA 2024 T3 samples after application of different levels of strain (scan rate: 0.2 mV/sec).

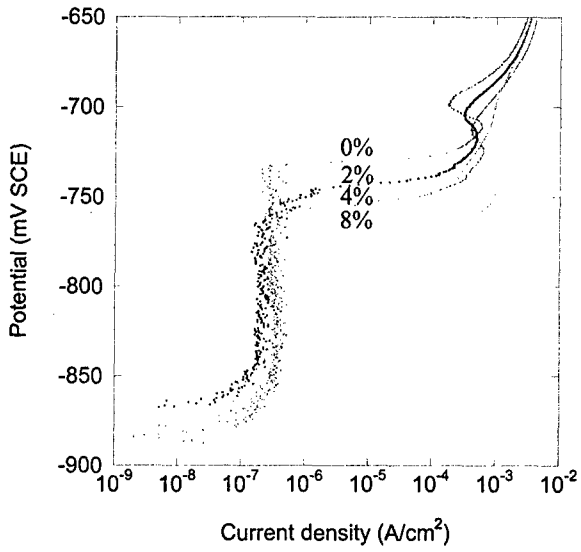

Figure 4. Potentiodynamic polarization tests on AA 7075 T6 in deareated 0.5 M NaCl solution (scanning rate is 0.1 mV/Sec)

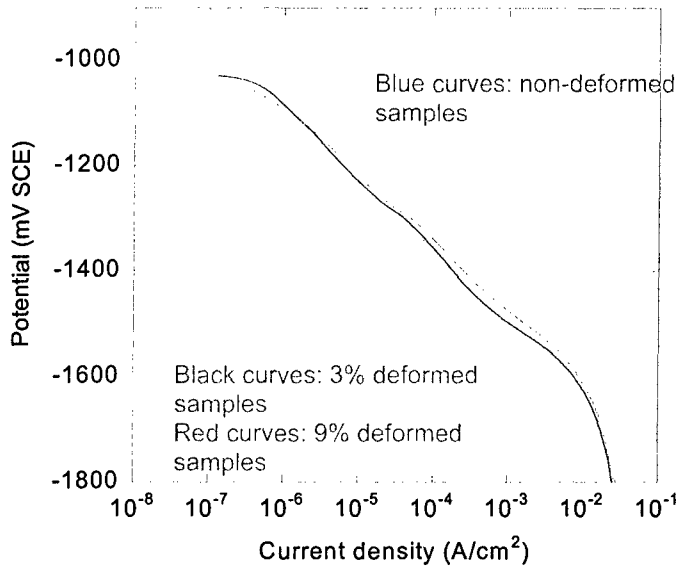

Figure 5. Cathodic polarization tests of AA 2024 T3 samples with different deformation strains in deaerated 1 M NaCl at 1 mV/s.

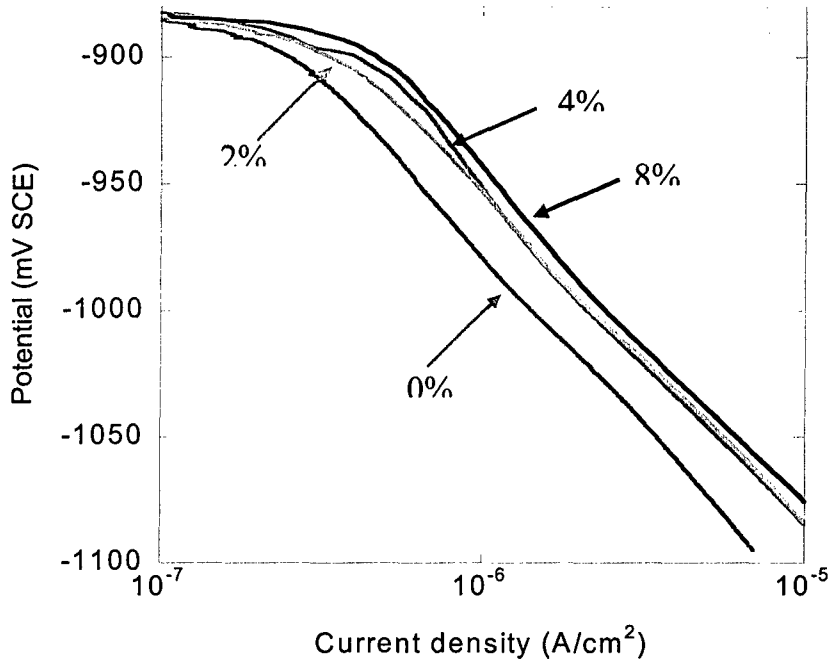

Figure 6. Cathodic polarization tests of AA 7075 T6 samples with different deformation strains in deaerated 0.5 M NaCl at 1 mV/s.

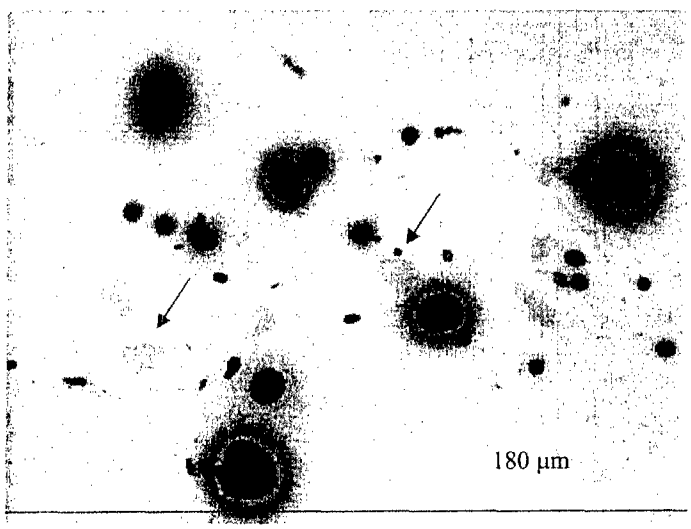

Figure 7. Optical microscopic image of non-deformed samples immersed in 0.0005 M NaCl solution for 20 hours. Arrows show particles that are unattacked.

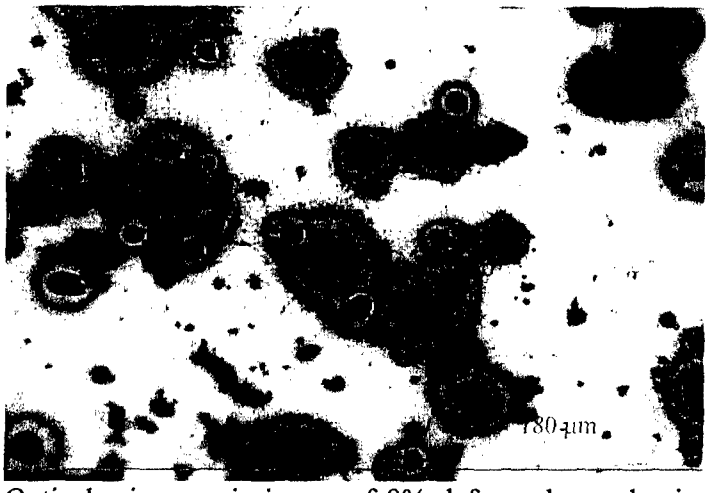

Figure 8. Optical microscopic image of 9% deformed samples immersed in 0.0005 M NaCl solution for 20 hours

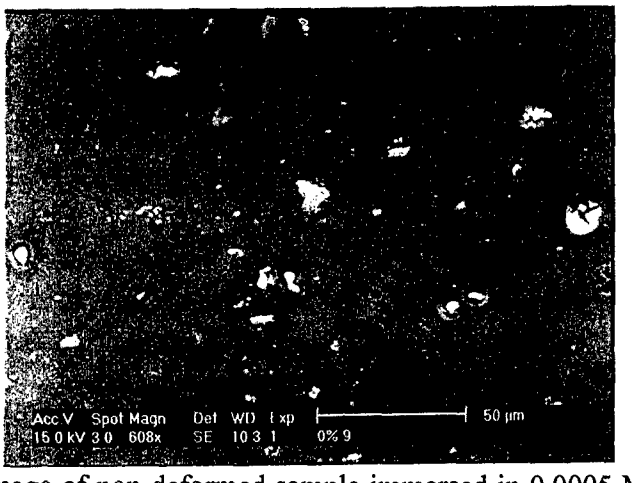

Figure 9. SEM image of non-deformed sample immersed in 0.0005 M NaCl solution for 20 hours. Red arrows indicate unattacked particles.

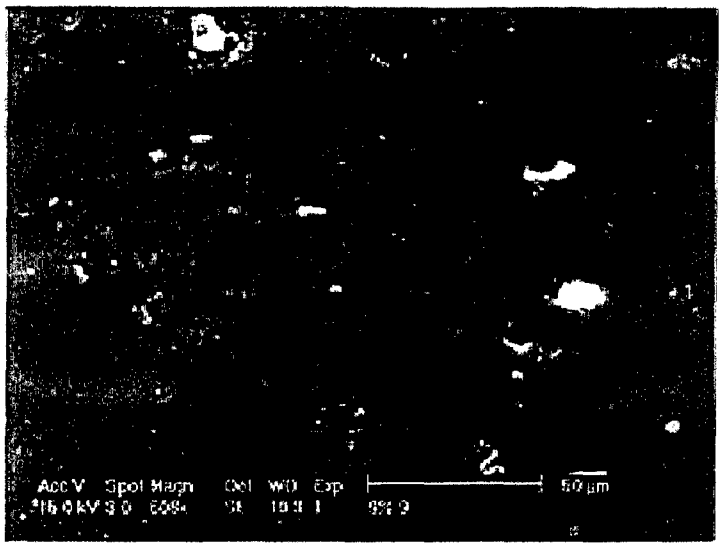

Figure 10. SEM image of 9% deformed samples immersed in 0.0005 M NaCl solution for 20 hours. Red arrows indicate attack around small particles.

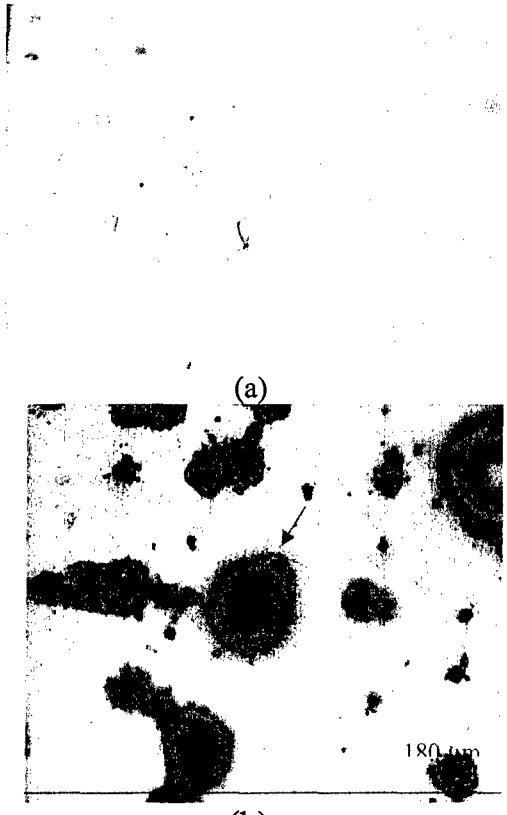

(b)

Figure 11 (a) Optical images with active micro-crack of the 9% deformed sample before corrosion test. (b) Optical image of the same sample after immersed in 0.001 M NaCl solution for 17 hours.

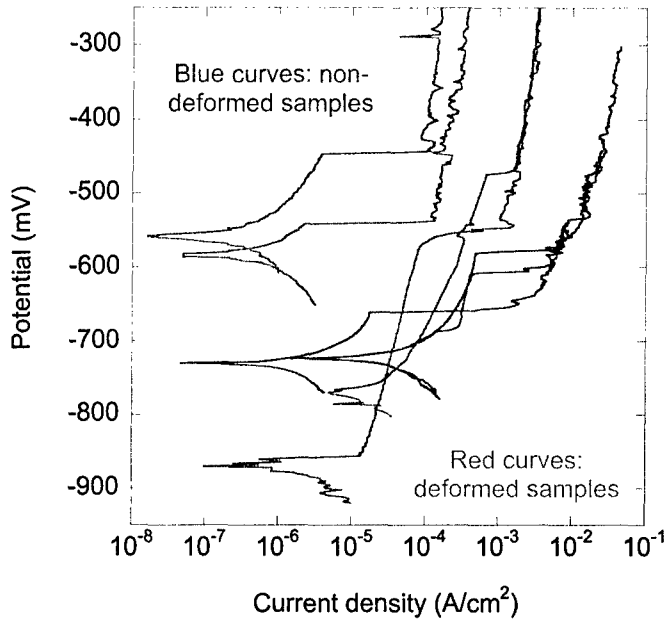

Figure 12. Potentiodynamic polarization tests on AA 2024 T3 with micro-cell.

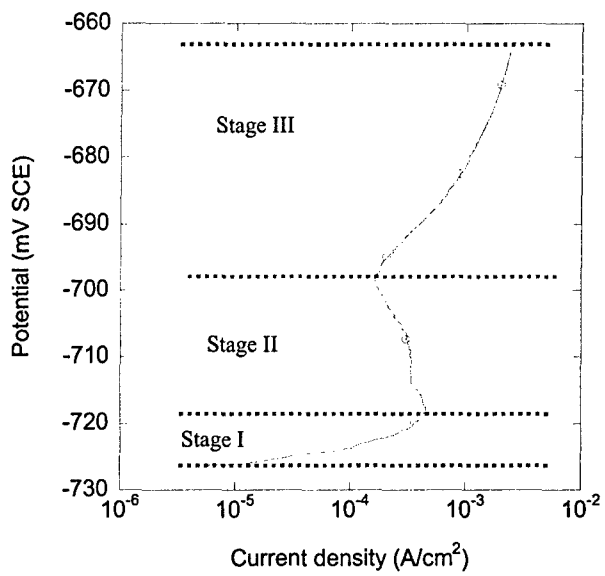

Figure 13. Typical potentiodynamic polarization curve of AA 7075 T6 in aerated NaCl solution.

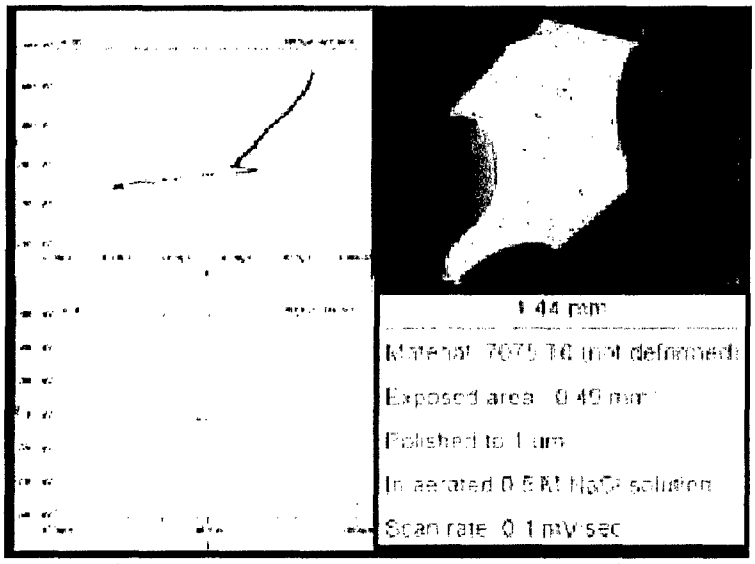

Figure 14 One frame of the movie showing surface reaction movie, animated polarization curve and a complete polarization curve

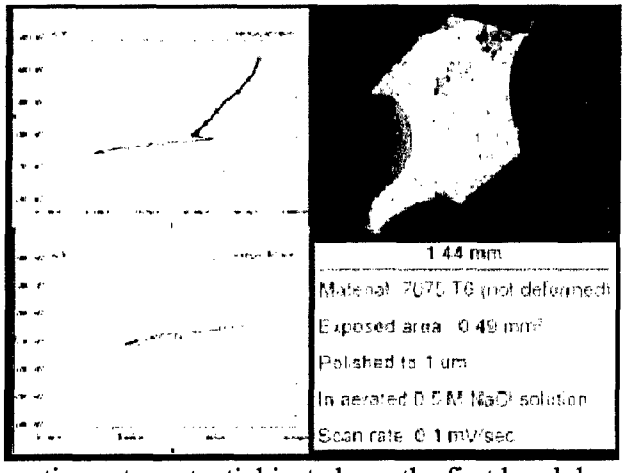

Figure 15 Surface reactions at a potential just above the first breakdown

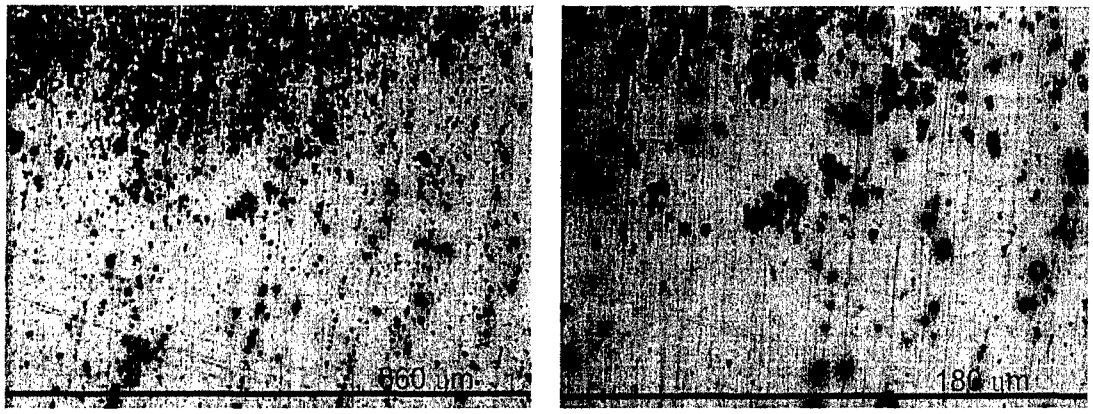

Figure 16 Optical microscopic images of the corroded surface at a potential in stage one

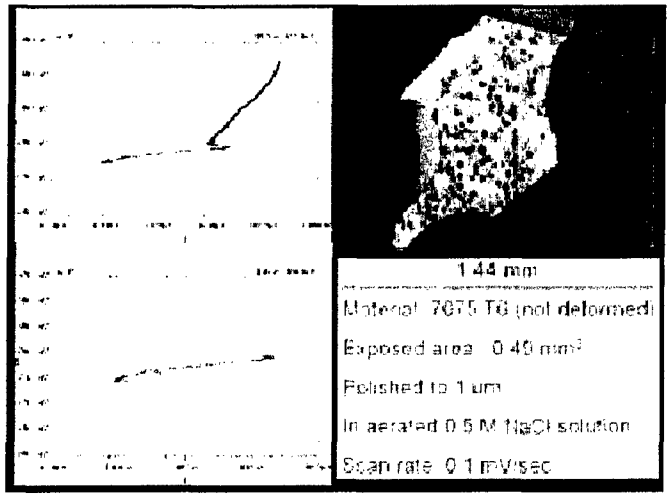

Figure 17 Surface reactions at a potential in stage two

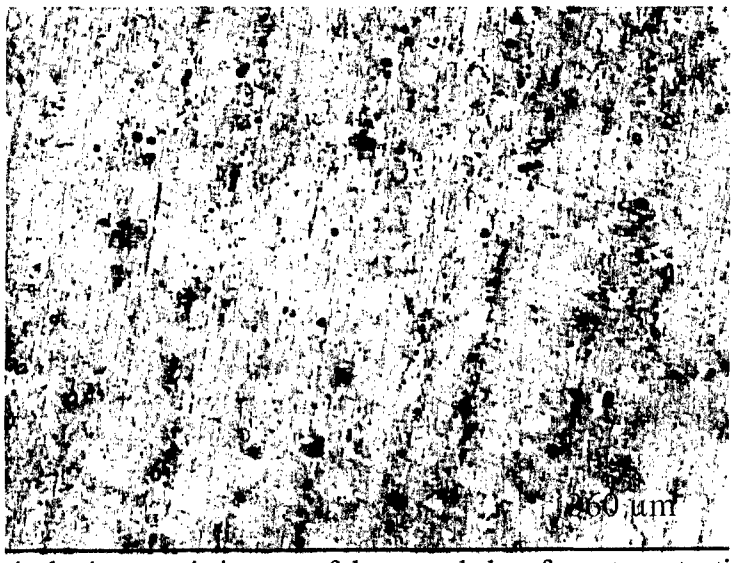

Figure 18 Optical microscopic images of the corroded surface at a potential in stage II.

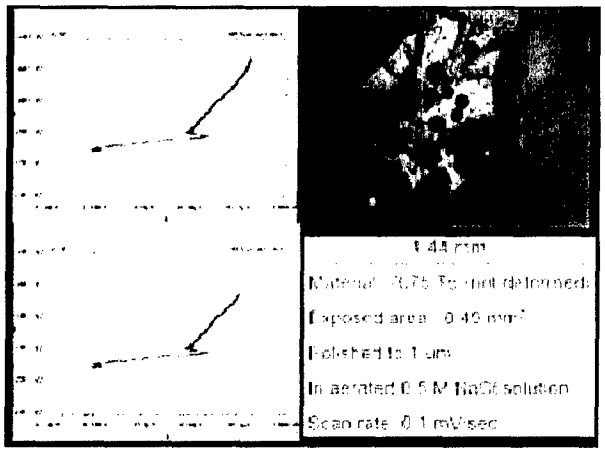

Figure 19. Surface reactions at a potential in stage III for AA7075-T6.

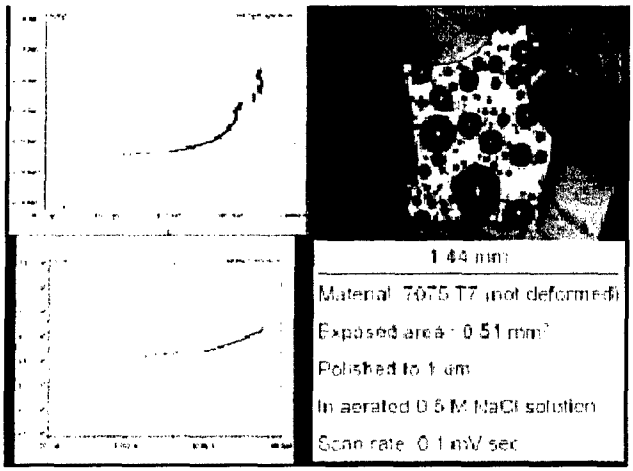

Figure 20 Surface reactions at a potential above OCP for AA 7075 T7

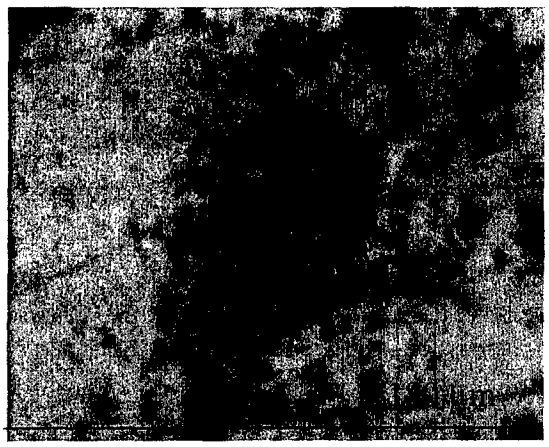

Figure 21 Evidence of localized corrosion above the breakdown potential of AA 7075 T7

In Situ Study of Intergranular Corrosion and Intergranular Stress Corrosion Cracking in AA2024-T3

Xiaodong Liu*, G. S. Frankel*, B. Zoofan** and S. Rokhlin**
*Fontana Corrosion Center, Department of Materials Science and Engineering
**Department of Industrial, Welding and Systems Engineering
The Ohio State University Columbus, OH 43210, USA

ABSTRACT

Microfocal x-ray radiography was used as an in situ non-destructive evaluation method to study intergranular corrosion (IGC) and intergranular stress corrosion cracking (IGSCC) in AA2024-T3. This method provides information on the morphology and growth kinetics of multiple IGC and IGSCC sites, as well as the transition between IGC and IGSCC. An elastic strain was applied using a modified ASTM G49 fixed displacement jig. Application of tensile stress in the transverse direction, parallel to the IGC faces growing in the L direction, led to coalescence of the IGC sites and transition into IGSCC that was nominally normal to the applied stress. Fractography and micrography of penetrated foils presented ex situ visions of the coalesced IGCs. Potentiodynamic polarization revealed that the small elastic strain decreased the breakdown potential. Current transient measured during potentiostatic polarization showed the effects of stress on IGC growth.

Keywords: aluminum alloys, intergranular corrosion, stress corrosion cracking, transition, coalescence, in situ, x-ray radiography.

INTRODUCTION

High strength aluminum alloys are susceptible to intergranular corrosion (IGC) and stress corrosion cracking (SCC). SCC in aluminum alloys is almost exclusively intergranular[1-3]. The relationship between IGC and intergranular stress corrosion cracking (IGSCC) has been discussed over dozens of years[4-7]. The combination of stress and electrochemical reactions can alter the local environment at the IGC tips, which can either accelerate or slow down the growth rate, or favor the initiation of IGC at other sites. It has been suggested that an intergranular (IG) crack subjected to a normal tensile stress can develop into IGSCC [8]. However, the influence of tensile stress parallel to a crack tip on the subsequent growth is unclear, as are the details of how IGC transitions into IGSCC. In order to predict the failure of real structures, IGC and SCC need to be monitored in situ. Zhao *et al.* used x-ray radiography as a non-destructive evaluation (NDE) to study IGC and exfoliation corrosion in AA2024 and AA7178[9]. We have described the use of x-ray radiography to image in situ the initiation and growth of multiple IGC sites in

AA2024 growing in the longitudinal direction with an applied normal tensile stress [10 11 12]. A competition between the IG cracks was observed. The deepest crack at the beginning of the experiment was found to slow and stop growing, and was then surpassed by another crack that eventually penetrated through the sample. The results of the radiography technique were found to be in agreement with data generated using the stressed foil penetration method. Although they are quite different, both approaches can accurately determine the rate of the fastest growing crack. In the current study, x-ray microfocal radiography was put to further use in the study of SCC of AA2024-T3.

EXPERIMENTAL

Two wrought AA2024-T3 plates (Cu 4.5%, Mg 1.45%, Mn 0.57%, Si 0.11%, Fe 0.25%, Zn 0.09%, Ti 0.02%, Cr 0.01%, and other elements total 0.05% max) with 19 and 89 mm thickness, respectively, were purchased from Metalmen Sales, Inc. The microstructures of the two plates are shown in Figure 1. Sheet samples were sliced from the plates in specific orientations relative to the rolling direction using electrical discharge machining (EDM). Figure 2 schematically shows the nomenclature used for sliced samples. L and T sheet samples were jointed with laser-welded tabs to extend their length [12]. For the sample designated L-T, tensile stress was applied in the T or transverse direction and the L or longitudinal section was exposed to solution, allowing cracking in in the L direction. Stress was applied using a modified ASTM G49 fixed-displacement jig. The sheets had dimensions of 79 x 5 mm, and were reduced in thickness to 1.05 mm by grinding and polishing. The stressing jig applied a fixed displacement along the sample length with initial strain about half of the strain at yield. The narrow edge (79 x 1.05 mm) of the sample was exposed to the solution so that cracks propagated along the width. A small electrochemical cell was sealed on the top of samples, allowing potentiostatic polarization of the sheets. The electrochemical cell has been described in detail elsewhere[12].

The details of the X-ray microfocal radiographic imaging technique and the electrochemical measurements were described previously[9, 13]. X-ray absorption through the sample thickness results in a negative, gray-scale, radiographic image in which higher density regions such as intermetallic particles are bright and lower density regions associated with intergranular threads or corrosion product are dark.

In all radiographic experiments, the samples were potentiostatially polarized at –580 mV SCE in 1 M NaCl. Potentiodynamic polarization was performed on both AA2024-T3 plates in deaerated 1 M NaCl at 0.1mV/s.

RESULTS AND DISCUSSION

Potentiodynamic polarization of L and L-T samples

Representative potentiodynamic polarization curves in deaerated 1 M NaCl for unstressed L surfaces and L-T samples stressed in tension to an initial strain of 0.28% are given in Figure 3. Three replicate measurements were made for each condition and representative curves are presented. Both samples exhibit spontaneous passivation and one breakdown potential, which was lower for the stressed L-T samples than for the unstressed L sample (averages of -780 and -670 mV SCE, respectively). Similar findings were reported for unstressed S and stressed S-T and S-L samples[14]. Metastable pitting current transients are is evident in the passive range for the L-T sample. Potentiodynamic polarization measurements were also made on unstressed L sections

and L-S samples cut from a thick plate (89 mm) of AA2024-T3, Figure 4. The L-S samples were stressed to an initial elastic strain of only 0.18% in the S direction (less than half of the strain at yield). Again, the elastic stress decreases the breakdown potential; the average values were -660 and -710 mV SCE for unstressed L and L-S, respectively. The elastic stress seems to enhance the stability of the initial breakdown events.

Radiography of Unstressed L and T Samples

Figure 5 shows a time sequence radiographic images of an unstressed L sample during polarization in 1 M NaCl at -580 mV SCE. The top edge of each image was the exposed L surface of the sample. The horizontal white line 1.5mm below the surface is from the lacquer used to seal the end of the cell lips [10] and the vertical white streaks are the result of intermetallic particles lined up in the L direction. With time, dark streaks associated with IGC grow from the top exposed surface downwards in the L direction. After 20 min, Figure 5a, only a few IGC sites are evident. During the time period from 1-3 hr, Figures 5b-d, more IGC sites initiated and their depth increased. Figure 5e shows the high density of straight and sharp IGC sites aligned in the L direction after 25.5h. The IGC density and the IGC length are approximately uniform along the full length of the sample.

Figure 6 shows the series of micrographic images for an unstressed T sample. These images exhibit different morphologies than those from the L sample in Figure 5. The intermetallic particles are less elongated, reflecting the shorter grain dimensions in the T compared to the L direction. The images from the first 20 minutes, Figures 6a-b, show almost no evidence of IGC, with attack just visible after 1 h of exposure, Figure 6c. With longer exposure, Figure 6d-e, more IGC sites initiated and grew in the T direction, but at a slower rate than in the L sample. Furthermore, the attack was diffuse rather than straight and sharp as in the L sample. Figures 6f and 6g show higher magnification images on the left and right sides of the sample, respectively, after 120 h exposure. The cracks are seen to link along the S direction, forming a network. Some white features, apparently unattacked grains, can be seen extruded out of the top surface, which might be attributed to stress generated by the corrosion process, as is discussed below.

The lengths of fastest growing cracks in L and T samples were measured as a function of time from the x-ray films and are shown in Figures 7 and 8, respectively. Also shown in these figures are data from foil penetration experiments. Recall that the foil penetration experiment measures only the time for the first site to penetrate the foil, or the fastest growing site [15-17]. The open circles in Figure 7 represent the depth of the deepest site at any given time in the in situ radiographic experiment, which is a combination of the data from different sites. These data almost overlie the data from the foil penetration experiments under the same condition, which are indicated as filled squares in the plots. The similarity in the data from two different techniques suggests that both approaches provide accurate assessments of crack growth rates. However, the foil penetration technique does not provide information on the propagation rates of individual sites, only the nominal fastest rate for an ensemble of sites [18, 19].

Transition of IGC to IGSCC in L-T sample

IGC is constrained to the intergranular region, which is primarily between the grains elongated in the L and T direction of a wrought microstructure. Stress is commonly applied to

such a microstructure along the L and T directions, or nominally parallel to the grain boundaries. It is of interest to know how IGC, constrained by the microstructure to be parallel to an applied stress develops into IGSCC that is perpendicular to the applied stress. To study this transition, an L-T sample was tested in the radiographic experiment. The sample was stressed in the T direction with initial strain of 0.28% and the corrosion attack grew from the exposed L face in the L direction. X-rays penetrated through the sample thickness in the S direction. Figure 9 shows a time series of radiographic images of the L-T sample. These images exhibit quite different cracking morphology than those of the L sample in Figure 5 and the T sample in Figure 6. The IGC is seen to be a wavy diffuse as it grows in the L direction. It was previously reported that the average dimension for the tested material at the ¼ T section was approximately 50 μm in the S direction [17, 20]. The thickness of sheet sample used in *in situ* x-ray radiography study was 1.05 mm, indicating that there were about 21 grains through the thickness of this sample in the S direction. All of these grains were illuminated by the X-rays. Note that it is impossible to distinguish the individual IGC or intermetallic particles in this orientation. The radiographic image is an integration of all individual IG attack through the sample thickness (S direction). The cracks appear wavy rather than straight as in the L sample because of this nature of the sample orientation relative to the IGC orientation. Many cracks were found along the length of the sample, but one site became longer than the others and almost penetrated the sample after 78.5 h. The sample was bent open at end of that crack even though the ends were constrained by the uniaxial tensile stressing jig. This suggests that the corrosion products produced a wedging stress that forced opened the sample. Figure 9e shows the sequence of images of the longest crack (indicated by an arrow in Figure 9a) at higher magnification. Instead of growing directly downward in the L direction, the IGC spread along the grain boundaries in the S plane. Figure 9e also exhibits the IGC in the S plane is aligned with rather than perpendicular to the T stressing direction. Figure 10 is an unetched optical metallographic section of the L-T sample after the experiment. The section is oriented in the same direction as the radiographic images. Most of the IGC was in the plane of the section, and only the grain boundary regions in the S direction between the elongated grains are visible. Branching of the attack is seen at triple points where a grain boundary in the L direction ends.

Further clarification of the morphology of the L-T samples was obtained using the stressed foil penetration experiment. Details of this approach are given elsewhere[14]. The time for corrosion to penetrate a stressed foil sample is measured. In this orientation, an area on the broad face of the sample is exposed to the solution rather than a thin edge as in the in situ radiography experiment. Because of the dimensions of the foil penetration sample, it is not possible to get in situ radiographic images so the sample was examined by radiography after the experiment, when corrosion had just penetrated through the sample. Figure 11 shows x-ray micrographic and cross sectional images for foil penetrated L-T samples. Similar to the L-T radiographic sample shown in Figure 9, the sample was stressed in the T direction and the exposed face is an L plane, so the attack grew in the L direction. In this case, however, the x-rays penetrated along the growth direction, or the L direction. The intermetallic particles are still evident in this orientation, Figure 11a. Also seen, and at higher magnification in Figure 11b, are short dark lines elongated in the T direction. These are the IGC sites that penetrated the sample in the L direction. Figure 11c is an unetched metallographic section along the T direction, or loading direction. The cracks are seen to have grown in the L direction, which is perpendicular to the loading direction, but figure 9b shows that the primary crack face was in the S plane, or parallel to the loading direction.

To better understand the initiation of singular IGC sites and their coalescence, a pre-notched sheet L sample (80 x 4 x 2 mm) was potentiostatically polarized in 1 M NaCl at -580 mV SCE for 4 h without the stressing jig. The thin edge, which was the L surface, was exposed to solution, allowing IGC growth in the L direction. After the exposure, the sample was pulled in tension in the T direction until it fractured, which occurred beneath the pre-notch. Figure 12 shows the T-oriented fracture plane and all IG cracks propagated in the L direction from top to bottom. Regions ruptured by mechanical overload are denoted in this figure by the letter "R." These regions separate parallel IGC regions, a large one of which is shown at the right part of Figure 12.

To further understand the coalescence process in IGSCC, a similar L-T sample as in Figure 9 was given the same polarization in 1 M NaCl. The sample was constrained in the stressing jig with a fix displacement (0.28% initial strain) and cracks grew in the form of IGSCC. The sample was pulled apart after the exposure, and the surface show the coalescence process of IGSCC, Figure 13.

Figure 14 is a schematic representation of the development of IGC propagating in the L direction into an IGSCC crack perpendicular to a stress applied in the T direction. The rectangles are meant to represent the microstructure of an exposed L surface, with grains elongated in the T direction and thin in the S direction. The grains are further elongated in the L direction perpendicular to the page. During the initial stages of exposure, Figure 14a, IGC is initiated and grows in the L direction along the grain boundaries. As the microstructure is weakened by this IGC growth, the grains start to slide apart along the S planes and open up along the grain edges on the T planes, Figure 14b. This process is like a deck of cards being split apart. When the grain edges coalesce into a single crack, Figure 14c, the transition from IGC to IGSCC is complete.

Growth Kinetics of IGC and IGSCC in L-T sample

The depth of the deepest site as a function of time for the L-T sample was determined from the radiographic images shown in Figure 9, and is shown in Figure 15. The growth rate is much slower than for L-S and T-S samples, which were stressed in the S direction[11]. Obviously, the stressing direction and crack propagation orientation have a large effect on the SCC growth kinetics. Also shown in Figure 15 are the IGC depths of unstressed L and T samples determined from radiographic experiments. The IGC growth rate in the T direction is slightly slower than that in the L direction, and IGC in stressed L-T is slightly faster than in the unstressed samples. Elastic tensile stress in the T direction increases the growth rate in the L direction despite the Poisson effect, which should exert a compressive stress in the S direction, which is the orientation of the IGC crack faces prior to transition to IGSCC (Figure 11b). This effect should close the IGC cracks and slow their growth. The primary effect of the T stress is to allow the T edges of the IGC to coalesce and form an IGSCC crack perpendicular to the applied stress in the T direction.

Current Responses of L and L-T samples

Figure 16a shows the current response from the L-T experiment shown in Figure 9 and from an unstressed L experiment that was performed in the same configuration as the in-situ radiography experiments (exactly like the experiment shown in Figure 5, but a different run without radiographic imaging). Both samples were polarized at -580 mV SCE in 1 M NaCl. It is

interesting that the current measured on the unstressed L sample was about twice that measured on the stressed L-T sample even though the rate of corrosion growth was faster on the L-T sample, as shown in Figure 16a. The explanation for this discrepancy lies in the number of corrosion sites in the two cases. Figures 5 and 9 show that the IGC density is much greater in the unstressed L sample than the crack density observed in the L-T sample. Note that the orientation of the L sample was different than the L-T sample. The length of the unstressed L sample was the S direction rather than the T direction. Had stress been applied, it would have been an L-S sample. The stacking of the thin grains in the S direction along the sample length provided many grain boundaries to be attacked, which resulted in a larger current. The current for the L-T sample also exhibits rather large and rather periodic fluctuations. Figure 16 b shows a magnified view of the current at the time of 62-64 h. Figure 9 shows that there was one predominant crack growing at this time, and the measured current might be primarily associated with the growth of that crack. During this time there were several oscillations that were similar in form. The current increased rapidly, reached a plateau value, and then decayed to a low value before it spiked upwards again. This current transient suggests that the crack growth was discontinuous on a scale that was not visible by the radiography. It is possible that the discontinuous growth was associated with the coalescence of the IGC into a crack perpendicular to the applied stress in the T direction, as described above.

CONCLUSIONS

1. Intergranular corrosion (IGC) and intergranular stress corrosion cracking (IGSCC) were characterized using the in situ x-ray micro-radiography technique.
2. Tensile stresses parallel or normal to the nominal crack progression significantly decreased the breakdown potentials.
3. The coalescence of IGC sites and the transition between IGC and IGSCC were clearly observed.
4. Tensile stress in the transverse direction oriented parallel to the IGC crack faces advancing in the L direction resulted in traverse IGC between the intact grains and integrated the IGC sites into IGSCC.

ACKNOWLEDGEMENTS

This work was supported by the United States Air Force Office of Scientific Research through Grant No. F49620-02-1-0148. The contract monitor has been Lt. Col. Paul Trulove and is now Major Jennifer Gresham.

REFERENCES

1 M.O. Speidel, *Metallurgical and Meterials Transactions A,* **6A,** 631 (1975).
2 D.O. Sprowls and R.H. Brown. *Stess Corrosion Mechanisms for Aluminum Alloys,* R.W. Staehle eds., Proc. of Conf. Fundamental Aspects of Stress Corrosion Cracking, OSU Columbus OH, (1967).
3 M.R. Bayoumi, *Engineering Fracture Mechanics,* **54,** 879 (1996).
4 H. Vogt and M.O. Speidel, *Corrosion Science,* **40,** 251 (1998).

5 C.S. Lee, Y. Choi, and I.G. Park, *METALS AND MATERIALS INTERNATIONAL,* **8:(2),** 191 (2002).
6 J.L. Searles, P.I. Couma, and R.G. Buchheit, *Metallurgical and Meterials Transactions A,* **32A,** 2859 (2001).
7 G.S. Frankel and Z. Xia, *Corrosion,* **55,** 139 (1999).
8 J.E. Finnegan and W.H. Hart, *Stress-Intensity Dependence of Stress-Corrosion Crack-Growth Rate in 7079-T651 Aluminum*, in Stress Corrosion-New Approaches, H. L. Craig, Jr. ed., (1976).
9 X. Zhao, G.S. Frankel, B.Zoofan, and S.I. Rokhlin, *Corrosion,* **59,** 1012 (2003).
10 X. Liu, G.S. Frankel, B. Zoofan, and S.I. Rokhlin. *Imaging and Characterization of Multiple Stress Corrosion Cracks in AA2024-3 by X-ray Radiography,* eds., Proceedings of 206 Electrochemistry Society, Honolulu, Oct. 2004, "Corrosion and Environmental Cracking of Aluminum, Corrosion in Marine and Saltwater Environments II " D. Shifler and T. Tsuru edt. p726, (2004).
11 X. Liu, G.S. Frankel, B. Zoofan, and S.I. Rokhlin, *Submitted to Corrosion,* (2005).
12 X. Liu, Z. Zhao, G.S. Frankel, B. Zoofan, and S.I. Rokhlin, *Proc.of Triservice Corr. Conf, 2003.,* (2003).
13 B. Zoofan and S.I. Rokhlin, *Materials Evaluation,* **52,** 191 (1998).
14 X. Liu, G.S. Frankel, B. Zoofan, and S.I. Rokhlin, *Corrosion Science,* **46,** 405 (2004).
15 A. Rota and H. Bohni, *Werkstoffe und Korrosion,* **40,** 219 (1989).
16 A. Rota and H. Bohni, *Werkstoffe und Korrosion,* **40,** 295 (1989).
17 W. Zhang and G.S. Frankel, *Electrochemical and Solid-State Letters,* **3,** 268 (2000).
18 F. Hunkeler and H. Bohni, *Corrosion,* **37,** 645 (1981).
19 F. Hunkeler and H. Bohni, *Corrosion,* **40,** 534 (1984).
20 W. Zhang and G.S.Frankel, *J. Electrochem. Soc.,* **149,** B510 (2002).

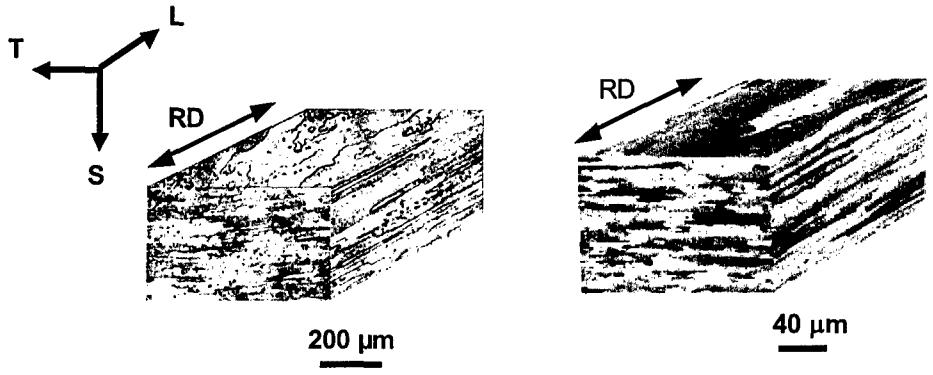

Figure 1. Microstructure and grain dimensions of AA2024-T3 (a) 19 mm thickness plate (b) 89 mm thick plate.

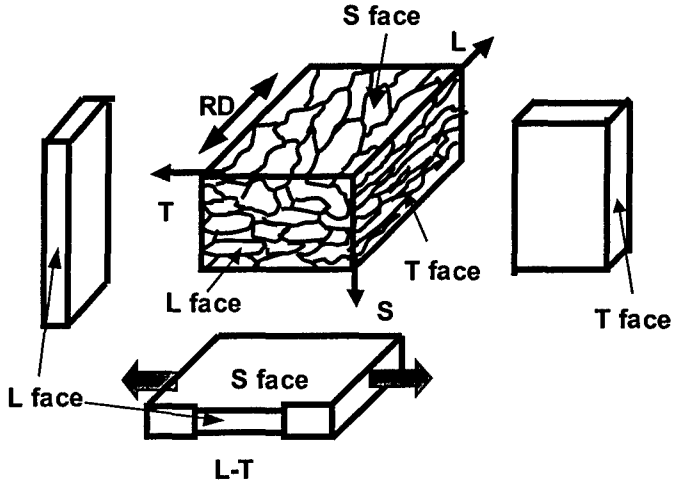

Figure 2. Notation and configuration of tested sheet sample.

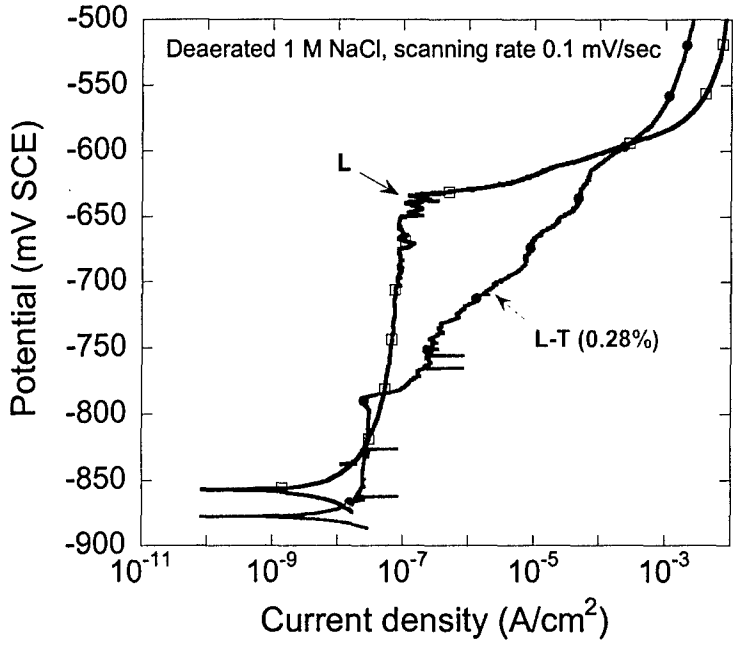

Figure 3. Potentiodynamic polarization curves for L and L-T (with 0.28% initial strain) in 1.0 M deaerated NaCl.

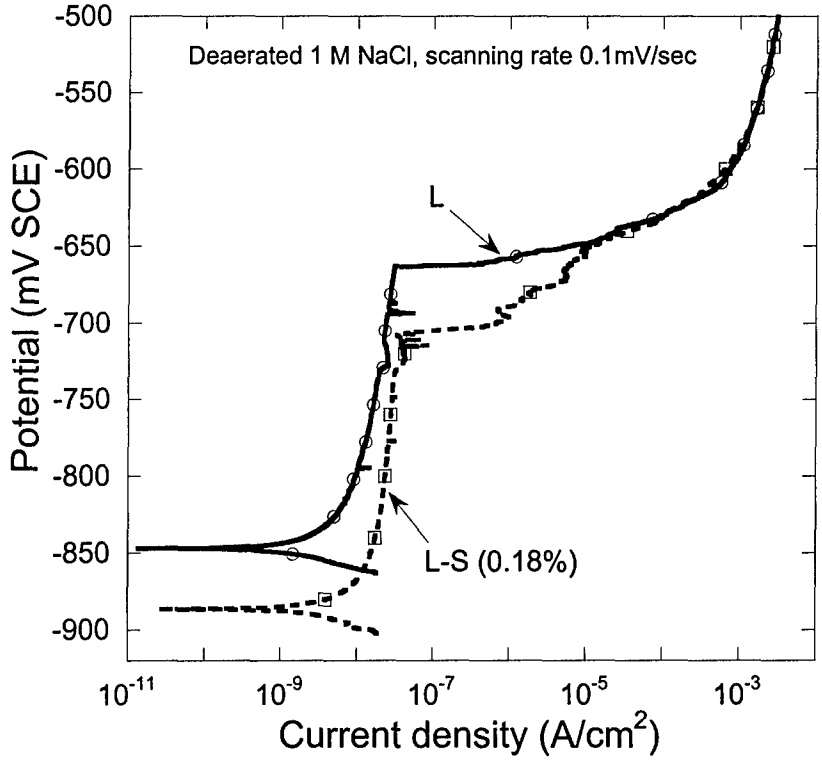

Figure 4. Potentiodynamic polarization curves for AA2024-T3 89 mm thick plate in samples of L and L-S (with 0.18% initial strain) in 1.0 M deaerated NaCl.

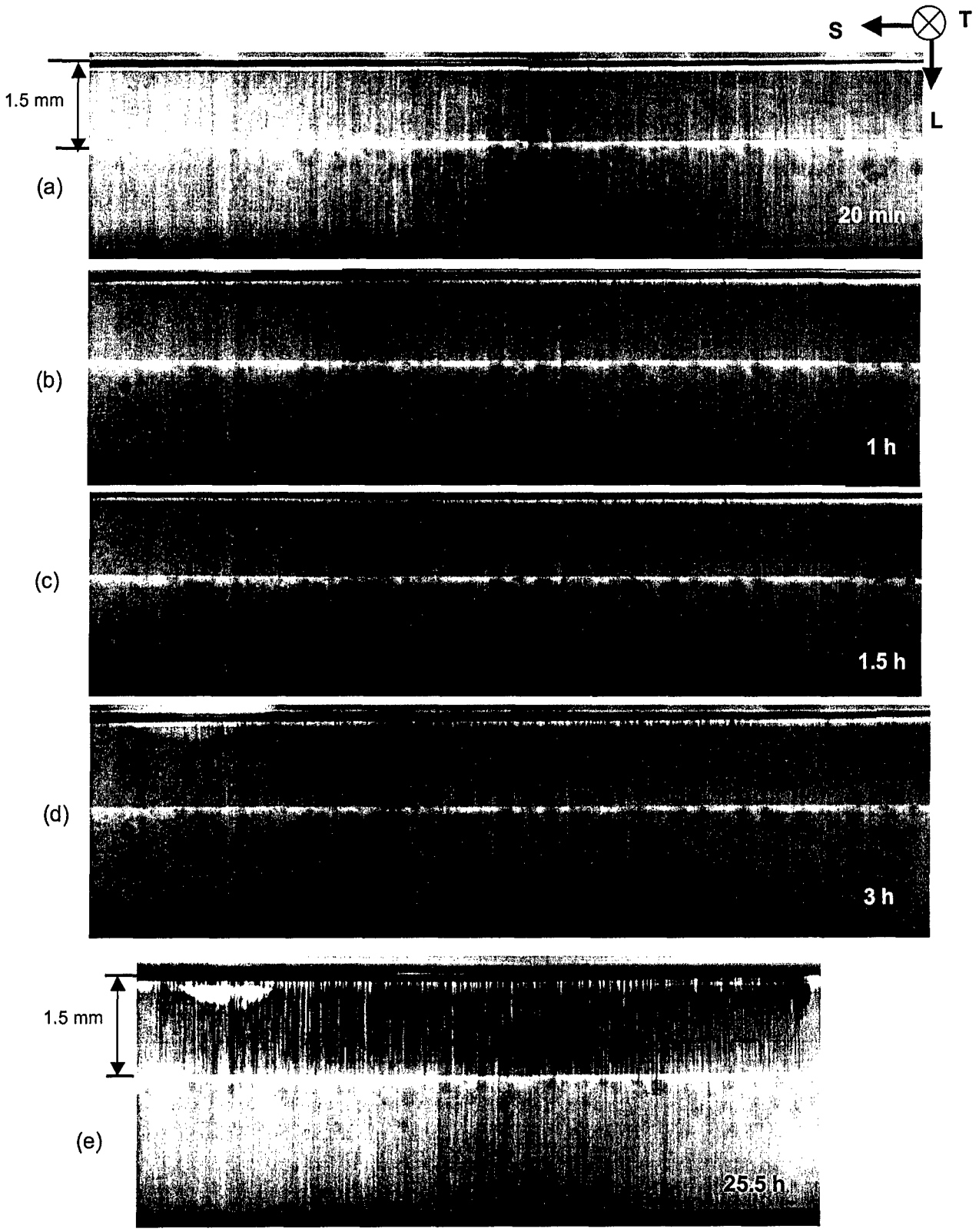

Figure 5. X-ray microfocal radiography images of IGC in unstressed L sample at –580 mV SCE in 1.0 M NaCl. (a) after 20 min, (b) after 1 h, (c) after 1.5h, (d) after 3h, (e) after 25.5h in low magnification.

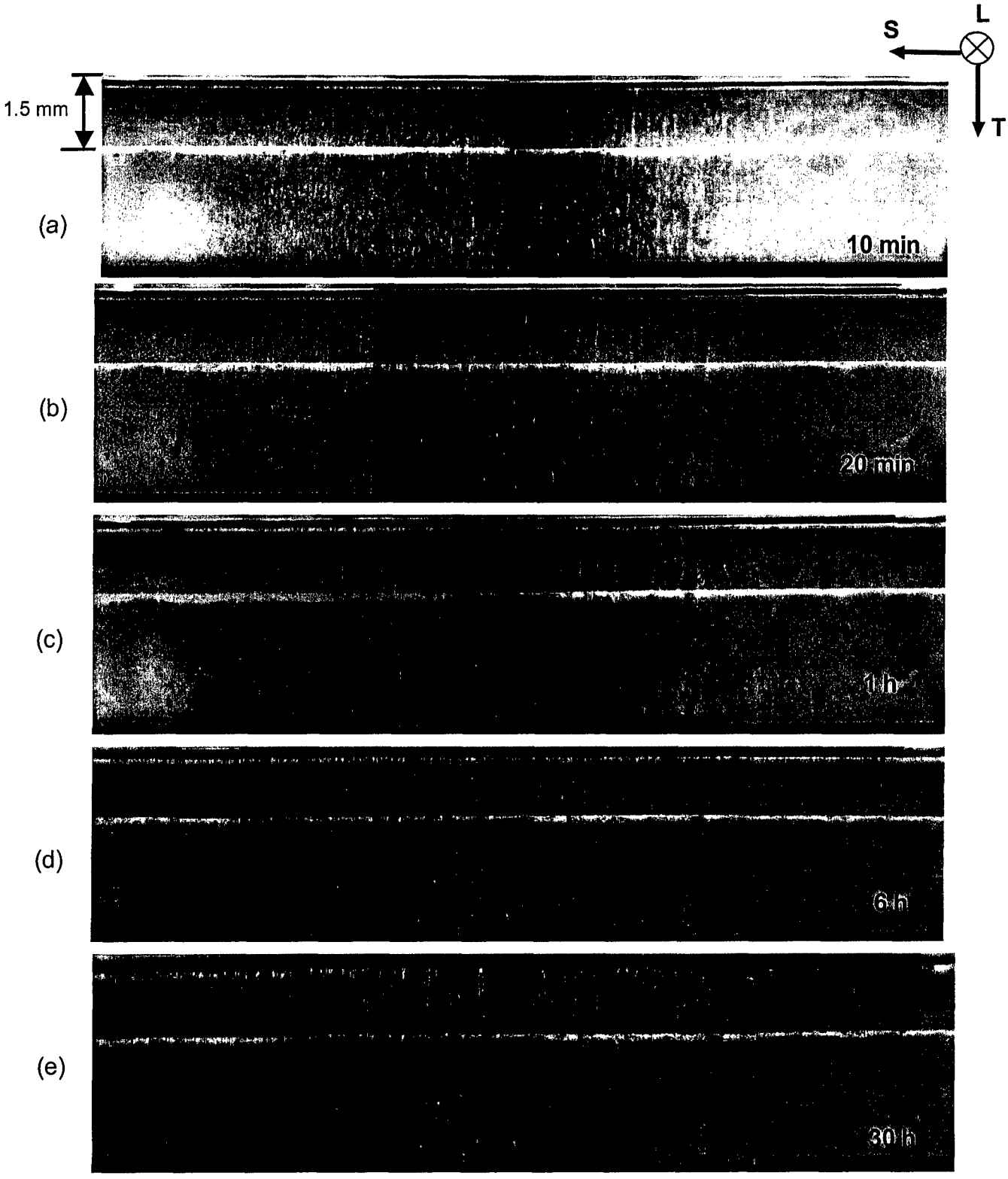
S
L
T
1.5 mm
(a)
10 min
(b)
20 min
(c)
1 h
(d)
6 h
(e)
30 h

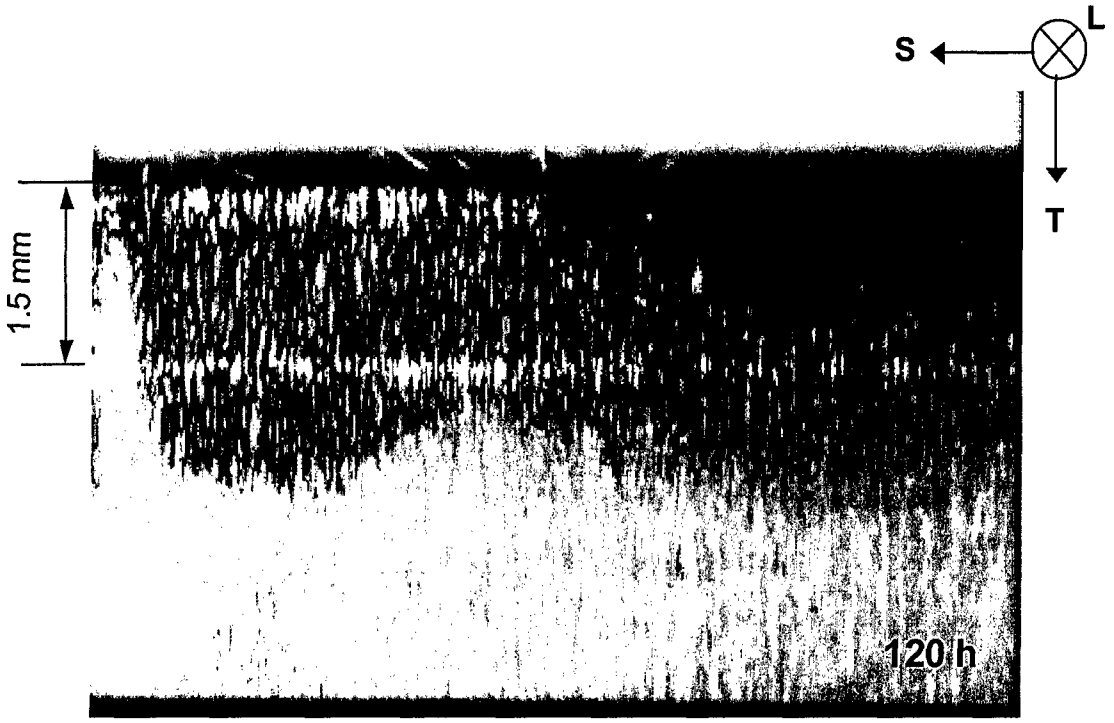

(f)

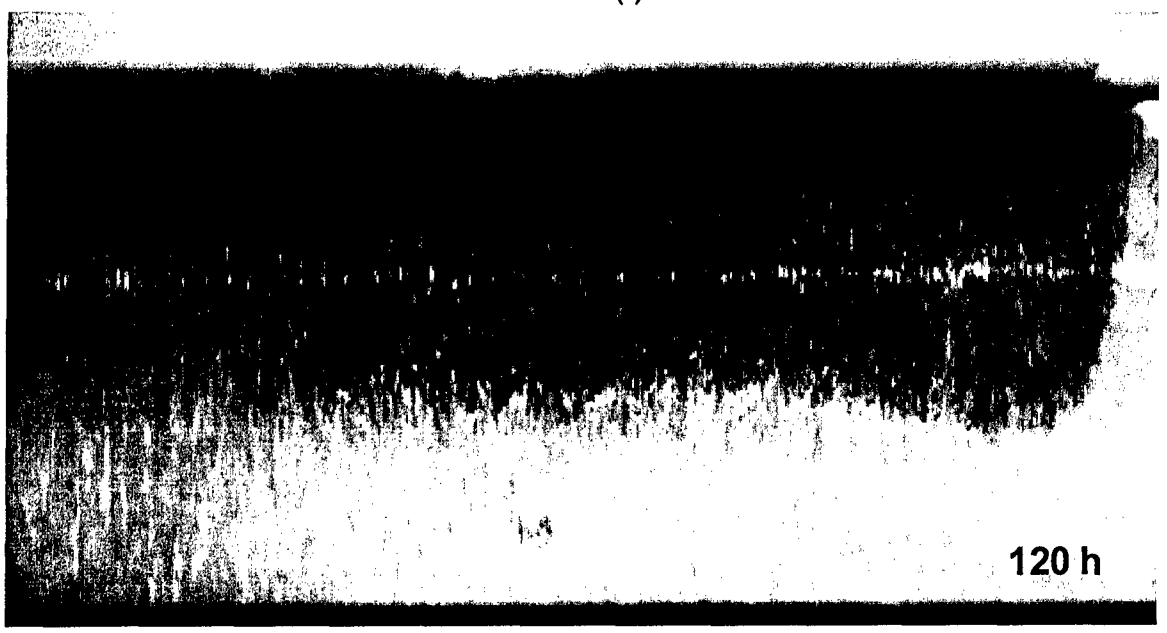

(g)

Figure 6. X-ray microfocal radiography images of IGC in unstressed T sample at –580 mV SCE in 1.0 M NaCl. (a) after 10 min, (b) after 20min, (c) after 1h, (d) after 6h, (e) after 30h, (f) after 120h, left side of the sample and (g) after 120h, right side of the sample

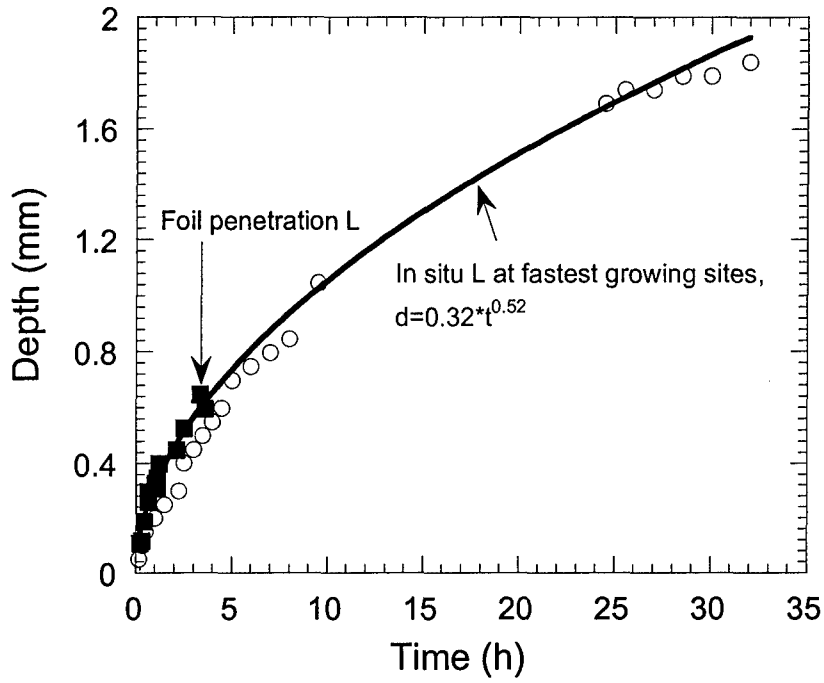

Figure 7. AA 2024-T3 at –580 mV SCE in 1.0 M NaCl. Growth rate for unstressed L of IGC from in situ radiographic experiments compared to foil penetration data.

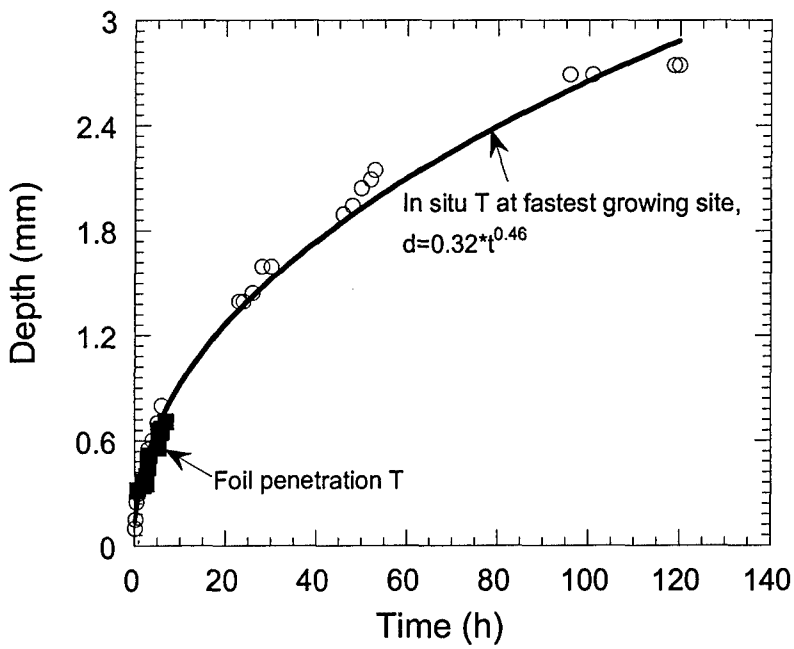

Figure 8. AA 2024-T3 at –580 mV SCE in 1.0 M NaCl. Growth rate for unstressed T of IGC from in situ radiographic experiments compared to foil penetration data.

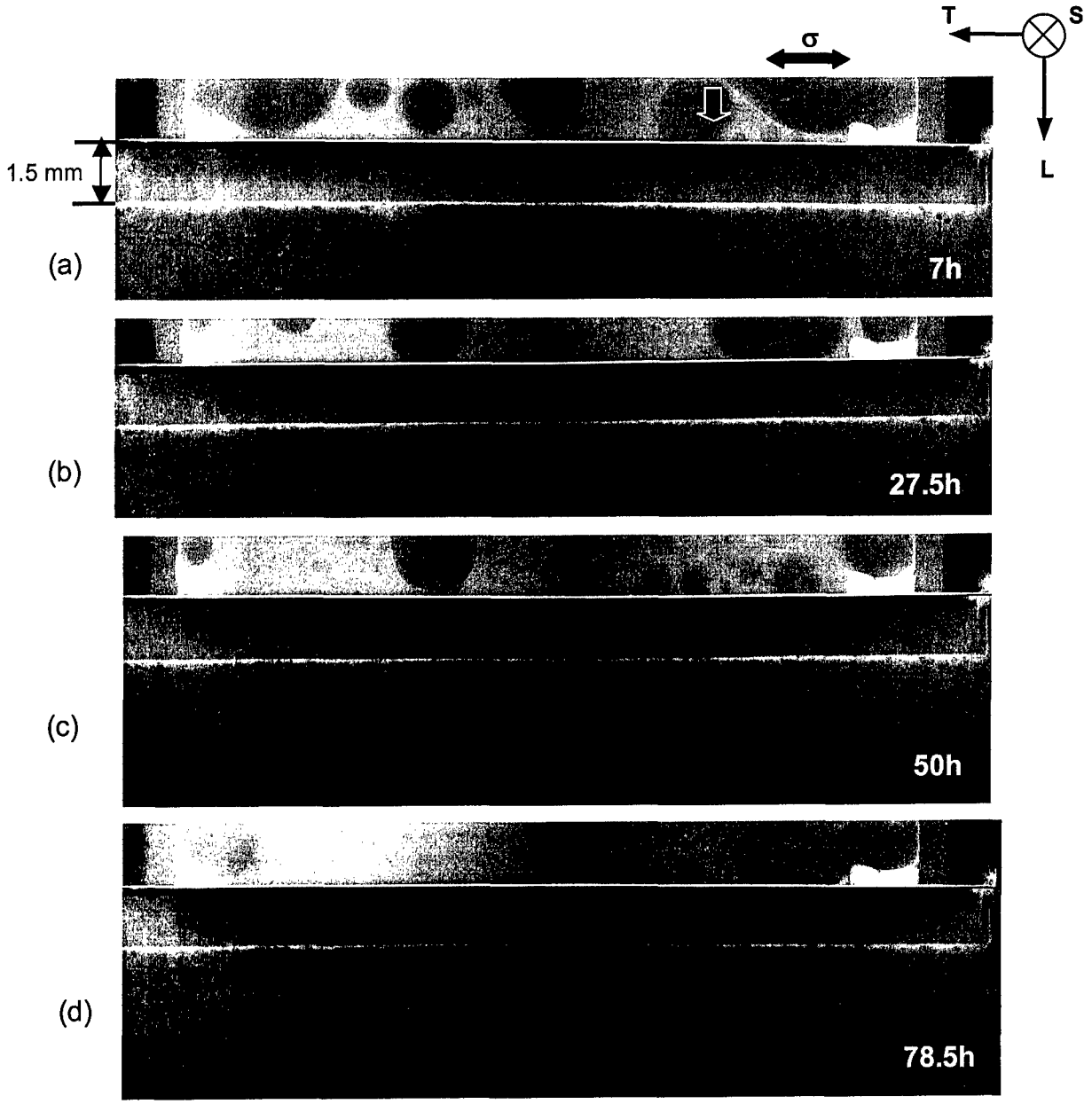
σ
T
S
L
1.5 mm
(a)
7h
(b)
27.5h
(c)
50h
(d)
78.5h

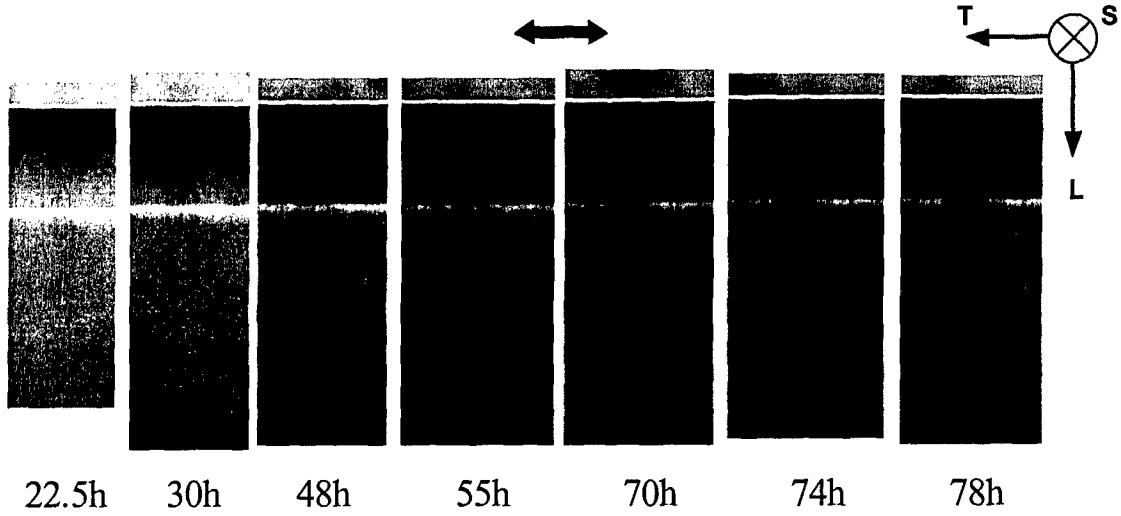

(e)

Figure 9. X-ray microfocal radiography images of IGSCC in L-T sample with initial 0.28% strain at –580 mV SCE in 1.0 M NaCl. (a) after 7h, (b) after 27.5h, (c) after 50 h., (d) after 78.5h. (e) series images of IGSCC at site 3.

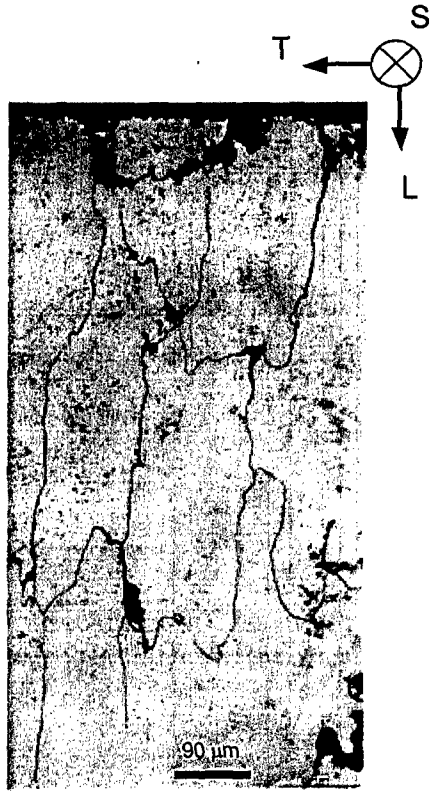

Figure 10. Metallurgical cross sectioning morphology of L-T sample after potentiostatic polarization at –580 mV SCE in 1.0 M NaCl. (a) pairs of IGCs, (b) spread crack tips.

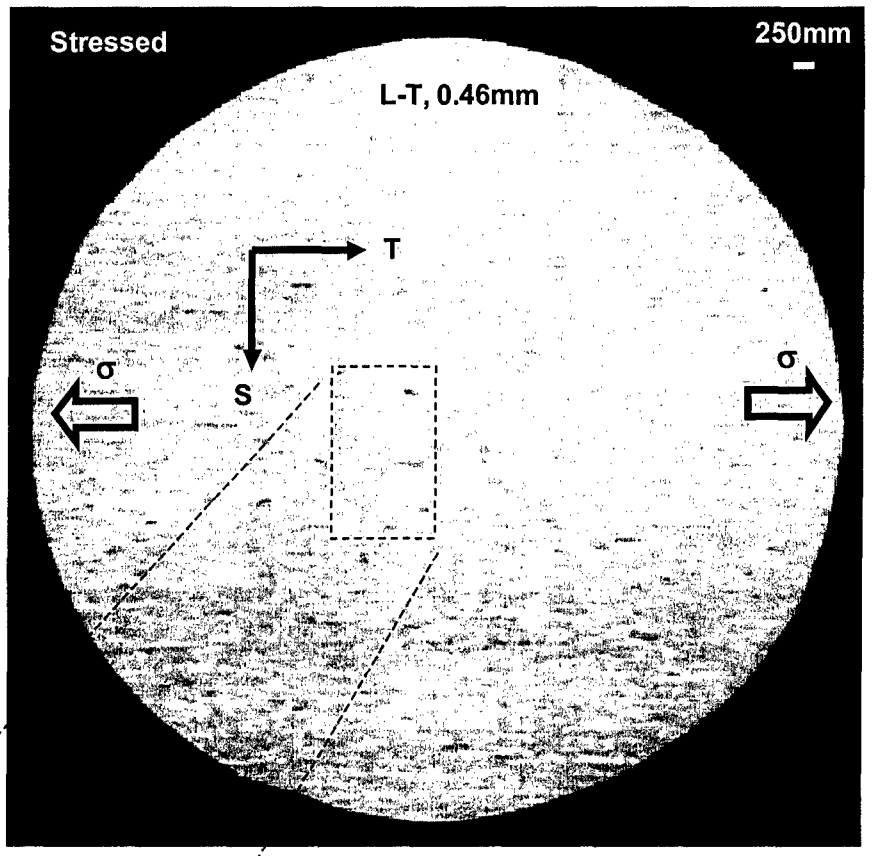

(a)

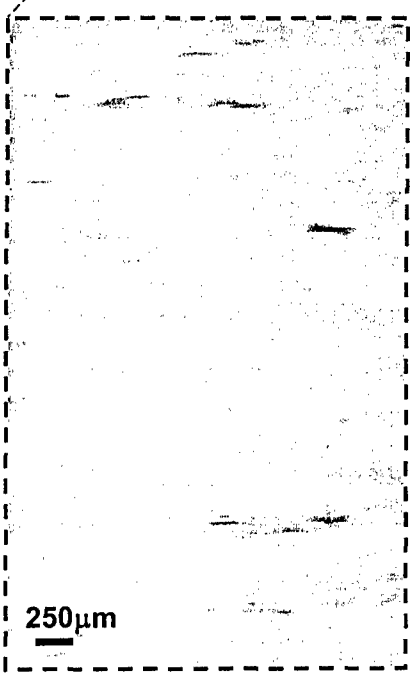

(b)

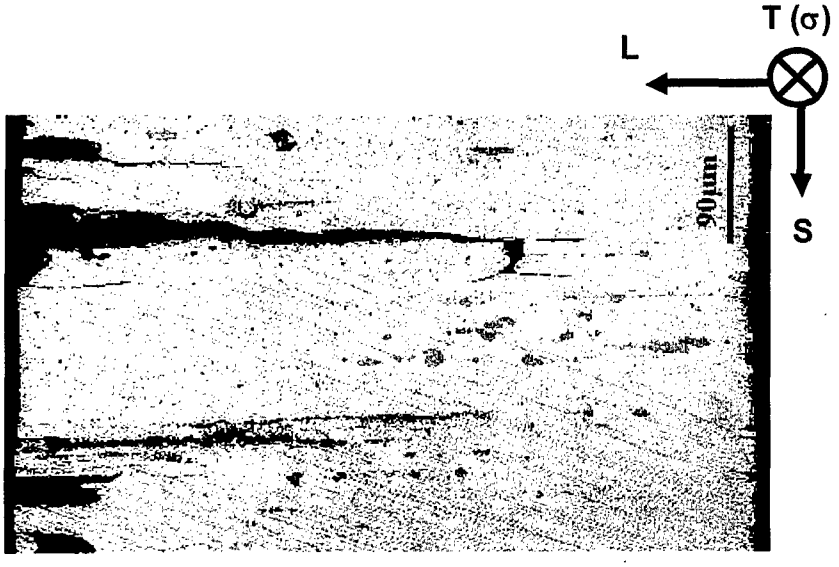

(c)

Figure 11. Images for crack in an L-T foil penetrated sample at –580 mV SCE in 1.0 M NaCl. (a) x-ray micrographic picture, (b) the magnified radiography image,(c) optical cross sectioning image.

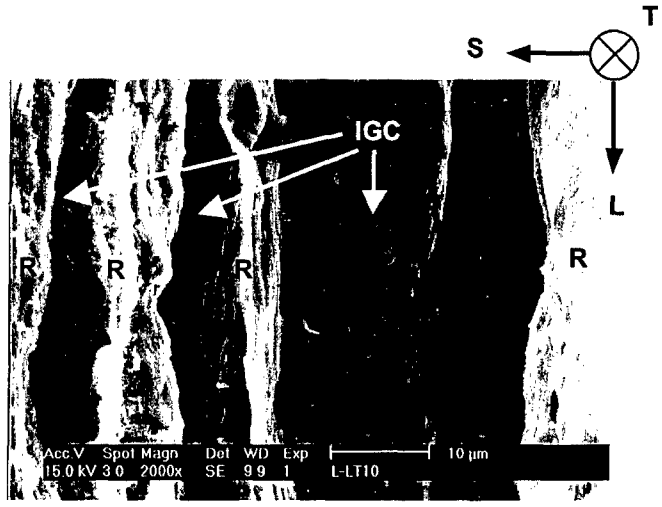

Figure 12. L sheet sample fractured in T direction. Letter "R" designates the mechanical rupture region and arrows indicate IGC regions.

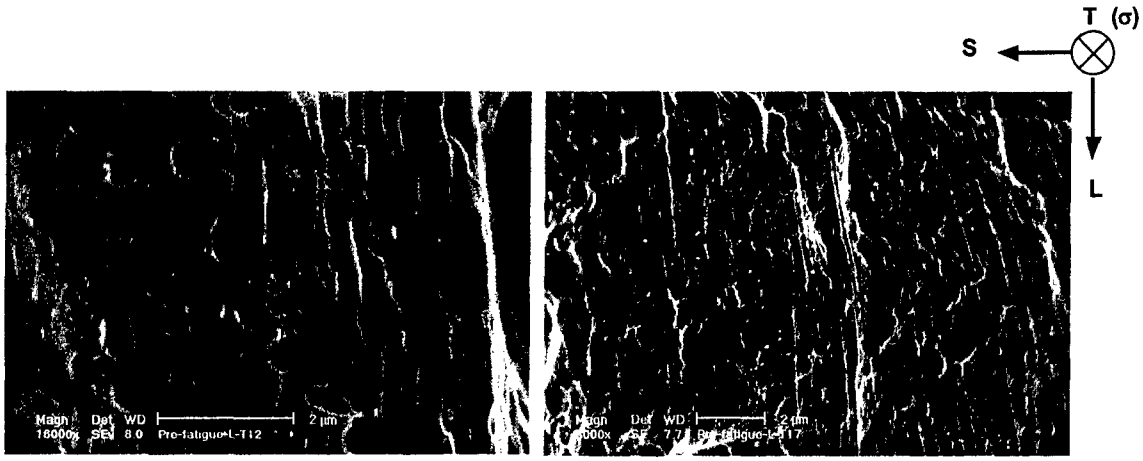

(a) (b)

Figure 13. Coalescence of multiple IGSCCs in fractured L-T sample.

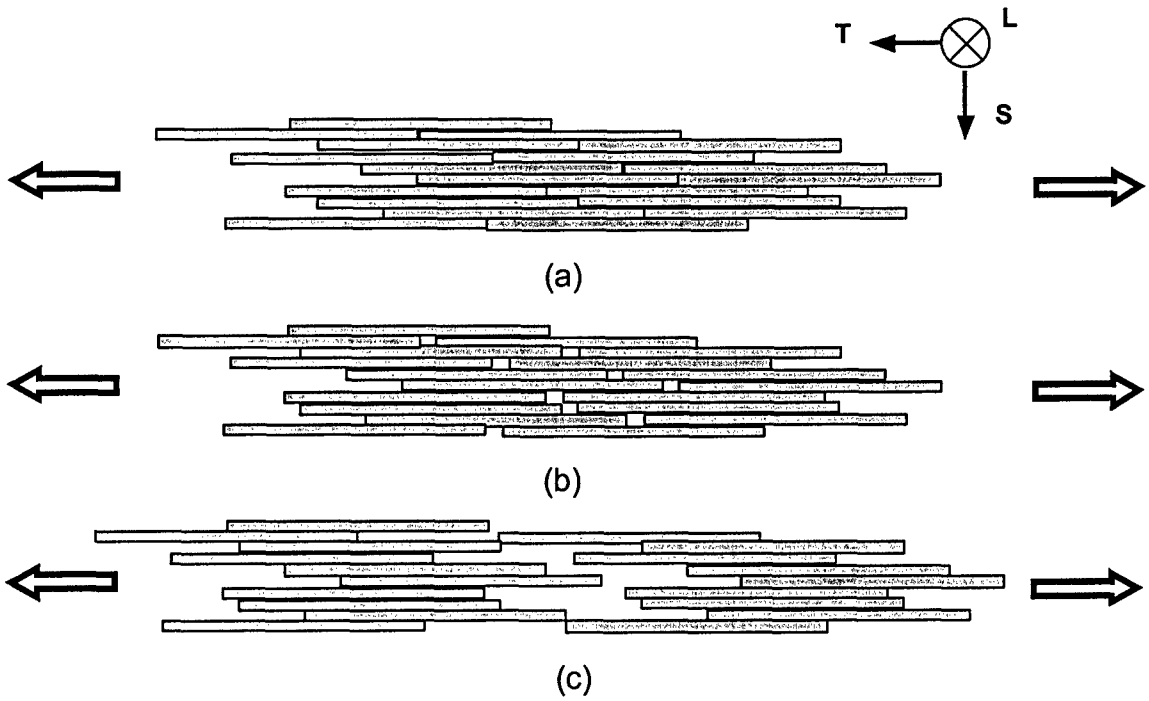

Figure 14. Schematics for crack configuration (view from L direction) in L-T sample. Rectangles represent the microstructure of an exposed L surface, with grains elongated in the T direction and thin in the S direction. (a) prior to IGC, (b) initiation of grain separation by parallel stress, (c) sparse IG cracks in turn coalesce a normal crack to the parallel stress.

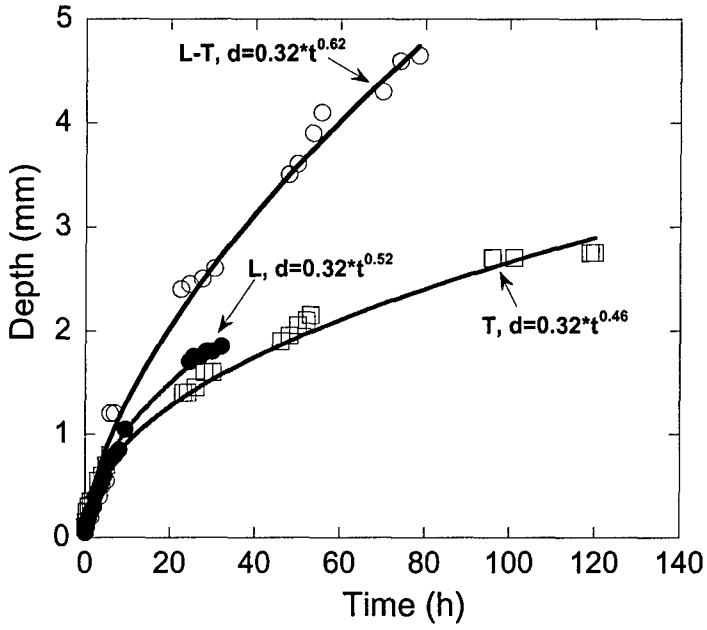

Figure 15. Growth rate of IGSCC for L, T and L-T sample at fastest growth sites at –580 mV SCE in 1.0 M NaCl from in situ radiographic experiments.

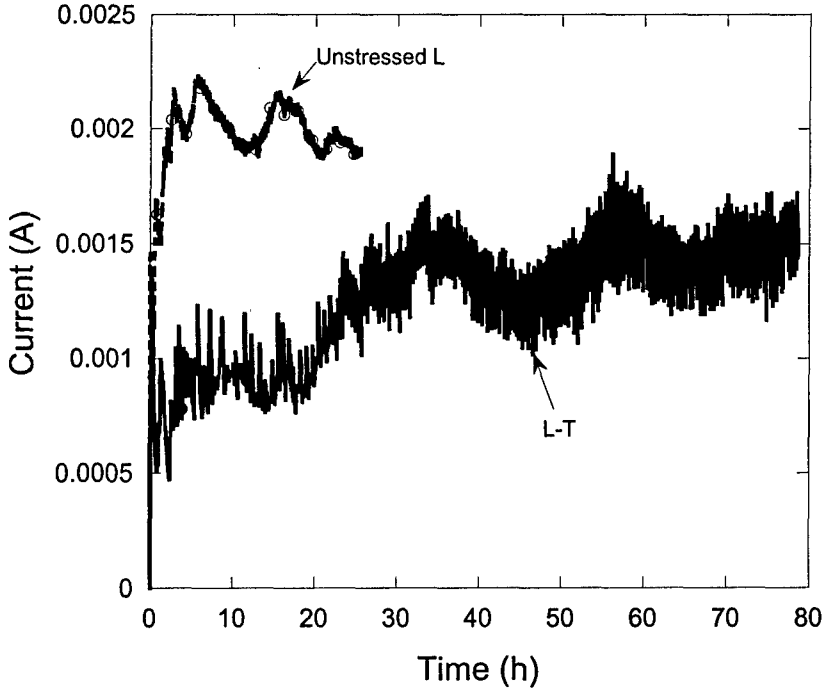

(a)

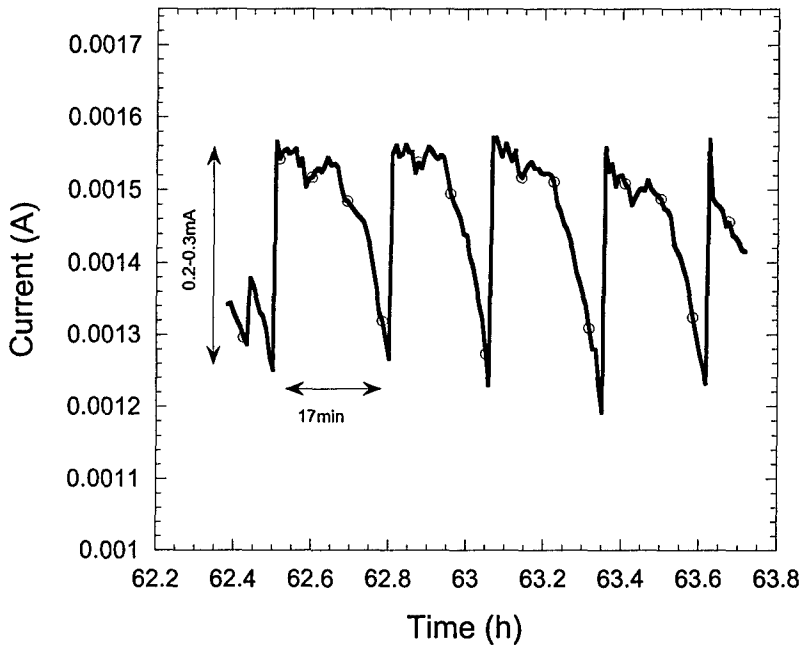

(b)

Figure 16. Current transient for L sample with and without T stress. (a) comparison of current transient in unstressed L and the L-T samples, (b) partial current transient in the L-T sample.